



**HAL**  
open science

# Radiotactic colloids: towards the Decontamination Nanobots

Vagisha Nidhi

► **To cite this version:**

Vagisha Nidhi. Radiotactic colloids: towards the Decontamination Nanobots. Micro and nanotechnologies/Microelectronics. Université Paris-Saclay, 2024. English. NNT: 2024UPASF052. tel-04807168

**HAL Id: tel-04807168**

**<https://theses.hal.science/tel-04807168v1>**

Submitted on 27 Nov 2024

**HAL** is a multi-disciplinary open access archive for the deposit and dissemination of scientific research documents, whether they are published or not. The documents may come from teaching and research institutions in France or abroad, or from public or private research centers.

L'archive ouverte pluridisciplinaire **HAL**, est destinée au dépôt et à la diffusion de documents scientifiques de niveau recherche, publiés ou non, émanant des établissements d'enseignement et de recherche français ou étrangers, des laboratoires publics ou privés.

# Radiotactic colloids: towards the Decontamination Nanobots

*Colloïdes radiotactiques: vers des nanorobots de décontamination*

**Thèse de doctorat de l'université Paris-Saclay**

École doctorale n° 571, Sciences chimiques : molécules, matériaux, instrumentations et biosystèmes (2MIB) Spécialité de doctorat : Chimie  
Graduate School : Chimie. Référent : Faculté des sciences d'Orsay

Thèse préparée dans l'unité de recherche **NIMBE** (Université Paris-Saclay, CEA, CNRS),  
sous la direction de **Jean-Philippe RENAULT**, Directeur de recherche CEA  
le co-encadrement de **Fabienne TESTARD**, Directrice de recherche CEA  
et le co-encadrement de **Florent MALLOGGI**, Directeur de recherche CEA

**Thèse soutenue à Paris-Saclay, le 10 Octobre 2024, par**

**Vagisha NIDHI**

## Composition du Jury

Membres du jury avec voix délibérative

<b>Yvette N'GONO</b> Directrice de recherche, CIMAP, Caen	Présidente
<b>Corinne CHANEAC</b> Professeur, Sorbonne Université	Rapporteuse & Examinatrice
<b>Jacques FATTACCIOLI</b> Mcf-HDR, Sorbonne Université	Rapporteur & Examineur
<b>Harold AURADOU</b> Directeur de Recherche, FAST, Université Paris Saclay	Examineur
<b>Gilgueng HWANG</b> Chargé de Recherche, LIMMS, CNRS- Université de Tokyo	Examineur

**Titre: Colloïdes radio-tactiques: vers des nanorobots de décontamination**

**Mots clés: Colloïdes actifs, particules Janus, Radiolyse, Microfluidique, Géométrie complexe, Suivi des particules**

**Résumé:** Les méthodes traditionnelles de décontamination sont confrontées à des défis importants, tels que la difficulté d'accès à des espaces complexes ou confinés (par exemple, une structure de pipeline), une grande quantité de déchets (en raison de l'élimination de parties contaminées inaccessibles), etc. Il existe toujours un besoin de développement de nouvelles méthodes pour atteindre des géométries complexes avec des processus de décontamination efficaces. Alors que les macro-robots ont été utiles dans les tâches de décontamination à grande échelle, leur taille limite leur capacité à naviguer dans des environnements complexes. Les micro ou nano robots, en revanche, peuvent traverser des espaces petits et complexes et cibler des sites de contamination spécifiques, ce qui les rend plus adaptés aux travaux de décontamination détaillés. Dans ce contexte, cette thèse étudie les capacités des micro/nanoparticules à se déplacer vers des points contaminés dans des géométries complexes, en imitant le chimiotaxisme guidé par  $H_2O_2$  (produit de la radiolyse de l'eau).

À cette fin, la synthèse et la mobilité à grande échelle de colloïdes actifs, en particulier de particules Janus, sont décrites.

Un ensemble de différents assemblages de particules d'or sur silice (assemblage isotrope ou Janus, nanoparticules discrètes ou couche d'or continue) ont été préparés, caractérisés et comparés. Leurs mouvements ont été suivis dans différents environnements. Une partie clé de ce travail a été le développement d'un dispositif microfluidique capable de générer des gradients stables de peroxyde d'hydrogène. Ce dispositif était essentiel pour étudier l'orientation directionnelle des différentes particules.

Ce travail a montré que les assemblages silice-or pouvaient se déplacer de manière autonome vers une source de  $H_2O_2$ , ce qui pourrait les rendre efficaces pour cibler des sites de contamination radioactive. Nous avons également montré que les assemblages isotropes, plus simples à préparer, peuvent également présenter un mouvement directionnel.

**Title: Radiotactic colloids: towards the Decontamination Nanobots**

**Keywords: Active Colloides, Janus particles, Radiolysis, Microfluidics, Complex Geometry, Particle Tracking**

Traditional methods of decontamination face significant challenges, such as difficulty in accessing complex or confined spaces (for example pipeline structure), high amount of waste (due to removal of unaccessible contaminated parts), etc. There is still a need for the development of new methods to reach complex geometries with effective decontamination processes. While macro-robots have been useful in large-scale decontamination tasks, their size limits their ability to navigate in intricate environments. Micro or nano robots, on the other hand, can traverse small, complex spaces and target specific contamination sites, making them more suitable for detailed decontamination work. In this context, this thesis studies the capacities of micro/nanoparticles to move towards contaminated spot in complex geometries, by mimicing the chemotaxism guided by  $H_2O_2$  (product of water radiolysis). To this end, the large-scale synthesis and mobility of active colloids, in particular Janus particles is described.

A set of different assemblies of gold particles on silica (isotropic or Janus assembly, discrete nanoparticles or continuous gold layer) were prepared, characterized and compared. Their movements were monitored in different environments. A key part of this work was the developement of a microfluidic device capable of generating stable hydrogen peroxide gradients. This device was essential to study the directionnal orientation of the different particles.

This work showed that silica-gold assemblies could move autonomously towards a source of  $H_2O_2$ , which could make them effective for targeting radioactive contamination sites. We have also shown that isotropic assemblies, which are simpler to prepare, can also exhibit directional movement.

## Résumé

Les méthodes traditionnelles de décontamination restent aujourd'hui confrontées à des défis importants, tels que la difficulté d'accès aux espaces complexes ou confinés, la quantité élevée de déchets, etc. Il est donc encore nécessaire aujourd'hui d'explorer de nouvelles méthodes permettant d'atteindre des géométries complexes avec des processus de décontamination efficaces. Même si les macrorobots se révèlent utiles dans les tâches de décontamination à grande échelle, leur taille limite leur capacité à naviguer dans des environnements complexes et confinés. Les micro ou nano robots, quant à eux, pourraient traverser de tels espaces et cibler des sites de contamination spécifiques, ce qui les rendrait plus adaptés aux travaux de décontamination en milieu confinés et complexes. Cette thèse se place dans ce contexte de recherche innovante dans le domaine de la décontamination nucléaire. L'objectif était d'explorer les potentialités de colloïdes actifs autonomes avec des propriétés chimiotactiques leur permettant de remonter des gradients de concentration de peroxyde d'oxygène ( $H_2O_2$ ), un sous-produit de la radiolyse de l'eau. Ces colloïdes aux propriétés radioactives pourraient ainsi se déplacer vers les points chauds de contamination. Pour atteindre cet objectif, le projet de thèse a porté sur la synthèse à grande échelle d'une famille de colloïdes actifs et l'étude de leur mobilité en milieu homogène ou en gradient stables de  $H_2O_2$ . Parmi les candidats possibles de particules actives, notre choix s'est porté sur les particules Janus, susceptibles d'être utilisées comme briques dans de nouvelles méthodes de décontamination.

Dans une première partie, le développement de voies de synthèses robustes a été réalisé pour produire des particules à base de Silice fonctionnalisées en surface par de l'or. Si l'asymétrie des particules Janus est majoritairement proposée comme solution pour produire des particules actives, des travaux récents dans la littérature montre que cette asymétrie n'est pas un élément indispensable pour la mobilité autonome. La comparaison particules Janus, particules isotropes est d'ailleurs rarement étudiée. Nous avons donc choisi dans ce travail d'élargir la famille de particules Janus aux particules isotropes. À cette fin, différents assemblages de particules/film d'or sur silice (assemblage isotrope ou Janus, nanoparticules discrètes ou couche d'or continue) ont été préparés, caractérisés et comparés. Des méthodes de synthèses par voie chimique en utilisant les approches émulsion/colloïdosomes pour la fonctionnalisation ou par voie physique avec les méthodes de dépôt physique par phase vapeur ont été comparées, quantifiées et discutées pour la production à grande échelle de particules.

Dans une seconde partie, les mouvements 3D et 2D de ces particules ont été suivis dans différents environnements. En milieu homogène de  $H_2O_2$ , les méthodes en volume de Diffusion Dynamique de la Lumière (DLS) et les méthodes de suivi individuel de vélocimétrie par suivi de particule (PTV) ont été utilisées. Ces analyses ont mise en évidence la nécessité de combiner les approches de mesure individuelles et collectives pour s'affranchir des limites de chaque technique, et la suffisance de l'asymétrie inhérente aux particules isotropes pour générer une mobilité autonome des particules. Ce point est important au regard de la complexité de synthèse de particules Janus contrôlées en forme, taille et taux de recouvrement.

Dans une dernière partie, le suivi de la mobilité des particules a été étudié dans un gradient stable de  $H_2O_2$ . Un élément clef de ce travail a consisté en particulier à développer un dispositif microfluidique capable de générer des gradients stables d'eau oxygénée, produit de la radiolyse de l'eau. Ce dispositif

s'est révélé essentiel pour l'analyse directionnelle du mouvement des différentes particules et a permis de renforcer les conclusions sur la comparaison entre particules Janus et particules isotropes.

En conclusion, ces travaux ont montré que les assemblages or silice pouvaient se déplacer de manière autonome vers une source d' $\text{H}_2\text{O}_2$ , ce qui pourrait les rendre efficaces pour cibler les sites de contamination radioactifs. Nous avons également montré que des assemblages isotropes, plus simples à préparer, pouvaient également présenter un mouvement directionnel. Enfin, ce projet a permis de développer des puces microfluidiques avec un gradient stable de réactifs permettant l'exploration d'autres systèmes.

*In the loving memory of my Naniji (grandmother) Lt. Suchitra Tiwari and my dearest, loving  
and proud friend Lt. Anand Verma*

*“Your wings were ready, but my heart was not.”*

- Amelia Hutchins

## Acknowledgment

*I am grateful for the financial support provided by FOCUSDEM, CEA and letting us, researchers explore in the domain of nuclear decontamination and decommissioning. My sincere gratitude to all those who have supported me throughout my research journey. First and foremost, I am grateful to my thesis director, Dr. Jean-Philippe Renault and co-director Dr. Fabienne Testard, for your invaluable guidance, and patience throughout this process. Your insightful feedback, challenging questions, and unwavering support are some key factors that shaped my work. I am incredibly indebted and grateful to Dr. Florent Malloggi, also a co-director of my thesis, for your encouragement, constructive feedback, and brainstorming sessions for my academic development. Your optimism and jovial nature played as an additional support and driving force for me, so a huge thanks to you Florent!*

*I would also like to extend my sincere appreciation to the CST members of my thesis; Dr. Harold Auradou, FAST- University of Paris Saclay and Dr. Emilie Brun, IPC – University of Paris Saclay, for their motivation, constructive feedbacks and valuable suggestions during each evaluation. My sincere thanks to Arthur Allaire and Zakariya Ait Athmane (Zak, as I/we call him) my amazing interns who were a big support to me in the final year (especially you Zak, thanks a ton for bearing with my requests). I cannot thank enough Dr. Patrick Guenoun and Dr. Sandip Wadhai for their valuable time, guidance and feedbacks. Your expertise and contributions have been invaluable. Especially Sandip, thank you for your presence and each time you extended a helping hand to me and for the times I needed a friend/guide (you are a great two in one package). In addition, I would like to thank Dr. Miguel Comesana-Hermo and his Ph.D. student Charlène Brissaud from one of our partner laboratory ITODYS, Paris, who welcomed me and trained me for silica particle synthesis at their laboratory. I would also like to thank Mr. Vincent Mertens, LEDNA – CEA Saclay and Dr. Vincent Derycke, LICSEN – CEA Saclay, for their support and guidance that helped me to achieve my targets.*

*Thank you Elodie (Mme. Elodie Collard) for your cheerfulness and the positivity you spread in our lives (we Ph.D. researchers highly benefit from that, for sure!), and thank you Mark (Dr. Mark Levenstein), PiBa (Dr. Pierre-Baptiste Flandrin), Eme (Mme. Emiline Courne) for your pep talks and timely check-ups on your office neighbour happily.*

*Finally, I am incredibly grateful to my friends and family (Maa (Mrs. Madhulata Dubey), Papa (Mr. Sudhir Kumar Dubey), Didi (Mrs. Jahnvi Gautam), Om (Mr. Kautilya Vinayak), Chilgu (M. Yuvan Srivastav) and Pappa (Prof. G. Achuthan Nair)) for your unwavering support and encouragement, as without you this journey would have been incomplete. So, a big thanks to each one of you.*

*Lastly, my special thanks to Dr. Adithya Nair, for being my spine and bearing with my mood swings throughout “this” phase!*



## Contents

<b>Chapter 1. Introduction .....</b>	<b>33</b>
1.1 General Context .....	33
1.2 Nuclear Decontamination and Decommissioning and Challenges .....	33
1.2.1 Technological Developments in Nuclear Decommissioning and the Challenges: .....	34
1.3 Working principle of decontamination nanorobots .....	35
1.3.1 Products of Water-Radiolysis as fuel for Decontamination Nanorobots .....	36
1.3.2 Particle Movement .....	37
1.3.2.1 Diffusion, Diffusiophoresis and self-diffusiophoresis .....	37
1.3.2.2 Chemophoresis .....	39
1.3.2.3 Self-thermophoresis .....	42
1.3.2.4 Bubble-propulsion .....	42
1.3.2.5 Collective Effects .....	43
1.4 Motion Study and Particles Tracking .....	44
1.4.1 Microfluidics System for Motion Study of Particles in Gradients. ....	47
1.5 Janus Particle .....	53
1.5.1 Janus Particle Synthesis: Multifaceted Approach .....	55
1.5.1.1 Masking Method .....	57
1.5.1.1.1 Phase-interface based technique .....	57
1.5.1.1.2 Template assisted .....	58
1.5.1.1.3 Evaporation based .....	60
1.5.1.1.4 Photochemical technique .....	62
1.5.1.1.5 Partial Masking based on toposelective surface modification .....	63
1.5.1.2 Phase separation Method .....	64
1.5.1.2.1 Directional flux .....	65
1.5.1.2.2 Solvent and Emulsion based method .....	66
1.5.1.3 Self-assembly .....	69
1.5.1.3.1 Langmuir-Blodgett .....	69
1.5.1.3.2 Spinning disk .....	70
1.5.1.3.3 Microfluidics .....	71
1.5.1.4 Choice of particle and method of synthesis .....	75

1.5.1.4.1	Particle to pursue .....	75
1.5.1.4.2	Particle-synthesis strategy to pursue .....	78
1.6	Points for exploration.....	80
1.6.1	Comparison of Gold/Silica Janus particles made from different methods .....	80
1.6.2	Need for particle-asymmetry for motion/propulsion? .....	81
1.7	Thesis Objective .....	81
1.8	Reference .....	83
<b>Chapter 2.</b>	<b>Particle Production .....</b>	<b>93</b>
2.1	Introduction.....	93
2.2	Material .....	94
2.2.1	Chemicals and Materials .....	94
2.2.2	Apparatus .....	94
2.2.3	Glassware and Plastic-ware.....	94
2.3	Method: Synthesis, Protocol-Optimization and Characterization Techniques.....	94
2.3.1	Synthesis of gold nanoparticles.....	94
2.3.2	Synthesis of silica particle.....	96
2.3.3	Synthesis of Janus AuNPs/Silica particles.....	98
2.3.3.1	Synthesis of Colloidosomes .....	98
2.3.3.2	Functionalization of Colloidosome .....	99
2.3.3.2.1	Procedure .....	100
2.3.4	Synthesis of Isotropic AuNPs/Silica Particles.....	102
2.3.5	Janus Gold/Silica Particle via Physical Vapour Deposition .....	104
2.3.6	Characterization techniques.....	106
2.3.6.1	UV-vis Spectroscopy: .....	106
2.3.6.2	Dynamic light scattering (DLS) and zeta potential .....	107
2.3.6.3	Scanning electron microscopy & Energy Dispersive X-ray spectroscopy (SEM/EDX): 108	
2.4	Result and Discussion .....	109
2.4.1	Gold Nanoparticles .....	109
2.4.2	Silica particle.....	112
2.4.3	Isotropic Gold/Silica Particle .....	115
2.4.4	Gold/Silica Janus Particle.....	119

2.4.4.1	Colloidosome Production .....	119
2.4.4.2	Wax Removal of Colloidosomes .....	124
2.4.4.3	Janus Particle (Functionalization with Gold Nanoparticle) .....	125
2.4.5	Gold/Silica Janus Particle via Physical Vapour Deposition Method .....	128
2.5	Conclusion .....	133
2.6	Reference .....	134
<b>Chapter 3.</b>	<b>Investigation of Particle Kinematics .....</b>	<b>138</b>
3.1	Introduction.....	138
3.2	Materials and Method.....	139
3.2.1	Material .....	139
3.2.1.1	Chemicals and Material.....	139
3.2.1.2	Apparatus .....	139
3.2.1.3	Glassware and Plastic ware .....	139
3.2.2	Method (Experiment and Data Treatment) .....	139
3.2.2.1	Experiment: Dynamic Light Scattering (DLS).....	139
3.2.2.2	Experiment: Particle Tracking Velocimetry (PTV).....	140
3.2.2.2.1	Soft Lithography (Microfabrication of PDMS microfluidic chip) .....	140
3.2.2.2.2	Experiment (PTV).....	141
3.2.2.3	Data Treatment (DLS).....	141
3.2.2.3.1	Curve Fitting of Correlogram from Samples comprising gold (Iso, JP and PVD) 146	
3.2.2.4	Data Treatment (PTV).....	148
3.2.2.4.1	An Optical Microscopy with Digital Imaging .....	149
3.2.2.4.2	Image Processing (TrackMate) .....	151
3.2.2.4.3	Data Processing (Python) .....	153
3.3	Result and Discussion .....	154
3.3.1	DLS (Result and Discussion).....	154
3.3.1.1	DLS Correlogram.....	154
3.3.1.2	Diffusion time ( $t_1$ and $T_1$ ) obtained from curve fitting of Correlograms .....	156
3.3.1.3	Apparent Particle Size .....	156
3.3.1.4	Diffusion Coefficient.....	158
3.3.2	PTV (Result and Discussion) .....	161

3.3.2.1	Motion orientation and displacement .....	161
3.3.2.2	Mean Speed.....	166
3.3.2.3	Derived Diffusion Coefficient .....	168
3.4	Conclusion .....	170
3.5	Reference .....	172
<b>Chapter 4.</b>	<b>Particle Motion in Gradient .....</b>	<b>174</b>
4.1	Introduction.....	174
4.2	Material and Method .....	174
4.2.1	Material .....	174
4.2.1.1	Chemicals and Materials .....	174
4.2.1.2	Apparatus and Softwares .....	174
4.2.1.3	Glassware and Plastic ware .....	175
4.2.2	Method.....	175
4.2.2.1	Design and Simulation (COMSOL) .....	176
4.2.2.2	Microfabrication.....	179
4.2.2.2.1	Photolithography.....	179
4.2.2.2.2	Soft Lithography .....	180
4.2.2.3	Chip Functioning Test and Alternate design.....	181
4.2.2.4	Alternative Chip design and Literature.....	184
4.2.2.5	Experiment (PTV).....	188
4.3	Result and Discussion .....	190
4.3.1	Motion Orientation .....	191
4.3.2	Mean Speed and Displacement.....	193
4.3.3	Mean Diffusion Coefficient.....	197
4.4	Conclusion .....	198
4.5	Reference .....	199
<b>Conclusion and Perspective.....</b>	<b>200</b>	
<b>Annex-1</b>	<b>206</b>	
<b>Annex-2</b>	<b>216</b>	
<b>Annex-3</b>	<b>217</b>	

## Acronym and Symbol

1.  $\varnothing$  - Diameter
2.  $^{\circ}\text{C}$  - degree Celsius
3.  $\mu\text{m}$  - Micrometer
4. AFM - Atomic Force Microscopy
5. APTES - (3-Aminopropyl)triethoxysilane
6. Au-Fe<sub>3</sub>O<sub>4</sub> - Gold/Iron Oxide
7. AuNP - Gold Nanoparticle
8. CCD - Charge-Coupled Device
9. CMC - Critical micellar concentration
10. CMR - Contrast ratio
11. COMSOL - Commercial finite element method software package for various physics and engineering applications
12. CTAB - Cetyltrimethylammonium Bromide
13. Cu@SiO<sub>2</sub> - Copper Silica (Copper deposited on Silica)
14. DHR - Dynamic light scattering (DLS) hydrodynamic radius
15. DI water - Deionized water
16. DLS - Dynamic Light Scattering
17. EDC - 1-Ethyl-3-(3-dimethylaminopropyl)carbodiimide
18. EDTA - Ethylenediaminetetraacetic Acid
19. EDX - Energy-dispersive X-ray spectroscopy
20. EIS - Electrochemical Impedance Spectroscopy
21. EtOH - Ethanol
22. FITC - Fluorescein isothiocyanate
23. FTIR - Fourier Transform Infrared Spectroscopy H<sub>2</sub>O<sub>2</sub> - Hydrogen Peroxide
24. G/P - Gold to particle ratio
25. GHz - Gigahertz
26. Gt/P - Thickness of gold layer deposited per Silica Particle
27. GTT - Gel Trapping Technique
28. H<sub>2</sub>O - Water
29. H<sub>2</sub>O<sub>2</sub> - Hydrogen Peroxide
30. H5MD - Hierarchical Data Format 5 (file format for storing molecular simulation data)
31. HAuCl<sub>4</sub> - Tetrachloroauric acid
32. HR-TEM - High-Resolution Transmission Electron Microscopy
33. IAEA - International Atomic Energy Agency
34. ICP-MS - Inductively Coupled Plasma Mass Spectrometry
35. IEP - Isoelectric Point
36. IRID - The International Research Institute for Nuclear Decommissioning
37. Iso - Isotropic gold on silica particles
38. JHMSNP - Hollow Mesoporous Silica Nanoparticles
39. JP - Chemically synthesized Gold/Silica Particles
40. K - Kelvin
41. kDa - Kilodalton
42. kHz - kilohertz

43. LoG - Laplacian of Gaussian
44. MEMS - Microelectromechanical Systems
45. Milli-Q - Milli-Q water
46. MOFs - Metal-Organic Frameworks
47. MRI - Magnetic resonance imaging
48. ms - milliseconds
49. mW - milliwatt
50. MW - molecular weight
51. NaCl - Sodium Chloride
52. NDN - Nuclear Decontamination Nanorobots
53. NHS - N-hydroxysuccinimide
54. nm - nanometer
55. NPP - Nuclear Power Plant
56. NPs - Nanoparticles
57. ns - nanoseconds
58. O/W - Oil-in-Water
59. PAH - Poly(allylamine hydrochloride)
60. PBS - Phosphate-buffered saline
61. PCV - Primary Containment Vessel
62. PDMS - Polydimethylsiloxane
63. PE - Polyethylene
64. PEO - Poly(ethylene oxide)
65. PET - Polyethylene Terephthalate
66. PLL - Poly-L-lysine
67. PLLA/PS - Poly(L-lactide)/Polystyrene
68. PNIPAAm-SPO-fluorophore-PMBA - Poly(N-isopropylacrylamide)-spironaphthoxazine-fluorophore-Poly(butyl methacrylate)
69. PNIPA-SPO - Poly(N-isopropylacrylamide-co-spironaphthoxazine methacryloyl)
70. PS - Polystyrene
71. PSA - Pressure Swing Adsorption
72. PS-b-P4VP - Polystyrene-b-poly(4-vinylpyridine)
73. PS-P2VP - Polystyrene/Poly(2-vinylpyridine)
74. PS-PI-PtBMA - Polystyrene-b-polyisoprene-b-poly(tert-butyl methacrylate)
75. PtBA/PS - Poly(tert-butyl acrylate)/Polystyrene
76. PTFE - Polytetrafluoroethylene
77. PTFE - Polytetrafluoroethylene
78. PTx - Poly[xylenol]
79. PVC - Polyvinyl Chloride
80. PVD - Physical Vapour Deposition
81. PVDF/P(St-co-tBA) - poly(vinylidene fluoride)/poly(styrene-co-tert-butyl acrylate)
82. PVP - Polyvinylpyrrolidone
83. PZC - Point of zero charge
84. RC - Relative Centrifugal Force (unit used for centrifugation speed)
85. RMPMD - Reverse Monte Carlo Procedure for Molecular Dynamics
86. RPM - Revolutions per Minute

87. SDS - Sodium Dodecyl Sulphate
88. SEM - Scanning Electron Microscope
89. SiO<sub>2</sub>@RF - Silica/resorcinol-formaldehyde
90. SiO<sub>2</sub>-Au - Silica/Gold
91. SiO<sub>2</sub>-Polymer - Silica-Polymer
92. SNP - Silica Nanoparticle
93. SPR - Surface Plasmon Resonance
94. tbsp - tablespoon
95. TEM - Transmission Electron Microscope
96. TEOS - Tetraethyl orthosilicate
97. TGA - Thermogravimetric Analysis
98. TIP - 1,3,5-Triisopropylbenzene
99. TMI - Three Mile Island (nuclear power plant)
- 100.TPD - Temperature-programmed Desorption
- 101.TPGDA/DMS - Tripropylene glycol diacrylate/Dimethyle Sulphate
- 102.TPP - Triphenylphosphine
- 103.Tris - Tris(hydroxymethyl)aminomethane
- 104.tsp - teaspoon
- 105.UV - Ultraviolet
- 106.UV-Vis - Ultraviolet-Visible Spectroscopy
- 107.VAuCap - Volume of gold cap
- 108.VAuNP - Volume of AuNP suspension
- 109.W/O - Water-in-Oil
- 110.WAuCap - Weight of gold cap
- 111.wp - Weight of single particle
- 112.wt % - weight percent
- 113.XPS - X-ray Photoelectron Spectroscopy
- 114.XRD - X-ray Diffraction
- 115.ZnO-PS - Zinc Oxide/Polystyrene

## List of Figures

Figure 1: Targeted key-features of prospective supra-molecular scale decontamination nanorobots proposed in this thesis .....	35
Figure 2: Water radiolysis and formation of primary products ( $H_2$ ; $HO^\bullet$ ; $H_2O_2$ ; $H_3O^+$ ; $HO^-$ ; $H^\bullet$ and $e_{aq}^-$ ) at respective time scale of events. <sup>14</sup> .....	36
Figure 3: Example of different types of mechanism for particle-movement.....	37
Figure 4: The concentration of atoms as a function of distance (standard deviation of mean value) for different times ( $\Delta t$ at 0.01, 0.5, 0.1 and 1) as per the central limit probability theorem. Image extracted from Campbell et al., 2009. <sup>74</sup> .....	38
Figure 5: MSD as a function of time indicating normal diffusion (linear progression) in blue, super and sub diffusion in red and green, respectively. <sup>55</sup> .....	38
Figure 6: (I) Scheme of Capillary experiment by Hong et al and (II) showing increasing population of Pt-Au rods in the respective capillaries (from (I)) with higher $H_2O_2$ concentration. Image extracted from Hong et al., 2007. <sup>78</sup> .....	40
Figure 7: Reaction causing movement in enzyme-linked Janus particles. Image extracted from Ortiz-Rivera et al., 2018. <sup>73</sup> .....	41
Figure 8: Image of different types of particles rotating in respective directions and rates in 10 wt% $H_2O_2$ (20 $\mu m$ scale). Image extracted from Brook et al, 2019. <sup>83</sup> .....	42
Figure 9: Scheme of self-electrophoresis and respective simulations (right side images) on (a) Pt layered Pt/SiO <sub>2</sub> micromotor, (b) Pt nanoparticles Pt/SiO <sub>2</sub> microsphere in $H_2O_2$ . Self-electrophoresis occurring on the Pt edges (thin or tapered parts) with its pole and equator act as the cathode and anode, respectively, while a self-generated electric field from equator to pole, propel it away from the thick part of Pt. Electrostatics numerical simulations results (images on right hand-side) showing the flow speeds along the z direction and normalized flow vectors. The bottom left inset in simulation of (b) shows the zoomed-in results of the electric potential near two Pt nanoparticles, where a total of 93 Pt nanoparticles ( $\phi$ 200 nm) arranged in concentric circles on one-half of a SiO <sub>2</sub> microsphere were considered for the study. Image extracted from Lyu et al, 2021. <sup>85</sup> .....	42
Figure 10: MOF-integrated photocatalytic micromotors for bubble propelled motion. (a) Optical snapshots showing the bubble propelled motion behaviour of micromotors in aqueous solution with 30% (w/v) $H_2O_2$ and 2% (w/v) SDS. (b) Optical snapshots showing the magnet-guided bubble-propelled motion behaviour of micromotors in aqueous solution with 10% (w/v) $H_2O_2$ and 1.5% (w/v) SDS. (c) SDS concentration-dependent velocity changes of micromotors in aqueous solutions with 30% (w/v) $H_2O_2$ . (d) $H_2O_2$ concentration-dependent velocity changes of micromotors in aqueous solutions with 1.5% (w/v) SDS. Scale bar is 1 mm. Image extracted from Chen et al., 2020. <sup>75</sup> .....	43
Figure 11: Analysis on the dynamic properties of the JHMSNP-Catalase nanomotors, (a) representative tracking trajectories of the nanomotor during 30 seconds. (b) MSD versus time interval ( $\Delta t$ ) analysed from tracking trajectories (insets are MSD curves of individual nanomotors at 0 and 1.5 wt. % $H_2O_2$ ). (c) Diffusion coefficient values determined from the slope of the linear fitting curves of average MSD plots (for panels a–c, 30 nanoparticles were analysed, and the error bars in panel c represent the standard error of mean, N = 30) and (d) diffusion coefficient histogram of the nanomotors measured by dynamic light scattering (DLS). Image extracted from Ma et al., 2015. <sup>61</sup> .....	45
Figure 12: Control over motion: (A) Average speed of polymer based nano-rockets ( $\blacktriangle$ ) at different bubble frequencies ( $\blacksquare$ ) and $H_2O_2$ concentrations in the range of 1–20 % at 22 °C. Inset shows	



dependence of the nano-rocket speed on low  $H_2O_2$  concentration at 37 °C. (B) Enzyme-Linked Janus Particles and reactions causing the movement. Image extracted from Ortiz-Rivera et al., 2018.<sup>73</sup>..... 46

Figure 13: Speed–time profiles of Au–Pt nanomotors during different 3 s heat pulses to 40 (a), 48 (b), and 58 °C (c) in a 5 wt. %  $H_2O_2$  solution. The arrows correspond to the time of switching the heating current on and off respectively. The raw data have been smoothed using fast Fourier transformation (via Origin software; 5 points). Inset displays the linear relation between the nanomotor speed and the temperature. Image extracted from Balasubramaniam et al., 2009.<sup>98</sup>..... 47

Figure 14: Summary representation of microfluidics-based gradient generator designs: (a) (left) “Christmas tree” design for 1D and (right) 2D gradient generator; (b) (left) Y-junction, (centre) T-junction, and (right) Flow splitter designs (c) (left) 1D gradient generator and (right) 2D gradient generation through pressure balance designs; d Moulded gels for (left) 1D, (centre) 2D, and (right) 3D gradient generation and (e) Submersible microfluidic probes. Image extracted from Toh et al., 2014.<sup>100</sup>..... 48

Figure 15: Solute-induced spreading/focusing colloidal labelled with fluorescein isothiocyanate (FITC), 200 nm silica particles in 1 mM TRIS buffer (pH: 9), injected with co-flowing buffer into a microfluidic channel (all inlets with same velocity). Images are recorded at the various distance  $z$  (0, 3, 7, 11, ~15, 23, 40, 50, 60 and 84 mm) from the inlet with a fluorescence CCD camera mounted on microscope at a 10x magnification (horizontal scale bar = 50  $\mu$ m). Image extracted from Abecassis et al., 2008.<sup>104</sup> 49

Figure 16: Chemotaxis by catalytic micromotors in a microfluidic device. A) 3D scheme of the microfluidic flow cell with three merging inlets in  $\Psi$ -shape (i1, i2, and i3) on the left and one larger outlet on the right. Fuel for catalytic motors, catalytic motors (Janus particles and micro-tubes) and water are inlet from i1, i2 and i3 respectively. Scale bar: 5  $\mu$ m. B) Flow test experimental model using fluorescent Rhodamine introduced from i1 for the visualization of flow-dependent diffusion of the dye molecules across the channel. Image extracted from Baraban et al., 2013.<sup>92</sup> ..... 49

Figure 17: A) Catalytic and non-catalytic particles flow with surrounding having no chemical gradient of fuel. B) Particles flowing in presence of fuel-gradient in the surrounding. Catalytic particles flow towards the higher concentration gradient of fuel, while non-catalytic particles being unaffected by the presence of fuel in B). Chemotactic behaviour of catalytic (tubes and sphere) motors quantified by determining the opening angle  $\alpha$  and  $\beta$ . Image extracted from Baraban et al., 2013.<sup>92</sup> ..... 50

Figure 18: Series A and B shows the simulation trajectories of particles from passive and active chemotaxis, respectively. The lines (orange, blue) represent average position of colloid in mesoscopic (stochastic) simulations and the corresponding filled area indicates  $\pm$  one standard deviation.  $\epsilon$  is the electric field, for  $N$  number of particles, and  $F$  resulting force experienced by these particles within the microfluidic environment. Image extracted from Deprez et al., 2017.<sup>72</sup> ..... 51

Figure 19: Intrinsic propulsion and chemotaxis of  $Cu@SiO_2$ . A) Operating principles of the positive and negative chemotaxis of  $Cu@SiO_2$  micromotors. B) Schematic diagram of the intrinsic propulsion of  $Cu@SiO_2$  micromotors in  $H_2O_2$ . C) SEM of  $Cu@SiO_2$  microsphere. D) Electric potential (colour code) and flow field lines (black arrows) around a  $Cu@SiO_2$  Janus micromotors. Image extracted from Xiao et al., 2022.<sup>105</sup> ..... 51

Figure 20: Statistical comparison between chemotaxis and non-chemotaxis behaviours of  $Cu@SiO_2$  micromotors. i) Optical micrographs, ii) trajectories and iii) distribution of the directionality of  $Cu@SiO_2$  micromotors moving in 2.5%  $H_2O_2$  without gradient A) and with the gradient B). Image extracted from Xiao et al., 2022.<sup>105</sup> ..... 52

Figure 21: a. The god Janus, beardless, Roman coin; in the Bibliothèque Nationale, Paris, while b. and c. are animations for spherical and cylindrical shaped Janus Particles; representing different structural properties, respectively. Image a extracted from Bibliothèque Nationale, Paris.<sup>108</sup> ..... 53

Figure 22: Mean squared displacement of JNPs and HNPs in bulk dispersion and at an interface showing lowest MSD for JNP at oil-water interface. Image extracted from Wang et al., 2020.<sup>66</sup> ..... 54

Figure 23: Brief overview of masking, phase separation, and self-assembly methods. Masking: particles (white circles) immobilized on template (blue base), modifying the exposed side, followed by template-removal and particle extraction. Phase Separation: emulsion of immiscible polymers is prepared and chemicals are separately cross-linked during solvent evaporation.<sup>127</sup> ..... 55

Figure 24: Different categories of methods for Janus particle synthesis..... 56

Figure 25: Example of different methods to obtain Janus particle: a) masking/unmasking method, b) Phase separation method, and f) Self-assembly method, along with strategies like c) micro-contact printing techniques, d) technique based on interfaces and partial contact and e) techniques using reactive directional fluxes or fields that fall under these methods.<sup>106,127,128,135</sup> ..... 56

Figure 26: (a) Schematic for Janus Particle produced from precursor particles arranged along a liquid/solid interface (left route) or an air-liquid interface (right route). (b) SEM image of half-raspberry-like particles made of 2  $\mu\text{m}$  reactive acrylic beads and 200 nm latex-particles. Image extracted from Fujimoto et al, 1999<sup>137</sup> ..... 57

Figure 27: (A) Scheme for micro-contact printing of surfactant (ODTAB) stamping onto a monolayer of oppositely charged particles (sulphate latex) for Janus Particles production by modifying the exposed surface. Fluorescence microscopy image B and C showing PS-latex Janus particle tagged with fluorescent dye. Image extracted from Cayre et al, 2003<sup>107</sup> ..... 59

Figure 28: Small polystyrene particles (50 nm) attached onto bigger polystyrene particles (100 nm) via PAH Snowmen like Janus Particle from layer by layer method and contact printing. Image extracted from Koo et al., 2004<sup>139</sup> ..... 59

Figure 29: Illustration of sandiwhe micro-contact printing technique for fabrication of Janus particles. Microparticles ( $\mu\text{cp}$ ) comprising reactive groups monolayered between two stamps (blue and red) getting stamped (after contact) differently on each side. Janus particles are obtained after lift-off. Image extracted from Kaufmann et al., 2012 ..... 60

Figure 30: Particle images from fluorescence microscopy showing different dyes printed on azide beads in respective observations: rhodamine alkyne (a) and dansyl alkyne (b) overlay of both images (c). Light microscope image of sample on the top right of image (c). Image extracted from Kaufmann et al., 2012.<sup>140</sup> ..... 60

Figure 31: Gold/Silica Janus nanoparticles on a glass substrate. Gold metal evaporated and deposited on exposed surface of monolayer silica nanoparticles (white circles) to obtain half surface coated with gold layer, via Physical Vapour Deposition method..... 61

Figure 32: Scheme of PVD followed by Love et al. to obtain gold/silica Janus particle, followed by dissolution of silica particles to obtain gold nano-shells (half shells). Image extracted from Love et al., 2002<sup>144</sup> ..... 61

Figure 33: Schematic representation of the experimental set-up for laser-induced Janus particle preparation by photochemical deposition of  $\text{Cr}(\text{OH})_3$  onto 10  $\mu\text{m}$  Silica beads centred in the beam. Image extracted from Hugonnot et al., 2003<sup>146</sup> ..... 62

Figure 34: Scheme of synthesis of Janus particles. A: Streams of rhodamine-labelled PEG-DA with cross linker (light grey) and PEG-DA (dark grey) co-flowing through channel. B and C: Images of rectangular Janus particles with the fluorescent labelled (orange) and the non-labelled (green) sections. The

scalebar in B and C are 50 and 100  $\mu\text{m}$ , respectively. Image extracted from Dendukuri et al.,2006.<sup>147</sup> ..... 63

Figure 35: (i) Scheme of the gel trapping technique for replicating microparticle monolayers at the oil-water and the air-water interfaces. (ii) a,b) SEM images of 3.9  $\mu\text{m}$  sulphate PS latex particles on the surface of PDMS obtained by the GTT at a decane-water interface. c) SEM image of the same surface after the mechanical removal of particles off the PDMS; producing an array of circular microholes. d) SEM image of a similar pattern of microholes produced with 2.5  $\mu\text{m}$  carboxylic PS latex particles at a decane-water interface.(iii) a,b) SEM images of Janus particles fabricated by gold sputtering on a monolayer of 2.7  $\mu\text{m}$  sulfate PS latex particles embedded on the surface of PDMS, obtained by the GTT at the decane-water interface ,followed by mechanical collection of the particles from the PDMS. c) A sample of similarly prepared 3.9  $\mu\text{m}$  PS latex/gold Janus particles collected from the PDMS with sticky tape. Image extracted from Paunov et al., 2004.<sup>149</sup> ..... 64

Figure 36: (a) Droplet generation in (top) flow-focusing glass capillary device and (bottom) co-flow or flow-focusing glass capillary device. Bottom: Examples of particles and fibers obtained from the process<sup>127,150</sup> (b). left: Scheme of electro-hydrodynamic co-jetting process, leading to either particles (electro-spraying) or fibers (electrospinning). Right: showing a typical Taylor cone used during electro-hydrodynamic co-jetting.. Image extracted from Ekanem, 2019<sup>150</sup> and Safaie, 2020.<sup>127</sup> ..... 65

Figure 37: External force fields (grey arrows) used to control the directional flux for metallic layer (black) (example gold) on top side of the particles, while having the other hemisphere protected by itself.<sup>127</sup> ..... 66

Figure 38: Silica–gold Snow like Janus Particle formed from directional fluxes (like in figure 31. A) and de-wetting half-shells of gold deposited on one of the silica hemisphere. (b) Half-shells of Gold, obtained after dissolution of the silica template. Image extracted from Love et al., 2002.<sup>144</sup> ..... 66

Figure 39: Scheme of Janus particle synthesis via Pickering Emulsion method. Emulsion made by stabilizing wax in water by particle, followed by surface functionalization of one side of particle (surface outside of wax) and lastly adding metallic nanoparticle (AuNP; Gold Nanoparticle).<sup>106,127,156,157</sup> ..... 67

Figure 40: Contact angle of particle in continuous phase and disperse phase deciding whether emulsion be 'oil-in-water' (a) or water in oil (b).<sup>152,157,159</sup> ..... 67

Figure 41: Diagram of mini-emulsion polymerization from Pickering emulsion. Image extracted from Nouri et al., 2018.<sup>161</sup> ..... 68

Figure 42: TEM images showing mushroom-like styrene/silica janus particles. Image extracted from Qiang et al., 2008<sup>160</sup> ..... 68

Figure 43: Gold/Silica Janus particle (A, B and C) synthesized from gas/liquid, liquid/solid and gas/solid interfaces, respectively. Image extracted from Petit et al., 2001<sup>165</sup> ..... 70

Figure 44:The Gyricon rotating ball display: (a) the dual-supplied spinning disk apparatus for the fabrication of bichromal balls, (b) 100  $\mu\text{m}$  black/white balls as organized on the corners of squares imaged with the gyricon display, (c) schematic cross section of the Gyricon display medium. Image extracted from Perro et al, 2005 ..... 71

Figure 45: Scheme of Wang's microfluidic set-up for the production of Gold/Silver Janus nanorods. Image extracted from Wang et al., 2019<sup>164</sup> ..... 72

Figure 46: Schematic illustration of the fabrication process of MOF-integrated photocatalytic micromotors. (a–d) Fabrication of the micromotors from O/W emulsion droplets (a) via migration of ZIF-8@ZnONPs and H<sub>2</sub>O (b), magnetic-deposition of Fe<sub>3</sub>O<sub>4</sub>@AgNPs (c), and UV polymerization (d). Image extracted from Chen et al., 2020.<sup>75</sup> ..... 72

Figure 47: Summary of key factors for deciding the materials for making Janus Particle in this thesis. ....	75
Figure 48: (a) SEM image of a Colloidosome; solidified paraffin droplet stabilized by 2 $\mu\text{m}$ aminated silica particles. (b) Confocal fluorescence microscopy image of solidified paraffin droplet stabilized by 2 $\mu\text{m}$ aminated silica particles post FITC labelling. Image extracted from Perro et al., 2005. <sup>106</sup> .....	79
Figure 49: SEM pictures showing surface of Colloidosome; monolayer of silica particles at the surface of solid wax droplet. Source: Perro et al., 2009. <sup>156</sup> .....	79
Figure 50: Diagram representing Radiotactic Nanorobots (White/Magenta circles) moving towards the source of radioactivity for decontamination (with prospective functionalization with Chelatants for grabbing the radioactive contaminants). .....	82
Figure 51: Scheme of reverse Turkevich protocol to synthesize gold nanoparticle (A) and Transition in colour during nucleation to growth phase and stabilization of synthesized gold nanoparticles (B). Starting with addition of sodium citrate to boiling water which acts as the reducing agent for the further added chloroauric acid to the boiling mixture. After the addition of precursors, the mixture is cooled down at room temperature giving a stable suspension of gold nanoparticles.....	95
Figure 52: Stöber Method mechanism for synthesis of Silica particles ( $\text{SiO}_2$ ); from hydrolysis and condensation of TEOS. Image extracted from Echesky, et al., 2023. <sup>223</sup> .....	96
Figure 53: Scheme of Silica particle (SP) synthesis and washing steps. Starting with a pre-calculated volume of MilliQ water and ethanol (EtOH) with step-wise addition of precursor molecules. After 2-3 minutes of addition of TEOS, the mixture starts turning milky with the formation of SP and finally after 2 hours excessive chemicals are washed from centrifugation. In the washing step (highlighted with green background), for the part of re-centrifugation, it is made sure that the pellet (SP) is well re-dispersed in the solvent (EtOH) by mixing it via vortex mixer before each centrifugation cycle. ....	97
Figure 54: Summary flowcharts of strategy used for Janus Particle Synthesis via Pickering Emulsion Method.....	98
Figure 55: Pickering Emulsion right after formulation process (A), after quenching in water cooled from ice-bath (B), Dry Colloidosomes appearing like a white powder (C), after filtering Pickering Emulsion and drying at room temperature. ....	99
Figure 56: Schematic representation of making Pickering Emulsion (left to right). Silica particle (SP) suspension and water mixture is given 10 minute under ultra-sonication followed by heating to 50 $^\circ\text{C}$ before adding CTAB. In parallel, wax is melted to liquid and water is cooled under ice-bath. After 30 minutes of magnetic stirring of CTAB+SP+Water mixture, melted wax is added and mixed instantly at 9500 RPM using an Ultra-turrax, giving resultant Pickering Emulsion. Emulsion was quenched (to solidify the wax droplets in Colloidosomes) and colloidosome were separated by filtering (Buchner Filter) and water-rinsing. Solidified residues of Colloidosomes are dried and stored.....	100
Figure 57: Scheme for Colloidosomes functionalization with APTES in water/ethanol mixture at 7% (v/v) of ethanol (in a Teflon container) and washing off wax with hexane, with further cleaning of APTES functionalized (partial) Silica particle ( $\text{NH}_2\text{-SP}$ ) via centrifugation. Teflon container is placed in ultra-sonic bath and vortex-mixing for wax dissolution, before centrifugation.....	101
Figure 58: Scheme of functionalization of APTES functionalized (partially) silica particle (SP- $\text{NH}_2$ ) with gold nanoparticles to obtain AuNPs/Silica Janus Particles. A pre-calculated volume of SP- $\text{NH}_2$ is taken into a polypropylene centrifuge tube and placed in an ultra-sonication bath. Suspension of AuNPs is added gradually to the SP- $\text{NH}_2$ suspension (while keeping the tube in ultra-sonic bath), followed by 10 hours mixing at a rotatory agitator. Lastly, excessive AuNPs is eliminated by centrifugation for 15 minutes at 2500 RPM. Depending upon the colour of supernatant (pink/pinkish colour indicates the	

presence of free gold nanoparticles), the step of centrifugation is done thrice with lastly re-dispersing the pellet; AuNPs/Silica Janus Particle (JP) is done in Milli-Q water..... 102

Figure 59: Scheme of synthesis of Isotropic gold/Silica Particles; starting with dispersion of silica particle (SP) in water/ethanol at 7% (v/v) Ethanol (EtOH) (in a polypropylene centrifuge tube) followed by the addition of APTES, the suspension is fixed on a rotatory agitator for 18 hours. Further, suspension is washed via centrifugation, to eliminate excessive APTES (in EtOH and Milli-Q water). Collected pellet (APTES functionalized SP; APTES-SP) is further re-dispersed in Milli-Q water in an ultrasonic bath followed after approximately 2 minutes, by the gradual addition of gold nanoparticle suspension and interaction on agitator for 18 hrs before final washing by centrifugation cycles..... 103

Figure 60: Scheme followed for the production of Gold/Silica Janus Particle via Physical Vapour Deposition method. Gold is deposited onto silica surface in second step, after a thin layer deposition (0.5 nm) of Chromium. .... 105

Figure 61: General scheme of steps followed for Gold/Silica Janus article production following Physical Vapour Deposition method. a. to c. shows plasma cleaning of glass substrate and spin coating Silica particle (SP) onto it, followed by coating Gold via physical vapour deposition on SP (c), and lastly extracting Gold/Silica Janus particle by ultra-sonic bath (d and e). .... 105

Figure 62: Schematic of a simple UV-Vis spectroscopy: Light enters the monochromator with selectively set-up wavelength of light interaction with the sample, followed by detection with the detector for output results. .... 107

Figure 63: Surface Plasmon Resonance peak for gold nanoparticles of different size showing SPR peak at around 520 nm for particles of diameter 9, 22 and 48 nm. Image extracted from Huang et al., 2010.<sup>247</sup> ..... 107

Figure 64: Scheme of Dynamic Light Scattering (DLS); speckle observation due to scattered photons observed from dynamic particles interacting with incident LASER beam. Correlator giving the autocorrelation of fluctuating scattered photons..... 108

Figure 65: Scanning Electron Microscope set-up (left) besides its display set-up (right) at LEDNA facility, CEA Saclay..... 108

Figure 66: Sodium citrate reacting with chloroauric acid producing Gold Nanoparticle (reverse Turkevich method). .... 109

Figure 67: SPR at ~520 nm for gold Nanoparticle (Red) from UV-Vis (comparison from H<sub>2</sub>AuCl<sub>4</sub> peaks in yellow spectrum) in 1mm path-length Helmma quartz cell..... 110

Figure 68: A. Correlogram for gold nanoparticles from Dynamic Light Scattering. B. Size distribution of gold nanoparticles (suspended in water) obtained from DLS measurement. .... 111

Figure 69: Correlogram of silica particles with smooth baseline indicating monodisperse particles (Broader plateau than in gold nanoparticle correlogram; Figure 67 refers to slower motion in silica particles than gold nanoparticle). .... 112

Figure 70: Smooth spherical Silica Particles confirmed from SEM at 5x and ~60x magnification (A and B respectively). Mean diameter obtained from fifty SP is 475±51 nm. Image b) shows quadruplet patten artistically arranged four silica particles..... 113

Figure 71: SEM images of SP at 10K x magnification confirming robustness and stability. A) Showing smooth surface and structure of SP before an hour long ultrasonic bath (USB). B) Showing SP after 60 min USB with no structural damage. C) Showing the size distribution of SP before (orange) and after (blue) 60 min USB. .... 113

Figure 72: Monolayer of SP from spin-coating (for PVD Janus particle production) ..... 114

Figure 73: SEM image of Isotropic Gold/Silica particle; A) functionalization of silica particles from PLL and b) functionalization of Silica particles (SP) from PAH. A) showing poor count of gold nanoparticles (AuNP) (small dots on bigger spheres; SP), while B) having higher AuNP population than A) but non-homogeneous coverage. .... 116

Figure 74: SEM images of isotropic gold/silica particles from APTES functionalization at 20K (image a) and 100K (image b). Gold nanoparticles (AuNP) (small dots on bigger spheres; silica particles (SP)) can be noticed covering big sphere (SP) homogeneously in B while some particles in A lack homogeneous distribution of gold nanoparticles. .... 116

Figure 75: Comparative UV-Vis of respective particles. LSPRs in Iso and AuNP is visible between 520-540 nm wavelengths. .... 116

Figure 76: Scheme of representing top view of Gold Nanoparticle (red circles) in simple compact 2D monolayer assembly neglecting the electrostatic repulsion. The black highlight represents a square lattice. .... 117

Figure 77: SEM-EDX image and Cartography result of Iso sample (A and B respectively). Cartography image and elemental spectra map confirming the presence of gold nanoparticles (Au) in Isotropic gold/silica particle. High intensity of Si is due to the silica wafer used for placing samples on. .... 118

Figure 78: Correlogram of Isotropic Gold/Silica Particles suspended in water, with not-smooth baseline signature. .... 119

Figure 79: Zeta potential values (mV) of silica particle (size~475 nm) suspension with CTAB, in function of the concentration of CTAB (mM). Measurements are taken 30 min after mixing SP and CTAB at a temperature of 50 °C. .... 120

Figure 80: SEM images of Colloidosomes at 250x magnification for respective concentrations of CTAB in A-D images. A) Featuring various size of Colloidosomes (spherical structures) clustered together, while D) has bigger Colloidosomes with rough surfaces. C) and D) features the desired spherical and smooth Colloidosomes with least size variations. .... 121

Figure 81: Mean size calculated from 60 Colloidosomes at respective concentration of CTAB. .... 122

Figure 82: SEM images of Colloidosome at ~1000x (Left) to and 5000x (Right) magnification for respective concentrations of CTAB in A-D images. A) Clusters of different size of Colloidosomes with majority surface lacking SP is observed. Big Colloidosomes with monolayer of partially embedded SP featured in B) and C), while D) featuring aggregated SP in D with rough surface and abruptions in spherical structures. .... 123

Figure 83: SEM images for wax dissolution off Colloidosomes using Toluene (A)) and Pentane (B)) and Hexane at 5K x and 10K x magnification (image C) and D) respectively). .... 124

Figure 84: SP with insufficient functionalization of APTES causing poor and non-homogeneous functionalization with AuNP. .... 125

Figure 85: Correlogram of chemically synthesized Janus gold/silica Janus Particle (JP) suspended in water. Observed plateau is similar to SP and Iso, while unsmooth baseline (in highlighted elliptical area) persists in JP samples. .... 125

Figure 86: UV-Vis spectra for respective samples. Highlighted area shows peaks from 520 to 540 nm for respective samples. .... 126

Figure 87: SEM images of Gold/Silica Janus Particle at 20K x magnification (a) and 100K x magnification (b). It can be clearly observed that half of the surface of silica particles (SP) is functionalized with AuNPs (small dots), confirming the synthesis of Gold/Silica Janus particles from chemical synthesis protocol of Pickering Emulsion. .... 126

Figure 88: SEM-EDX image and Cartography result for chemically synthesized Gold/Silica Janus particle (JP) sample (A and B respectively). Cartography image and elemental spectra map (C) confirms the presence of gold nanoparticles (Au) in JP. Contaminated stub giving Na-K $\alpha$  and Cl-K $\alpha$  peaks. .... 127

Figure 89: Comparison of chemically synthesized Gold/Silica Janus Particle (JP) from Pickering Emulsion Method in this thesis (A) versus JP synthesized by Perro<sup>227</sup> (B). JP showing one half of the total AuNP population in SEM and TEM images with SP $\phi$  475 and 300 nm, respectively (A and B, respectively). ..... 127

Figure 90: Correlogram for gold/silica Janus Particles produced from Physical Vapour Deposition technique. Plateau resembles with SP, Iso and JP, while fluctuating baseline signature is smoother than that in Iso and JP. .... 129

Figure 91: SEM images of PVD-JP. Image A shows PVD-JP with intermediate Chromium Layer between Gold and Silica. Image B shows PVD-JP with direct Gold Layer deposited onto the surface of Silica particles (no intermediate Chromium layer). Smooth boundaries of gold layer in A proves homogenous and better quality particle than that with rough boundaries in B. .... 130

Figure 92: Summary flowchart briefing all the particle synthesis/ key steps with their respective characterization techniques (Particles inside Bold borders have been characterized and the underlined particles are further used in Chapter 3 and 4). .... 132

Figure 93: 3D illustration of H-design microfluidic channel (left); parallel channels (1 and 2) connected with a horizontal channel (3) of length  $\ell$  called bridge while the width and height throughout the chip is  $w$  and  $h$ . Microfluidic chip adhered onto a glass slide with inlets and outlets punched (centre) and zoomed image of chip (right) ..... 140

Figure 94: Microfluidic chip with H-design channels (red highlighted region, zoomed image is shared in figure 1), connected with inlet and outlet tubes ..... 141

Figure 95: Mean correlograms for SP samples at respective concentrations of H<sub>2</sub>O<sub>2</sub>. Correlograms dropping in the same range (red-squared region) and have smooth baseline at all the concentrations of H<sub>2</sub>O<sub>2</sub> (black-encircled region). .... 142

Figure 96: Mean correlograms for Iso samples at respective concentrations of H<sub>2</sub>O<sub>2</sub>. The red squared area highlights different behaviours regarding the H<sub>2</sub>O<sub>2</sub> concentration while unsmooth/fluctuating baseline (black-encircled zone) observed with all the Iso samples. .... 142

Figure 97: Mean correlograms for JP samples at respective concentrations of H<sub>2</sub>O<sub>2</sub>. The red squared area highlights different behaviours regarding the H<sub>2</sub>O<sub>2</sub> concentration. Highly unsmooth/fluctuating baseline (black-encircled zone) observed with JP at 0% H<sub>2</sub>O<sub>2</sub> (light blue) vs. comparatively lesser unsmooth baseline for rest of the samples..... 143

Figure 98: Mean correlograms for PVD at respective H<sub>2</sub>O<sub>2</sub> concentrations. Slope in the red squared area show at 0% H<sub>2</sub>O<sub>2</sub> (light blue) bends first (left most) and have more unsmooth/fluctuating baseline (black-encircled zone) than others..... 143

Figure 99: Curve fitting of SP sample at 0% H<sub>2</sub>O<sub>2</sub>. Solid lines represent the correlograms from DLS experiment, along the fit (single exponential decay function) represented with dotted (red) line... 146

Figure 100: Curve fitting of SP sample at 0.5, 1, 3 and 5% (v/v) H<sub>2</sub>O<sub>2</sub> (A, B, C and D respectively). Solid line denotes autocorrelation function (Correlogram) obtained from DLS measurements. Red colour dotted lines denote the curve fitting from single exponential decay function. .... 146

Figure 101: Curve fitting of Iso sample at 0% H<sub>2</sub>O<sub>2</sub> from Round 1 experiment. Solid lines represents the mean correlograms from a single DLS experiment, along the fits with single exponential decay function (represented by the dotted lines) and double exponential decay function (represented by the dashed lines). .... 147

Figure 102: Curve fitting of correlograms from JP and PVD samples in 0% H<sub>2</sub>O<sub>2</sub>. Solid lines represents the correlograms from DLS experiment and curve fittings are represented with dotted and dashed line in red. Dot-lines denote fit from single exponential decay function, and dash-lines denote fits from double exponential decay function. In both JP and PVD double exponential decay (dash-lines) fits better..... 147

Figure 103: Raw image of SP suspended in Milli-Q water observed from Optical Microscopy (40x magnification). Image A shows the highlighted area of microfluidic chip (top left corner) with channel walls, but not the particles. Image B is after basic image treatment (brightness and contrast adjustments) of ROI (yellow square in image A) shows particles as white spots (encircled in yellow). ..... 149

Figure 104: Example of Results from TrackMate for tracking pristine silica particles. .... 150

Figure 105: Identification of particles for tracking; elimination of weak signals (less bright or small spots) in image. White spots in the image from observations made for SP sample suspended in Milli-Q water. A: shows all the bright spots in various size, while B: Shows selected spots with an overall size 5.5 pixel size and signal quality threshold above 45 (TrackMate detector thresholds Greyscale). .... 152

Figure 106: Example of filtration of short tracks by manually set track filters; A with low value of filter for tracks: tracks longer than 18.12 (pixel) to be accounted during tracking, while B having higher value of track-filter of 55.19 (pixels). The corresponding observations for tracked particles are C and D respectively. Due to low filter, more number of total tracks (colourful lines) seen in C and on the contrary, high filter values corresponded in lesser number of track but bigger path. .... 152

Figure 107: Trajectories obtained from SP in 0% [H<sub>2</sub>O<sub>2</sub>] sample. Trajectories from Tracking (Left) shows tracks for SP as given by TrackMate, whereas Trajectories Repositioned (Right) show all the tracks brought to a starting point of zero axis. The x and y-axis represents respective coordinates of trajectories. .... 153

Figure 108: Comparison of Pristine Silica (Blue) correlogram (autocorrelation function (y-axis) as a function of decay time (x-axis)) with modified particles (Isotropic gold/silica (Red), Chemically synthesized Gold/Silica Janus Particle (Purple) and Physically produced Gold/Silica Janus Particle (Yellow) in pure water. Only pristine silica has smooth baseline signature. Iso, JP and PVD (Yellow and Purple correlograms) having higher delay time is indicative of being bigger particle..... 154

Figure 109: Comparison of correlograms in pure water (Black: 0R1') and 5% (v/v) hydrogen peroxide (Red: 5R1'). Black correlograms (pure water) of Iso, JP and PVD are bumpier than smoother red correlograms (5% hydrogen peroxide). Correlograms for Gold/Silica PVD Janus particle is similar to correlograms for Platinum/Polystyrene PVD Janus particles in McGlasson's results<sup>1</sup> ..... 155

Figure 110: Mean Diffusion Time in milliseconds, obtained from curve fitting of DLS correlograms for respective samples. Diffusion time for Iso and JP decreases with introduction of hydrogen peroxide (and almost stable after 1% concentration)..... 156

Figure 111: Apparent mean diameter (nm) for particles (SP, Iso, JP and PVD) at respective concentration of H<sub>2</sub>O<sub>2</sub>. In Iso and JP samples, particle size decreases with increase in [H<sub>2</sub>O<sub>2</sub>], but stays in constant-range for SP and PVD samples. .... 158

Figure 112: Mean diffusion coefficient of particles at respective concentration of hydrogen peroxide. Diffusion Coefficient is unaffected with increasing hydrogen peroxide for SP (blue square) and PVD (yellow triangle) samples, unlike the Iso (red rhombus) and JP (purple triangle) samples, which increases with addition of hydrogen peroxide. High-rise in value and error found in Iso-1% [H<sub>2</sub>O<sub>2</sub>] in comparison to other sample with low error. .... 160



Figure 113: Trajectories from origin coordinates (0,0) showing overall non-directional motion in particles for respective samples at 0% [H<sub>2</sub>O<sub>2</sub>]. The x and y-axis are representative of track coordinates in pixels for particles observed in ROI. .... 161

Figure 114: Representation of the trajectories in pixels from origin coordinates (0,0) showing overall non-directional motion in particles for respective samples at 10% [H<sub>2</sub>O<sub>2</sub>]. JP in 10% [H<sub>2</sub>O<sub>2</sub>] has longer tracks than in 0% [H<sub>2</sub>O<sub>2</sub>] (Figure 19.C)..... 162

Figure 115: Displacement graphs for particles trajectories at 0%<sub>v/v</sub> H<sub>2</sub>O<sub>2</sub> calculated from total distance covered by particles throughout the observation window. Particle-displacement overall fitting Normal distribution indicates non-directional displacement of particles. .... 163

Figure 116: Displacement graphs for particles trajectories at 10%<sub>v/v</sub> H<sub>2</sub>O<sub>2</sub>. Particle-displacement overall fitting Normal distribution indicates non-directional displacement of particles. .... 164

Figure 117: Mean square displacement (MSD) ( $\mu\text{m}^2$ ) as a function of time (s) for particles at respective concentration of H<sub>2</sub>O<sub>2</sub>. No significant differences in the trend of particle-motion is evident. Dip in PVD@0% (G) due to poor statistics. .... 165

Figure 118: i) Mean Velocity of particles at respective concentration of H<sub>2</sub>O<sub>2</sub> showing highest velocity in Janus Particles. ii) Graphical representation of speed-distribution in respective particles in absence of hydrogen peroxide (0% H<sub>2</sub>O<sub>2</sub>) obtained from particle tracking via TrackMate and treating TrackMate result via Python..... 166

Figure 119: Graphical representation of speed-distribution in respective particles in 5% and 10% [H<sub>2</sub>O<sub>2</sub>] obtained from particle tracking via TrackMate and treating TrackMate result via Python..... 167

Figure 120: Mean values of derived diffusion coefficient of particle at respective concentration of hydrogen peroxide from Particle Tracking Velocimetry (PTV) technique shows Janus particle with highest diffusion rate. .... 169

Figure 121: Comparison of diffusion coefficient from PTV (solid lines) and DLS (dash-lines) at 0% and 5% (v/v) hydrogen peroxide. Particles other than PVD-PTV have similar range of diffusion coefficient. .... 169

Figure 122: (A) Labelled diagram of microfluidics channel Design-H with expected [H<sub>2</sub>O<sub>2</sub>] gradient across Bridge of length 'l', (B) showing the [H<sub>2</sub>O<sub>2</sub>] gradient across Bridge and Channel dimension width and height. Inlets and outlets are in the main channels parallel to each other (Parallel Channel 1 and 2), which are connected by the horizontal bridge (Connecting Channel 3)..... 175

Figure 123: Shows crucial factors like flow rate (A) and length (B) for achieving diffusion in bridge of H-design microfluidic channel. A (i) shows convection across bridge due to unequal flow rate, A (ii) is compatible for diffusion across bridge due to complete decoupling of parallel channel from equal flow rate. B (i) shows partial decoupling of parallel channels unlike B (ii). .... 177

Figure 124: COMSOL result to achieve stable gradient for 2 mm long bridge..... 178

Figure 125: Stable gradient of H<sub>2</sub>O<sub>2</sub> across Bridge of 'l' = 2 mm from COMSOL simulation in H-design microfluidic channel. .... 178

Figure 126: Schematic of Photolithography to obtain master mould on silica wafer with desired design ..... 180

Figure 127: H-design for microfluidic channel photolithographed on silica wafers in A (i) and bridge height assessed via interferometer in A (ii). .... 180

Figure 128: Illustration of the step-by-step microfabrication of PDMS chip microfabrication: a. Selection of master mould (photolithographed on a silica wafer) PDMS+curing agent (Sylgard) mixture preparation (10:1 w/w). b. PDMS mixture onto the master mould followed by incubation at 70°C for PDMS solidification; c. Solidified negative replica of PDMS peeled off the master mould; d. Inlet and

outlet holes punched; e-f Surface activation in PDMS chip and glass slide, by plasma treatment for facilitating the bonding; g. PDMS chip bonded on glass ready to use. ....	181
Figure 129: Schematic of Chip Functioning Test for stable gradient generation. ....	182
Figure 130: H-design chip with channels and bridge of different heights and width; $h_1 > h_2$ and $w_1 > w_2$ . ....	183
Figure 131: Modifications in H-design microfluidic channel for higher hydraulic resistance in image A) has decreased height ( $h_2$ ) and width ( $w_2$ ) in diffusion channel. Different colour lines (image B) and C)) represent mean speed and respective path of particles; dark red being the fastest and dark blue being the slowest. At equal flow rate in parallel channels, particles entering diffusion channel has light blue, green and yellow lines (white highlighted oval) in image B) confirming convection-driven movement. A little adjustment in flow-rate (red square in image C) gives convection-free diffusion of particles through the diffusion channel (confirmed by the darker blue lines in highlighted in white). ....	184
Figure 132: Two solutions A and B of different concentration flowing through channels, creating concentration gradient across the array of connecting channels. <sup>9</sup> The colour reflects the concentration; dark blue is minimum and dark red is the maximum. Figure regenerated from Irimia et al. <sup>9</sup> ....	184
Figure 133: First and second layer after photolithography (in A and B respectively) at 10 x magnification. (C) Dimensional details of the concentration gradient generating microfluidic chip used for PTV experiments. ....	186
Figure 134: Y-design microfluidic channel (A). Image (ii) of B and C are the profilometric analysis (credit: Dr. Florent Malloggi), of the developed microfluidic channels. $h_2 \sim 7 \mu\text{m}$ measured from interferometer in B (ii), is after the photolithography of first layer (array of bridges) of the microfluidic channel (B (i)). C shows image after second layer of is photolithographed and measured height from interferometer in (ii) shows $h_1 \sim 56 \mu\text{m}$ . Magnification of the images B and C (i) is 10 x. ....	187
Figure 135: Chip functioning test for Y-shaped chip for continuous gradient generation. Highlighted areas (green) from simulation result in image (i) (credit: Zakariya Ait Athmane), are compared with experimental observation in image (ii). Image (ii) is obtained after 5 minutes stabilization time with water flow dominating over R6G flow (highlighted in blue). The reducing gray scale intensity in the highlighted (red) diffusion channel in image (iii) shows stable gradient achievement at time (t) 0 to 20 seconds. Red arrow ( ) represent the direction of diffusion of R6G (higher to lower concentration). ....	188
Figure 136: Scheme of PTV experiment set-up with microfluidic chip connected to a pressure pump. ....	189
Figure 137: ROI in central region of diffusion channel, away from boundary walls of the channel..	190
Figure 138: Complete trajectories of observed SP in one of the diffusion channel (from bridge-array) at 0% H <sub>2</sub> O on left. Selected highlighted regions are zoomed and show initial and end-points of trajectories (black and red triangles, respectively). Each colour denotes different trajectories for its respective particles. ....	190
Figure 139: SP trajectory at respective concentration gradient of hydrogen peroxide showing non-directional motion. ....	191
Figure 140: Trajectories for Iso, JP and PVD (A,B and C, respectively) at respective concentration gradient of H <sub>2</sub> O <sub>2</sub> showing directional motion in 5% and 10% (v/v) H <sub>2</sub> O <sub>2</sub> gradient by all the particles. ....	192
Figure 141: Mean Velocity of particles at respective concentration gradient of hydrogen peroxide	193

Figure 142: Displacement graphs (calculated from particle-displacement between two consecutive images) for particles at respective H <sub>2</sub> O <sub>2</sub> gradient. Negative shift in displacement from centre at 5% and 10% H <sub>2</sub> O <sub>2</sub> plots in B – D indicates directional motion towards the H <sub>2</sub> O <sub>2</sub> .....	195
Figure 143: Comparison of MSD at different concentration of H <sub>2</sub> O <sub>2</sub> . With 0% H <sub>2</sub> O <sub>2</sub> (blue) as reference, positive shift in MSD at 5% (orange) and 10% (blue) H <sub>2</sub> O <sub>2</sub> confirms hyper-diffusive motion for Iso, JP and PVD in gradient of hydrogen peroxide.....	196
Figure 144: SEM images of PVD samples in 0% hydrogen peroxide (at 20 and 40x in A(i) and (ii), respectively), showing smooth gold layers (green highlights) on SP, while B(i) and (ii) showing PVD samples in 5% hydrogen peroxide, with melted gold layers (yellow highlights) on SP. ....	196
Figure 145: Diffusion Coefficient mean values for particles at respective concentration of hydrogen peroxide. With increasing hydrogen peroxide gradient concentration diffusion coefficient of Iso, PVD and PVD increases, while SP is unaffected.....	198
Figure 146: Labelled diagram of working principle of a Scanning Electron Microscope (FEG-SEM) with Field Emission Gun. FEG SEM allows a better resolution.....	208
Figure 147: A Perro's <sup>26</sup> gold/silica janus particle (mean diameter ~300 nm and 15 nm for SP and AuNP respectively) <sup>26</sup> . Size of gold nanoparticles was calculated by ImageJ from the image extracted from the paper. Image extracted from Perro, 2009. <sup>26</sup> .....	211
Figure 148: Petit's <sup>27</sup> gold/silica Janus nanoparticle (Silica nanoparticle mean diameter 90-120 nm and AuNP mean diameter 8 – 10 nm) <sup>27</sup> . Left image is from synthesis in gas-liquid phase of synthesis while right image is from particles synthesis from liquid-solid interface. Image extracted Petit, 2001 <sup>27</sup> ....	212
Figure 149: Gold/Silica Janus particles synthesized by Yang. JB <sup>a</sup> ; Janus Balance is the surface area ratio of the gold nanoparticle and silica particles. Image extracted from Yang, 2013 <sup>28</sup> .....	212
Figure 150: SEM images of gold/silica janus particles. ~650 nm dia. gold patch on 1.5 µm dia. silica particle (top) and ~100 nm dia. gold patch on 200 nm dia. silica particle (bottom). Image extracted from Lu et al., 2003. <sup>29</sup> .....	212
Figure 151: TEM images of gold/silica janus particles. A) ~13 nm dia. gold nanoparticle on ~21 nm dia. silica particle. B) Magnified images of Gold/Silica Janus particle. Image extracted from Percebom et al., 2015. <sup>30</sup> .....	212
Figure 152: TEM images of gold/silica janus particles. A and D having 10 nm dia. gold nanoparticle in ~80 nm and ~165 nm dia. silica particles, respectively. B and E (top) having 30 nm dia. gold nanoparticle in ~100 nm and ~270 dia. silica particles, respectively. While C and F having ~70 nm dia. gold nanoparticle in ~140 nm and ~230 nm dia. silica particle, respectively. Image extracted from Vega et al., 2019. <sup>31</sup> .....	213
Figure 153: TEM images of gold nanoparticles (AuNP) and gold/mesoporous silica janus particles (AuMS). Mean diameter of gold nanoparticle is 62.5 ± 6.4 nm, while mean diameter of AuMS is 155 ± 11.4 nm. Image extracted from Trayford et al., 2022. <sup>9</sup> .....	213
Figure 154: SEM images used for estimating the approximate mean diameter of AuNP (~25 nm)...	215
Figure 155: SEM images of Iso sample used for calculating average mean count of AuNP per Iso ...	215

## List of Table

Table 1: The advantage/disadvantages of various methods for the production of Janus Particles, along with the range of particle size obtainable, and application.....	73
---	----

Table 2: Enlists various types of Janus Particles, synthesis techniques, morphologies, particle size-scale, movement mechanism and rate of diffusion. ....	74
Table 3: Enlisted are the features of Janus Particles summarised in the table.....	77
Table 4: Comparison of Gold/Silica Janus particles shared by various researchers, with respect to the producible size range of particle, yield, advantages and disadvantages of the respective methods. <sup>106,127,156,158</sup> .....	77
Table 5: Summary of key factors in the methods followed for synthesising particles and their respective mean diameter. ....	106
Table 6: Surface Plasmon Peak by gold nanoparticle, absorbance at 400 nm of a typical AuNPs batches with the respective hydrodynamic size (Mean size) issued from DLS. The [Au(0)] concentration and the AuNPs density numbers have been calculated from $A_{\lambda=400nm}$ and from equation 1. ....	111
Table 7: Properties of silica particle synthesized and utilized to make isotropic and Janus gold/silica particles (*).....	114
Table 8: Theoretical Values for number of gold nanoparticles per Isotropic Gold/Silica Particles calculated from AuNP radius, SP radius. ....	117
Table 9: Colloidosome mean size at respective CTAB concentration .....	122
Table 10 : Minimal volume of SP suspension required for a monolayer deposited on a glass substrate. ....	128
Table 11: Result for properties of PVD-JP (gold/silica Janus particle produced from Physical Vapour Deposition method) with silica density of 2.32 g/cc .....	131
Table 12: Features of particles synthesized in this thesis work (*). ....	131
Table 13: Theoretically values of diffusion coefficient (from Eq. 4) for respective samples. ....	145
Table 14: Mean values of 'diffusion time' obtained from fitting correlogram of each rounds of experiment for respective sample with single or double exponential models. $t_1$ denotes time obtained from single exponential while $T_1$ and $T_2$ values of time obtained from double exponentials fits. Number in $nR_i$ refers to $n$ the concentration of $H_2O_2$ in % v/v and $i$ to the number of DLS analysis, while $R$ refers to number of round of experiment. ....	148
Table 15: Mean diameter of particles from each round of experiment for respective samples. ....	157
Table 16: Mean diameter of SP, Iso, JP and PVD samples at respective concentration of hydrogen peroxide. JP samples showing decrement in mean diameter with increasing percentage of hydrogen peroxide, while for Iso sample diameter reduced on introduction of hydrogen peroxide (0.5%) and stays in same range further. Unlike JP and Iso, diameter of SP and PVD samples remaining unaffected with addition of hydrogen peroxide.....	157
Table 17: Mean values of diffusion coefficient from each round of experiment for respective samples. ....	159
Table 18: Mean diffusion coefficient at 0, 0.5, 1, 3 and 5% (v/v) hydrogen peroxide for SP, Iso, JP and PVD samples showing increased value of diffusion coefficient with addition of hydrogen peroxide in Iso and JP sample, while values for SP and PVD samples remaining unaffected.....	160
Table 19: Mean speed of particles in respective concentration of hydrogen peroxide. JP, SP and Iso follow PVD having highest speed in 0 and 5% (v/v) hydrogen peroxide, while JP and SP having equal mean speed in absence of hydrogen peroxide. ....	168
Table 20: Mean Diffusion Coefficient values for particles at respective concentration of hydrogen peroxide. SP showing no impact of hydrogen peroxide, while Janus particles (JP and PVD) shows highest relative difference amongst all the samples. ....	169

Table 21: Diffusion coefficient comparison table between DLS and PTV. Iso shows fastest diffusion in 3D experiments (DLS), Janus particles faster diffusion in 2D experiment (PTV).....	170
Table 22: Relative change (%) in mean diffusion coefficient calculated from DLS and PTV experiments for respective samples. ....	170
Table 23: Mean Velocity of particles at respective concentration gradient of hydrogen peroxide ...	193
Table 24: Comparison of relative change (%) in diffusion coefficient from gradient/no-gradient experiments.....	197
Table 25: Mean Diffusion Coefficient of particles at respective gradient concentration of hydrogen peroxide.....	198
Table 26: Featuring values of properties utilized for the calculation of concentration of gold nanoparticle from the synthesis.....	208
Table 27: Parameter for Iso and JP synthesized in this thesis, compared (JP) with JP from A Perro's work <sup>26</sup> (both JP followed chemical synthesis protocol of Pickering Emulsion).....	209
Table 28: Summary of number of chemical species present in respective particles .....	209
Table 29: Calculation table showing different properties for respective particles.....	210
Table 30: Values for APTES for covering 0.75 m <sup>2</sup> area of silica particles for making Isotropic Gold/Silica particles.....	211
Table 31: Sample composition for respective DLS experiments. Volume of water and H <sub>2</sub> O <sub>2</sub> is in $\mu$ L.	216
Table 32: DLS Observations for polydispersity (PDI), Particle size (Mean $\phi_{nm}$ ) and sample quality (Intercept). Obtained PDI range and intercept values confirms that the samples preparation is in optimal range to conduct DLS studies.....	216
Table 33: Mean values for physical properties (size and weigh) of particles studied in this thesis summarized in the table. Calculated values are obtained from properties (like density, size, and gold layer-thickness for PVD) shared in section 2.4 of Chapter 2.....	216
Table 34: Number of tracked spots obtained from Particle Tracking via TrackMate (Spot Result)....	216
Table 35: Velocity of particles from each round of experiments.....	217
Table 36: Diffusion Coefficient for particles from each round of experiment.....	217
Table 37: Comparison of diffusion coefficient from experiments with hydrogen peroxide gradient and no-gradient.....	217

## GENERAL INTRODUCTION

### A Potential Alternative of Radiotactic Colloids Towards Nuclear Decontamination Nanorobot

Nuclear power is a significant source of electricity globally and largest in France with ~70% of total electricity generation from nuclear power plants.<sup>1</sup> Additionally, nuclear decontamination is crucial across various sectors beyond the nuclear power industry. In healthcare, it ensures that medical equipment and facilities exposed to radioactive materials are safe for patients and staff, preventing harmful radiation exposure.<sup>2-4</sup> Once the life of a nuclear power plant is over, decommissioning it is essential. Decontamination; a major part of nuclear decommissioning, is the process of removing radioactive contaminants and is crucial for waste management.<sup>7,8</sup> In the defence sector, decontamination procedures are necessary to manage radioactive contamination from nuclear weapons testing or accidents, protecting military personnel and civilians. Effective decontamination processes also support environmental remediation efforts, ensuring that land and water sources contaminated by industrial activities or accidents are restored to safe conditions.<sup>5,6</sup>

Conventional decontamination methods often have limitations. Some of these limitations are high exposure risks and complex waste generation. Decontamination robots; an advancement in this field face challenge of limited accessibility, especially with complex geometries and higher radiation dose.<sup>8,9</sup> Therefore, the transition from macro-robots to nanorobots in decontamination efforts can be an option to address these limitations. While macro robots are effective in handling large-scale decontamination tasks, their size and mechanical constraints, limit their ability to access and clean intricate or confined areas. On the other hand, nanorobots, due to their small size, can offer an alternative to these limitations, allowing them to navigate through complex geometries and precisely targeting contamination-sites. This transition from macro-robots to nanorobots in decontamination efforts represents a significant technological advancement in the field of decontamination, enhancing the effectiveness along with micro- to nano- scale decontamination-specificity. This thesis explores the potential of radiotactic colloids, a novel approach to nuclear decontamination nanorobots (NDN) (radiotactic colloid). These nano/sub-micro sized active particles are designed for autonomous motion towards radioactive contamination sources, especially alpha and beta emitters.

Proposed NDN would benefit their motion from the products of water-radiolysis; the process by which radiation breaks down water molecules, generating hydrogen peroxide ( $H_2O_2$ ). Radiotaxis is the term we want to define for motion induced (directly/indirectly) from nuclear radiation. Inspired from Chemotaxis in nature; movement in microorganisms towards a chemical source or food,<sup>10,11</sup> we aim to achieve self-propulsion in these particles by using the gradient of  $H_2O_2$  (a product of water-radiolysis)<sup>12</sup> as fuel. These particles could target and decontaminate specific areas through surface functionalized with chelating agents (specific for nuclear contaminants). For this purpose, Janus particle<sup>13</sup> appear as a promising candidate, which along with other particles (particles with isotropic surface-modifications) are studied in this thesis. Our research investigates the development of radiotactic colloids through the synthesis and characterization of Janus particles, a specific type of particle with two or more distinctive surfaces. In this thesis, motion of these particles in response to  $H_2O_2$  gradients the groundwork for future exploration of the chemically synthesized Janus Particles as a potential candidate in nuclear decontamination.

The first chapter of this thesis provides background on nuclear decommissioning, decontamination challenges, and introduces the concept of radiotactic colloids along with the prospective particles compatible for the production of Janus Particles; Gold/Silica Janus Particles. It essentially guides this thesis for identifying reproducible protocol for bulk production of particles, techniques to conduct comparative motion study; Dynamic Light Scattering (DLS) and Particle Tracking Velocimetry (PTV) and understand the impact of particle-morphology on its motion in chemical surrounding. The second chapter describes the synthesis and characterization of the different types of Gold/Silica Janus particles and other particle; Pristine Silica Particle and Isotropic gold-on-silica particles. As the morphology of these particles differ, the complexity in their synthesis also differ. Upon a successful synthesis and characterization of particles, it can be interesting to compare motion and interaction of these particles in chemical surrounding. Chapter 3 is focused on the motion in bulk and in different concentrations of H<sub>2</sub>O<sub>2</sub> by using Dynamic Light Scattering (DLS) and Particle Tracking Velocimetry (PTV). During this motion study it is found that unlike pristine Silica Particles, particles with modified surface (with gold on it) show hyper-diffusive motion trend but lacks directional preference, therefore, further motion study is conducted in presence of a continuous stable gradient of H<sub>2</sub>O<sub>2</sub>. A stable chemical gradient is crucial for the precise study of motion as it offers a controlled environment facilitating model-simulation, accurate measurements, therefore, enhancing the understanding of particle kinematics.<sup>14,15</sup>

Particle motion in H<sub>2</sub>O<sub>2</sub> gradient presents a need for a stable-gradient generator device. For this purpose, microfluidic device is a good candidate because of multiple benefits like small sample requirement, predictability and reproducibility, well-defined environment, control over fluid flow and mixing. Therefore, the last chapter of this thesis focuses on the designing and developments of a microfluidics device for concentration gradient generation. Once the stable-gradient generator device is made, particle motion in stable gradient of H<sub>2</sub>O<sub>2</sub> is analyzed. Overall, our work highlights the potential of studied particles as radiotactic colloids towards nuclear decontamination, and proposes future research directions towards an alternative of a potentially safer and complex-geometry targeted approach to nuclear decontamination.

- (1) PR-FY-2023-V16.02.2024.Pdf. <https://www.edf.fr/sites/groupe/files/epresspack/7068/PR-FY-2023-V16.02.2024.pdf>.
- (2) Procedures for Radiation Decontamination - Radiation Emergency Medical Management. [https://remm.hhs.gov/ext\\_contamination.htm#caution](https://remm.hhs.gov/ext_contamination.htm#caution).
- (3) Cibulsky, S. M.; Sokolowski, D.; Lafontaine, M.; Gagnon, C.; Blain, P. G.; Russell, D.; Kreppel, H.; Biederbick, W.; Shimazu, T.; Kondo, H.; Saito, T.; Jourdain, J.-R.; Paquet, F.; Li, C.; Akashi, M.; Tatsuzaki, H.; Prosser, L. *Mass Casualty Decontamination in a Chemical or Radiological/Nuclear Incident with External Contamination: Guiding Principles and Research Needs. PLoS Curr* **2015**. <https://doi.org/10.1371/currents.dis.9489f4c319d9105dd0f1435ca182eaa9>.
- (4) First-in-human trial of oral drug to remove radioactive contamination begins. National Institutes of Health (NIH). <https://www.nih.gov/news-events/news-releases/first-human-trial-oral-drug-remove-radioactive-contamination-begins>.
- (5) TE-2001web.Pdf. <https://www-pub.iaea.org/MTCD/Publications/PDF/TE-2001web.pdf>.
- (6) Datta, S.; Radhapyari, K.; Saha, N.; Samanta, S. K. Chapter 7 - Recent Trends in the Application of Biowaste for Hazardous Radioactive Waste Treatment. In *Environmental Sustainability and Industries*; Singh, P., Bassin, J. P., Rajkhowa, S., Hussain, C. M., Oraon, R., Eds.; Elsevier, 2022; pp 159–192. <https://doi.org/10.1016/B978-0-323-90034-8.00010-5>.
- (7) PRIS - Trend reports - Nuclear Power Capacity. <https://pris.iaea.org/PRIS/WorldStatistics/WorldTrendNuclearPowerCapacity.aspx>.
- (8) Decontamination Techniques Used in Decommissioning Activities. Nuclear Energy Agency (NEA). [https://www.oecd-nea.org/jcms/pl\\_13258/decontamination-techniques-used-in-decommissioning-activities?details=true](https://www.oecd-nea.org/jcms/pl_13258/decontamination-techniques-used-in-decommissioning-activities?details=true).
- (9) Hussein, T. From Chernobyl to Iron Man suits: the development of nuclear waste robotics. *Power Technology*. <https://www.power-technology.com/features/cleaning-up-nuclear-waste-robotics/>.
- (10) Pohl, O. Chemotaxis of Self-Phoretic Active Particles and Bacteria. 2016. <https://doi.org/10.14279/depositonce-5409>.

- (11) Huang, Z.; Chen, P.; Zhu, G.; Yang, Y.; Xu, Z.; Yan, L.-T. *Bacteria-Activated Janus Particles Driven by Chemotaxis*. *ACS Nano* **2018**, *12* (7), 6725–6733. <https://doi.org/10.1021/acsnano.8b01842>.
- (12) Lousada, C. M.; Soroka, I. L.; Yagodzhinsky, Y.; Tarakina, N. V.; Todoshchenko, O.; Hänninen, H.; Korzhavyi, P. A.; Jonsson, M. *Gamma Radiation Induces Hydrogen Absorption by Copper in Water*. *Sci Rep* **2016**, *6* (1), 24234. <https://doi.org/10.1038/srep24234>.
- (13) Casagrande, C.; Fabre, P.; Raphaël, E.; Veyssié, M. “Janus Beads”: Realization and Behaviour at Water/Oil Interfaces. *EPL* **1989**, *9* (3), 251–255. <https://doi.org/10.1209/0295-5075/9/3/011>.
- (14) Parittotokkaporn, S.; Dravid, A.; Bansal, M.; Aqrawe, Z.; Svirskis, D.; Suresh, V.; O’Carroll, S. J. *Make It Simple: Long-Term Stable Gradient Generation in a Microfluidic Microdevice*. *Biomed Microdevices* **2019**, *21* (3), 77. <https://doi.org/10.1007/s10544-019-0427-4>.
- (15) Irimia, D.; Geba, D. A.; Toner, M. *Universal Microfluidic Gradient Generator*. *Anal. Chem.* **2006**, *78* (10), 3472–3477. <https://doi.org/10.1021/ac0518710>.



# CHAPTER 1

# Chapter 1. Introduction

## 1.1 General Context

As per the International Atomic Energy Agency (IAEA) nuclear power is the second-largest source of electricity with 411 operating plants; 10% of the global electricity supply (till 2022) with low-carbon outcome.<sup>1</sup> Mostly, nuclear power plants (NPP) have operating lifetimes of between 20 to 40 years, post which it is decommissioned. The process of nuclear decommissioning follows strict decontamination and decommissioning protocols. Apart from a NPP (where materials at reactor-site, storage of radioactive elements, pipeline-materials, etc. gets contaminated via irradiation), decontamination is important at various different events and sites, for example: at hospitals, on a site of incident/accident or when pollution by radioactive material occurs, etc. These contaminated or degraded materials, structure, structural-parts, etc. are decontaminated conventionally by various methods like washing, heat-treatment, mechanical cleaning, chemicals treatments, electro-chemical treatments, etc.<sup>2</sup> The challenges that come along with these conventional methods of nuclear decontamination are various, for example: higher release and uptake of contaminants, higher dose and exposure of radiation, requirement of more numbers of equipment, and more number of waste packages, etc.<sup>3-5</sup> To overcome these challenges, professionals have adopted robotic approach. Although nuclear decontamination robots are helpful at many occasions, the major drawbacks of robotic approach are 'difficulty in decontamination of complex geometry' and 'the ability to withstand high radiation dose'.<sup>2-4,6,7</sup> Therefore, there is still a need for research and innovation in the field of nuclear decontamination. Thus, as a prospect to it, this thesis proposes the exploration of possibilities of Radiotactic Colloids: towards decontamination nanorobots. This Ph.D. research is a part of the program named FOCUSDEM, under the leadership of the high commissioner for atomic energy: the CEA, an R&D program aiming to provide fundamental research in the field of nuclear decontamination and decommissioning. FOCUSDEM is structured around three major research themes: the characterization and monitoring of installations and sites; decontamination and conditioning of waste and effluents; control of risks associated with processes and rehabilitation methods, while this work is a part of the unit decontamination and conditioning of waste and effluents.

## 1.2 Nuclear Decontamination and Decommissioning and Challenges

In decommissioning program, decontamination is one of the major activity. Accurately pinpointing radioactive contamination hotspots within complex geometries is crucial for effective decommissioning, waste management, and personnel safety in the nuclear industry. Decontamination not only aims for the removal of loose radioactive contaminants but also has other goals like reduction of occupational exposures, limitation of potential releases and uptakes of the radioactive materials, reuse of component; salvaging equipment/material, facilitating waste management; reduction of the volume of materials for storage/disposal at licensed disposal facilities, etc.<sup>1,2</sup> For the purpose of hotspot localization radiation detectors and gamma cameras are used but their efficacy are limited for structures with complex geometries, with limited penetration depth imposed by intricate shapes or when shielding materials capable of hindering detection are present. For examples tight spaces, intricate components, and remote locations within structures can restrict access for traditional handheld detectors.<sup>6-8</sup> For classical decontamination procedures, the minimal practice involves

cleaning of the floors, walls, external structural surfaces, followed by a simple water rinsing. However, these methods are not effective for complex geometries like piping systems, tanks.<sup>2,6</sup>

Therefore, to save both occupational exposure and cost, decontamination of complex geometries is achieved by simply removing the contaminated systems and its components, followed by certain packaging activities (e.g., welding the end caps of the pipe sections, cutting and crimping smaller piping). This contributes to an additional cost for the disposal of materials and these additional activities may cause an increased occupational exposure and a potential release/uptake of radioactive contaminants. To overcome these drawbacks, experts recommend to go towards alternatives and optimization of waste reduction.<sup>2</sup>

### 1.2.1 Technological Developments in Nuclear Decommissioning and the Challenges:

As a solution to these challenges in nuclear decontamination and decommissioning (D&D), robotics and remote manipulation equipped with radiation detectors are utilized. These robots can operate into intricate spaces and access hard-to-reach areas allowing improved precision in positioning of detectors for hotspot identification while minimizing personnel exposure. However, the development and deployment of specialized robots for small and complex geometries is still a challenge and expensive matter. Thus, making localization of radioactive hotspots in limited accessibility and complex geometries a major challenge in nuclear decontamination. Another major challenge in D&D is the failure of robot after exposure to high level of radioactivity, for example failure of the STR-1 robot at TMI site (Three Mile Island - 2, USA), or the failure of Komatsu D-355W robot at Cherebyl sites.<sup>7</sup>

In the last years, notable innovations for agile and resilient robots emerges in the sector of nuclear decontamination. For examples, the compact robot named Vega (developed in 2021 by the University of Chester, UK), the robot dog named Spot (developed by Boston Dynamics in 2019), the shape-changing robot (developed by Hitachi GE). The motivation behind these advances was the need for better accessibility of the interiors of contaminated reactor vessels.<sup>8,9</sup> Whilst there are continuous development in the robotic approach for nuclear decontamination, traditional robots often struggle with intricate environments and tight spaces (for example: pipes with a few cm wide diameters) due to their bulky size and the challenge of 'reaching out to complicated smaller structures' sustains.<sup>9</sup> Therefore, exploration of a cost-effective alternative that is small in size and efficient in localization of radiation hotspot is needed (especially in decontamination of complex geometries). For this purpose, robots of supramolecular-scale can be a potential alternative. Being much smaller, these supramolecular-scale robots can navigate complex geometries and access areas inaccessible to larger robots offering decontamination of intricate areas effectively. While traditional robots can malfunction or become inoperable after exposure to high radiation levels,<sup>7</sup> supramolecular robots, due to their simpler design and potentially radiation-resistant materials, can offer greater resilience in high-radiation environments. This would reduce the need for frequent replacements and minimizing worker exposure during retrieval. Also, recovering large robots after use can be challenging and pose additional radiation exposure risks,<sup>7,9</sup> which can be reduced by the use of supramolecular-scale robots that (due to their size) might simplify retrieval or even allow for biodegradation (if designed with environmentally friendly materials). Additionally, developing and deploying specialized robots for various D&D scenarios can be expensive and time-consuming. Supramolecular robots, produced

through scalable synthesis methods (with an additional benefit of customizable designing), could offer a more cost-effective solution for D&D tasks.<sup>9</sup>

Therefore, this thesis project finds its motivation here that considers autonomous microsystems as a prospect. In this Ph.D. we study about whether it is possible to develop a robot operating at the supramolecular scale (making them highly agile and reachable at narrow complex geometries) and capable of moving towards contamination spot without any added energy supplier (Figure 1). Overall, the transition to supramolecular-scale robots for nuclear D&D represents a paradigm shift towards a more agile, resilient, and potentially cost-effective approach. And as an innovative route in rupture with former strategies, we propose in this project to explore self-propelled nanomotors that can have a prospective future as nuclear decontamination nanorobots (NDN).

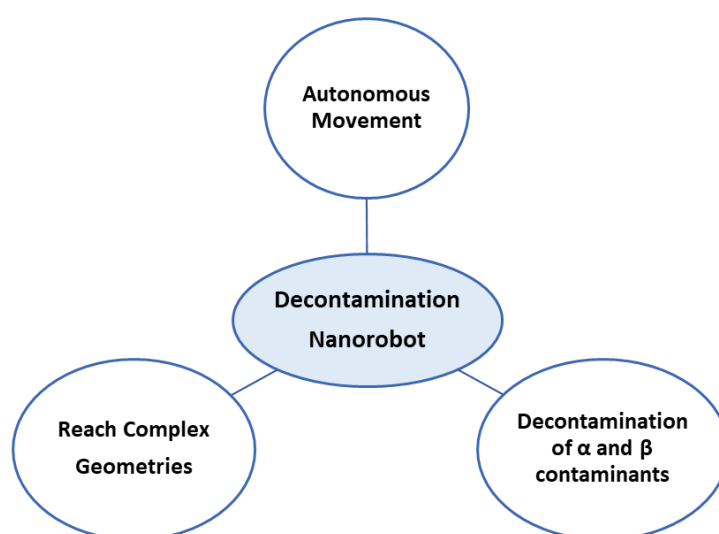


Figure 1: Targeted key-features of prospective supra-molecular scale decontamination nanorobots proposed in this thesis

### 1.3 Working principle of decontamination nanorobots

The fundamental principle of movement of the proposed decontamination nanorobots; Radiotactic colloids lies in mimicking movement-mechanism available in nature. Nature is well known to exhibit examples of self-propelling organisms like *Escherichia coli*, *Bacillus subtilis*, *Clostridium Botulinum*.<sup>10–12</sup> Many bacteria are capable of transforming chemical energy into mechanical movement, and capable of going autonomously toward their nutrition source following its concentration gradient (a biological phenomenon called chemotaxis).<sup>10</sup> The main idea in this thesis project is to use the products of radiolysis of water (detailed in “1.3.1”) generated in the presence of radioactive contaminants<sup>13,14</sup> to induce the movement of the so-called radiotactic colloids. The understanding of the underlying mechanisms would enable us to have a precise control over particle behaviour in complex environments. Since the mid of the twentieth century, numerous work have highlighted various biomimetic approach for particle movement.<sup>15–18</sup> A few of these several biomimetic strategies are discussed in section “1.3.2”.

### 1.3.1 Products of Water-Radiolysis as fuel for Decontamination Nanorobots

In nuclear decontamination, both alpha and beta contaminants play significant roles.<sup>2,3,19,20</sup> Alpha particles are typically emitted by heavy, unstable nuclei and are of significant concern in nuclear waste management and decommissioning activities. While beta particles have high energy and high-speed emitting electrons or positrons.<sup>21–24</sup> Alpha emitting contaminants such as isotopes of uranium, plutonium, radium, and americium, and beta contaminants like isotopes of strontium, cesium, tritium, and iodine are obtainable from nuclear fuel, natural uranium and thorium ores, by-products of nuclear reactors, fission products and nuclear weapons production.<sup>19,20,24–31</sup> Alpha and beta contaminants can induce radiolysis of water, leading to the production of reactive species (Figure 2) that can further affect the environment and complicate decontamination processes.<sup>13,14</sup> Hydrogen peroxide ( $\text{H}_2\text{O}_2$ ) and hydrogen ( $\text{H}_2$ ) are two stable products that can be considered as prospective fuel or source of energy for particle-movement, thus, act as a motor for nuclear decontamination nanorobots (NDN).<sup>32–36</sup>

While  $\text{H}_2$  offers high energy content,<sup>37–39</sup>  $\text{H}_2\text{O}_2$  is the most practical and effective fuel as it can accumulate at a higher concentration, has high energy density, decomposes catalytically with release of water and oxygen. This gives the ability for propulsion through mechanisms like diffusophoresis, chemophoresis, etc. as explained in “1.3.2”.<sup>34,36,40,41</sup> Additionally, controllable reaction rates of  $\text{H}_2\text{O}_2$  makes it ideal for driving micro- and nano-scale particles. Nonetheless, production rates of  $\text{H}_2\text{O}_2$  depends upon the radioactive contaminants because the amount of  $\text{H}_2\text{O}_2$  produced, varies with the type and energy of radiation, as well as environmental conditions.<sup>34</sup> Alpha particles have a high linear energy transfer (LET) therefore, they deposit a significant amount of energy over a short distance in water.<sup>21–24</sup> This results in the production of relatively large amounts of  $\text{H}_2\text{O}_2$ . For quantification of the processes, the G-value can be used, it is the number of molecules formed/destroyed per 100 eV of energy absorbed by the water.<sup>42</sup> Studies show that G-value of  $\text{H}_2\text{O}_2$  for high LET ranges from  $\sim 1 - 2$  (while  $\sim 1 - 1.5$  for hydrogen).<sup>42–44</sup>

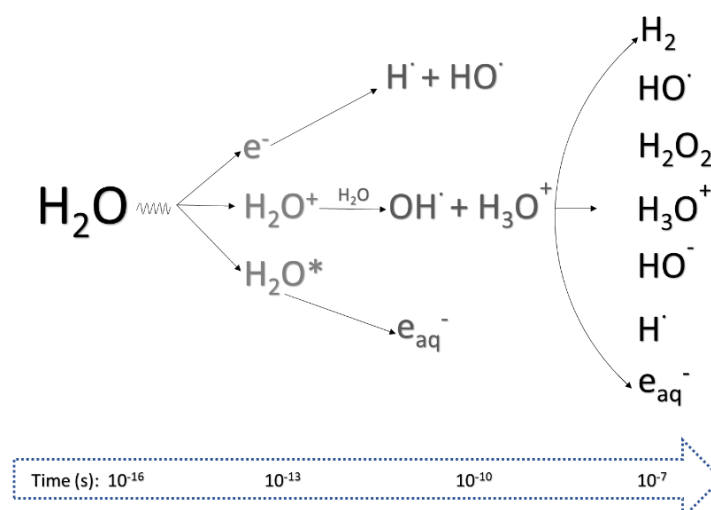


Figure 2: Water radiolysis and formation of primary products ( $\text{H}_2$ ;  $\text{HO}^\bullet$ ;  $\text{H}_2\text{O}_2$ ;  $\text{H}_3\text{O}^+$ ;  $\text{HO}^-$ ;  $\text{H}^\bullet$  and  $\text{e}_{\text{aq}}^-$ ) at respective time scale of events.<sup>14</sup>

Whereas, beta particles have a lower LET compared to alpha particles, resulting into more dispersed energy deposition and consequently lower yield of  $\text{H}_2\text{O}_2$ . Beta radiation typically produces  $\sim 0.7$  molecules of  $\text{H}_2\text{O}_2$  per 100 eV of energy absorbed (while G-value of hydrogen is  $\sim 0.45$ ).<sup>36,45</sup>

Observations from Fukushima Daichi site show  $\text{H}_2\text{O}_2$  production range of  $0.1 \mu\text{M} - 1.5 \text{mM}$ <sup>213</sup> and while microbes present in soil from Chernobyl site showed resistant to  $0.3 - 1.0 \text{M}$   $\text{H}_2\text{O}_2$ <sup>214</sup>; reflecting higher production of higher concentration of  $\text{H}_2\text{O}_2$ . But, before going into the detail of using  $\text{H}_2\text{O}_2$  as fuel, the next paragraph focuses on the origin of particle movement and how it can be measured.

### 1.3.2 Particle Movement

Movement-mechanism acting in particles depends on various factors like particle size, environment and external forces. Therefore, understanding how these parameters drive the movement would help in mimicking natural mechanisms for movement in the developed supramolecular-scale NDN.<sup>15-18</sup>

Figure 3 shows particle movement triggered by external forces (1.3.2). The particularity of mobile active nanoparticle is that they contain an energy conversion system to create a local force that applies on themselves. Therefore, they will move by self-phoresis (self-diffusiophoresis, self-thermophoresis, etc.).

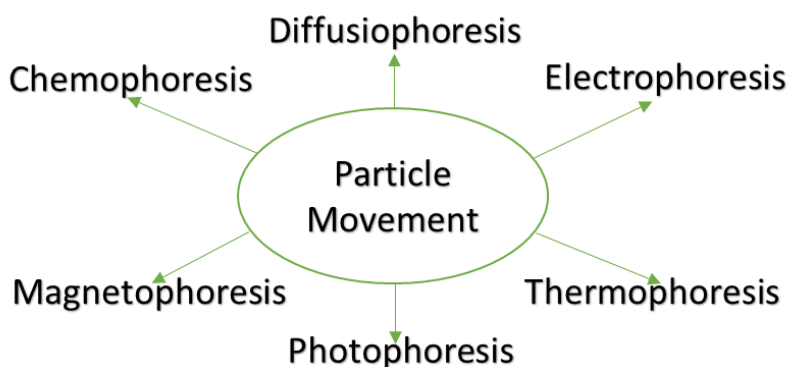


Figure 3: Example of different types of mechanism for particle-movement.

#### 1.3.2.1 Diffusion, Diffusiophoresis and self-diffusiophoresis

The random movement of atoms, molecules, particles or organisms due to its thermal energy is termed as Brownian motion and the tendency of particle to move from higher concentration to lower via Brownian motion is termed as diffusion.<sup>46-49</sup> The average displacement of a particle undergoing a random walk is zero, but in case of high population, particles starting from the same point tend to spread out with some finite displacement after a finite time and can align with the Central limit theorem (Figure 4).<sup>50</sup> The rate at which a particle migrates through a particular material to attain equilibrium is called diffusivity or diffusion coefficient, which is dependent on the temperature, composition gradient, and pressure.<sup>49,51,52</sup>

For a spherical particle relationship between the diffusion coefficient and particle hydrodynamic radius is defined by Stokes-Einstein Equation ( $D = kT/6 \pi \eta R_h$ , where  $k$  is the Boltzmann constant,  $T$  is the temperature,  $\eta$  is the viscosity of the suspension medium and  $R_h$  is the hydrodynamic radius of particle).<sup>53</sup> Einstein-Smoluchowski equation;  $\text{MSD}^2 \propto Dt^\alpha$  ( $\text{MSD}^2 = 2nDt$  with  $n=2$  for 2D system) helps in the determination of diffusivity with respect to particle motion. Here MSD is the Mean Square Displacement<sup>54</sup> of particles,  $D$  is the diffusivity or diffusion coefficient,  $n$  is the dimension-number of

the observed system and  $t$  is the time,  $\alpha$  represents the anomalous diffusion exponent (mathematical parameter to quantify the rate and pattern of particle movement in anomalous diffusion processes).<sup>51</sup>

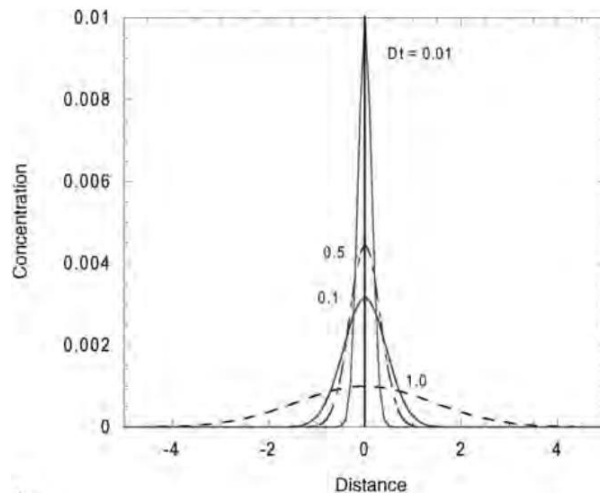


Figure 4: The concentration of atoms as a function of distance (standard deviation of mean value) for different times ( $Dt$  at 0.01, 0.5, 0.1 and 1) as per the central limit probability theorem. Image extracted from Campbell et al., 2009.<sup>74</sup>

Typical diffusion described by Einstein and Smoluchowski<sup>51</sup> states linear relationship between MSD and time<sup>51</sup> (blue plot in Figure 5) in comparison to hyper and suppressed motion of particle determines the collective motion in particles.

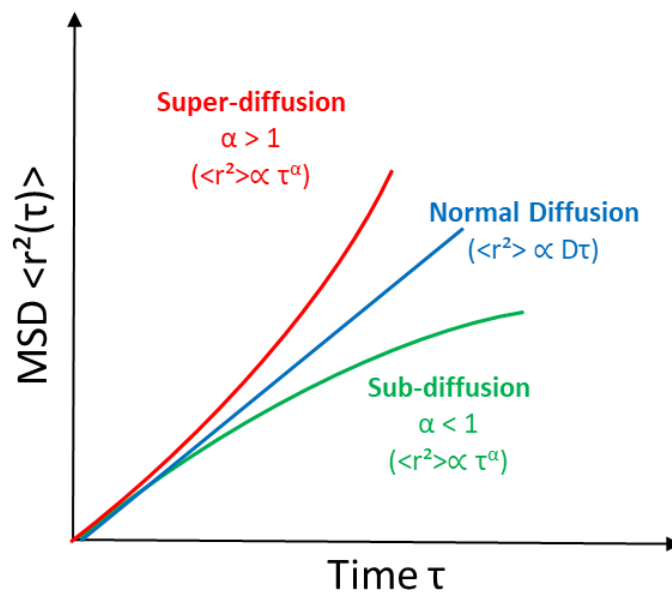


Figure 5: MSD as a function of time indicating normal diffusion (linear progression) in blue, super and sub diffusion in red and green, respectively.<sup>55</sup>

When the particles are in a medium with a non-uniform solute concentration like a gradient concentration, the chemically induced movement of the particles is called diffusiophoresis.<sup>49,56,57</sup> Diffusiophoresis occurs from the interactions between the solute molecules and the particle surface and can involve various forces, such as friction, electrostatic attraction/repulsion, or solvation effects.

It is achievable by embedding reactants within the particles slowly releasing solutes into the surrounding environment, creating a localized concentration gradient.<sup>60,61</sup> Diffusiophoresis encountered in natural and artificial systems (nanomotors or swimmers)<sup>60</sup> plays a significant role in various fields, including colloidal science, microfluidics, etc. It can be utilized for particle manipulation and transport in complex fluid environments. Nanomotors are nano to micro meter sized machines that uses a local (internal or found in the close environment) source of energy for movement (or an action performance).<sup>61,62</sup>

Self-diffusiophoresis occurs when the active particle is capable to create itself a concentration gradient (for example by harbouring catalytic sites on its surface),<sup>58,63</sup> which generates a force at the origin of the movement of the particles. Figure 5 shows hyper-diffusive and under-diffusive motion as super diffusion and sub diffusion respectively (red and green plots, respectively). Diffusion plays crucial role in understanding the behaviour of materials at micro and nano scale.<sup>54</sup> In this context, an asymmetric nature of particles can allow to create locally gradients and thus enhance self phoresis motions.<sup>58,64,65</sup> This asymmetry can be achieved for example by the preparation of Janus particles which are particles with an asymmetry on the surface (explained in detail in "1.5").<sup>56,58,66,67</sup> For example, in Janus particle movement of particles can be hindered at a water-oil interface causing slow interfacial diffusion than that in homogeneous medium and homogenous particles.<sup>66</sup>

### 1.3.2.2 Chemophoresis

Similar to chemotaxis in cells or organisms, chemophoresis is the directional movement of a particle or colloid induced from a gradient of chemical potential in its environment.<sup>10–12,68</sup> In that sense, the term is both more general and less precise than diffusiophoresis and self-diffusiophoresis. Conversion of chemical stimulus in order to obtain a mechanical outcome is one of the commonly found mechanism for movement in particles. Initial observation of chemotaxis was in biological organisms. For example: *E.coli* bacterium and *D. discoideum* amoeba use chemotaxis to navigate towards favourable conditions, such as sugars or amino acids, by sensing changes in chemical concentrations.<sup>69,70</sup> Another example of chemotaxis is seen in sperm cells of many mammals that uses chemotaxis to navigate towards eggs by following a chemical gradient of substances released by the female reproductive system; helping them to locate and fertilize the egg).<sup>71</sup> Research to mimic this phenomena has been the topic of intense research to produce synthetic active particles (ex: micromotors, nanomotors) since a while now.<sup>11,72</sup> Studies on some synthetic nanomotors/swimmers<sup>73,74</sup> shows that the major factors contributing towards motion and velocity of nano/micro motors through chemophoresis are catalyst-activity, temperature and fuel-concentration (that can act by the gradient of reactant or product concentration, or by local heating or due to local charging effects, see below).<sup>73,74</sup> Additionally, surface modified particles with metallic composition appear as widely studied kind.<sup>74,75</sup>

Since the early work on catalytic motor (like nanodimers fueled by a chemical reaction studied by Kapral<sup>76</sup> and catalytic gold/platinum nanorods by Paxton<sup>77</sup>) there has been immense advancement in the field of self-propelled micro-jets and motors.<sup>77</sup> Work on Gold/Platinum nanorods by Paxton<sup>77</sup> showed chemotaxis-like movement from catalytic asymmetry of the nanorods and subsequent production of a chemical gradient by the catalyst.<sup>77</sup> The catalytic conversion of a chemical fuel on surface modified colloids have been utilized successfully for different types of nano/micro motors like metallic rods, silica Janus particles, etc.



However, chemophoresis mechanism differs depending on whether the catalytic reaction produces molecules or gas. Molecular chemophoresis occurs when a catalyst produces molecules and accumulates around the particle, creating a concentration gradient. This gradient generates a force on the particle due to differences in pressure, causing the particle to move from self-propulsion.<sup>78</sup> An example of study conducted Hong et al.<sup>78</sup> showed chemotaxis in Platinum-Gold (Pt-Au) colloidal rods (length 2  $\mu\text{m}$ ), similar to the movement observed in biological systems like bacteria in a capillary experiment.<sup>78</sup> The capillary experiment (Figure 6.(I)) highlighted the active chemotaxis of these colloidal rods in presence of hydrogen peroxide, where capillaries without  $\text{H}_2\text{O}_2$  (Figure 6.(II).A) lacked Pt-Au rods while the count increased in capillaries with higher concentration of  $\text{H}_2\text{O}_2$  (Figure 6.(II).B-D).<sup>78</sup>

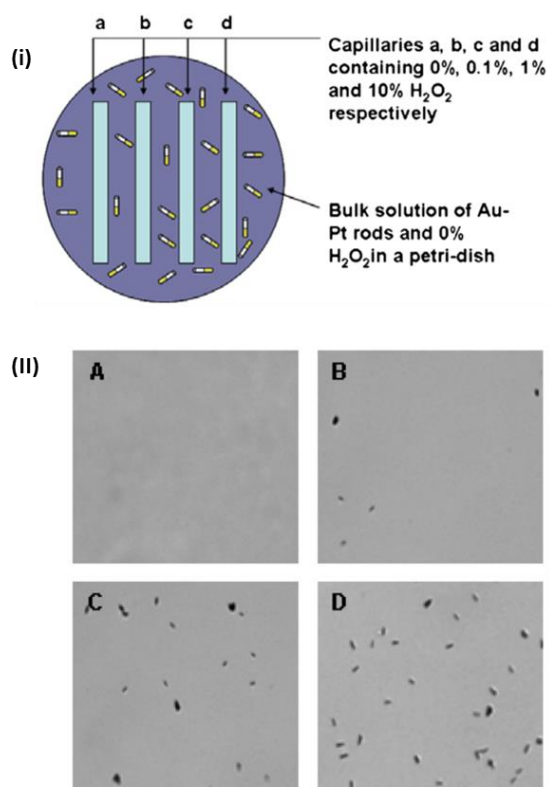


Figure 6: (I) Scheme of Capillary experiment by Hong et al and (II) showing increasing population of Pt-Au rods in the respective capillaries (from (I)) with higher  $\text{H}_2\text{O}_2$  concentration. Image extracted from Hong et al., 2007.<sup>78</sup>

In gaseous chemophoresis, a catalyst produces gas, forming bubbles around the particle. The asymmetric formation of these bubbles generates a thrust force, propelling the particle forward. This mechanism is often referred to as "bubble propulsion" (discussed further in "1.3.2.4"). An example of self-propelling micro-jets are from the decomposition of hydrogen peroxide ( $\text{H}_2\text{O}_2$ ) into water ( $\text{H}_2\text{O}$ ) and oxygen ( $\text{O}_2$ ) ( $2\text{H}_2\text{O}_2 \rightarrow 2\text{H}_2\text{O} + \text{O}_2$ ) (Figure 7) that has gotten attention from a lot of researchers in past couple decade.<sup>61,73,79-81</sup> Catalase, known for its catalytic decomposition of  $\text{H}_2\text{O}_2$  has been one of the most widely preferred enzyme for this purpose. The key difference between chemophoresis from gas production and concentration gradient is that the movement is directly caused by the physical force (exerted by the gas bubbles), rather than by a chemical concentration gradient. While both

molecular and gaseous chemophoresis involve catalytic reactions, the driving force for particle movement differs significantly.

There are studies that has shown these two mechanisms ('catalytic conversion' and 'gas production') inter-twinned. For example, Ma et al.,<sup>61</sup> studied the positive impact of  $\text{H}_2\text{O}_2$  on motion of hollow mesoporous silica nanoparticles half-covered by enzymes (JHMSNP)) due to the enzymatic activity.<sup>61</sup>

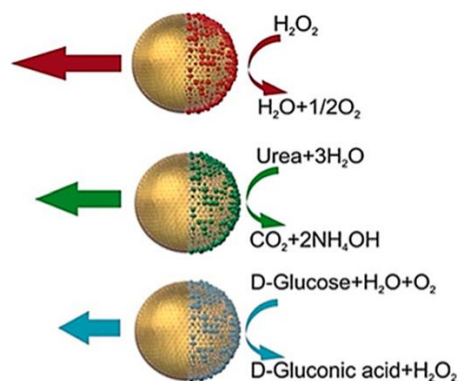


Figure 7: Reaction causing movement in enzyme-linked Janus particles. Image extracted from Ortiz-Rivera et al., 2018.<sup>73</sup>

In addition to chemophoresis, electrophoresis can be observed when the concentration gradient produces an electrical field.<sup>65,82-84</sup> When the concentration gradient and the resulting electric field is produced by the particles itself, it is a self-electrophoresis.<sup>83</sup> Study by Brooks<sup>83</sup> on Platinum microparticles (twisted star shaped of average diameter  $5.8 \mu\text{m}$  and  $100 \text{ nm}$  thickness) in presence of hydrogen peroxide showed controlled rotation of micromotors using catalytic self-electrophoresis (Figure 8). This study revealed that asymmetrical shape of micromotors induced anodic oxidation and cathodic reduction occurred at different rates at different locations on the particle surface, causing directional motion under an electric field that was generated because of catalytic reactions.<sup>83</sup>

Lyu et al.<sup>85</sup> in their work on platinum/silica and catalase/silica Janus particles ( $\phi \sim 5 \mu\text{m}$ ) challenged that asymmetric bubble generation from catalytic decomposition of  $\text{H}_2\text{O}_2$  alone is insufficient for robust propulsion and that the self-electrophoresis is more dominant mechanism. This occurred due to the electrochemical imbalance created by the catalytic reaction, which they also showed from numerical simulation. The thicker region of the Pt film (in Pt/Silica Janus particle) acted as the oxidation site, while the thinner region acted as the reduction site (Figure 9). This electrochemical difference generated an electric field, driving the micromotor through the solution. This study also concluded that at same parameters, Janus particle with metal-layer attained higher velocity ( $\sim 5.7 \mu\text{m/s}$ ) than that of Janus particle with metallic nanoparticles ( $\sim 0.1 \mu\text{m/s}$ ).<sup>85</sup>

## Introduction

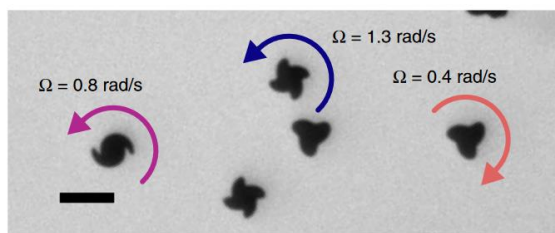


Figure 8: Image of different types of particles rotating in respective directions and rates in 10 wt%  $H_2O_2$  (20  $\mu m$  scale). Image extracted from Brook et al, 2019.<sup>83</sup>

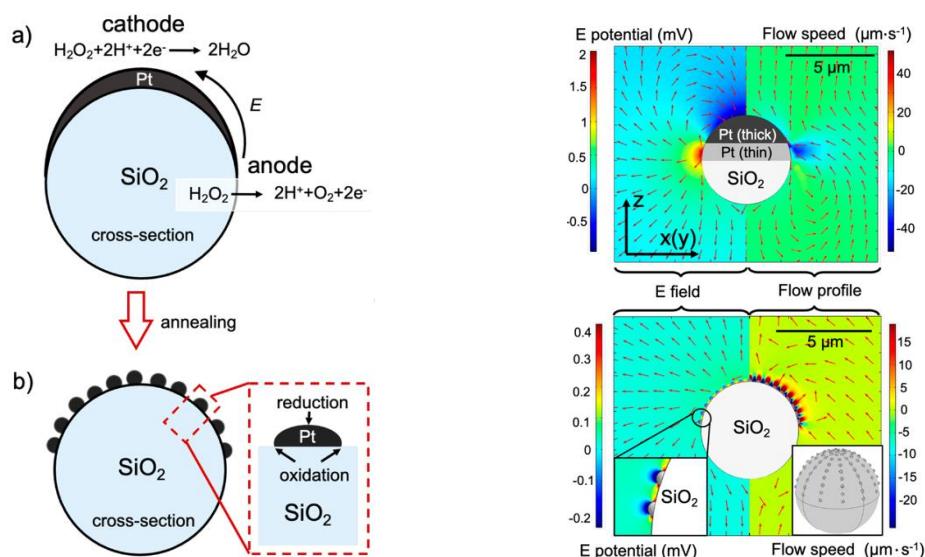


Figure 9: Scheme of self-electrophoresis and respective simulations (right side images) on (a) Pt layered Pt/SiO<sub>2</sub> micromotor, (b) Pt nanoparticles Pt/SiO<sub>2</sub> microspheres in H<sub>2</sub>O<sub>2</sub>. Self-electrophoresis occurring on the Pt edges (thin or tapered parts) with its pole and equator act as the cathode and anode, respectively, while a self-generated electric field from equator to pole, propel it away from the thick part of Pt. Electrostatics numerical simulations results (images on right hand-side) showing the flow speeds along the z direction and normalized flow vectors. The bottom left inset in simulation of (b) shows the zoomed-in results of the electric potential near two Pt nanoparticles, where a total of 93 Pt nanoparticles ( $\phi$  200 nm) arranged in concentric circles on one-half of a SiO<sub>2</sub> microspheres were considered for the study. Image extracted from Lyu et al, 2021.<sup>85</sup>

### 1.3.2.3 Self-thermophoresis

When a particle exhibits motion in a specific direction due to a temperature gradient within its surrounding, it is referred to as self-thermophoresis.<sup>86</sup> For example, Simoncelli et al<sup>87</sup> stretched (or otherwise influenced) DNA structure by using laser and self-thermophoresis property of gold/silica Janus particle. Simoncelli<sup>87</sup> made gold/silica Janus particle ( $\phi \sim 1.3 \mu m$ ), that had heat-sensitive gold-side, unlike the non-sensitive silica-side. This, on exposure of laser created a hot spot on gold side of the particle, causing the formation of temperature gradient in particle with hot gold-side and cooler silica-side. The uneven surface temperature drove molecules to interact differently with hot and cold surfaces, creating a force on the particle and pushing it towards the cooler silica side and against the direction of beam-propagation.<sup>87</sup>

### 1.3.2.4 Bubble-propulsion

Amongst several work on particle-motion from asymmetric self-electrophoresis, a study by Lyu et al.,<sup>85</sup> described how the asymmetric catalytic activities for the decomposition of H<sub>2</sub>O<sub>2</sub> causing self-

electrophoresis in microspheres is not always sufficiently powerful enough to attain movement, and there can be other factors like bubble propulsion mechanism; supportive to cause motion in particles.<sup>85</sup> Contrary to Lyu<sup>85</sup>, Chen et al,<sup>75</sup> studied on motion from catalytic activities in porous Janus micromotors of diameter 180 nm (metal–organic frameworks (MOFs)) for enhanced degradation of organic contaminants and showed strong bubble propulsion motion.<sup>75</sup> These self-propelling micromotors were designed for environmental clean-up, where micromotors were decorated with special nanoparticles that would break down  $\text{H}_2\text{O}_2$  unevenly, creating a kind of miniaturized bubble engine. Here, the nanoengine ( $\text{Fe}_3\text{O}_4@\text{AgNPs}$ ,  $\phi 180$  nm) in micromotors did the task of generating oxygen bubble from  $\text{H}_2\text{O}_2$  decomposition, thrusting for strong propulsion. Additionally, the porous structures of these micromotors provided more surface area for the nanoparticles to interact with  $\text{H}_2\text{O}_2$  and made the micromotors light weighed, which ultimately aided the fast motion of particles. For the tracking aspect, the team used optical snapshots to monitor bubble propelled motion of micromotors in presence of  $\text{H}_2\text{O}_2$  and Sodium Dodecyl Sulphate (SDS) (Figure 10) and found that in  $\text{H}_2\text{O}_2$  nanoengine in the micromotors exhibited self-propelled bubble-motion in the opposite direction.<sup>75</sup> In this study impact of SDS on the bubble-propelled motion of the micromotors was observed by varying the concentration of SDS, the researchers can gain insights into the factors influencing the micromotors' movement.<sup>75</sup> Therefore, it can be interesting to consider 'motion of particles from bubble propulsion mechanism', as one of the possible motion-mechanism in particles interacting with chemicals that cause release of gases (for example decomposition of hydrogen peroxide).

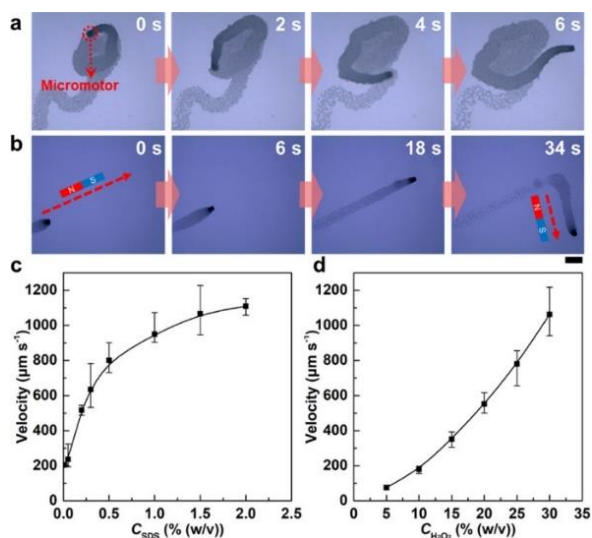


Figure 10: MOF-integrated photocatalytic micromotors for bubble propelled motion. (a) Optical snapshots showing the bubble propelled motion behaviour of micromotors in aqueous solution with 30% (w/v)  $\text{H}_2\text{O}_2$  and 2% (w/v) SDS. (b) Optical snapshots showing the magnet-guided bubble-propelled motion behaviour of micromotors in aqueous solution with 10% (w/v)  $\text{H}_2\text{O}_2$  and 1.5% (w/v) SDS. (c) SDS concentration-dependent velocity changes of micromotors in aqueous solutions with 30% (w/v)  $\text{H}_2\text{O}_2$ . (d)  $\text{H}_2\text{O}_2$  concentration-dependent velocity changes of micromotors in aqueous solutions with 1.5% (w/v) SDS. Scale bar is 1 mm. Image extracted from Chen et al., 2020.<sup>75</sup>

### 1.3.2.5 Collective Effects

An important aspect of motion study is collective diffusion<sup>64</sup> and motion of particle. Collective motion of particles can hinder our control over precise positioning of particles and also lead to undesired aggregations that might also pose an interesting aspect to motor in our applications.<sup>67,88</sup> Appel's<sup>67</sup> work

with micro-emulsions discussed that the collective motion in particles likely arises from interactions between the charged particles themselves. These interactions could be Electrostatic or hydrodynamic. Particles with like charge might repel each other, leading to a coordinated movement away from densely packed regions. While as they move, they can also create fluid flows that influences the movement of neighbouring particles. In this study Appel<sup>67</sup> utilized Dynamic Light Scattering (DLS) to observe these collective motions.<sup>67</sup> DLS measures how light scatters from the moving particles, providing insights into their average motion and potential collective behaviour.<sup>89</sup>

Similarly, research by Dai<sup>88</sup> explored collective motion, where particles exhibited coordinated movement beyond simple, random walks. This work focused on how individual particles suspended in a liquid might move in a more organized way, potentially influenced by a "Universe field", a concept introduced in the research. This field could represent some external force or interaction that goes beyond simple collisions with liquid molecules. Dai's<sup>88</sup> research highlighted the possibility that particle motion in certain systems might not be entirely random and directed interactions and external fields were highlighted as the potential mechanisms for collective motion in particles. If the particles have some inherent attraction or repulsion towards each other, they might exhibit coordinated movements. While an external field, like a light source or a magnetic field, could influence the movement of charged particles, leading to collective behaviour.<sup>88</sup>

Collective motion may lead to unclear movement pattern of individual particles, which can also be capable of overshadowing any possible complex/interesting interactions and biasing our understandings of fundamental interactions between particles and surrounding.<sup>88,90,91</sup> Therefore, need for suppressing the challenge of collective motion of particles is crucial for our study and better understanding of the effect of hydrogen peroxide on motion of Janus particles. Researchers have found the field of microfluidics capable of overcoming this challenge by well-controlled flow of fluid in well-defined boundaries.<sup>72,92-94</sup> Therefore, incorporation of microfluidics for the characterization of motion of individual/isolated particles and other characteristics can be interesting in our work.

### 1.4 Motion Study and Particles Tracking

Active motion exhibited by particles can also be studied by calculating the mean-square displacement (MSD) of particles. In the study of Ma et al.,<sup>61</sup> the MSD of particles ( $\phi \sim 400 \text{ nm} \pm 6 \text{ nm}$ ) exhibiting different types of phoresis (chemophoresis by gas and molecule, self-diffusiophoresis and self-electrophoresis) were measured.<sup>61</sup> Diffusion coefficient of particles was calculated in presence of different concentrations of  $\text{H}_2\text{O}_2$  (Figure 11.a-c).

## Introduction

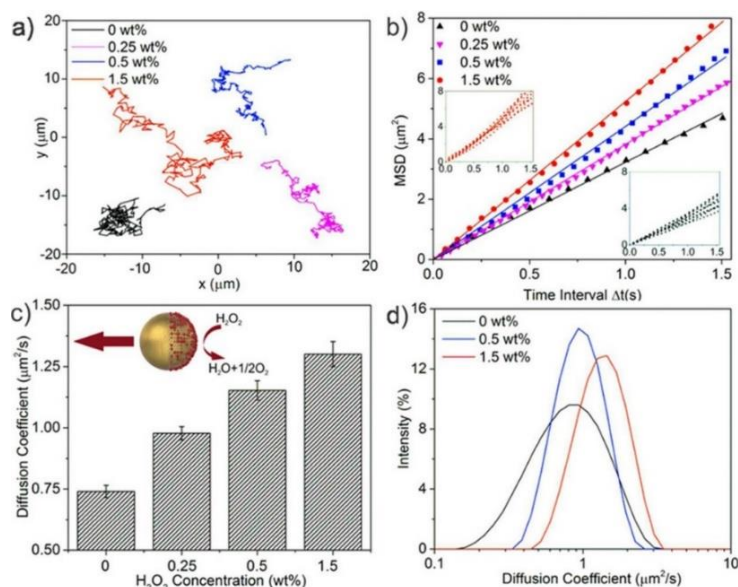


Figure 11: Analysis on the dynamic properties of the JHMSNP-Catalase nanomotors, (a) representative tracking trajectories of the nanomotor during 30 seconds. (b) MSD versus time interval ( $\Delta t$ ) analysed from tracking trajectories (insets are MSD curves of individual nanomotors at 0 and 1.5 wt. % H<sub>2</sub>O<sub>2</sub>). (c) Diffusion coefficient values determined from the slope of the linear fitting curves of average MSD plots (for panels a–c, 30 nanoparticles were analysed, and the error bars in panel c represent the standard error of mean,  $N = 30$ ) and (d) diffusion coefficient histogram of the nanomotors measured by dynamic light scattering (DLS). Image extracted from Ma et al., 2015.<sup>61</sup>

The observations for calculating MSD were performed via optical video recordings for 30 seconds (at 20 frames per second (FPS)) via CCD<sup>95</sup> camera, and further confirmations were made by dynamic light scattering (DLS) measurements (Figure 11.d). They found that the apparent diffusion coefficient of their nanoparticles was enhanced by up to 83%.<sup>61</sup> Both DLS and optical recording with a CCD camera and microscopy are valuable tools for investigating motion at microscopic scale, but they differ in approach and the information they provide. DLS uses laser beam interaction with sample and the scattered light is analysed over time to calculate the diffusion coefficient of the particles in a 3D environment (which can also be related to their size). Whereas microscopy with CCD camera captures high-resolution images of sample allowing direct visualization of individual particles, their morphology (shape), and even their behaviour in real-time but more often in 2D. Statistical data in this study was processed via Python using OpenCV library.<sup>61,96</sup>

In the study by Wu<sup>97</sup> synthesized multi-functional tubular nano-rockets from multi-layer polymer based rolled-up method capable of autonomous motion from bubble propulsion, self-diffusiophoresis and catalytic decomposition mechanisms.<sup>60</sup> These nano-rockets assembled with platinum nanoparticles (PtNPs) on their inner surface, catalytically decomposed hydrogen peroxide into water and oxygen, leading to propulsion in increasing concentration of H<sub>2</sub>O<sub>2</sub> from 1% to 20% with an increased acceleration (5 to 70 μm/s) of the particles (Figure 12).<sup>73</sup> Factors influencing the velocity in this study was H<sub>2</sub>O<sub>2</sub> concentration and solution temperature while the observations were made via dark-field optical (inverted) microscope and a CMOS camera at 12 FPS.<sup>97</sup>

Particle tracking by Wu<sup>97</sup> was performed via manual tracking and MTrack2 plugins in ImageJ software.<sup>97</sup>

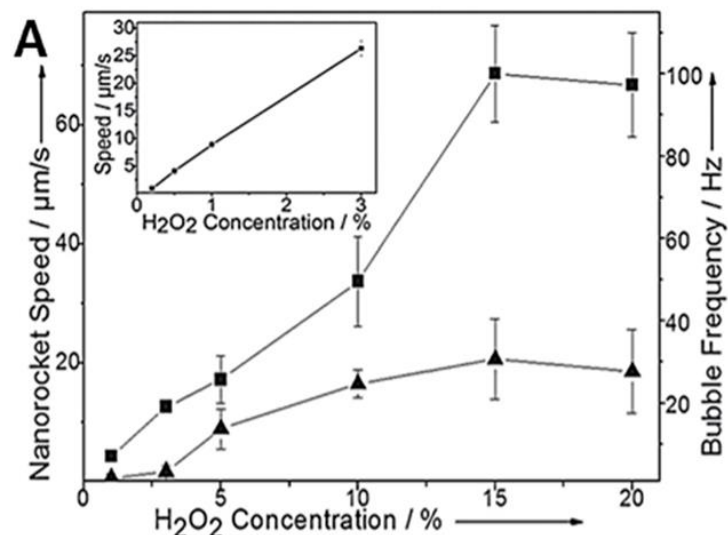


Figure 12: Control over motion: (A) Average speed of polymer based nano-rockets (▲) at different bubble frequencies (■) and H<sub>2</sub>O<sub>2</sub> concentrations in the range of 1–20 % at 22 °C. Inset shows dependence of the nano-rocket speed on low H<sub>2</sub>O<sub>2</sub> concentration at 37 °C. (B) Enzyme-Linked Janus Particles and reactions causing the movement. Image extracted from Ortiz-Rivera et al., 2018.<sup>73</sup>

In addition to enzyme linked Janus Particles for motion, researchers have also worked extensively on varied range of spherical and tubular micro- and nano-swimmers, comprising metallic compositions for motion study. For example, use of gold, platinum, and other metals to make janus micro/nano motors from catalytic decomposition of H<sub>2</sub>O<sub>2</sub> for motion. In a study,<sup>98</sup> motion from rise in temperature (from 25 to 65 °C); thermophoresis of Au coated Pt nanowires showed an increase in speeds from 12 to 37 μm/s (Figure 13). Here, the real-time movement of nanomotors (more than 50) was observed and recorded at 200× magnification from an optical microscope (starting ~5 min after the preparation of the final solution).

The speed measurement in this work by Balasubramaniam<sup>98</sup> was done by using MetaMorph 7's tracking software. Position of nanomotors per frame was determined for calculating the displacement between each frame to obtain the average velocity of each nanomotor.<sup>98</sup>

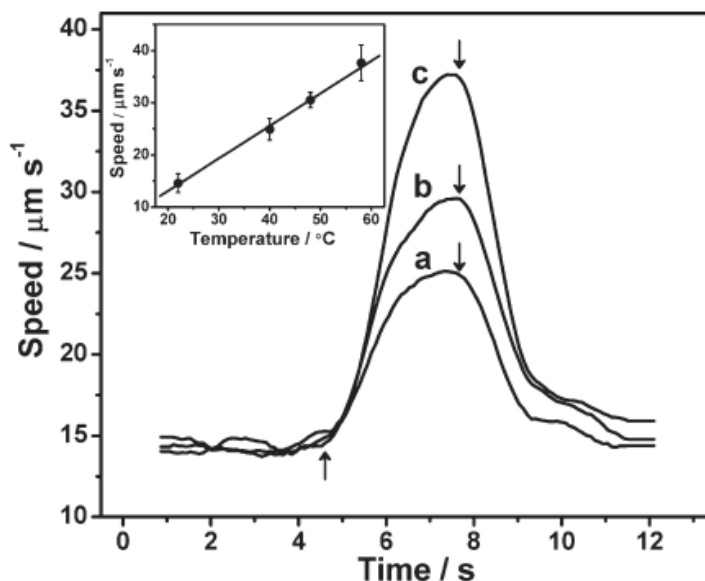


Figure 13: Speed–time profiles of Au–Pt nanomotors during different 3 s heat pulses to 40 (a), 48 (b), and 58 °C (c) in a 5 wt. %  $\text{H}_2\text{O}_2$  solution. The arrows correspond to the time of switching the heating current on and off respectively. The raw data have been smoothed using fast Fourier transformation (via Origin software; 5 points). Inset displays the linear relation between the nanomotor speed and the temperature. Image extracted from Balasubramaniam et al., 2009.<sup>98</sup>

Particle tracking is thus the reference method for diffusion studies, but it is usually possible only on a small number of particle and short observation time. A more ensemble averaged method like DLS<sup>99</sup> may be an interesting complement.

#### 1.4.1 Microfluidics System for Motion Study of Particles in Gradients.

Application of microfluidics<sup>94</sup> devices has great impact in the scientific community. They serve several benefits like a well-controlled environment, less samples, etc. and have been using in wide range of fields, motion-study being one of them.<sup>72,92–94,100–102</sup> In addition to a well-controlled hydrodynamic and mass transport conditions, studies in the field of diffusiophoresis show a wide range of options for gradient generator device on microfluidics platform. A microfluidic device like gradient generators can offer higher gradient resolutions (submicron- to micrometre sized channels), than a non-microfluidic system. This can be insightful in understanding particle motion in gradient of hydrogen peroxide. As a microfluidic gradient generator requires a very small volume of reagents (usually nL –  $\mu\text{L}$ ), the miniaturization of channel dimensions directly correlates with the time reduction for the transportation of targeted entities. Microfluidic gradient generators also enable integration and manipulation of multiple design spaces, chemical species, and chemical concentration, into a single platform.<sup>48,49</sup> A few of the commonly described designs are Christmas Tree Mixer, Junction-types (T-junctions, Y-Junctions), Pressure balancing chips, Extracellular Matrices (ECM), open-cell configuration, etc. (Figure 14 (i))<sup>100,103</sup>



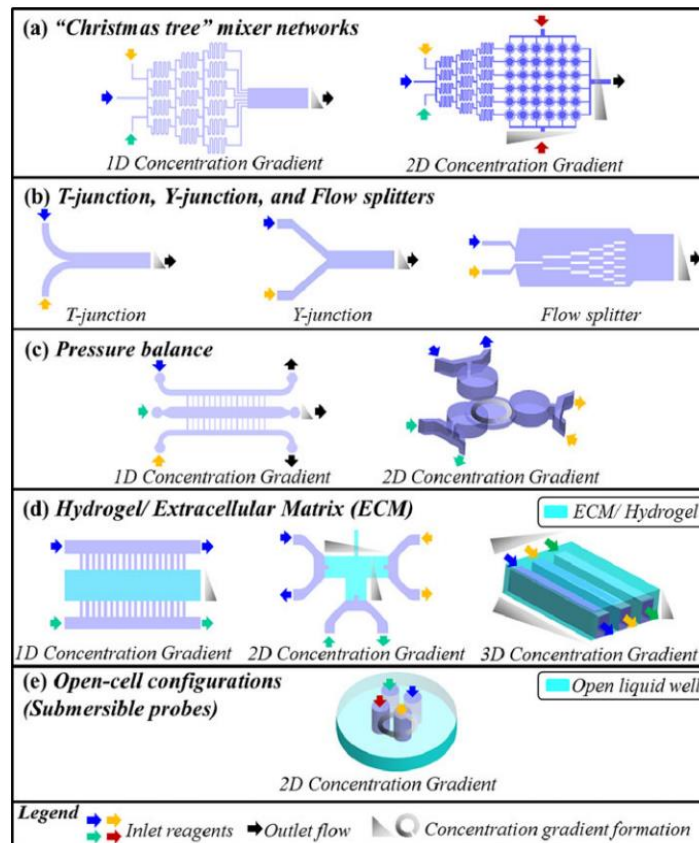


Figure 14: Summary representation of microfluidics-based gradient generator designs: (a) (left) "Christmas tree" design for 1D and (right) 2D gradient generator; (b) (left) Y-junction, (centre) T-junction, and (right) Flow splitter designs (c) (left) 1D gradient generator and (right) 2D gradient generation through pressure balance designs; d Moulded gels for (left) 1D, (centre) 2D, and (right) 3D gradient generation and (e) Submersible microfluidic probes. Image extracted from Toh et al., 2014.<sup>100</sup>

A simple approach for diffusiophoresis in microfluidic system followed by Abecassis<sup>104</sup> showed the impact of concentration on the motion of particles. In this study, Abecassis<sup>104</sup> had utilized a microfluidic chip with three inlets merging to a common channel to monitor different conditions for colloids in buffers (Figure 15). Abecassis<sup>104</sup> demonstrated that the presence of solute gradients can significantly accelerate particle-motion, which is contrary to traditional understanding (where solutes tend to hinder particle migration). For monitoring the density of colloid, intensity of fluorescence was measured in this work. A good correlation between theoretical and experimental results was observed that showed ~40% increase in the particle velocity with a little increase in chemical concentration.<sup>104</sup>

## Introduction

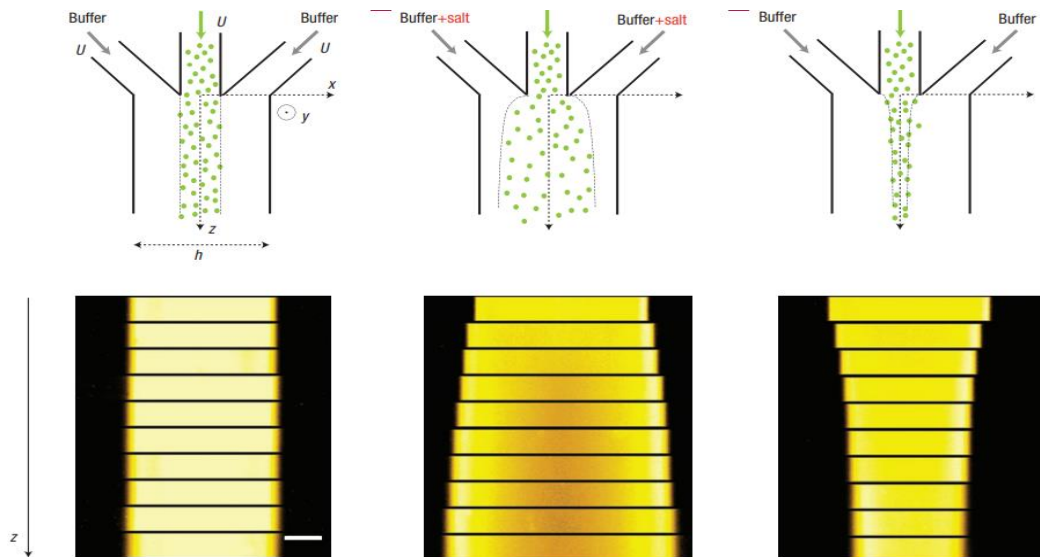


Figure 15: Solute-induced spreading/focusing colloidal labelled with fluorescein isothiocyanate (FITC), 200 nm silica particles in 1 mM TRIS buffer (pH: 9), injected with co-flowing buffer into a microfluidic channel (all inlets with same velocity). Images are recorded at the various distance  $z$  (0, 3, 7, 11, ~15, 23, 40, 50, 60 and 84 mm) from the inlet with a fluorescence CCD camera mounted on microscope at a 10x magnification (horizontal scale bar = 50  $\mu\text{m}$ ). Image extracted from Abecassis et al., 2008.<sup>104</sup>

Another strategy used by Baraban et al.,<sup>92</sup> to study chemotactic motion of chemically powered Platinum/Titanium catalytic motors (micro-tubes and Janus Particles) in a microfluidic channel was done by utilizing a  $\Psi$ -shaped PDMS microfluidic channel with catalytic motors and fuel. Micro-jets (Figure 16. A (left top)) in this study were  $\sim 25\mu\text{m}$  long and prepared by rolling up nano-membranes from a photoresist, followed by physical vapour deposition of Titanium/Platinum layer (20 and 1 nm respectively via electron beam deposition and magnetron sputtering, respectively).

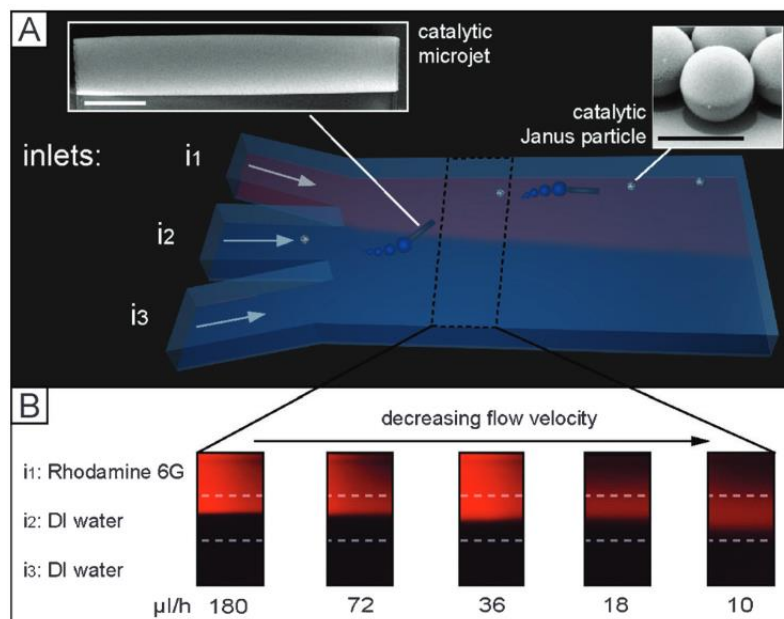


Figure 16: Chemotaxis by catalytic micromotors in a microfluidic device. A) 3D scheme of the microfluidic flow cell with three merging inlets in  $\Psi$ -shape ( $i_1$ ,  $i_2$ , and  $i_3$ ) on the left and one larger outlet on the right. Fuel for catalytic motors, catalytic

## Introduction

*motors (Janus particles and micro-tubes) and water are inlet from  $i_1$ ,  $i_2$  and  $i_3$  respectively. Scale bar:  $5 \mu\text{m}$ . B) Flow test experimental model using fluorescent Rhodamine introduced from  $i_1$  for the visualization of flow-dependent diffusion of the dye molecules across the channel. Image extracted from Baraban et al., 2013.<sup>92</sup>*

The spherical Platinum/Silica Janus particles ( $\phi \sim 5\mu\text{m}$ ) (Figure 16. A (left top)) were prepared by depositing thin bilayer of Pt (15 nm)/Ti (2 nm) via electron beam evaporation onto monolayer of Silica particles (spread on glass substrate). Both catalytic particles and non-catalytic particles were loaded in the  $\Psi$ -shaped PDMS microfluidic chip in presence of  $\text{H}_2\text{O}_2$  (as fuel) and observed lateral deviation in the catalytic motors towards the fuel (Figure 17. A), unlike the unaffected non-catalytic particles (Figure 17. B).<sup>92</sup>

In addition to chemotaxis in Janus motor due to  $\text{H}_2\text{O}_2$ , this study highlighted the importance of shape of particles, where Baraban<sup>92</sup> found spherical Janus motors with faster motion than the micro-jets and addressed higher rotational diffusion (in spherical particles) as the reason behind it. Observations made by Baraban<sup>92</sup> utilized a CCD Camera integrated with optical Microscope, followed by analysis of the images/videos via ImageJ.<sup>92</sup>

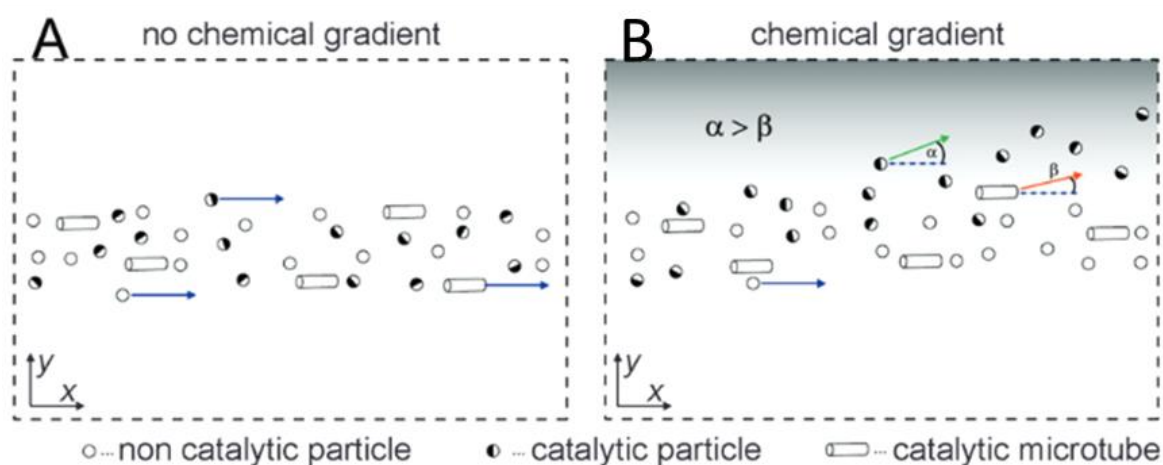


*Figure 17: A) Catalytic and non-catalytic particles flow with surrounding having no chemical gradient of fuel. B) Particles flowing in presence of fuel-gradient in the surrounding. Catalytic particles flow towards the higher concentration gradient of fuel, while non-catalytic particles being unaffected by the presence of fuel in B). Chemotactic behaviour of catalytic (tubes and sphere) motors quantified by determining the opening angle  $\alpha$  and  $\beta$ . Image extracted from Baraban et al., 2013.<sup>92</sup>*

Work by Deprez<sup>72</sup> and team on colloid (mesoscopic particle-based colloid) to understand both passive and active colloidal chemotaxis (Figure 18) in a controlled environment evaluated the chemical concentration profiles on colloidal particles. Passive chemotaxis refers to the movement of these colloidal particles to a chemical gradient without energy consumption/expenditure, whereas active chemotaxis refers to the movement in particles towards/way from the gradient by consuming energy.<sup>72</sup>

Use of a microfluidic device allowed Deprez<sup>72</sup> for precise control over the flow conditions, chemical gradients, and interactions between colloidal particles and the surrounding fluid. In their theoretical work, Deprez<sup>72</sup> and team has proposed a stochastic model for colloidal chemotaxis by computing the

chemotactic force, and demonstrated the applicability of their model by explaining the results of an earlier simulation work with a simpler geometry.<sup>72</sup>

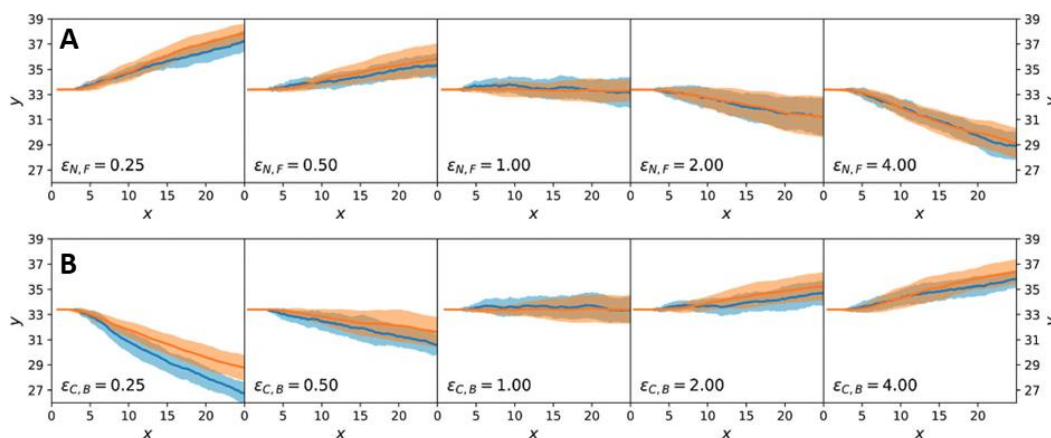


Figure 18: Series A and B shows the simulation trajectories of particles from passive and active chemotaxis, respectively. The lines (orange, blue) represent average position of colloid in mesoscopic (stochastic) simulations and the corresponding filled area indicates  $\pm$  one standard deviation.  $\epsilon$  is the electric field, for N number of particles, and F resulting force experienced by these particles within the microfluidic environment. Image extracted from Deprez et al., 2017.<sup>72</sup>

In another study, Xiao<sup>105</sup> and team have developed a strategy for highly sensitive (flow control) gradient generating (Figure 19) microfluidics set-up. This strategy combined a stopped-flow technique for chemotaxis assay using Cu@SiO<sub>2</sub> Janus micro-swimmers. Their set-up involved a retroactive loop ensuring zero pressure difference and counteracted any backflow. The microfluidic chip comprised of a compartment for a stop flow gradient development of H<sub>2</sub>O<sub>2</sub> followed its effect on the motion of Janus micro-swimmers.

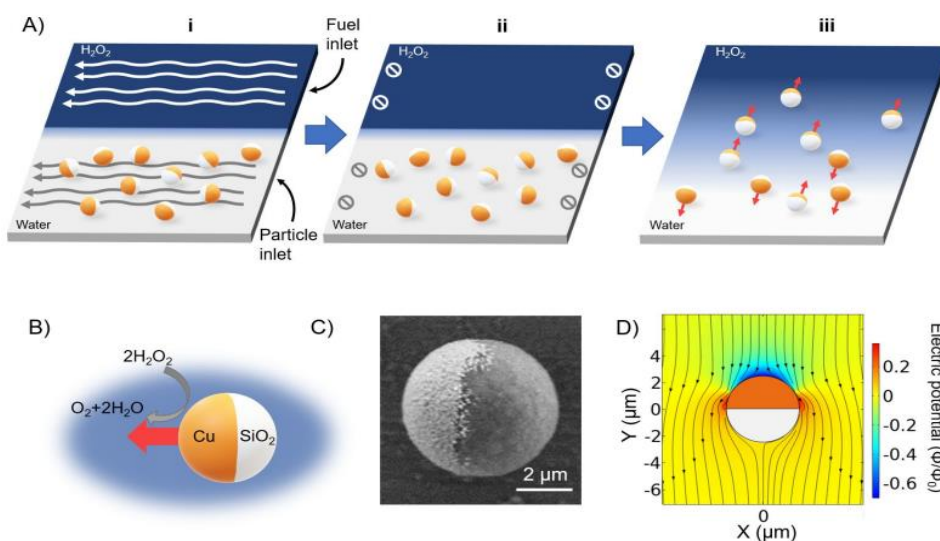


Figure 19: Intrinsic propulsion and chemotaxis of Cu@SiO<sub>2</sub>. A) Operating principles of the positive and negative chemotaxis of Cu@SiO<sub>2</sub> micromotors. B) Schematic diagram of the intrinsic propulsion of Cu@SiO<sub>2</sub> micromotors in H<sub>2</sub>O<sub>2</sub>. C) SEM of Cu@SiO<sub>2</sub> microsphere. D) Electric potential (colour code) and flow field lines (black arrows) around a Cu@SiO<sub>2</sub> Janus micromotors. Image extracted from Xiao et al., 2022.<sup>105</sup>

This study found a symmetry in the behaviour with both positive (upward motion of particles towards the higher concentration of fuel) and negative chemotaxis. For understanding of forces and torques influencing the orientation of particles in fuel ( $\text{H}_2\text{O}_2$ ) gradient, COMSOL simulations were modelled (Figure 19. D). Theoretically, propulsion force is proportional to the amount of ions created during the chemical decomposition of  $\text{H}_2\text{O}_2$ . This means that higher the fuel concentration, higher the propulsion force and drag force. Likewise, lower fuel concentrations can attribute to weaker drag force, which leads to particles not being able to overcome the rotational diffusion and reorientation along the gradient (causing more random directional-motion). Studied Copper/Silica ( $\text{Cu@SiO}_2$ ) micro-swimmer confirmed the theory about the effect of ion-concentration on drag force and particle-orientation in fuel concentration, for particles possessing Chemotaxis behaviour of motion.<sup>105</sup>

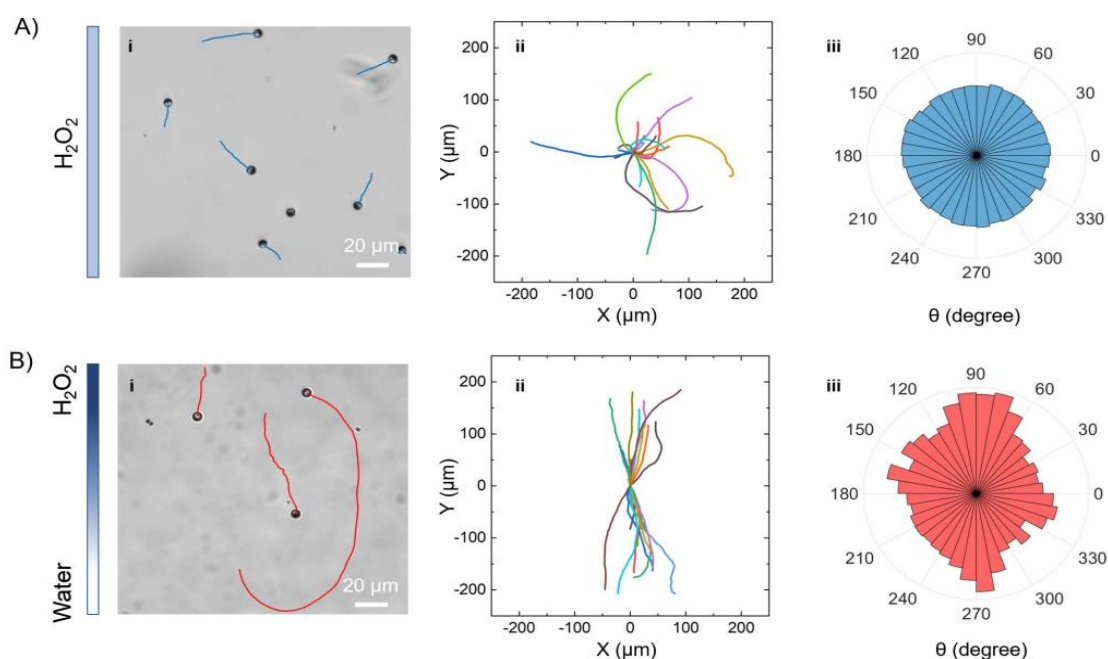


Figure 20: Statistical comparison between chemotaxis and non-chemotaxis behaviours of  $\text{Cu@SiO}_2$  micromotors. i) Optical micrographs, ii) trajectories and iii) distribution of the directionality of  $\text{Cu@SiO}_2$  micromotors moving in 2.5%  $\text{H}_2\text{O}_2$  without gradient A) and with the gradient B). Image extracted from Xiao et al., 2022.<sup>105</sup>

Therefore, it is conclusive that the fuel concentration along with the activity of the catalyst (in the Janus Particle) are the factors of key importance for the motion of particle. In case of systems having  $\text{H}_2\text{O}_2$  as fuel, metallic nanoparticles behaved as a good alternative to catalase for catalytic decomposition of  $\text{H}_2\text{O}_2$  and held major importance on the structural benefits. Considering the literature, and our concept for nuclear decontamination nanorobots, synthesizing Janus Particles comprising metal-nanoparticles for catalytic activity (gold/silica Janus particles) and  $\text{H}_2\text{O}_2$  as fuel, seemed a good starting point for this thesis work. Nevertheless, particle sensitivity to nuclear contaminant and move toward it are the primary requirements towards making our radiotactic colloid; nuclear decontamination nanorobots for which an in-depth understanding of movement of our Janus Particle is very crucial.

This can be achieved by having  $\text{H}_2\text{O}_2$  (an inevitable products of water-radiolysis) gradient; mimicking nuclear decontamination for our study at laboratory-scale. For this purpose, a microfluidic system can

prove to be of great benefit, not only because of its capabilities to obtain a stable gradient of  $H_2O_2$ , but also due other key benefits like small quantity sample requirement, cost-effectivity, and easy control for experimental adjustments.

## 1.5 Janus Particle

The term Janus is derived from Roman mythology, referring to the god of beginnings, endings, duality, etc. and is depicted as having two faces (Figure 21. a). The first scientific work with term 'Janus' was by C. Casagrande et al., 1989<sup>4</sup> (a semi-quantitative study on amphiphilic Janus Beads at water/oil interfaces), where they purposely designed Janus beads (from commercial glass beads with 50-90  $\mu\text{m}$  dia.). These beads possessed special properties of half-hydrophilic and half-hydrophobic at liquid-liquid interfaces, but because of limited synthesis and characterization techniques at the time, Janus particles did not receive much attention in research domain. Since three decades, significant advancements have emerged in the area of synthesis of Janus particles and the concept of Janus particles/materials has expanded to various shapes and morphologies (for example rod, sheet, snowball and dumbbell shaped).<sup>106</sup> To describe Janus Particles (JP) discreetly, these are one structure system with two or more chemically discrepant compositions (Figure 21. b to d). This can serve as fundamental units for constructing complex assemblies, dual-functional devices, or specialized surfactants, depending on whether one hemisphere is hydrophilic while the other is hydrophobic, or building a dipole with segregated positive and negative charges.<sup>107</sup> Janus Particles have been developed for a wide range fields of application: solid surfactants agents, micro/nanomotors, biosensor, drug delivery, bio-imaging, cancer therapy. In each application case, one specificity of Janus particles is explored.

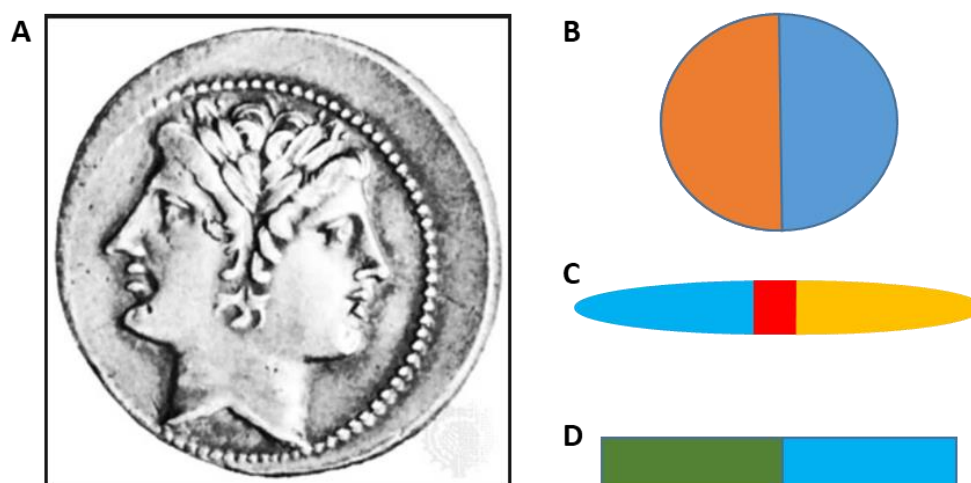


Figure 21: a. The god Janus, beardless, Roman coin; in the Bibliothèque Nationale, Paris, while b. and c. are animations for spherical and cylindrical shaped Janus Particles; representing different structural properties, respectively. Image a extracted from Bibliothèque Nationale, Paris.<sup>108</sup>

For Janus particles with dual hydrophilicity and hydrophobicity, amphiphilic behaviour is obtained and particles could self-assemble and decrease the water/oil interfacial tension.<sup>109-111</sup> Figure 22 shows the difference in the slopes of homogeneous particles (denoted as HNP) in red and Janus Particles

(denoted as JNP) in black, similar to each other but with different intensities: this highlights the influence of interactions between the non-wetting face (of HNP and JNP) with its surrounding medium. Contrary to this, reactive side of Janus particle in a surrounding medium with chemical affinity (with one of all the faces of Janus particle) can lead to enhanced motion following hyper-diffusive behaviour.<sup>62,65,68,83</sup> The self-propelling nature of certain active Janus particles can lead to a correlation between their movement and orientation. Furthermore, recent studies also suggest interplay between the translational and rotational diffusion in Janus particles causing spontaneous movement, and tendency to rotate its non-wetting face in the direction of motion, thereby reducing drag.<sup>62,65,68,83,112–114</sup> However, a study also suggest that this rotational diffusion can also lead to sedimentation of particles.<sup>115</sup> But, to understand this dynamics, it is crucial to understand aspects like diffusion, collective diffusion and other potential mechanisms for movement. In the case of active Janus Particles, the precise role of the reactivity of one side of particles is important to better understand the movement of the particles.

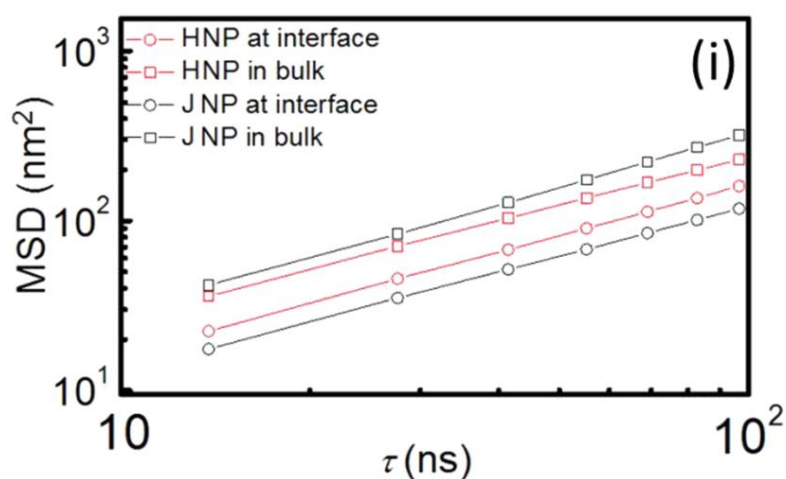


Figure 22: Mean squared displacement of JNPs and HNPs in bulk dispersion and at an interface showing lowest MSD for JNP at oil-water interface. Image extracted from Wang et al., 2020.<sup>66</sup>

The spherical shape is the most studied Janus particles, but plate-like Janus particles (with single sided positive charges and grafted polymer on the other side) can also decrease interfacial tension.<sup>116</sup> As the separation of electrical charges (with negative and positive charges concentrated on opposite halves), would cause a significant dipole moment allowing for their manipulation from a distance by rotating them in response to the direction of an applied electric field.<sup>117</sup> Janus particles have also potentials for biological applications, for example, a work by Yoshida<sup>118</sup> shows the interaction between the anisotropic Janus particles and endothelial cells. In this work, electro-hydrodynamic co-jetting method was followed to synthesize Janus particles with two biologically distinct hemispheres; one side with good binding properties for endothelial cells while the other side with resistive properties.<sup>118</sup> This can be useful in enhancing the targeting and functionality-sensitivity for drug delivery.<sup>119,120</sup> In addition, Janus particles can also be utilized as high efficient catalyst,<sup>121</sup> fabricating blocks for self-assembling polymers<sup>122–124</sup> and as the functional material for the manufacturing of some electronic devices.<sup>125,126</sup> Finally, such kind of particles can be used for their abilities to be activated by an external stimuli to acquire a movement. For example, a work by Howse<sup>121</sup> showed autonomous propulsion motion in

Platinum/Polystyrene artificial micro-swimmer by using catalytic reaction on its surface. This study showed that the velocity of these micro-swimmers depended upon the concentration of chemical in the surrounding (fuel).<sup>121</sup> While Janus particles have application for wide range fields, its potential is particularly significant in fields such as robotics and smart materials, where precise control over movement and interaction with surroundings is essential.

### 1.5.1 Janus Particle Synthesis: Multifaceted Approach

Janus particles are fabricated in various micro-sized and nano-sized structures such as diblock copolymer, nanoparticles and nano-cylinders, etc. and are of three types: polymeric, inorganic and hybrid (polymeric/inorganic). Presently, the following kinds of nanoparticle-structures/molecules can be considered as Janus particles: patchy and multi-compartment particles, anisometric or anisotropic building blocks, colloidal self-assembly and colloidal molecules.<sup>127–130</sup> Progress in the fields of polymer and inorganic chemistry has led to the advancements in Janus particles synthesis giving us some widely used methods (for example partial contact, directional flux, micro-contact printing, etc).<sup>127,128,131–134</sup> While the strategy to synthesize janus particles can be purely chemical-based, physical-based and hybrid (both physical and chemical) based (Figure 24), these synthesis methods are broadly categorised under masking, phase separation and self-assembly (Figure 23).

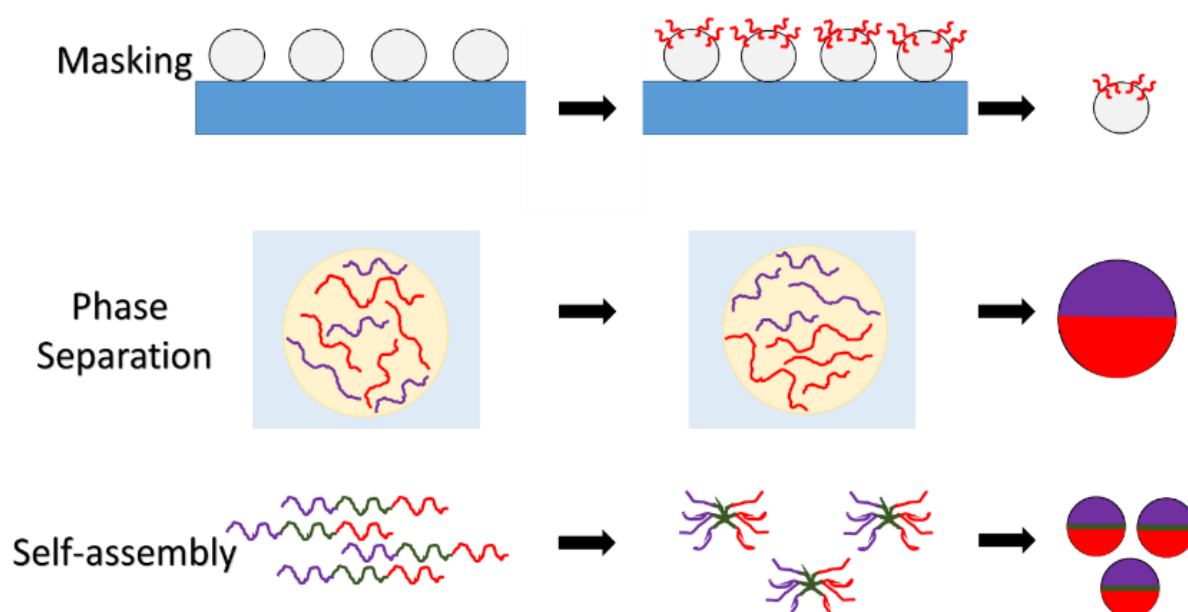


Figure 23: Brief overview of masking, phase separation, and self-assembly methods. Masking: particles (white circles) immobilized on template (blue base), modifying the exposed side, followed by template-removal and particle extraction. Phase Separation: emulsion of immiscible polymers is prepared and chemicals are separately cross-linked during solvent evaporation.<sup>127</sup>

Chemical methods involve reactions that selectively modify one side of a pre-existing particle, while physical techniques like physical vapour deposition utilize directed beams to deposit material on a specific hemisphere. Hybrid approaches on the other hand interplays between both chemical and



physical methods to create Janus structures, for example, droplet based microfluidic approach. Figure 25 briefs some of the different methods allowing researchers to tailor and synthesis their desired materials and functionalities of the Janus particles.

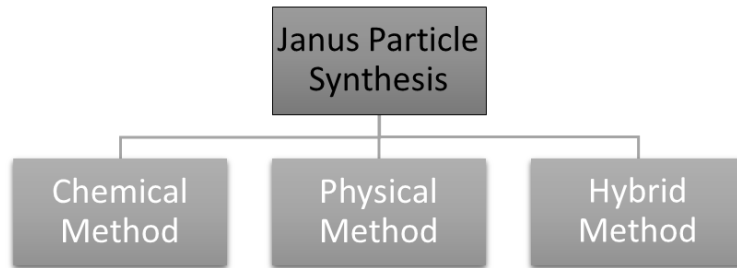


Figure 24: Different categories of methods for Janus particle synthesis

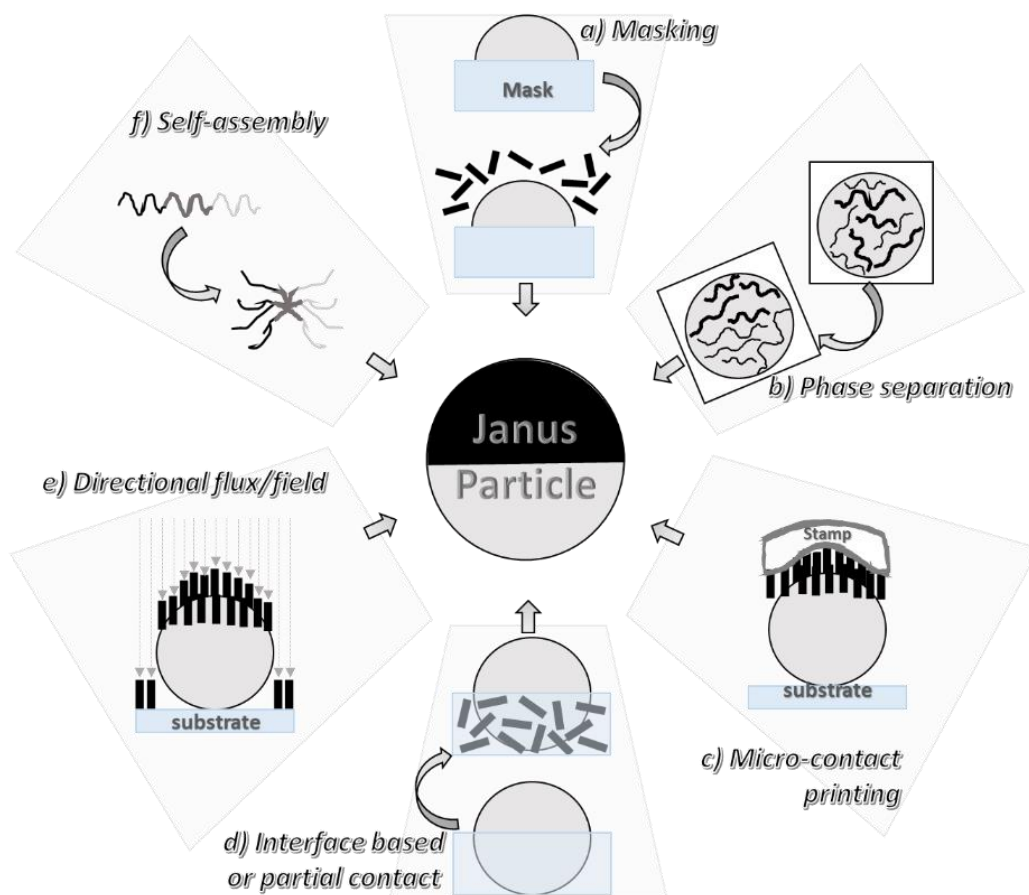


Figure 25: Example of different methods to obtain Janus particle: a) masking/unmasking method, b) Phase separation method, and f) Self-assembly method, along with strategies like c) micro-contact printing techniques, d) technique based on interfaces and partial contact and e) techniques using reactive directional fluxes or fields that fall under these methods.<sup>106,127,128,135</sup>

Example of the different methods<sup>135</sup> of fabrication are shared in detail in the next sections.

### 1.5.1.1 Masking Method

Masking refers to the method where one side of a homogeneous particle is protected or masked while the exposed side undergoes the modification particles, followed by the removal of the template.<sup>106,127</sup> This leads to regions with different chemical composition in the particles, creating distinct differences in properties between the two hemispheres of the particle.<sup>106,127,128,136</sup> Different techniques that can fall under the method of masking are techniques based on phase-interface, partial-masking and toposelective modifications, template assisted, evaporation based (explained from “1.5.1.1.1” to “1.5.1.1.4”).

#### 1.5.1.1.1 Phase-interface based technique

The phase-interface based techniques involve partial contact with two distinct reactive media (air/liquid and liquid/solid) having precursor particles at the interface. One of the media contains the reactive species, while the second medium is maintained inert. For example, following this method, Fujimoto et al.<sup>137</sup> transformed polymer latex particles (200 nm dia.) into half-raspberries like structures with human immunoglobulin G on half of the surface (Figure 26).

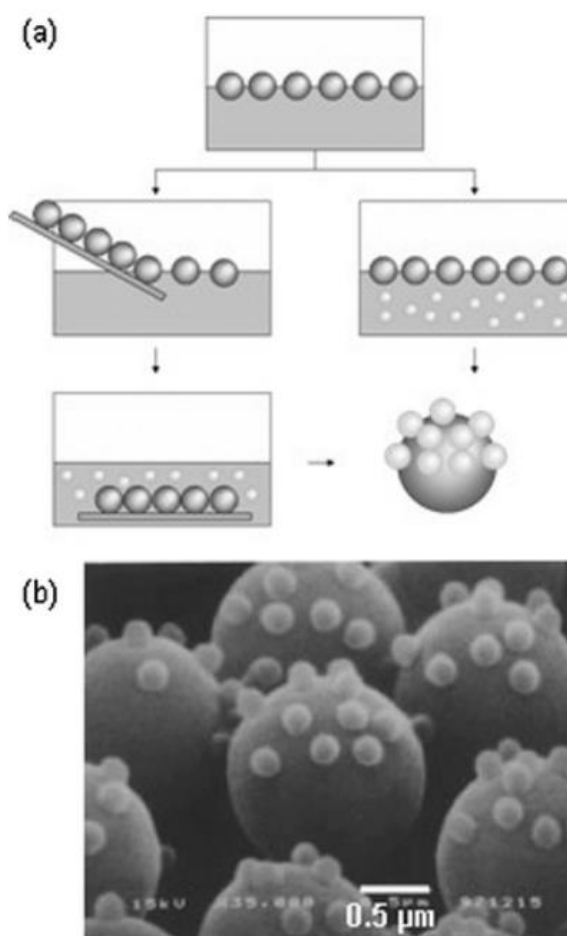
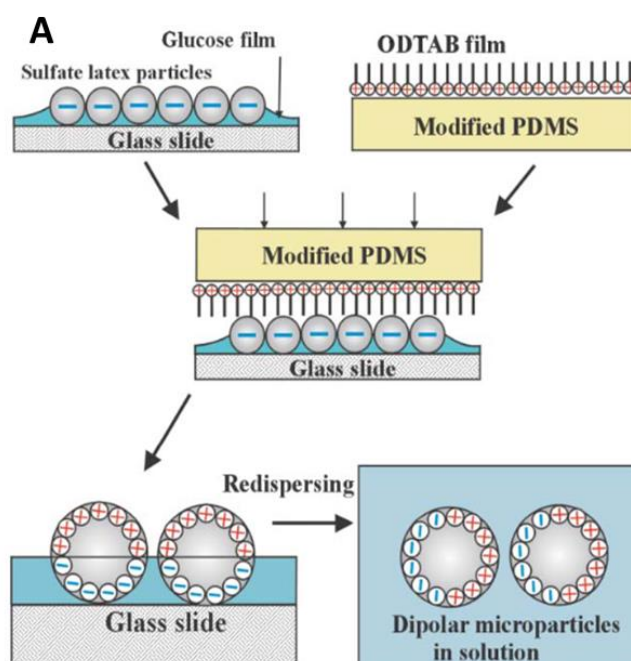


Figure 26: (a) Schematic for Janus Particle produced from precursor particles arranged along a liquid/solid interface (left route) or an air-liquid interface (right route). (b) SEM image of half-raspberry-like particles made of 2 μm reactive acrylic beads and 200 nm latex-particles. Image extracted from Fujimoto et al, 1999<sup>137</sup>

### 1.5.1.1.2 Template assisted

An example of techniques based on template assisted masking method is microcontact printing. This approach involves transferring a pattern from an elastomeric stamp onto a surface. This technique is applicable to produce patterns of self-assembled mono-layered particle with a sub-micron lateral resolution (making it as a limitation for smaller particles). The key parameter of this approach is the contact angle between the particles and the layer (they are mono-layered upon). Cayre<sup>107</sup> fabricated janus particle by selective deposition of octadecyltrimethylammonium bromide (ODTAB) a water-insoluble cationic surfactant onto one hemisphere of a negatively charged colloidal particle (sulphate latex particles) via micro-contact printing technique. Initiation of this procedure was evaporation of latex suspension spread on a glass substrate followed by spreading particle monolayer onto it. (Figure 27. A). Then, elastomeric stamp was fabricated (with the desired pattern by using photolithography) and inked with ODTAB. Inked stamp was brought into contact of the top surface of the mono-layered particles, and thus, ODTAB was stamped onto one hemisphere of sulphate latex particles creating Janus particles. Lastly, the janus particles were recovered from the substrate and re-dispersed in water for further use.<sup>107</sup> Three important factors in this work were: 1) stamp material and Ink properties: the choice of elastomer (e.g., polydimethylsiloxane, PDMS) influenced the printing resolution and ink transfer efficiency. While ink's viscosity, surface tension, and compatibility with the substrate were crucial for successful transfer. 2) Contact Pressure: The force applied during stamp contact influences the amount of material transferred. 3) Environmental Conditions: Factors like humidity and temperature can affect the printing process and the quality of the Janus particles.<sup>107</sup>

The same authors prepared half raspberry-like particles through a similar process by arranging small sulphate latex particles onto the stamp and larger amino-alkyl latex particles onto the glass substrate.<sup>107,138</sup> For these kind of techniques (surface modification of particles attached to a substrate in monolayer), biggest drawbacks are limited yield of final product (thus incompatibility for bulk production), efficiency of Janus Particle production highly depends upon the mono-dispersity and mono-layering of particles (on the substrate).



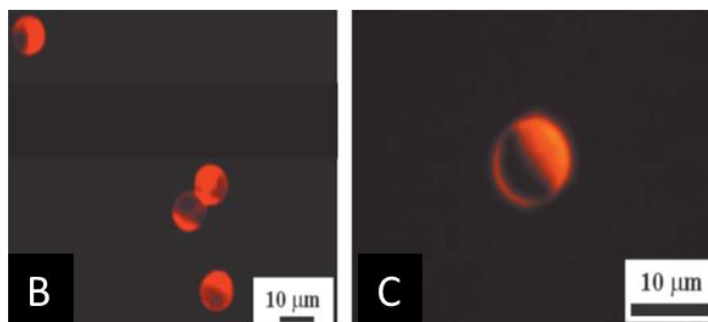


Figure 27: (A) Scheme for micro-contact printing of surfactant (ODTAB) stamping onto a monolayer of oppositely charged particles (sulphate latex) for Janus Particles production by modifying the exposed surface. Fluorescence microscopy image B and C showing PS-latex Janus particle tagged with fluorescent dye. Image extracted from Cayre et al, 2003<sup>107</sup>

Another work by Koo et al.,<sup>139</sup> demonstrated the creation of Janus particle arrays resembling snowmen (Figure 28) for the development of anti-reflecting surfaces, following surface modification via layer-by-layer self-assembly method followed by contact printing method. This work comprised of layers of charged polymer colloids and polyelectrolytes. On this spherical polystyrene (PE) particles of 100 nm diameter were adsorbed, followed by contact printing of PAH (using a PDMS stamp) onto them. Lastly, smaller PE particles (50 nm dia.) were attached onto this and snowman like Janus particles were obtained.<sup>139</sup> While microcontact printing has good resolution for wide size range of particles, low throughput with limited quantity production limits the application of this method.<sup>106,138,139</sup>

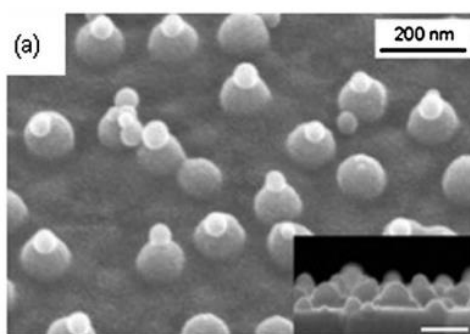


Figure 28: Small polystyrene particles (50 nm) attached onto bigger polystyrene particles (100 nm) via PAH Snowmen like Janus Particle from layer-by-layer method and contact printing. Image extracted from Koo et al., 2004<sup>139</sup>

Similarly, Kaufmann et al.,<sup>140</sup> utilized “Sandwich” micro-contact printing technique for fabricating Janus particles. This technique involved sequential application of different materials to opposite sides of a particle using two micro-contact stamps (Figure 29). In this work, a monolayer of porous spherical particles was formed on the first PDMS stamp, followed by ink application of the first ink. Then second stamp was prepared and inked, followed by sandwiching particle-monolayer as ‘stamp-particles-stamp’ with the help of a homemade, hand-operated press. This was followed by heat/irradiated to initiate the reaction of micro-contact printing. When the reaction was complete, stamps were separated and janus particles (Figure 30) with distinct functionalities on each hemisphere were washed with water and other solvents like ethanol, acetone and diethylether.<sup>140</sup>

In work like this, precise alignment of the two stamps is utmost crucial for accurate particle transfer and Janus particle formation.

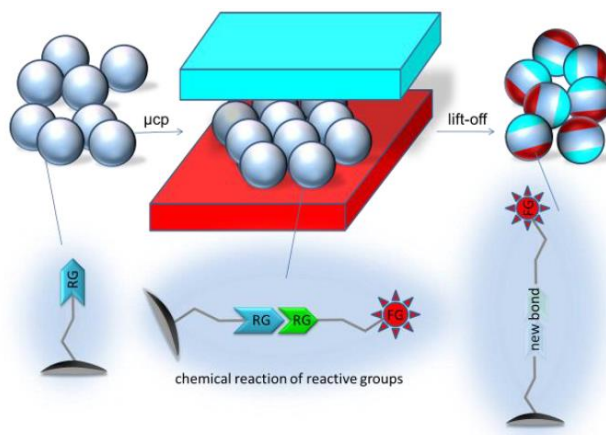


Figure 29: Illustration of sandwich micro-contact printing technique for fabrication of Janus particles. Microparticles ( $\mu\text{cp}$ ) comprising reactive groups monolayered between two stamps (blue and red) getting stamped (after contact) differently on each side. Janus particles are obtained after lift-off. Image extracted from Kaufmann et al., 2012

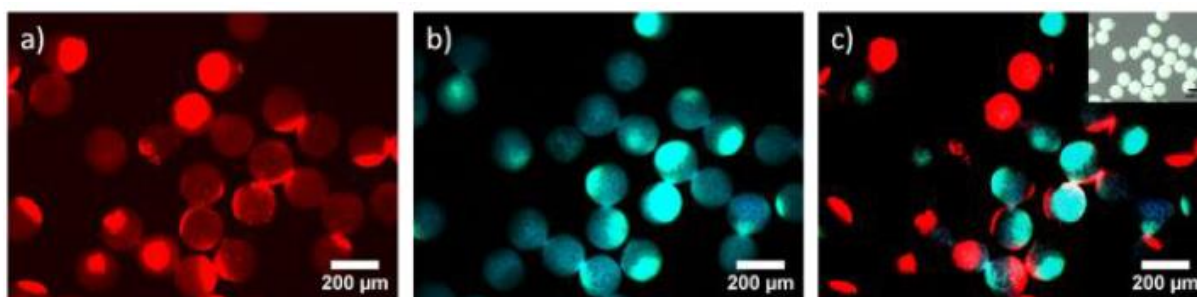


Figure 30: Particle images from fluorescence microscopy showing different dyes printed on azide beads in respective observations: rhodamine alkyne (a) and dansyl alkyne (b) overlay of both images (c). Light microscope image of sample on the top right of image (c). Image extracted from Kaufmann et al., 2012.<sup>140</sup>

#### 1.5.1.1.3 Evaporation based

Evaporation based techniques deals with a different approach for the functionalization of a part of the particles to produce Janus particles by bringing particles and layer (to be deposited) in contact, physically. Examples of evaporation based techniques are physical vapour deposition (PVD) (illustrated in Figure 31) and chemical vapour deposition (CVD)<sup>106,127,128,136</sup>. PVD utilizes physical phenomena like sputtering or evaporation to eject atoms from a target material and deposit it as a thin-film onto the substrate.<sup>141</sup> The process of metal evaporation is versatile and can be utilized with particles of different compositions and dimensions. This technique has been readily investigated to obtain monolayers of gold/silica Janus nanoparticles for their potential as optical sensor devices.<sup>82,106,142,143</sup>

Studies show that in PVD, an intermediate layer adhesion layer can enhance the robustness of the end product (Janus particle with stronger bonding between target particle and deposited layer). For example, a work on half shell of gold (Figure 32) and other metals (platinum and palladium) described

## Introduction

by Love et al.<sup>144</sup> highlighted that before depositing gold layer during the production of Gold/Silica Janus Particle, a preliminary deposition of Ti-W layer was essential for better adhesion between gold layer and the surface of silica particle.<sup>144,145</sup>

However, difference between the compatibility of materials and deposition techniques (example: sputtering, evaporation, etc.) also limit the type of janus particles producible from this technique.

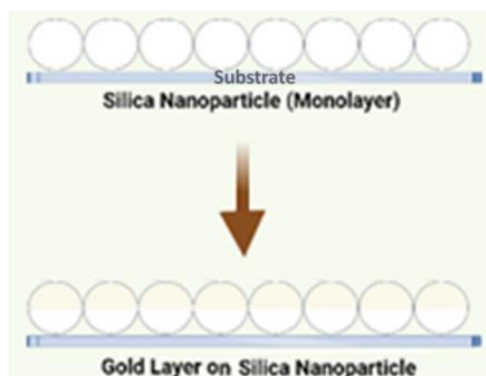


Figure 31: Gold/Silica Janus nanoparticles on a glass substrate. Gold metal evaporated and deposited on exposed surface of monolayer silica nanoparticles (white circles) to obtain half surface coated with gold layer, via Physical Vapour Deposition method.

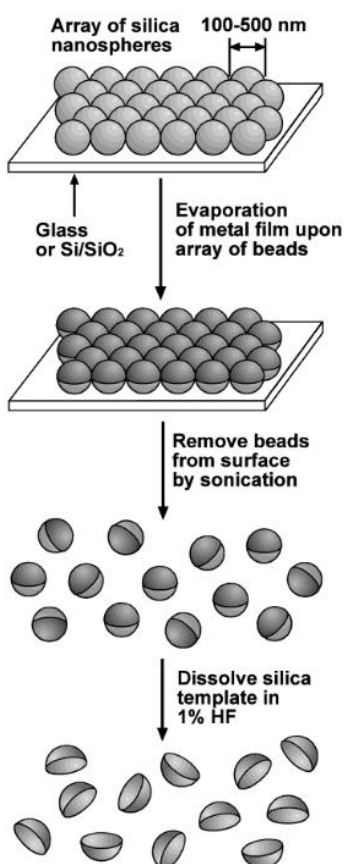


Figure 32: Scheme of PVD followed by Love et al. to obtain gold/silica Janus particle, followed by dissolution of silica particles to obtain gold nano-shells (half shells). Image extracted from Love et al., 2002<sup>144</sup>

#### 1.5.1.1.4 Photochemical technique

A work by Hugonnot et al.<sup>146</sup> showed the ability to create asymmetric surfaces on silica micro-particles, through a laser photochemical deposition process.<sup>146</sup> This technique extends from the lithographic technique. In this study, silica beads were immobilized in an acidic solution containing chromium ions (Figure 33) and top hemisphere were projected to a 514 nm wavelength laser, causing photo-reduction of Chromium ions for the growth of  $\text{Cr}(\text{OH})_3$  cap on the surface of the silica beads. However, due to optical resolution constraints, it is worth noting that this technique is limited to micro-particles at small quantity production.<sup>146</sup> In addition to the limitation in particle size and low throughput, material combination and compatibility with the required fluxes for selective deposition over target particle-surface limits the application of this method, ultimately raising the need for cost-effective alternative methods, especially for bulk production of Janus particles.<sup>144–146</sup>

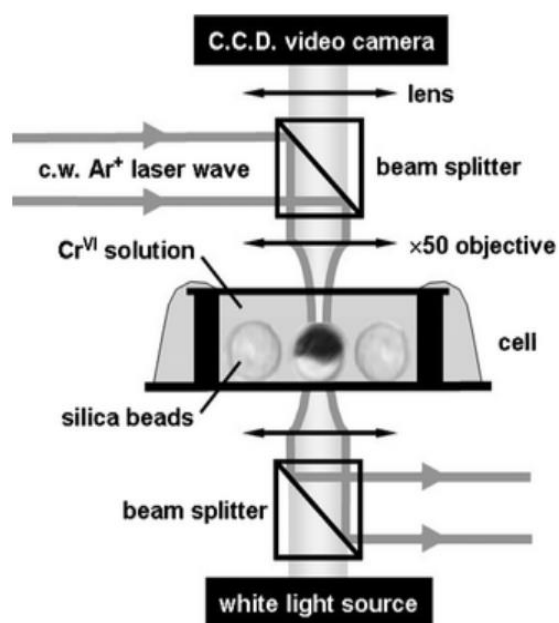


Figure 33: Schematic representation of the experimental set-up for laser-induced Janus particle preparation by photochemical deposition of  $\text{Cr}(\text{OH})_3$  onto  $10\ \mu\text{m}$  Silica beads centred in the beam. Image extracted from Hugonnot et al., 2003<sup>146</sup>

Another commonly used version of lithography technique is flow lithography. This method involves creating a controlled laminar flow environment within a channel/microchannel along with photo-curable material. A focused ultraviolet (UV) light beam (often with a mask to define specific patterns) is projected directly onto this fluid stream having the photo-curable material. This causes polymerization of the photo-curable material, resulting in the formation of solid particles (while the particle-shape is determined by the microchannel geometry and the UV light pattern). Manipulation of the flow conditions, UV light intensity, and mask design, can be exploited to obtain a wide range of anisotropic particle morphologies.

In a work by Dendukuri et al.<sup>147</sup> continuous-flow lithography technique was followed to produce particles of different shapes and size. Here, bifunctional Janus particles (rectangular shape) were synthesized by polymerizing rectangular particles at co-flowing fluid (photo-initiator added poly(ethylene glycol)(400) diacrylate (PEG-DA) and rhodamine-labelled PEG-DA) interface. This

comprised a mixture of photoresist and photo-initiators that was flown through a microfluidic device (with channels shaped according to the desired particle design) (Figure 34). To this, UV light was exposed through a patterned mask, causing the solidification of the photoresist solution in specific targeted areas, and therefore, forming Janus microparticles. The collection of the particle was done by simply flushing out of the channel.<sup>147</sup>

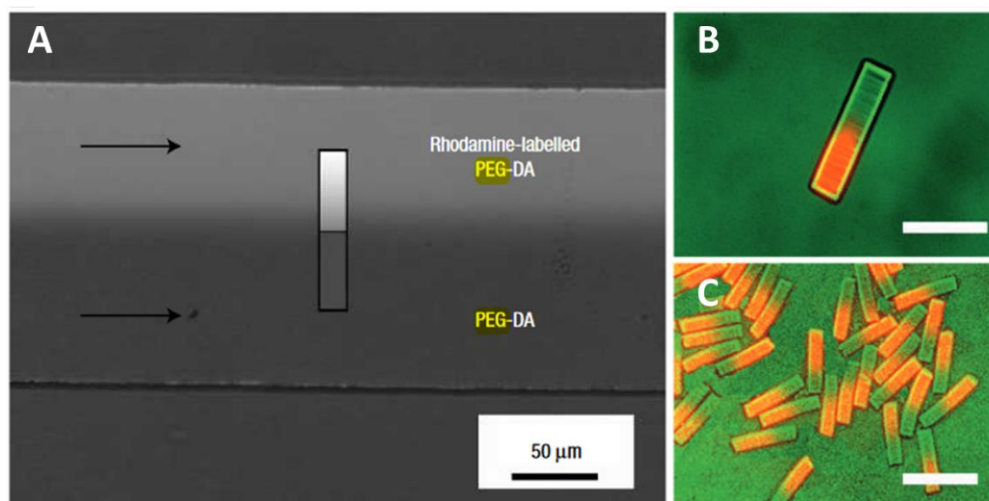


Figure 34: Scheme of synthesis of Janus particles. A: Streams of rhodamine-labelled PEG-DA with cross linker (light grey) and PEG-DA (dark grey) co-flowing through channel. B and C: Images of rectangular Janus particles with the fluorescent labelled (orange) and the non-labelled (green) sections. The scalebar in B and C are 50 and 100  $\mu\text{m}$ , respectively. Image extracted from Dendukuri et al.,2006.<sup>147</sup>

#### 1.5.1.1.5 Partial Masking based on toposelective surface modification

In the former paragraphs, different masking methods have been described (a) Phase-interface based technique (“1.5.1.1.1”), (b) Evaporation based technique (“1.5.1.1.3”), (c) Employing micro-contact printing (“1.5.1.1.2”), (d) Photochemical technique (“1.5.1.1.4”).<sup>106,127</sup> Another technique that falls under masking method is a partial masking technics, an example of which is highlighted in Paunov’s work.<sup>148</sup> Here gel trapping technique (GTT) was followed, where polystyrene (PS) colloid was injected at the interface between a hot hydrocolloid aqueous solution (gellan 2 wt. %) and a pre-warmed decane phase (Figure 35.i). The decane phase was then replaced with polydimethylsiloxane (PDMS) oil and subsequently, particle-monolayer trapped on the gel-surface was transferred onto the elastomer surface (similar to microcontact printing techniques). Lastly, after gold evaporation, the PS particles were half covered by gold (Figure 35.iii). This technique is also effective for particles <100 nm dia.<sup>149</sup>

When compared to traditional masking method, partial masking and topo-selective surface modification allows for fine-tuning of the masked area and enables the creation of complex Janus particle. It can be applied to various particle shapes and materials, in fewer processing steps compared to traditional masking. Nonetheless, the masking method in general is mostly manual and time-consuming, while the scale up of Janus particle for large-scale production is a major drawback of this method. While discarding masking materials increases production costs, it also creates more waste for environment.<sup>148</sup>



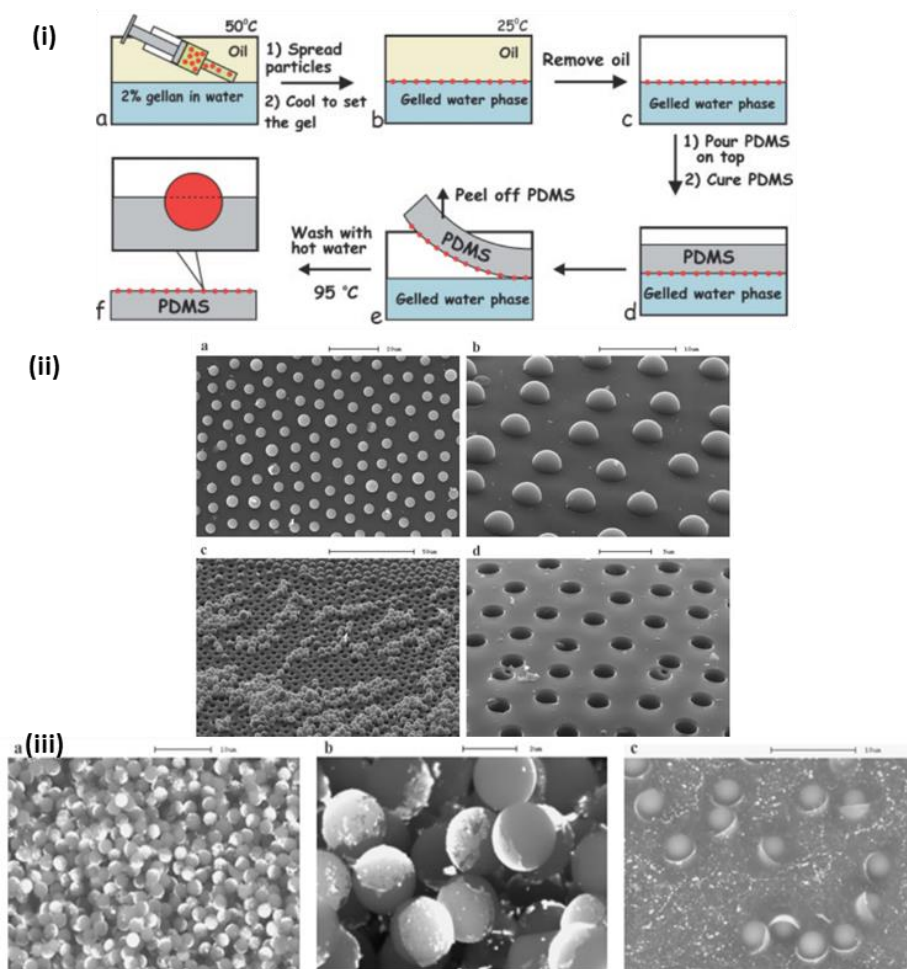


Figure 35: (i) Scheme of the gel trapping technique for replicating microparticle monolayers at the oil-water and the air-water interfaces. (ii) a,b) SEM images of 3.9  $\mu\text{m}$  sulphate PS latex particles on the surface of PDMS obtained by the GTT at a decane-water interface. c) SEM image of the same surface after the mechanical removal of particles off the PDMS; producing an array of circular microholes. d) SEM image of a similar pattern of microholes produced with 2.5  $\mu\text{m}$  carboxylic PS latex particles at a decane-water interface. (iii) a,b) SEM images of Janus particles fabricated by gold sputtering on a monolayer of 2.7  $\mu\text{m}$  sulphate PS latex particles embedded on the surface of PDMS, obtained by the GTT at the decane-water interface, followed by mechanical collection of the particles from the PDMS. c) A sample of similarly prepared 3.9  $\mu\text{m}$  PS latex/gold Janus particles collected from the PDMS with sticky tape. Image extracted from Paunov et al., 2004.<sup>149</sup>

### 1.5.1.2 Phase separation Method

Phase separation relies on the segregation of two or multiple non-compatible ingredients within a mixture. For example, immiscible polymers are dispersed in an emulsion followed by solvent-evaporation; locking the bonds between different species via chemical cross-linking.<sup>106,127</sup> From this pathway janus particle of inorganic, polymeric, or polymeric-inorganic hybrid materials types are obtainable.<sup>106,127</sup> The phase separation method can be obtained through bulk approaches or fluidic approaches like fluidic nanoprecipitation systems (FNPS) or electro hydrodynamic (EHD) co-jetting, directional flux/field based technique.<sup>106,127,128,136</sup> In comparison to masking, phase separation methods permit higher mass production and scale-up. However, achieving smaller janus particles (below 100 nm) is a challenge faced in phase separation method.<sup>106,127</sup> Figure 36. a. and b. illustrate co-flow method and electrohydrodynamic co-jetting method, respectively.

Ekanem<sup>150</sup> (Figure 36.b) generated Janus droplets of poly( $\epsilon$ -caprolactone) (PCL) with a functional end-group (e.g., thiol, silane) and poly(lactic acid) (PLA) by controlling the evaporation time of the solvent.<sup>150</sup>

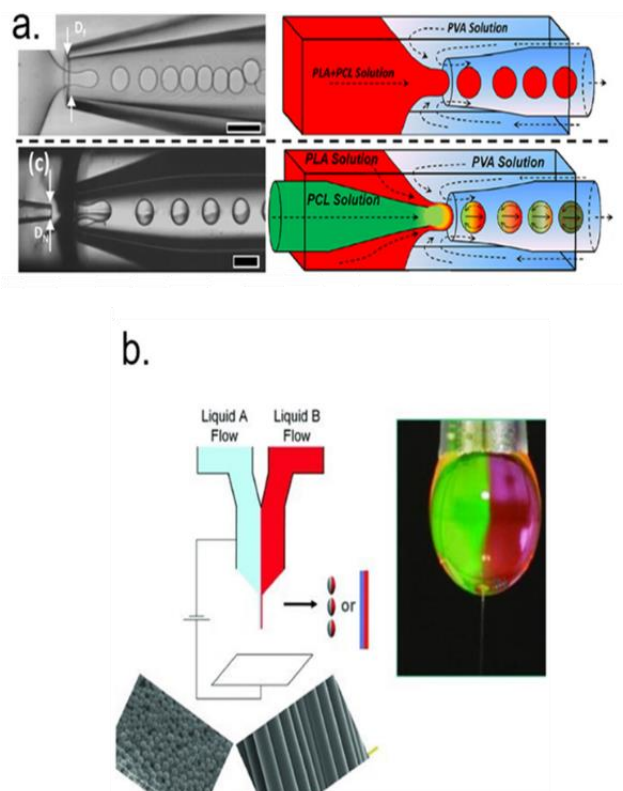


Figure 36: (a) Droplet generation in (top) flow-focusing glass capillary device and (bottom) co-flow or flow-focusing glass capillary device. Bottom: Examples of particles and fibers obtained from the process<sup>127,150</sup> (b). left: Scheme of electro-hydrodynamic co-jetting process, leading to either particles (electro-spraying) or fibers (electrospinning). Right: showing a typical Taylor cone used during electro-hydrodynamic co-jetting.. Image extracted from Ekanem, 2019<sup>150</sup> and Safaie, 2020.<sup>127</sup>

#### 1.5.1.2.1 Directional flux

Directional flux/field applies external electric or magnetic field on target particles and metal ions or nanoparticles are directed towards one side of the particles modifying exposed hemisphere of particles, while having the other hemisphere protected by itself (Figure 37).<sup>127,144,145</sup>

Following this method, development of Janus particles with non-spherical morphology is possible as well (Figure 38. a illustrating snowman-like-shaped Gold/Silica Janus particle produced from directional fluxes method).<sup>127,144,145</sup> Nonetheless, success of these techniques rely greatly upon a good monolayer spreading of particles on surface and precise management of the thickness of deposited layer on particles.<sup>82,106,142,143</sup>

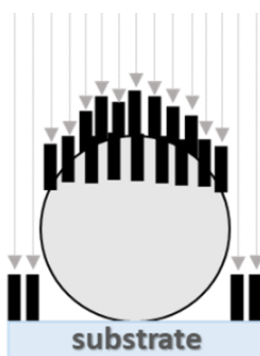


Figure 37: External force fields (grey arrows) used to control the directional flux for metallic layer (black) (example gold) on top side of the particles, while having the other hemisphere protected by itself.<sup>127</sup>

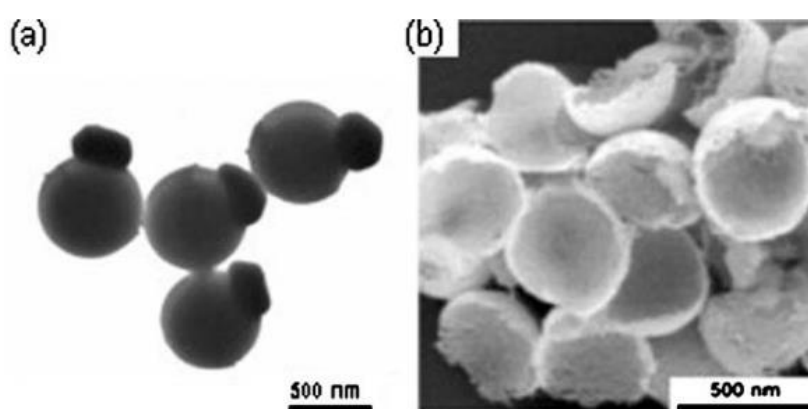


Figure 38: Silica–gold Snow like Janus Particle formed from directional fluxes (like in figure 31. A) and de-wetting half-shells of gold deposited on one of the silica hemisphere. (b) Half-shells of Gold, obtained after dissolution of the silica template. Image extracted from Love et al., 2002.<sup>144</sup>

#### 1.5.1.2.2 Solvent and Emulsion based method

One of the simple and popular ways for obtaining Janus particle is Pickering Emulsion method. In this, emulsion is stabilized via irreversible adsorption of nanoparticles (instead of molecular surfactants) at the interfaces of two immiscible liquids ex: water and oil.<sup>151</sup> This kind of emulsion can be used to functionalize particle-surface differently. Figure 39 illustrates the scheme of Janus particle synthesis via Pickering Emulsion method, with the immobilization of particles at the interface of 2 liquids (reactive or not, containing additives or not). Due to the large interfacial area of emulsion this method promotes a high yield of Janus particles in comparison to flat interfaces.<sup>152–155,151</sup> This method centres on liquid/liquid interfaces and can also be exploited to obtain magnetic Janus particles as well, which can be beneficial in recovering these magnetic particles during/after their suitable application.<sup>106</sup>

Hong et al<sup>158</sup> introduced an original approach in the field of emulsification by transforming a liquid/liquid interface into a solid/liquid interface. This offered advantages over previous techniques, including simplicity, scalability, and the ability to produce particles with well-defined and customizable surface properties.

## Introduction

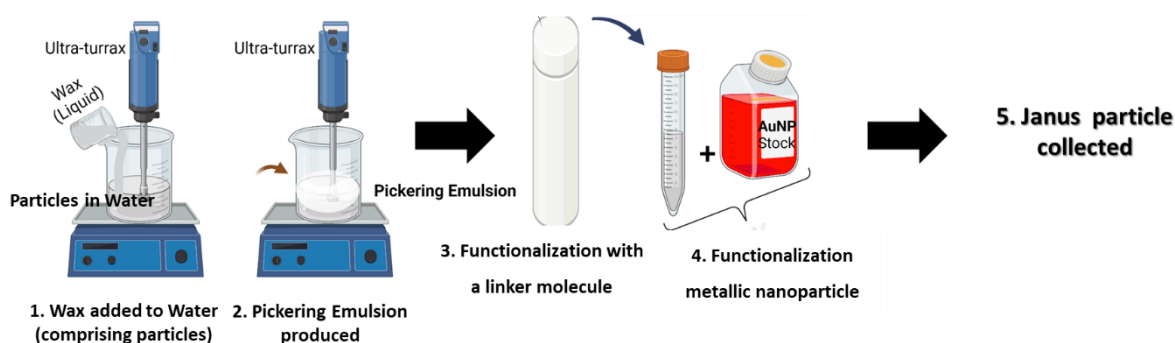


Figure 39: Scheme of Janus particle synthesis via Pickering Emulsion method. Emulsion made by stabilizing wax in water by particle, followed by surface functionalization of one side of particle (surface outside of wax) and lastly adding metallic nanoparticle (AuNP; Gold Nanoparticle).<sup>106,127,156,157</sup>

They immobilized silica particles at liquid paraffin wax-water interface in their Pickering emulsion, followed by cooling it down below the melting point of the wax to produce solid wax particles stabilized by silica particles. The subsequent chemical modification by APS (aminopropylsilane) on the exposed side of fused silica nanoparticles and lastly, removal of wax (using chloroform as wax solvent). This resulted in the production of APS/Silica Janus microparticles of 1.5  $\mu\text{m}$  diameter.<sup>158</sup> This work showed how Janus particle can be synthesized in bulk quantity (gram scale) by following simple and robust strategy of Pickering emulsion method.<sup>158</sup>

During emulsification the predictability of either oil-in-water (O/W) Pickering emulsion or water-in-oil (W/O) Pickering emulsion hinges on the wettability characteristics of solid particles present at the oil-water interface. Specifically, if one liquid exhibits better wetting of the solid particles compared to the other, it becomes the continuous phase. For an O/W emulsions, the three-phase contact angle  $\theta$  (angle formed at the three-phase boundary involving solid particles, continuous phase, and dispersed phase) must be less than  $90^\circ$  (Figure 40. (a)); observed in materials such as silica in liquids like water and oil, toluene. Conversely, a W/O emulsions are expected to form when the three-phase contact angle  $\theta$  exceeds  $90^\circ$  (Figure 40. (b)).<sup>152,157,159</sup>

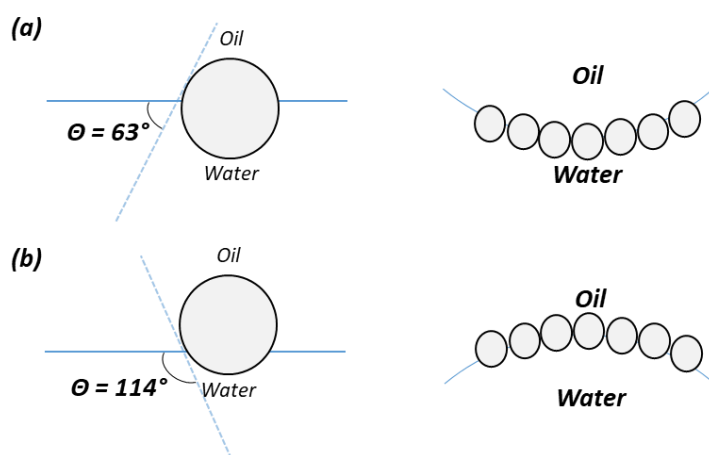


Figure 40: Contact angle of particle in continuous phase and disperse phase deciding whether emulsion be 'oil-in-water' (a) or water in oil (b).<sup>152,157,159</sup>

This is why for some systems, the particles are first functionalized to change their wetting properties prior to the formation of the Pickering emulsion.

Emulsification method can also be used to attain a higher complexity in the Janus particles. For example, Qiang et al.,<sup>160</sup> obtained asymmetric nanocomposite pairs of silica and Polystyrene (PS) via local surface modification of silica particles in two stages of Pickering emulsification combined to in situ polymerisation (Figure 41). In the first stage, localized surface modification of the substrate (silica particles) was utilized for partial surface functionalization by *n*-octadecyltrimethoxysilane (ODMS) making it hydrophobic (Figure 41). Further, mini-emulsion polymerization was employed to polymerize monomers in the presence of these modified substrates in second stage of Janus particle synthesis. This allowed for the formation of the polymer component of the Janus particles. In this work oil used to obtain Pickering water in oil (w/o) emulsion comprised of styrene particles, resulting into styrene attachment on the hydrophobic side of silica particle and making it asymmetric mushroom-like styrene/silica nanocomposite particles (Figure 42).<sup>160</sup>

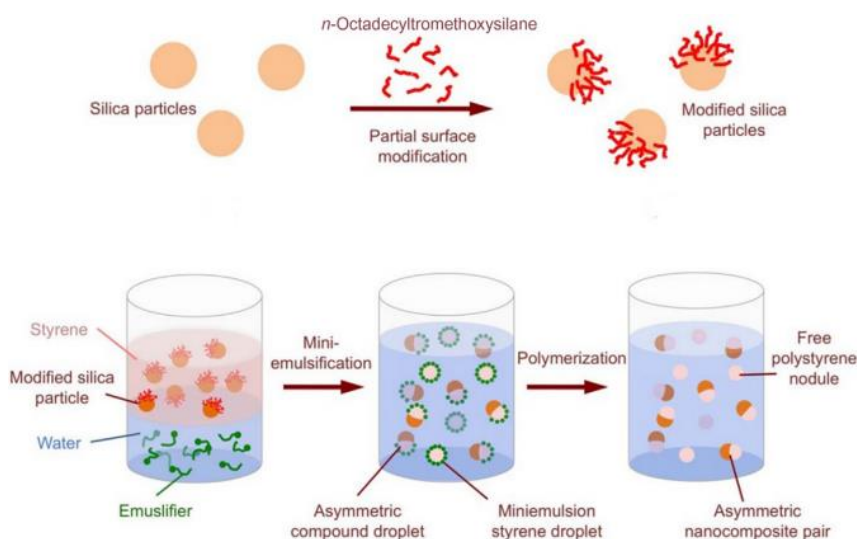


Figure 41: Diagram of mini-emulsion polymerization from Pickering emulsion. Image extracted from Nouri et al., 2018.<sup>161</sup>

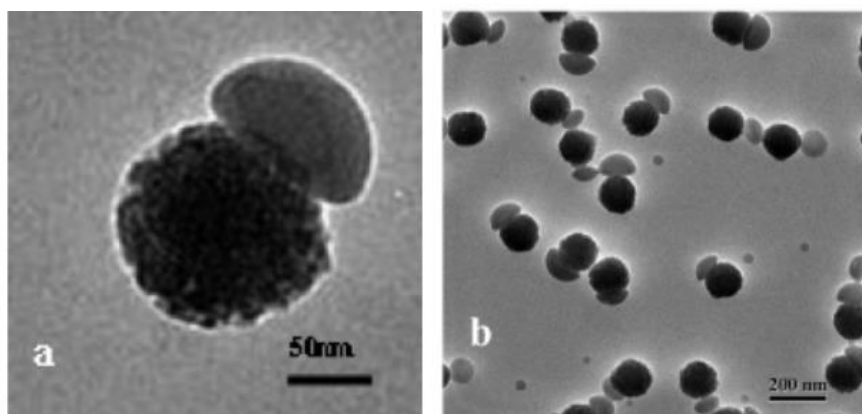


Figure 42: TEM images showing mushroom-like styrene/silica Janus particles. Image extracted from Qiang et al., 2008<sup>160</sup>

### 1.5.1.3 Self-assembly

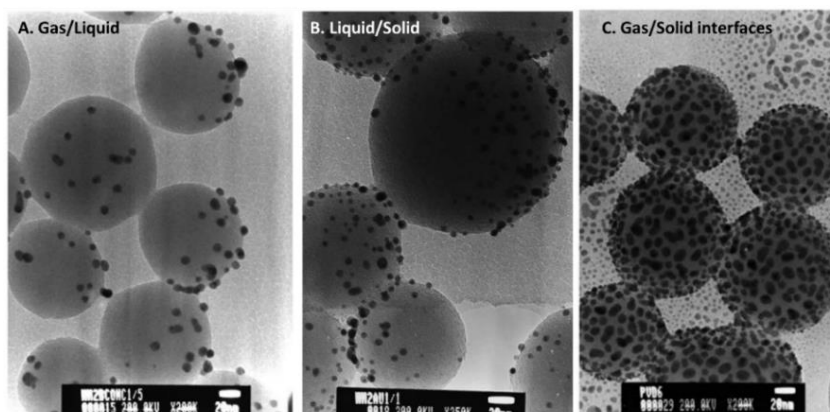
In self-assembly method for janus particle synthesis, a spontaneous organization of components into distinct regions occurs within a particle without external direction or guidance. This process is driven by specific local interactions between the different chemical ingredients through intermolecular forces and interfacial interactions.<sup>127</sup> These interactions can be hydrophobic<sup>128</sup>, hydrogen bonding (between hydrogen atoms and electronegative atoms), weak forces (like van der waals) between molecules, electrostatic (attractive or repulsive).<sup>127,128,161,162</sup> The interplay of these forces drives the components to adopt specific arrangements that minimize the system's energy, and forming Janus structures by approaching equilibrium. By carefully managing key factors like 'intermolecular interactions between the chosen components', 'environmental conditions like temperature and pH of the solvents', self-assembly method can be utilized to create complex structures with desired properties.<sup>127,128,161–163</sup>

This method includes techniques like Langmuir-Blodgett, microfluidics, spinning-disk that uses controlled fluid flows to produce particles with different properties on each side. junction.<sup>127,128,161–166</sup> In microfluidic approaches a microfluidic device is designed with channels for different fluids followed by droplet formation at channel junction.<sup>126,127,164</sup>

#### 1.5.1.3.1 Langmuir-Blodgett

Langmuir-Blodgett (LB) technique is used to transfer a monolayer of molecules from the air-water interface onto a solid substrate (Figure 43. A and B).<sup>165</sup> It involves spreading a material on the water surface, forming a thin film. This film is then compressed to form a tightly packed monolayer. By dipping a solid substrate through the monolayer, the molecules are then transferred onto the substrate, creating a uniform, single-layer coating. This process can be repeated multiple times to build up multilayer films with precise control over thickness. Petit et al<sup>165</sup> utilized the LB technique to create gold/silica janus particles by spreading a monolayer of silica particles (dia. 90-120 nm) at the air-water interface, followed by the introduction of gold nanoclusters.

Petit et al<sup>165</sup> half covered silica particle by gold nanoparticles (dia. ~8-10 nm) via air-liquid, liquid-solid from Langmuir film and Langmuir-Blodgett methods, respectively (Figure 43. A. and B, respectively).<sup>165</sup> These silica particles were first functionalized with amine function with aminopropyl-trimethoxysilane (APTES), and then functionalized with gold nanoparticles through contact with gold cluster suspensions in a Langmuir trough.



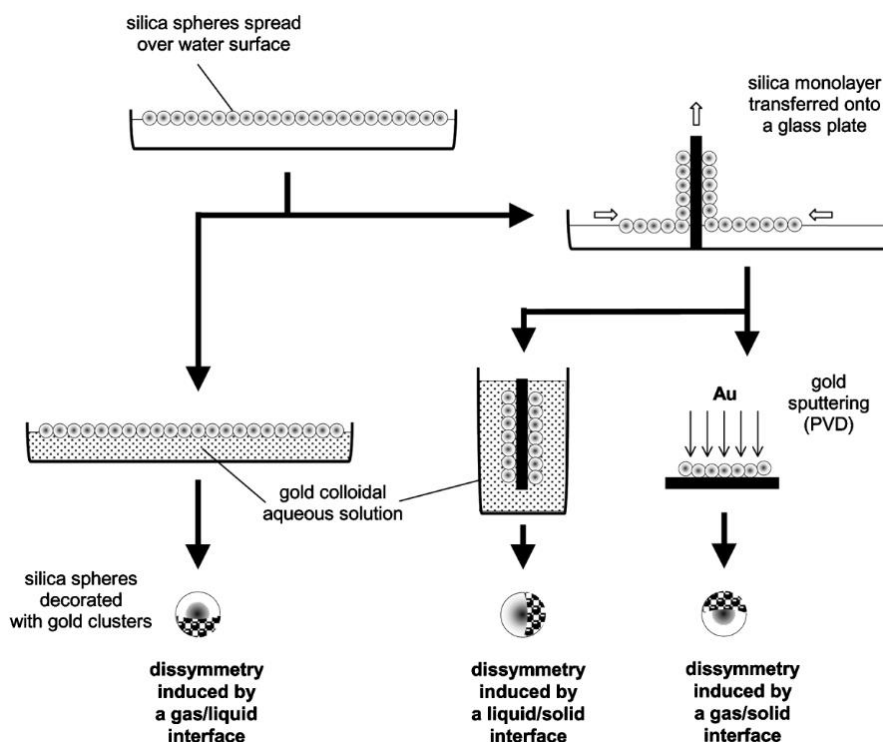


Figure 43: Gold/Silica Janus particle (A, B and C) synthesized from gas/liquid, liquid/solid and gas/solid interfaces, respectively. Image extracted from Petit et al., 2001<sup>165</sup>

### 1.5.1.3.2 Spinning disk

Another example of a self-assembly method is spinning-disk techniques. It is an approach that utilizes a spinning disk with two different materials (precursors or solutions) supplied from opposing sides. Once the disk spins rapidly, the centrifugal force makes these supplied materials flow outwards towards the edge forming a Janus particle with one side composed of material A and the other side composed of material B.

This technique is readily utilized for production of Gyricon sheets by efficient synthesis of polymer particles with two distinct compartments. Gyricon is a very thin electronic sheet and the polymer used in it are of black and white colour. In the process of Gyricon production, two different molten polymers (one white in color and other black, as shown in Figure 44. (a)) are simultaneously introduced from opposite sides onto rapidly spinning disk (~2700 rpm). As the polymers move towards the disk's edge, they form narrow streams, resulting in the creation of small spherical particles (~100  $\mu\text{m}$ ) due to Rayleigh instability.

As illustrated in Figure 44. (a) exhibits one polymer (black colour) on one side and the other polymer (white colour) on the other. It is noteworthy that the spin rate influences the proportion of small beads produced in this process and can provide particles diameter of 50 - 100  $\mu\text{m}$  and above.<sup>106,167,168</sup>

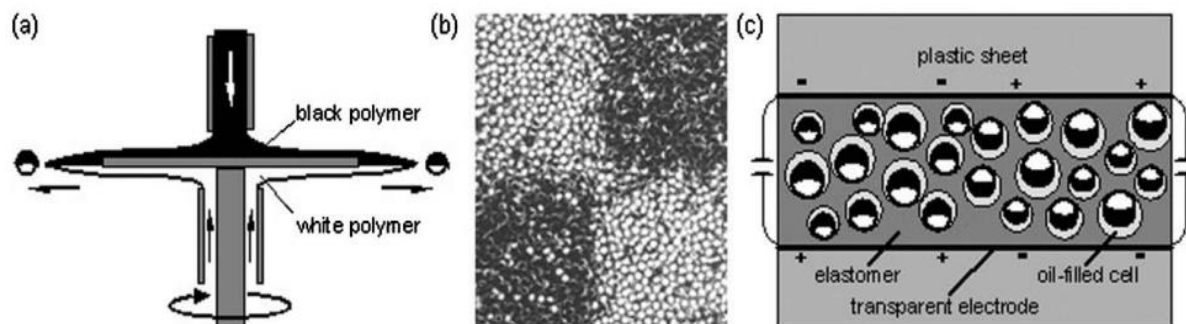


Figure 44: The Gyricon rotating ball display: (a) the dual-supplied spinning disk apparatus for the fabrication of bichromal balls, (b) 100  $\mu\text{m}$  black/white balls as organized on the corners of squares imaged with the gyricon display, (c) schematic cross section of the Gyricon display medium. Image extracted from Perro et al, 2005

Being a single step approach, this technique simplifies the production of Janus particles in comparison to other multi-step methods and is used for different materials too. For example: magnetic composite based on polyethylene Janus microparticles ( $\phi \sim 100 \mu\text{m}$ ) made by Ghosh et al.<sup>166</sup> However, controlled mixing and compatibility between the introduced materials are some major challenges which restrict the impact of this technique. This method finds comparatively lesser popularity than other methods for Janus particle production (like phase separation, masking, physical vapour deposition, etc.).

#### 1.5.1.3.3 Microfluidics

Microfluidic systems is a high throughput technique that can produce large quantities of particles in a continuous, cost-effective and efficient manner. Microfluidic technique allows for precise control over droplet size, composition, and flow rates. This results in highly uniform and reproducible Janus particles.

In the study by Wang et al.,<sup>164</sup> droplet-based microfluidics techniques (Figure 45) was followed to synthesize (Au nanorod@Ag)-polyaniline Janus nanoparticles. A microfluidic device containing gold nano rods (AuNr), silver precursors (Ag-pc), and polyaniline monomers was used to generate droplets. AuNr, Ag-pc and polyaniline monomers were distributed as per their solubility, interfacial tension, and hydrodynamic forces. This was followed by the reduction of Ag ions to form Ag nanoparticles and aniline polymerized to form polyaniline. This led to the formation of distinct regions within the droplet, and therefore set the foundation for the (Au nanorod@Ag)-polyaniline Janus droplet structure. Later these droplets were solidified, forming desired gold/silver Janus nanorods.<sup>164</sup>

A work by Chen et al.,<sup>75</sup> reported a general strategy for continuous fabrication of self-propelled micromotors having photocatalytic metal-organic frameworks (MOFs) for enhanced degradation of organic contaminants. Few of the major advantages of utilizing microfluidic technique was that it is a high throughput method, that allowed precise control over particle size in a cost-effective and efficient manner with reduced reagent consumption and waste generation. Chen<sup>75</sup> used a capillary microfluidic device for phase separation of particles inside an emulsion droplet.



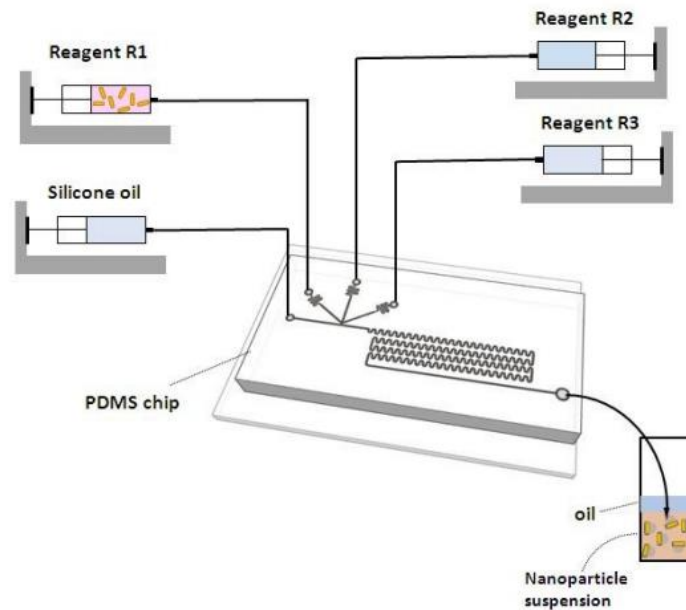


Figure 45: Scheme of Wang's microfluidic set-up for the production of Gold/Silver Janus nanorods. Image extracted from Wang et al., 2019<sup>164</sup>

This enabled them for the creation of complex Janus particle structures, including core-shell and compartmentalization. Emulsion-microdrops comprised of  $\text{Fe}_3\text{O}_4$ @Ag nanoparticles ( $\text{Fe}_3\text{O}_4$ @AgNPs) and zeolitic imidazolate-8@ZnO nanoparticles (ZIF-8@ZnONPs). While zeolitic imidazolate (ZIF) were adsorbed at the interface of the droplet, the  $\text{Fe}_2\text{O}_4$  particles were forced to migrate directionally through magnetic field in one part of the droplet to make polarized matrix of porous Janus micromotor (Figure 46)<sup>75</sup> This example demonstrated how step by step controlled localisation of particles can be used to form complex Janus particles.

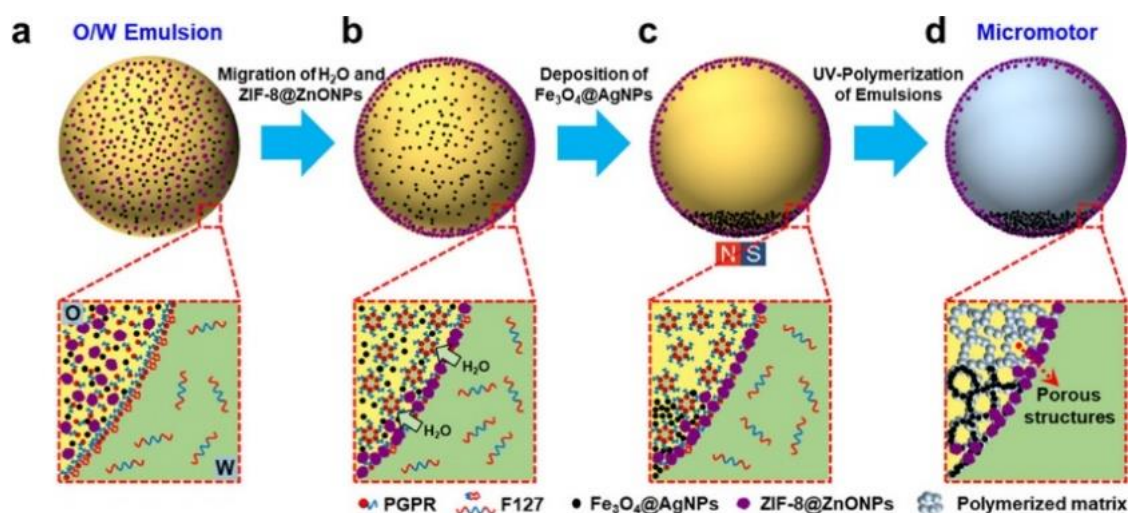


Figure 46: Schematic illustration of the fabrication process of MOF-integrated photocatalytic micromotors. (a–d) Fabrication of the micromotors from O/W emulsion droplets (a) via migration of ZIF-8@ZnONPs and  $\text{H}_2\text{O}$  (b), magnetic-deposition of  $\text{Fe}_3\text{O}_4$ @AgNPs (c), and UV polymerization (d). Image extracted from Chen et al., 2020.<sup>75</sup>

To conclude, Table 2 briefs the composition, morphologies and the size-scale of Janus particles obtainable from various fabrication-methods (briefed in Table 1), based on the different methods described in the paragraphs “1.5.1.1 “ to “1.5.1.3 “.

Table 1: The advantage/disadvantages of various methods for the production of Janus Particles, along with the range of particle size obtainable, and application.

Method	Technique	Advantages	Disadvantages	Applications	Particle Size Range
<b>1 Masking and Selective Etching</b> <sup>106,127–129,135,150,161,162,169</sup>	Template-assisted <sup>106,107,138–140,170</sup>	High control over size and shape, high reproducibility	Complex template removal, template limited material compatibility	Drug delivery, catalysis, sensors, biomedical	100 nm to several $\mu\text{m}$
	Phase interface based <sup>137</sup>	Simple set-up	Limited control over particle uniformity	Catalysis, drug delivery	100 nm to several $\mu\text{m}$
	Evaporation based <sup>106,127,128,136,144,145</sup>	Control over layer thickness, uniform coating, high purity, wide range of materials	Complex setup, limited quantity end-product	Surface coating, electronics, catalysis	50 nm to several $\mu\text{m}$
<b>2 Phase separation</b> <sup>106,127–129,135,150,161,162,169</sup>	Directional flux <sup>82,106,127,142,143</sup>	High precision, control over particle orientation and deposition direction	Complex setup, may be costly	Magnetic separation, targeted drug delivery	50 nm to several $\mu\text{m}$
	Solvent and Emulsion based <sup>152–155,151,156</sup>	Simple setup, scalable, cost-effective	Limited control over particle orientation, polydispersity	Emulsification, catalysis, targeted drug delivery	100 nm to few $\mu\text{m}$
<b>3 Self-assembly</b> <sup>127,128,161–166</sup>	Langmuir-Blodgett technique <sup>165,171</sup>	Control over particle packing, Scalable	Specialized equipment, sensitivity to environmental conditions	Thin films, sensors	100 nm to several $\mu\text{m}$
	Spinning disk <sup>106,125,166–168</sup>	Scalable, control on particle size	Specialized equipment, limited material, limited control over particle-shape	Gyricon, sensors, microarrays	few $\mu\text{m}$ to several 100 $\mu\text{m}$
	Microfluidics <sup>75,126,164</sup>	High precision and control over particle formation, scalable	Specialized equipment, complex setup	Drug delivery, biosensors, diagnostics,	100 nm to several $\mu\text{m}$

## Introduction

Considering the application of Janus particles (and advantage/disadvantages of different synthesis techniques) summarized in the Table 1, different examples of Janus particles with the shapes, size, nature of materials, movement mechanism (and the available diffusion coefficient) along with their respective synthesis techniques are summarized in Table 2.

*Table 2: Enlists various types of Janus Particles, synthesis techniques, morphologies, particle size-scale, movement mechanism and rate of diffusion.*

Janus Particle Composition	Shape	Size ( $\mu\text{m}$ )	Nature	-Phoresis	Diffusion Coefficient ( $\mu\text{m}^2/\text{s}$ )	Synthesis Techniques
<b>Au, SiO<sub>2</sub>, PS, Pt Katuri<sup>172</sup></b>	Tube, rod, sphere	0.2, 3	Magnetic, Non-magnetic	Chemo, Self-diffusio Self-electro	3 - 9	Pickering Emulsion, GLAD, Microfluidics, Template assisted Enzyme linking, self-assembly
<b>SiO<sub>2</sub>, Pt, Mn, Fe<sub>3</sub>O<sub>4</sub>, Fluorescein Schattling<sup>173</sup></b>	Sphere	0.8, 2.7	Magnetic	Chemo, Magneto	0.05 – 0.4	Sol-gel, Seeded Growth
<b>Hollow Mesoporous SiO<sub>2</sub>, Pt Ma<sup>61</sup></b>	Sphere	0.4	Non-magnetic	Catalysis	0.7 – 1.3	Wet Chemistry Grafting, Seeded Growth
<b>SiO<sub>2</sub>, TiO<sub>2</sub>, Co, Ni Šířpová-Jungová<sup>174</sup></b>	Sphere, Helix	1, 2, 40	Non-magnetic	Diffusio	0.01 - 0.1	Microcontact Printing, Layer-by-Layer Deposition, GLAD
<b>Pt, SiO<sub>2</sub> Jalilvand<sup>175</sup></b>	Sphere	5, 8	Non-magnetic	Chemo	0.02 – 0.5	Microcontact Printing, PVD
<b>Au, SiO<sub>2</sub> Simoncelli<sup>87</sup></b>	Sphere	1.3	Non-magnetic	Optical Trapping	-	PVD
<b>Fe<sub>2</sub>O<sub>3</sub>, Au Baraban<sup>176</sup></b>	Sphere	3	Magnetic	Thermo	0.15	PVD, Co-precipitation
<b>ZnO/Pt Pourrahimi<sup>177</sup></b>	sphere	1.5, 5	Non Magnetic	Diffusio	1.25 – 2.5	PVD
<b>Au, Ni, SiO<sub>2</sub> Si<sup>178</sup></b>	Sphere, disk, rod	5	Magnetic	Magneto	~ 1.75	Electrodeposition, Colloidal Assembly

### 1.5.1.4 Choice of particle and method of synthesis

#### 1.5.1.4.1 Particle to pursue

Considering various key points (Figure 47) like stability, ease in functionalization, optical transparency, and unique properties of Silica (discussed further) can set it as the base of our Janus particle. In the reviewed papers (section “1.5”), combination of hydrophilic silica and conductive metal components in janus metal/silica particles demonstrate significant potential in applications such as sensing and catalysis (summarized in Table 4).

The hydrophilic nature of silica provides excellent colloidal stability in aqueous environments. In addition to non-toxic biocompatibility, well-established synthesis methods (to obtain silica particles) and easy functionalization capabilities makes silica a versatile particle for further modifications with various functional chemical-species. In addition, silica offers thermal stability at high temperatures, which is beneficial in catalytic processes. Innate property of silica particles (SP) like good stability in presence of  $H_2O_2$  is a key advantage for  $H_2O_2$  surrounding (product of radiolysis).<sup>179,180</sup> Interactions between SNP and  $H_2O_2$  causes silanol<sup>181</sup> groups (on the silica surface) act as sites for Lewis acid.<sup>182</sup> This facilitates the activation of  $H_2O_2$ , followed by the generation of reactive oxygen species.<sup>180,183–187</sup> Therefore, an easy and cost effective production of SNP<sup>188</sup> in addition to favourable surface chemistry makes silica a suitable base material for the desired Janus Particle.

Other important aspects for optimizing particle performance are the janus component (polymer, metal, etc.), fabrication method, size, and shape, which are usually based on the requirements of application-specificities, balancing between sensitivity, stability, and functionality. As the isotropic surface would simplify theoretical modelling, calculations, and analysis (unlike anisotropic shapes like rod, disk, star, etc.), we focused on working with spherical particles in this thesis study. Also, in addition to minimal hydrodynamic resistance (allowing for easier experimentation in fluid environment), spherical particles would provide most efficient packing in the process of Janus particle synthesis (for example, mono-layering on solid substrate or mono-layering on phase-interface), which can be beneficial for producing higher number of Janus particles per batch of synthesis.

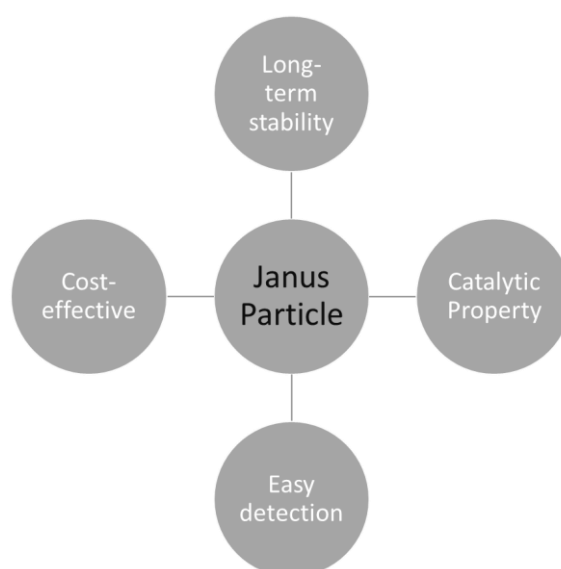


Figure 47: Summary of key factors for deciding the materials for making Janus Particle in this thesis.

While the particle size typically ranges from nanometers to several micrometers, smaller particles generally offer better surface-area-to-volume ratios, enhancing catalytic efficiency and sensitivity in sensing applications. Although larger particles can be beneficial for structural stability, providing more surface area and easier functionalization, they would also experience sedimentation issues (quicker sedimentation in larger and bulkier particles). This would ultimately cause difficulties in 'motion study of particles' and 'understanding their interaction in hydrogen peroxide surroundings'. Additionally, as discussed in "1.3.2.1" smaller particles (micron scale and below) would exhibit significant Brownian motion, which aligns with our interest. Therefore, we narrowed down to the size of 500 nm for silica particles, as 500 nm size falls within the observational range from optical microscopy; allowing for particle-tracking and analysis of particle behaviour in different environment.

Amongst various available options (like polymers, metal) for making Janus from silica particle, we found metallic composition most suitable for developing Radiotactic Colloids (for the decontamination nanorobots) in this thesis work. Even though polymers can offer biocompatibility and flexibility, they often lack thermal stability and surface plasmonic resonance (SPR) (collective oscillation by free electrons on interaction with light, creating strong absorption band in the visible spectrum)<sup>189</sup> like that in metallic nanoparticles. Additionally, polymer surfaces may not provide the same level of catalytic activity as metal surfaces. Therefore, factors like stability, catalytic properties, etc. highlighted in Figure 47 are crucial to consider before choosing the metal (for example copper (Cu), platinum (Pt), titanium (Ti), gold (Au)) for Janus particle synthesis.

The choice of metal significantly influences the properties of the Janus particle and the careful selection of metal components is often decided by their SPR properties. In addition to providing catalytic activity, metal nanoparticles enable SPR that is helpful in designing and optimizing plasmonic nanoparticles. This enhances the optical properties of these particle and improves the sensitivity for real-time detection of metallic nanoparticles (unlike the polymers). Multiple metals possess SPR, for instance, gold (Au) is often used for its biocompatibility, excellent conductivity, and plasmonic properties. Silver (Ag) is another popular choice in biomedical field because of its antimicrobial properties.

Amongst several metallic Janus particles, Cu/Silica Janus particle can be well interactive in H<sub>2</sub>O<sub>2</sub> surroundings, but it is prone to oxidation and corrosion, which limits its applications requiring long-term stability.<sup>190,191</sup> Pt offering better stability and catalytic properties (often superior to gold, which would also cause more bubble than gold), is not a cost-effective option. Whereas gold offers good stability and stronger SPR, making it easy for detection and is more economical choice (than Platinum).<sup>80,192-194</sup> Similarly, Ti lacks the plasmonic properties with lesser versatile catalytic activity than that of Au or Pt.<sup>195,196</sup>

Research studies confirm good stability of gold nanoparticles (AuNP),<sup>197-199</sup> easy detection and production. Despite the inert nature in bulk form, AuNP exhibits catalytic properties at the nanoscale,<sup>15,79,80</sup> attributing to high surface area-to-volume ratio and providing active catalytic sites, especially towards the decomposition of hydrogen peroxide (H<sub>2</sub>O<sub>2</sub>), thus making it active/sensitive for radioactive hotspots.<sup>193</sup> AuNP exhibiting easy functionalization with thiols, strong plasmonic properties, unique catalytic properties, along with good chemical stability and resistance to oxidation ensures long-term functionality, makes it (gold/silica janus particle) good candidate for this study.<sup>193</sup> Additionally, ability to degrade environmental pollutants like organic dyes through H<sub>2</sub>O<sub>2</sub>-mediated oxidation processes is an add-on benefit for choosing AuNP for our Janus Particle.<sup>200-204</sup>

Table 3 represents different advantages of adopting Janus Particle for Radiotactic colloids and decontamination properties, i.e. to be applied for decontamination nanorobots. While the type of Janus particles is chosen (Gold/Silica Janus particle), there is still a need for further research into the synthesis methods and selection of the method/technique to be followed in our work to establish a robust and dependable strategies that can be scaled up for mass production; proving more cost-effective yield.

Table 3: Enlisted are the features of Janus Particles summarised in the table

✓ <b>Multiple synergetic functionality</b>
✓ <b>High agility due to small size (~500 nm) (than conventional robots)</b>
✓ <b>Tolerance to high level of ionization radiation exposure</b>
✓ <b>Reusability and low cost of production</b>
✓ <b>Easier customization due to easy surface modification/functionalization (Compared to other approaches).</b>

Parameters like size-range (compatibility for nano to micro scale range) and advantages like simple set-up, high-yielding, scale-up), summarized in Table 1 and Table 4 helped in choosing Pickering emulsion method for the synthesis of Gold/Silica Janus particle in this thesis work.

Table 4: Comparison of Gold/Silica Janus particles shared by various researchers, with respect to the producible size range of particle, yield, advantages and disadvantages of the respective methods.<sup>106,127,156,158</sup>

Reference	Method	Shape	Size range	Yield	Advantages	Disadvantage
<b>Bao (2002)<sup>142</sup></b>	Self-assembly	Patterned spheres	Micro	Moderate	Controllable patterns	Requires specific substrates
<b>Love (2002)<sup>144</sup></b>	Masking	Hemispherical	Submicron	Moderate	Precise control over shape	Complex fabrication, limited material options
<b>Perro (2009)<sup>156</sup></b>	Emulsion-based	Spherical	Micro/nano	High	Simple, versatile, Bulk yield	Potential for polydispersity
<b>Lin (2010)<sup>205</sup></b>	Phase separation, template-based	Asymmetric	Micro	Moderate	Control over shape, potential for complex structures	Requires specialized equipment

## Introduction

<b>Fujii (2013)<sup>206</sup></b>	Emulsion-based Evaporation-based	Spherical	Micro	Moderate	Simple, Versatile	Potential for emulsion instability
<b>Yang (2017)<sup>130</sup></b>	Phase separation	Spherical	Nano/micro	Moderate	Control over composition,	Requires specific polymers
<b>Le (2019)<sup>207</sup></b>	Bioconjugation, self-assembly	Diverse	Nano	Varies	Biocompatibility	Complexity, yield variations
<b>Vega (2019)<sup>169</sup></b>	Seed-mediated growth	Spherical	Nano	Moderate	Control over porosity	Multiple steps involved
<b>Ye (2019)<sup>196</sup></b>	Self-assembly	Diverse	Micro/nano	Varies	Complex structures, biocompatibility	Low control over particle size
<b>Karadkar (2023)<sup>133</sup></b>	Bioconjugation	Spherical	Nano	Moderate	Biocompatibility	Requires biological components, limited applications
<b>Tan (2023)<sup>129</sup></b>	Bioconjugation, self-assembly	Spherical	Nano	Moderate	Biomedical applications, drug delivery	Requires biological components, complex synthesis

### 1.5.1.4.2 Particle-synthesis strategy to pursue

As shared in “1.5.1.2.2”, for the purpose of bulk quantity production of Janus particles Pickering emulsion strategy has been developed that follows quenching of particles during the functionalization process and solidify the Pickering emulsion to produce colloidosome.<sup>158</sup> Colloidosome is a term referred to when the Pickering emulsion droplets are solidified and emulsion stabilizing-particles are partially embedded onto the solid droplets.<sup>156,157</sup> Paraffin wax is a good candidate and has been used by several authors<sup>156–158,208</sup> as described in the next paragraphs.

Perro et al.,<sup>106</sup> shared about the use of solidified paraffin droplets, for production of Janus Particle. A primary emulsion using paraffin, water and aminated silica particles (2  $\mu\text{m}$ ) was formed with an average droplet size of 100  $\mu\text{m}$  (see Figure 48. (a)). Further, surface modification of aminated silica particles embedded at the solid wax/water interface was achieved by using FITC (isothiocyanate derivative of fluorescein).<sup>106,127</sup>

Gu and team<sup>209</sup> showed that the ultrasonic emulsification with precursor nanoparticles and suitable organic solvents gave more controllable reaction kinetics (rate at which the nanoparticles assemble at the oil-water interface forming Colloidosomes), and therefore gave control over the sizes of colloidosome from the oil-in-water emulsion.<sup>209</sup>

Although there are multiple work for Janus Particle production via chemical synthesis protocols (summarized in Table 4), researchers have followed simple, robust and cost effective method of Pickering. For example, Perro<sup>156</sup> followed emulsion method to produce large quantity of Janus particles (as small as 100 nm dia.).<sup>156,158</sup> Their work was a simple method elaborating Pickering emulsions method of wax-in-water. By controlling the stabilization of wax droplet, they succeeded in high yield (gram-sized quantities) of Gold/Silica Janus Particles.

The major factor behind the gram-size quantity yield of particles by Perro<sup>156</sup> in their followed protocol was based on limited coalescence process allowing the prediction of high interface-quantity (with their known mass of wax). This ensured absorption of all the silica particles on the wax surface (Figure 49) and giving high yield of colloidosomes.

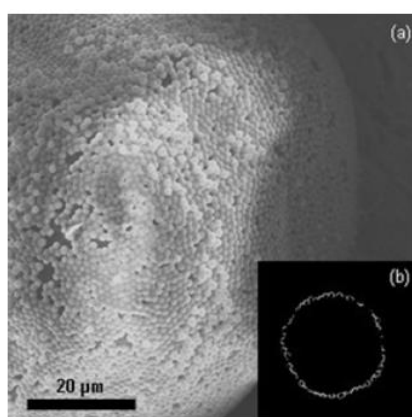


Figure 48: (a) SEM image of a Colloidosome; solidified paraffin droplet stabilized by 2  $\mu\text{m}$  aminated silica particles. (b) Confocal fluorescence microscopy image of solidified paraffin droplet stabilized by 2  $\mu\text{m}$  aminated silica particles post FITC labelling. Image extracted from Perro et al., 2005.<sup>106</sup>

In his protocol, Perro<sup>156</sup> partially hydrophobized the hydrophilic surface of Silica Nanoparticles by introducing a well quantified amount of cetyltrimethylammonium bromide (CTAB) prior to the emulsion formation. Further partial surface modification was made by amino-functionalization and lastly the introduction of gold nanoparticles to obtain gold/silica Janus particles in bulk quantity (gram-size).<sup>156</sup>

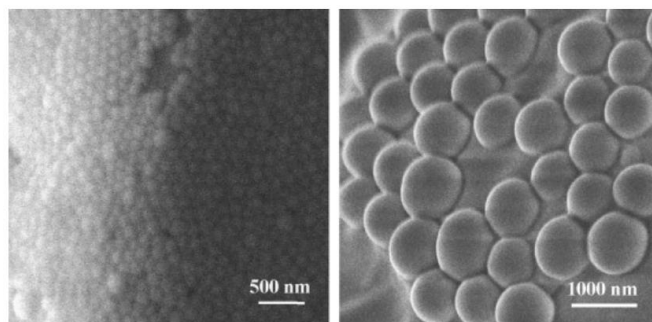


Figure 49: SEM pictures showing surface of Colloidosome; monolayer of silica particles at the surface of solid wax droplet. Source: Perro et al., 2009.<sup>156</sup>



It is affirmative to conclude that Pickering emulsion method for the production of Janus particles (gold/silica in our case) allowed simpler, one-step amphiphilic-modification of nanoparticles with versatile and facile surface functionalization. It is a powerful method to enhance the control over Janus Particle Morphology with bulk quantity product yield, while facilitating the formation of highly surface-functionalized Janus nanoparticles. Additionally, this method can be adapted to a greener and more sustainable synthesis approach. Unlike traditional emulsions that often rely on large quantities of organic solvents, the Pickering emulsion method can employ water as the continuous phase and solid, biocompatible particles such as silica as stabilizers in comparison to liquid emulsion formed by volatile organic solvent. .

Thus, for the project we will focus primarily upon Pickering emulsion method to produce bulk quantity of the chosen Gold/Silica Janus particle. The chosen methodology was inspired and adapted from the work shared by Perro et al.<sup>156</sup>, with a protocol for the synthesis of silica nanoparticles of desired size (500 nm) from the thesis work of Ibisate Muñoz<sup>188</sup> (2003). However, it clearly appeared that the concentration of all the chemicals (ethanol, water, ammonia and TEOS) have to be adjusted as per the targeted size of silica particles (500 nm) and the chosen wax to optimize the reproducibility in term of coverage rate of gold nanoparticles and yields.

### 1.6 Points for exploration

#### 1.6.1 Comparison of Gold/Silica Janus particles made from different methods

The comparison of the different methods permit to identify two different class of Gold/Silica Janus nanoparticles. The first one consists of SiO<sub>2</sub> bearing gold nanoparticles while the other one consists of SiO<sub>2</sub> half-covered by a thin layer of gold. Regarding literature, studies have highlighted distinctions between chemically synthesized and PVD-derived Janus Particles by showing that Janus particles with nanoparticles on its surface often experience enhanced reactivity with its surrounding. While PVD-derived Janus particles (having partially coated surface with a layer of metal) exhibit lower reactivity but are capable of more controlled and tailored reactivity (dependent upon the deposition materials and conditions).<sup>133,134,210</sup>

Contrary to this, a study by Lyu<sup>211</sup> show that the higher reactivity of Janus particles in the presence of hydrogen peroxide was found in their Janus particle having metal layer (copper layer onto the surface of silica micro-particles), rather than the Janus particles having metal nanoparticles.<sup>211</sup> Therefore, to understand the influence of synthesis mechanism better, it can be interesting to compare the reactivity and motion of both types of Janus particles (one with metallic nanoparticles and other with metal layer) in the presence of hydrogen peroxide. Therefore, we choose to explore this as one of the part of this Ph.D. project.

Furthermore, the final application may require very significant amount of particles. Amongst the presented methods, only a few of them allows to prepare such amounts, while their reproducibility is yet to be tested. This being another objective of the thesis; optimization of the conditions for formulation of Colloidosomes for Au/SiO<sub>2</sub> Janus particles.

### 1.6.2 Need for particle-asymmetry for motion/propulsion?

We must notice that all these efforts to develop motile nanoparticles assume that the asymmetry is mandatory to obtain a motion. However some studies have demonstrated directed movement (taxi) even in symmetrical particles, directed movement due to kinetic asymmetry and diffusive asymmetry.<sup>212</sup> For example Chao Gao et al.<sup>212</sup> discussed the use of micro-nano motors (MNMs) in biomedical applications, where the structure of these MNMs with a helical side helped in enabling spinning and self-propulsion; providing autonomous navigation in various environmental stimuli (like chemical reactions, light, magnetic fields, and acoustic waves) and allowing versatile application.<sup>212</sup> Whereas a work by Mandal et al<sup>52</sup> studied the fundamental symmetries in non-equilibrium chemical systems for enzyme-based chemotactic systems by exploring interaction of particles with the environment. The key highlight of this study was that kinetic asymmetry (differences in off rates for substrate and product) and diffusion asymmetry (differences in diffusivities between bound and free enzyme forms) primarily determined the direction of chemotaxis.<sup>52</sup>

This presents an intriguing possibility, and since synthesizing symmetrical particles is generally tremendously simpler, we decided to investigate the potential for motion in both Janus (asymmetric) and non-Janus (symmetric) particles in this thesis. This comparative approach would expand our understanding on the following aspects: 1) Necessity of asymmetry: By comparing the behaviour of both types of particles (asymmetric and symmetric), we can gain valuable insights into whether asymmetry is truly essential for achieving directed motion in our system. 2) Simplified fabrication: If symmetrical particles demonstrate sufficient motion, we can potentially benefit from a significantly easier and more cost-effective fabrication process compared to creating complex Janus structures. 3) Underlying mechanisms: Studying both types of particles can help us understand the underlying mechanisms driving motion in our system. Perhaps factors beyond asymmetry, such as surface properties or interactions with the surrounding environment playing a role.

## 1.7 Thesis Objective

The initial objective of this Ph.D. research (Radiotactic Colloids: towards decontamination nanorobots) was to produce colloidal solution of Gold/Silica Janus particles and quantify its motion in the presence of hydrogen peroxide gradient. But, from the literature described above, we have identified the following additional objectives:-

1. Development of a protocol that allows reproducible production of large amounts of Janus particles.
2. Comparison of the mobility of these Janus particles, with the more resembling Non-Janus particles
3. Comparison of the activity of gold particle vs gold layers, and symmetric vs asymmetric. We will rely on four family of particles, derived from the same silica platform while the chosen size of ~500 nm, is chosen to ensure reduced impact of sedimentation on particle movement, but still possible to follow optically.
4. Try to identify eventual collective effects, by going from bulk solutions to micro-channels
5. Comparison of the effect of homogeneous and heterogeneous H<sub>2</sub>O<sub>2</sub> concentration on the mobility.

To achieve this, it is important to choose the best method for producing the particles of interest: Gold/Silica Janus particle. The literature study gives us the insight that Pickering emulsion method (a chemical-synthesis protocol) is the best strategy to follow for bulk quantity production of Gold/Silica Janus Particle. While to understand the effect of hydrogen peroxide on produced Janus particles all the aspects in regards to motion, have to be considered, which brings the need of elimination of collective motion in particles. Therefore, to address the motion study in 3D, a simple, non-destructive technique of Dynamic Light Scattering (DLS) will be utilized observing particles suspended in different concentration of  $H_2O_2$ , and microfluidics platform would be utilized for controlled flow and observation parameters along with suppressed collective motion of particles (at different concentrations of  $H_2O_2$ ) in 2D. For the purpose of particle tracking aspect of the work, a simple methodology of microscopy-camera-aided particle tracking would be followed in addition to open source platforms like ImageJ software. As particle motion due to catalytic decomposition of  $H_2O_2$  can be more complex in Janus system, with our experiment set-up we may find limited, but interesting insights towards the possible alternative of decontamination nanorobots; active Janus Particles.

This Ph.D. is the first step in the project of search for nuclear decontamination nanorobots, with an emphasis towards decontamination of complex geometries. The idea is to have nano/sub-micron-sized (aiding in high agility) materials with autonomous sensitivity and motion towards radioactive contamination sources. Autonomous sensitivity of radiation hotspot and mobility towards it, would require a material with self-propulsion capabilities. For this, we conceptualize to benefit from the gradient of hydrogen peroxide; inevitably present at the site of contamination, and thus, act as a fuel for nanorobots with catalytic properties. While the nanorobots-motion will be due to gradient<sup>85</sup> (of radiolysis product), decontamination task would be accomplished by chelatants (specific for radioactive materials) grafted on the surface of these robust nanorobots; thus aiding nuclear decontamination of complex geometries at supramolecular scale.

In this Ph.D., we focus on the first part on the development of nano/sub micron sized nanorobot.

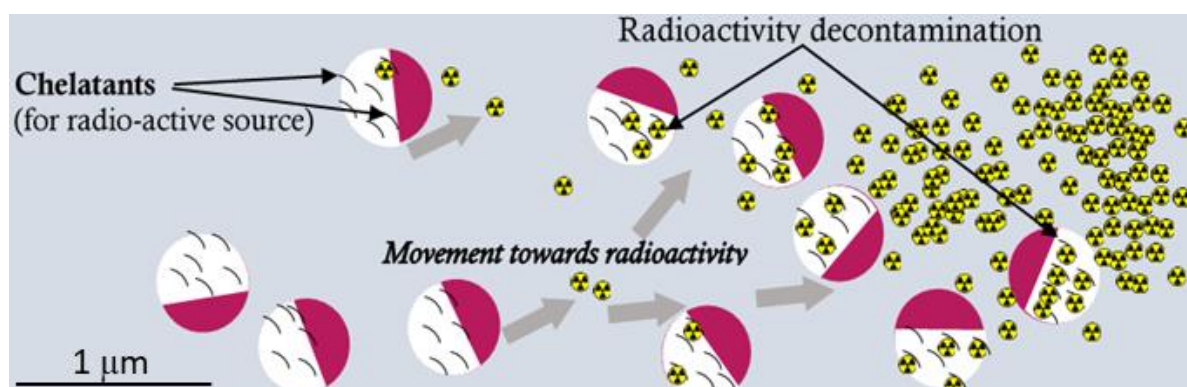


Figure 50: Diagram representing Radiotactic Nanorobots (White/Magenta circles) moving towards the source of radioactivity for decontamination (with prospective functionalization with Chelatants for grabbing the radioactive contaminants).

## 1.8 Reference

- (1) PRIS - Trend reports - Nuclear Power Capacity. <https://pris.iaea.org/PRIS/WorldStatistics/WorldTrendNuclearPowerCapacity.aspx>.
- (2) Decontamination Techniques Used in Decommissioning Activities. Nuclear Energy Agency (NEA). [https://www.oecd-nea.org/jcms/pl\\_13258/decontamination-techniques-used-in-decommissioning-activities?details=true](https://www.oecd-nea.org/jcms/pl_13258/decontamination-techniques-used-in-decommissioning-activities?details=true).
- (3) Kumar, V.; Goel, R.; Chawla, R.; Silambarasan, M.; Sharma, R. K. Chemical, Biological, Radiological, and Nuclear Decontamination: Recent Trends and Future Perspective. *J Pharm Bioallied Sci* **2010**, 2 (3), 220–238. <https://doi.org/10.4103/0975-7406.68505>.
- (4) Sawano, T.; Ozaki, A.; Tsubokura, M. Review of Health Risks among Decontamination Workers after the Fukushima Daiichi Nuclear Power Plant Accident. *Radioprotection* **2020**, 55 (4), 277–282. <https://doi.org/10.1051/radiopro/2020080>.
- (5) Cibulsky, S. M.; Sokolowski, D.; Lafontaine, M.; Gagnon, C.; Blain, P. G.; Russell, D.; Kreppel, H.; Biederbick, W.; Shimazu, T.; Kondo, H.; Saito, T.; Jourdain, J.-R.; Paquet, F.; Li, C.; Akashi, M.; Tatsuzaki, H.; Prosser, L. Mass Casualty Decontamination in a Chemical or Radiological/Nuclear Incident with External Contamination: Guiding Principles and Research Needs. *PLoS Curr* **2015**. <https://doi.org/10.1371/currents.dis.9489f4c319d9105dd0f1435ca182ea9>.
- (6) Bird, B.; Nancekievill, M.; West, A.; Hayman, J.; Ballard, C.; Jones, W.; Ross, S.; Wild, T.; Scott, T.; Lennox, B. Vega—A Small, Low Cost, Ground Robot for Nuclear Decommissioning. *Journal of Field Robotics* **2022**, 39 (3), 232–245. <https://doi.org/10.1002/rob.22048>.
- (7) Hussein, T. From Chernobots to Iron Man suits: the development of nuclear waste robotics. *Power Technology*. <https://www.power-technology.com/features/cleaning-up-nuclear-waste-robotics/>.
- (8) Huang, C.; Huang, C.; Hung, Y.; Chang, C. Sensing Pipes of a Nuclear Power Mechanism Using Low-Cost Snake Robot. *ADVANCES IN MECHANICAL ENGINEERING* **2018**, 10 (6). <https://doi.org/10.1177/1687814018781286>.
- (9) Remote and digital technologies for decommissioning - Nuclear Engineering International. <https://www.neimagazine.com/features/featureremote-and-digital-technologies-for-decommissioning-10005991/>.
- (10) Pohl, O. Chemotaxis of Self-Phoretic Active Particles and Bacteria. 2016. <https://doi.org/10.14279/depositonce-5409>.
- (11) Huang, Z.; Chen, P.; Zhu, G.; Yang, Y.; Xu, Z.; Yan, L.-T. Bacteria-Activated Janus Particles Driven by Chemotaxis. *ACS Nano* **2018**, 12 (7), 6725–6733. <https://doi.org/10.1021/acsnano.8b01842>.
- (12) Gómez Nava, L.; Großmann, R.; Hintsche, M.; Beta, C.; Peruani, F. A Novel Approach to Chemotaxis: Active Particles Guided by Internal Clocks. *EPL* **2020**, 130 (6), 68002. <https://doi.org/10.1209/0295-5075/130/68002>.
- (13) Leotlela, M. J. Radiolysis of Water by  $\alpha$ - and  $\beta$ -Particles from Spent Nuclear Fuel. *Radiation Physics and Chemistry* **2024**, 216, 111361. <https://doi.org/10.1016/j.radphyschem.2023.111361>.
- (14) Lousada, C. M.; Soroka, I. L.; Yagodzinskyy, Y.; Tarakina, N. V.; Todoshchenko, O.; Hänninen, H.; Korzhavyi, P. A.; Jonsson, M. Gamma Radiation Induces Hydrogen Absorption by Copper in Water. *Sci Rep* **2016**, 6 (1), 24234. <https://doi.org/10.1038/srep24234>.
- (15) Arcadi, A. Alternative Synthetic Methods through New Developments in Catalysis by Gold. *Chem. Rev.* **2008**, 108 (8), 3266–3325. <https://doi.org/10.1021/cr068435d>.
- (16) Morgan, A. R.; Dawson, A. B.; McKenzie, H. S.; Skelton, T. S.; Beanland, R.; Franks, H. P. W.; Bon, S. A. F. Chemotaxis of Catalytic Silica–Manganese Oxide “Matchstick” Particles. *Mater. Horiz.* **2014**, 1 (1), 65–68. <https://doi.org/10.1039/C3MH00003F>.
- (17) Kocher, C.; Agozzino, L.; Dill, K. Nanoscale Catalyst Chemotaxis Can Drive the Assembly of Functional Pathways. *J. Phys. Chem. B* **2021**, 125 (31), 8781–8786. <https://doi.org/10.1021/acs.jpcc.1c04498>.
- (18) Krist, K. T.; Noid, W. G. Relating the Artificial Chemotaxis of Catalysts to a Gradient Descent of the Free Energy. *The Journal of Chemical Physics* **2023**, 158 (21), 214113. <https://doi.org/10.1063/5.0131550>.
- (19) Cfarqu, F.; Shyti, M.; Berdufi, I.; Dhoqina, P.; Bylyku, E. Determination of Gross Alpha Beta Surface Contamination by Handheld Equipment. *AIP Conference Proceedings* **2019**, 2075 (1), 130029. <https://doi.org/10.1063/1.5091314>.
- (20) The Analysis of Regulated Contaminant Occurrence Data from Public Water Systems in Support of the Second Six-Year Review of National Primary Drinking Water Regulations. **2010**. <https://www.epa.gov/sites/default/files/2014-12/documents/815b09006.pdf>
- (21) Behr, T. M.; Béhé, M.; Stabin, M. G.; Wehrmann, E.; Apostolidis, C.; Molinet, R.; Strutz, F.; Fayyazi, A.; Wieland, E.; Gratz, S.; Koch, L.; Goldenberg, D. M.; Becker, W. High-Linear Energy Transfer (LET) Alpha versus Low-LET Beta Emitters in Radioimmunotherapy of Solid Tumors: Therapeutic Efficacy and Dose-Limiting Toxicity of  $^{213}\text{Bi}$ - versus  $^{90\text{Y}}$ -Labeled CO17-1A Fab’ Fragments in a Human Colonic Cancer Model. *Cancer Res* **1999**, 59 (11), 2635–2643.
- (22) Nawawi, N. A. A.; Tajudin, S. M.; Nasir, F. M.; Mohamed, N. S.; Abdullah, N.; Zainudin, N. H. M.; Radzi, J. M. Attenuation Range of Particle Radiations (Alpha and Beta) in Human Skin by Monte Carlo Simulation. *IOP Conf. Ser.: Mater. Sci. Eng.* **2023**, 1285 (1), 012012. <https://doi.org/10.1088/1757-899X/1285/1/012012>.
- (23) Abdollahi, H.; Uribe, C.; Rahmim, A.; Saboury, B. Radiobiology of Alpha and Beta Particles in Radiopharmaceutical Therapy: What to Unlearn from External Beam Radiotherapy. *Journal of Nuclear Medicine* **2023**, 64 (supplement 1), P1468–P1468. [https://jnm.snmjournals.org/content/64/supplement\\_1/P1468](https://jnm.snmjournals.org/content/64/supplement_1/P1468).
- (24) Contaminant of the Month: Alpha Particles. *Water Technology*. <https://www.watertechnology.com/wastewater/article/15543137/contaminant-of-the-month-alpha-particles>.
- (25) Ogunbare, F. O.; Adekoya, O. I. Gross Alpha and Beta Radioactivity in Surface Soil and Drinkable Water around a Steel Processing Facility. *Journal of Radiation Research and Applied Sciences* **2015**, 8 (3), 411–417. <https://doi.org/10.1016/j.jrras.2015.02.009>.

- (26) Sáez-Muñoz, M.; Ortiz, J.; Martorell, S. Rapid Evaluation of Gross Alpha and Gross Beta in Water Samples for Emergency Response. *Radiation Physics and Chemistry* **2020**, *171*, 108717. <https://doi.org/10.1016/j.radphyschem.2020.108717>.
- (27) Pérot, B.; Jallu, F.; Passard, C.; Gueton, O.; Allinei, P.-G.; Loubet, L.; Estre, N.; Simon, E.; Carasco, C.; Roure, C.; Boucher, L.; Lamotte, H.; Comte, J.; Bertaux, M.; Lyoussi, A.; Fichet, P.; Carrel, F. The Characterization of Radioactive Waste: A Critical Review of Techniques Implemented or under Development at CEA, France. *EPJ Nuclear Sci. Technol.* **2018**, *4*, 3. <https://doi.org/10.1051/epjn/2017033>.
- (28) Radioactive Waste & Myths and Realities - World Nuclear Association. <https://world-nuclear.org/information-library/nuclear-fuel-cycle/nuclear-waste/radioactive-wastes-myths-and-realities>.
- (29) Nuclear Waste Conditioning; Parisot, J.-F., France, Eds.; DEN monographs; Editions Le Moniteur: Paris, 2009. [https://www.cea.fr/english/Documents/scientific-and-economic-publications/nuclear-energy-monographs/CEA\\_Monograph5\\_Nuclear-waste-conditioning\\_2009\\_GB.pdf](https://www.cea.fr/english/Documents/scientific-and-economic-publications/nuclear-energy-monographs/CEA_Monograph5_Nuclear-waste-conditioning_2009_GB.pdf).
- (30) Maringer, F. J.; Šuráň, J.; Kovář, P.; Chauvenet, B.; Peyres, V.; García-Toraño, E.; Cozzella, M. L.; De Felice, P.; Vodenik, B.; Hult, M.; Rosengård, U.; Merimaa, M.; Szücs, L.; Jeffery, C.; Dean, J. C. J.; Tymiński, Z.; Arnold, D.; Hincă, R.; Mirescu, G. Radioactive Waste Management: Review on Clearance Levels and Acceptance Criteria Legislation, Requirements and Standards. *Applied Radiation and Isotopes* **2013**, *81*, 255–260. <https://doi.org/10.1016/j.apradiso.2013.03.046>.
- (31) Handling and Processing of Radioactive Waste from Nuclear Applications; Internationale Atomenergie-Organisation, Internationale Atomenergie-Organisation, Eds.; Technical reports series / International Atomic Energy Agency; International Atomic Energy Agency: Vienna, 2001. [https://www-pub.iaea.org/MTCD/publications/PDF/TRS402\\_scr.pdf](https://www-pub.iaea.org/MTCD/publications/PDF/TRS402_scr.pdf).
- (32) PNNL-21554.Pdf. [https://www.pnnl.gov/main/publications/external/technical\\_reports/PNNL-21554.pdf](https://www.pnnl.gov/main/publications/external/technical_reports/PNNL-21554.pdf).
- (33) Pikaev, A. K.; Ershov, B. G. PRIMARY PRODUCTS OF THE RADIOLYSIS OF WATER AND THEIR REACTIVITY. *Russ. Chem. Rev.* **1967**, *36* (8), 602. <https://doi.org/10.1070/RC1967v036n08ABEH001675>.
- (34) Backhurst, J. D.; Johnson, G. R. A.; Scholes, G.; Weiss, J. Determination of the Yields of Molecular Hydrogen Peroxide in the Radiolysis of Water Labelled with Oxygen-18. *Nature* **1959**, *183* (4655), 176–177. <https://doi.org/10.1038/183176a0>.
- (35) Dzaugis, M. E.; Spivack, A. J.; D'Hondt, S. A Quantitative Model of Water Radiolysis and Chemical Production Rates near Radionuclide-Containing Solids. *Radiat Phys Chem Oxf Engl* **1993**, *2015*, *115*, 127–134. <https://doi.org/10.1016/j.radphyschem.2015.06.011>.
- (36) Iwamatsu, K.; Sundin, S.; LaVerne, J. A. Hydrogen Peroxide Kinetics in Water Radiolysis. *Radiation Physics and Chemistry* **2018**, *145*, 207–212. <https://doi.org/10.1016/j.radphyschem.2017.11.002>.
- (37) Power, F. Hydrogen Fuel Cell Advantages and Disadvantages in Material Handling. <https://www.fluxpower.com/blog/hydrogen-fuel-cell-advantages-and-disadvantages-in-material-handling>.
- (38) What are the major drawbacks of hydrogen fuel, and how can they be mitigated?. *Hydrogen Newsletter*. <https://www.hydrogennewsletter.com/what-are-the-major-drawbacks-of-hydrogen-fuel-and-how-to-mitigate-those/>.
- (39) Hydrogen Safety: Let's Clear the Air. <https://www.nrdc.org/bio/christian-tae/hydrogen-safety-lets-clear-air>.
- (40) Lv, P.; Le The, H.; Eijkel, J.; Van den Berg, A.; Zhang, X.; Lohse, D. Growth and Detachment of Oxygen Bubbles Induced by Gold-Catalyzed Decomposition of Hydrogen Peroxide. *J. Phys. Chem. C* **2017**, *121* (38), 20769–20776. <https://doi.org/10.1021/acs.jpcc.7b04994>.
- (41) Tavakoli, H.; Baghbanan, A. A. Measuring Hydrogen Peroxide Due to Water Radiolysis Using a Modified Horseradish Peroxidase Based Biosensor as an Alternative Dosimetry Method. *Bioelectrochemistry* **2015**, *104*, 79–84. <https://doi.org/10.1016/j.bioelechem.2015.03.006>.
- (42) Elliot, A. J.; Chenier, M. P.; Ouellette, D. C. G-Values for  $\gamma$ -Irradiated Water as a Function of Temperature. *Can. J. Chem.* **1990**, *68* (5), 712–719. <https://doi.org/10.1139/v90-111>.
- (43) Domnanich, K. A.; Severin, G. W. A Model for Radiolysis in a Flowing-Water Target during High-Intensity Proton Irradiation. *ACS Omega* **2022**, *7* (29), 25860–25873. <https://doi.org/10.1021/acsomega.2c03540>.
- (44) Pastina, B.; LaVerne, J. A. Effect of Molecular Hydrogen on Hydrogen Peroxide in Water Radiolysis. *J. Phys. Chem. A* **2001**, *105* (40), 9316–9322. <https://doi.org/10.1021/jp012245j>.
- (45) Wasselin-Trupin, V.; Baldacchino, G.; Bouffard, S.; Hickel, B. Hydrogen Peroxide Yields in Water Radiolysis by High-Energy Ion Beams at Constant LET. *Radiation Physics and Chemistry* **2002**, *65* (1), 53–61. [https://doi.org/10.1016/S0969-806X\(01\)00682-X](https://doi.org/10.1016/S0969-806X(01)00682-X).
- (46) Nanoparticle Brownian motion and hydrodynamic interactions in the presence of flow fields - PMC. <https://www.ncbi.nlm.nih.gov/pmc/articles/PMC3172128/>.
- (47) Einstein, A. -INVESTIGATIONS ON THE THEORY, THE BROWNIAN MOVEMENT. [https://www.damtp.cam.ac.uk/user/gold/pdfs/teaching/old\\_literature/Einstein1905.pdf](https://www.damtp.cam.ac.uk/user/gold/pdfs/teaching/old_literature/Einstein1905.pdf).
- (48) Hassan, P. A.; Rana, S.; Verma, G. Making Sense of Brownian Motion: Colloid Characterization by Dynamic Light Scattering. *Langmuir* **2015**, *31* (1), 3–12. <https://doi.org/10.1021/la501789z>.
- (49) Campbell, C. E. Diffusivity and Mobility Data. In *Fundamentals of Modeling for Metals Processing*; Furrer, D. U., Semiatin, S. L., Eds.; ASM International, 2009; pp 171–181. <https://doi.org/10.31399/asm.hb.v22a.a0005430>.
- (50) Central Limit theorem: the cornerstone of modern statistics. <https://ekja.org/journal/view.php?doi=10.4097/kjae.2017.70.2.144>.
- (51) Islam, M. A. Einstein–Smoluchowski Diffusion Equation: A Discussion. *Phys. Scr.* **2004**, *70* (2–3), 120–125. <https://doi.org/10.1088/0031-8949/70/2-3/008>.

- (52) Mandal, N. S.; Sen, A.; Astumian, R. D. Kinetic Asymmetry versus Dissipation in the Evolution of Chemical Systems as Exemplified by Single Enzyme Chemotaxis. *J. Am. Chem. Soc.* **2023**, *145* (10), 5730–5738. <https://doi.org/10.1021/jacs.2c11945>.
- (53) Kholodenko, A. L.; Douglas, J. F. Generalized Stokes-Einstein Equation for Spherical Particle Suspensions. *Phys. Rev. E* **1995**, *51* (2), 1081–1090. <https://doi.org/10.1103/PhysRevE.51.1081>.
- (54) Nandi, A.; Heinrich, D.; Lindner, B. Distributions of Diffusion Measures from a Local Mean-Square Displacement Analysis. *Phys. Rev. E* **2012**, *86* (2), 021926. <https://doi.org/10.1103/PhysRevE.86.021926>.
- (55) Oliveira, F. A.; Ferreira, R. M. S.; Lapas, L. C.; Vainstein, M. H. Anomalous Diffusion: A Basic Mechanism for the Evolution of Inhomogeneous Systems. *Front. Phys.* **2019**, *7*. <https://doi.org/10.3389/fphy.2019.00018>.
- (56) Saad, S.; Natale, G. Diffusiophoresis of Active Colloids in Viscoelastic Media. *Soft Matter* **2019**, *15* (48), 9909–9919. <https://doi.org/10.1039/C9SM01801H>.
- (57) Derjaguin, B. V.; Sidorenkov, G.; Zubashchenko, E.; Kiseleva, E. Kinetic Phenomena in the Boundary Layers of Liquids 1. the Capillary Osmosis. *Progress in Surface Science* **1993**, *43* (1–4), 138–152. [https://doi.org/10.1016/0079-6816\(93\)90023-0](https://doi.org/10.1016/0079-6816(93)90023-0).
- (58) Asmolov, E. S.; Nizkaya, T. V.; Vinogradova, O. I. Self-Diffusiophoresis of Janus Particles That Release Ions. *Physics of Fluids* **2022**, *34* (3), 032011. <https://doi.org/10.1063/5.0085746>.
- (59) Huang, M.-J.; Schofield, J.; Gaspard, P.; Kapral, R. From Single Particle Motion to Collective Dynamics in Janus Motor Systems. *The Journal of Chemical Physics* **2019**, *150* (12), 124110. <https://doi.org/10.1063/1.5081820>.
- (60) Velegol, D.; Garg, A.; Guha, R.; Kar, A.; Kumar, M. Origins of Concentration Gradients for Diffusiophoresis. *Soft Matter* **2016**, *12* (21), 4686–4703. <https://doi.org/10.1039/C6SM00052E>.
- (61) Ma, X.; Jannasch, A.; Albrecht, U.-R.; Hahn, K.; Miguel-López, A.; Schäffer, E.; Sánchez, S. Enzyme-Powered Hollow Mesoporous Janus Nanomotors. *Nano Lett.* **2015**, *15* (10), 7043–7050. <https://doi.org/10.1021/acs.nanolett.5b03100>.
- (62) Wang, L.; Hao, X.; Gao, Z.; Yang, Z.; Long, Y.; Luo, M.; Guan, J. Artificial Nanomotors: Fabrication, Locomotion Characterization, Motion Manipulation, and Biomedical Applications. *Interdisciplinary Materials* **2022**, *1* (2), 256–280. <https://doi.org/10.1002/idm2.12021>.
- (63) Huang, M.-J.; Schofield, J.; Kapral, R. Chemotactic and Hydrodynamic Effects on Collective Dynamics of Self-Diffusiophoretic Janus Motors. *New J. Phys.* **2017**, *19* (12), 125003. <https://doi.org/10.1088/1367-2630/aa958c>.
- (64) Collective\_diffusion. [https://www.chemeurope.com/en/encyclopedia/Collective\\_diffusion.html](https://www.chemeurope.com/en/encyclopedia/Collective_diffusion.html).
- (65) Lee, T.-C.; Alarcón-Correa, M.; Miksch, C.; Hahn, K.; Gibbs, J. G.; Fischer, P. Self-Propelling Nanomotors in the Presence of Strong Brownian Forces. *Nano Lett.* **2014**, *14* (5), 2407–2412. <https://doi.org/10.1021/nl500068n>.
- (66) Wang, D.; Zhu, Y.-L.; Zhao, Y.; Li, C. Y.; Mukhopadhyay, A.; Sun, Z.-Y.; Koynov, K.; Butt, H.-J. Brownian Diffusion of Individual Janus Nanoparticles at Water/Oil Interfaces. *ACS Nano* **2020**, *14* (8), 10095–10103. <https://doi.org/10.1021/acsnano.0c03291>.
- (67) Appell, J.; Porte, G.; Buhler, E. Self-Diffusion and Collective Diffusion of Charged Colloids Studied by Dynamic Light Scattering. *J. Phys. Chem. B* **2005**, *109* (27), 13186–13194. <https://doi.org/10.1021/jp051016k>.
- (68) Popescu, M. N.; Uspal, W. E.; Bechinger, C.; Fischer, P. Chemotaxis of Active Janus Nanoparticles. *Nano Lett.* **2018**, *18* (9), 5345–5349. <https://doi.org/10.1021/acs.nanolett.8b02572>.
- (69) Adler, J. Chemotaxis in Bacteria. *Science* **1966**, *153* (3737), 708–716. <https://doi.org/10.1126/science.153.3737.708>.
- (70) Bonner, J. T.; Savage, L. J. Evidence for the Formation of Cell Aggregates by Chemotaxis in the Development of the Slime Mold *Dictyostelium Discoideum*. *Journal of Experimental Zoology* **1947**, *106* (1), 1–26. <https://doi.org/10.1002/jez.1401060102>.
- (71) Friedrich, B. M.; Jülicher, F. Chemotaxis of Sperm Cells. *Proceedings of the National Academy of Sciences* **2007**, *104* (33), 13256–13261. <https://doi.org/10.1073/pnas.0703530104>.
- (72) Deprez, L.; De Buyl, P. Passive and Active Colloidal Chemotaxis in a Microfluidic Channel: Mesoscopic and Stochastic Models. *Soft Matter* **2017**, *13* (19), 3532–3543. <https://doi.org/10.1039/C7SM00123A>.
- (73) Ortiz-Rivera, I.; Mathesh, M.; Wilson, D. A. A Supramolecular Approach to Nanoscale Motion: Polymersome-Based Self-Propelled Nanomotors. *Acc. Chem. Res.* **2018**, *51* (9), 1891–1900. <https://doi.org/10.1021/acs.accounts.8b00199>.
- (74) Patiño, T.; Arqué, X.; Mestre, R.; Palacios, L.; Sánchez, S. Fundamental Aspects of Enzyme-Powered Micro- and Nanoswimmers. *Acc. Chem. Res.* **2018**, *51* (11), 2662–2671. <https://doi.org/10.1021/acs.accounts.8b00288>.
- (75) Chen, L.; Zhang, M.-J.; Zhang, S.-Y.; Shi, L.; Yang, Y.-M.; Liu, Z.; Ju, X.-J.; Xie, R.; Wang, W.; Chu, L.-Y. Simple and Continuous Fabrication of Self-Propelled Micromotors with Photocatalytic Metal–Organic Frameworks for Enhanced Synergistic Environmental Remediation. *ACS Appl. Mater. Interfaces* **2020**, *12* (31), 35120–35131. <https://doi.org/10.1021/acsmi.0c11283>.
- (76) Tao, Y.-G.; Kapral, R. Design of Chemically Propelled Nanodimer Motors. *J Chem Phys* **2008**, *128* (16), 164518. <https://doi.org/10.1063/1.2908078>.
- (77) Paxton, W. F.; Kistler, K. C.; Olmeda, C. C.; Sen, A.; St. Angelo, S. K.; Cao, Y.; Mallouk, T. E.; Lammert, P. E.; Crespi, V. H. Catalytic Nanomotors: Autonomous Movement of Striped Nanorods. *J. Am. Chem. Soc.* **2004**, *126* (41), 13424–13431. <https://doi.org/10.1021/ja047697z>.
- (78) Hong, Y.; Blackman, N. M. K.; Kopp, N. D.; Sen, A.; Velegol, D. Chemotaxis of Nonbiological Colloidal Rods. *Phys. Rev. Lett.* **2007**, *99* (17), 178103. <https://doi.org/10.1103/PhysRevLett.99.178103>.
- (79) Goszner, K. The Decomposition of Hydrogen Peroxide on Silver-Gold Alloys. *Journal of Catalysis* **1974**, *32* (2), 175–182. [https://doi.org/10.1016/0021-9517\(74\)90066-9](https://doi.org/10.1016/0021-9517(74)90066-9).

- (80) Bianchi, G.; Mazza, F.; Mussini, T. Catalytic Decomposition of Acid Hydrogen Peroxide Solutions on Platinum, Iridium, Palladium and Gold Surfaces. *Electrochimica Acta* **1962**, 7 (4), 457–473. [https://doi.org/10.1016/0013-4686\(62\)80034-6](https://doi.org/10.1016/0013-4686(62)80034-6).
- (81) Ma, X.; Hortelão, A. C.; Patiño, T.; Sánchez, S. Enzyme Catalysis To Power Micro/Nanomachines. *ACS Nano* **2016**, 10 (10), 9111–9122. <https://doi.org/10.1021/acsnano.6b04108>.
- (82) Kim, S.-H.; Jeon, S.-J.; Jeong, W. C.; Park, H. S.; Yang, S.-M. Optofluidic Synthesis of Electroresponsive Photonic Janus Balls with Isotropic Structural Colors. *Adv. Mater.* **2008**, NA-NA. <https://doi.org/10.1002/adma.200801167>.
- (83) Brooks, A. M.; Tasinkevych, M.; Sabrina, S.; Velegol, D.; Sen, A.; Bishop, K. J. M. Shape-Directed Rotation of Homogeneous Micromotors via Catalytic Self-Electrophoresis. *Nat Commun* **2019**, 10 (1), 495. <https://doi.org/10.1038/s41467-019-08423-7>.
- (84) Pacheco, M.; López, M. Á.; Jurado-Sánchez, B.; Escarpa, A. Self-Propelled Micromachines for Analytical Sensing: A Critical Review. *Anal Bioanal Chem* **2019**, 411 (25), 6561–6573. <https://doi.org/10.1007/s00216-019-02070-z>.
- (85) Lyu, X.; Liu, X.; Zhou, C.; Duan, S.; Xu, P.; Dai, J.; Chen, X.; Peng, Y.; Cui, D.; Tang, J.; Ma, X.; Wang, W. Active, Yet Little Mobility: Asymmetric Decomposition of H<sub>2</sub>O<sub>2</sub> Is Not Sufficient in Propelling Catalytic Micromotors. *J. Am. Chem. Soc.* **2021**, 143 (31), 12154–12164. <https://doi.org/10.1021/jacs.1c04501>.
- (86) Avital, E. J.; Miloh, T. Self-Thermophoresis of Laser-Heated Spherical Janus Particles. *Eur. Phys. J. E* **2021**, 44 (11), 139. <https://doi.org/10.1140/epje/s10189-021-00128-4>.
- (87) Simoncelli, S.; Johnson, S.; Kriegel, F.; Lipfert, J.; Feldmann, J. Stretching and Heating Single DNA Molecules with Optically Trapped Gold-Silica Janus Particles. *ACS Photonics* **2017**, 4 (11), 2843–2851. <https://doi.org/10.1021/acsp Photonics.7b00839>.
- (88) Dai, J. Macroscopic Anisotropic Brownian Motion Is Related to the Directional Movement of a “Universe Field.” *Natural Science* **2014**, 6 (2), 54–58. <https://doi.org/10.4236/ns.2014.62009>.
- (89) Stetefeld, J.; McKenna, S. A.; Patel, T. R. Dynamic Light Scattering: A Practical Guide and Applications in Biomedical Sciences. *Biophys Rev* **2016**, 8 (4), 409–427. <https://doi.org/10.1007/s12551-016-0218-6>
- (90) Eins1905EN.Pdf. <https://www2.stat.duke.edu/courses/Spring12/sta357/refs/Eins1905EN.pdf>.
- (91) Intermolecular and Interparticle Forces. In *Introduction to Applied Colloid and Surface Chemistry*; John Wiley & Sons, Ltd, 2016; pp 11–33. <https://doi.org/10.1002/9781118881194.ch2>.
- (92) Baraban, L.; Harazim, S. M.; Sanchez, S.; Schmidt, O. G. Chemotactic Behavior of Catalytic Motors in Microfluidic Channels. *Angewandte Chemie International Edition* **2013**, 52 (21), 5552–5556. <https://doi.org/10.1002/anie.201301460>.
- (93) Buescher, J.; John, T.; Boehm, A. K.; Weber, L.; Abdel-Hafez, S. M.; Wagner, C.; Kraus, T.; Gallei, M.; Schneider, M. A Precise Nanoparticle Quantification Approach Using Microfluidics and Single-Particle Tracking. *Journal of Drug Delivery Science and Technology* **2022**, 75, 103579. <https://doi.org/10.1016/j.jddst.2022.103579>.
- (94) Team, E. Microfluidics: A General Overview of Microfluidics. *Elveflow* **2021**. <https://www.elveflow.com/microfluidic-reviews/general-microfluidics/a-general-overview-of-microfluidics/>.
- (95) Hui, R. Chapter 4 - Photodetectors. In *Introduction to Fiber-Optic Communications*; Hui, R., Ed.; Academic Press, 2020; pp 125–154. <https://doi.org/10.1016/B978-0-12-805345-4.00004-4>.
- (96) OpenCV. *ImageJ Wiki*. <https://imagej.github.io/software/opencv>.
- (97) Wu, Z.; Wu, Y.; He, W.; Lin, X.; Sun, J.; He, Q. Self-Propelled Polymer-Based Multilayer Nanorockets for Transportation and Drug Release. *Angewandte Chemie International Edition* **2013**, 52 (27), 7000–7003. <https://doi.org/10.1002/anie.201301643>.
- (98) Balasubramanian, S.; Kagan, D.; Manesh, K. M.; Calvo-Marzal, P.; Flechsig, G.-U.; Wang, J. Thermal Modulation of Nanomotor Movement. *Small* **2009**, 5 (13), 1569–1574. <https://doi.org/10.1002/sml.200900023>.
- (99) Misono, T. Dynamic Light Scattering (DLS). In *Measurement Techniques and Practices of Colloid and Interface Phenomena*; Abe, M., Ed.; Springer: Singapore, 2019; pp 65–69. [https://doi.org/10.1007/978-981-13-5931-6\\_10](https://doi.org/10.1007/978-981-13-5931-6_10).
- (100) Toh, A. G. G.; Wang, Z. P.; Yang, C.; Nguyen, N.-T. Engineering Microfluidic Concentration Gradient Generators for Biological Applications. *Microfluid Nanofluid* **2014**, 16 (1), 1–18. <https://doi.org/10.1007/s10404-013-1236-3>.
- (101) Akther, F.; Yakob, S. B.; Nguyen, N.-T.; Ta, H. T. Surface Modification Techniques for Endothelial Cell Seeding in PDMS Microfluidic Devices. *Biosensors* **2020**, 10 (11), 182. <https://doi.org/10.3390/bios10110182>.
- (102) Forigua, A.; Kirsch, R. L.; Willerth, S. M.; Elvira, K. S. Recent Advances in the Design of Microfluidic Technologies for the Manufacture of Drug Releasing Particles. *Journal of Controlled Release* **2021**, 333, 258–268. <https://doi.org/10.1016/j.jconrel.2021.03.019>.
- (103) Mosadegh, B.; Kuo, C.-H.; Tung, Y.-C.; Torisawa, Y.; Bersano-Begey, T.; Taviana, H.; Takayama, S. Integrated Elastomeric Components for Autonomous Regulation of Sequential and Oscillatory Flow Switching in Microfluidic Devices. *Nature Phys* **2010**, 6 (6), 433–437. <https://doi.org/10.1038/nphys1637>.
- (104) Abécassis, B.; Cottin-Bizonne, C.; Ybert, C.; Ajdari, A.; Bocquet, L. Boosting Migration of Large Particles by Solute Contrasts. *Nature Mater* **2008**, 7 (10), 785–789. <https://doi.org/10.1038/nmat2254>.
- (105) Xiao, Z.; Nsamela, A.; Garlan, B.; Simmchen, J. A Platform for Stop-Flow Gradient Generation to Investigate Chemotaxis. *Angewandte Chemie International Edition* **2022**, 61 (21), e202117768. <https://doi.org/10.1002/anie.202117768>.
- (106) Perro, A.; Reculosa, S.; Ravaine, S.; Bourgeat-Lami, E.; Duguet, E. Design and Synthesis of Janus Micro- and Nanoparticles. *J. Mater. Chem.* **2005**, 15 (35–36), 3745–3760. <https://doi.org/10.1039/B505099E>.
- (107) Cayre, O.; Paunov, V. N.; Velez, O. D. Fabrication of Asymmetrically Coated Colloid Particles by Microcontact Printing Techniques. *J. Mater. Chem.* **2003**, 13 (10), 2445–2450. <https://doi.org/10.1039/B308817K>.

- (108) Janus | Myth, Meaning, & Facts | Britannica. <https://www.britannica.com/topic/Janus-Roman-god>.
- (109) Takahara, Y. K.; Ikeda, S.; Ishino, S.; Tachi, K.; Ikeue, K.; Sakata, T.; Hasegawa, T.; Mori, H.; Matsumura, M.; Ohtani, B. Asymmetrically Modified Silica Particles: A Simple Particulate Surfactant for Stabilization of Oil Droplets in Water. *J Am Chem Soc* **2005**, 127 (17), 6271–6275. <https://doi.org/10.1021/ja043581r>.
- (110) Glaser, N.; Adams, D. J.; Böker, A.; Krausch, G. Janus Particles at Liquid–Liquid Interfaces. *Langmuir* **2006**, 22 (12), 5227–5229. <https://doi.org/10.1021/la060693i>.
- (111) Kim, J.; Lee, D.; Shum, H. C.; Weitz, D. A. Colloid Surfactants for Emulsion Stabilization. *Advanced Materials* **2008**, 20 (17), 3239–3243. <https://doi.org/10.1002/adma.200800484>.
- (112) Crespín, B.; Tran, C. T.; Cerbelaud, M.; Videcoq, A.; Darles, E. Two-Dimensional Stochastic Rotation Dynamics for Fluid Simulation. *JCC* **2020**, 08 (02), 27–38. <https://doi.org/10.4236/jcc.2020.82003>.
- (113) Parker, E. T.; Lollar, P. Measurement of the Translational Diffusion Coefficient and Hydrodynamic Radius of Proteins by Dynamic Light Scattering. *Bio Protoc* **2021**, 11 (20), e4195. <https://doi.org/10.21769/BioProtoc.4195>.
- (114) Measurement of the Translational Diffusion Coefficient and Hydrodynamic Radius of Proteins by Dynamic Light Scattering. <https://bio-protocol.org/en/bpdetail?id=4195&type=0>.
- (115) Shelukhin, V. Rotational Particle Separation in Solutions: Micropolar Fluid Theory Approach. *Polymers* **2021**, 13 (7), 1072. <https://doi.org/10.3390/polym13071072>.
- (116) Yin, T.; Yang, Z.; Zhang, F.; Lin, M.; Zhang, J.; Dong, Z. Assembly and Mechanical Response of Amphiphilic Janus Nanosheets at Oil-Water Interfaces. *Journal of Colloid and Interface Science* **2021**, 583, 214–221. <https://doi.org/10.1016/j.jcis.2020.09.026>.
- (117) Bajaj, M. G.; Laibinis, P. E. Selective DNA-Directed Assembly on Dual-Functionalized Microparticles.
- (118) Yoshida, M.; Roh, K.-H.; Mandal, S.; Bhaskar, S.; Lim, D.; Nandivada, H.; Deng, X.; Lahann, J. Structurally Controlled Bio-Hybrid Materials Based on Unidirectional Association of Anisotropic Microparticles with Human Endothelial Cells. *Advanced Materials* **2009**, 21 (48), 4920–4925. <https://doi.org/10.1002/adma.200901971>.
- (119) Wu, L. Y.; Ross, B. M.; Hong, S.; Lee, L. P. Bioinspired Nanocorals with Decoupled Cellular Targeting and Sensing Functionality. *Small* **2010**, 6 (4), 503–507. <https://doi.org/10.1002/smll.200901604>.
- (120) Roh, K.-H.; Yoshida, M.; Lahann, J. Compartmentalized, Multiphasic Nanocolloids with Potential Applications in Drug Delivery and Biomedical Imaging. *Materialwissenschaft und Werkstofftechnik* **2007**, 38 (12), 1008–1011. <https://doi.org/10.1002/mawe.200700245>.
- (121) Howse, J. R.; Jones, R. A. L.; Ryan, A. J.; Gough, T.; Vafabakhsh, R.; Golestanian, R. Self-Motile Colloidal Particles: From Directed Propulsion to Random Walk. *Phys. Rev. Lett.* **2007**, 99 (4), 048102. <https://doi.org/10.1103/PhysRevLett.99.048102>.
- (122) van Blaaderen, A. Colloids Get Complex. *Nature* **2006**, 439 (7076), 545–546. <https://doi.org/10.1038/439545a>.
- (123) Smoukov, S. K.; Gangwal, S.; Marquez, M.; Velev, O. D. Reconfigurable Responsive Structures Assembled from Magnetic Janus Particles. *Soft Matter* **2009**, 5 (6), 1285–1292. <https://doi.org/10.1039/B814304H>.
- (124) Edwards, E. W.; Wang, D.; Möhwald, H. Hierarchical Organization of Colloidal Particles: From Colloidal Crystallization to Supraparticle Chemistry. *Macromolecular Chemistry and Physics* **2007**, 208 (5), 439–445. <https://doi.org/10.1002/macp.200600655>.
- (125) Ghosh, A.; Sheridon, N.; Fischer, P. Janus Particles with Coupled Electric and Magnetic Moments Make a Disordered Magneto-Electric Medium. **2007**. <https://doi.org/10.1002/smll.200701301>.
- (126) Nisizako, T.; Torii, T.; Takahashi, T.; Takizawa, Y. Synthesis of Monodisperse Bicolored Janus Particles with Electrical Anisotropy Using a Microfluidic Co-Flow System. *Advanced Materials* **2006**, 18 (9), 1152–1156. <https://doi.org/10.1002/adma.200502431>.
- (127) Safaie, N.; Ferrier, R. C., Jr. Janus Nanoparticle Synthesis: Overview, Recent Developments, and Applications. *Journal of Applied Physics* **2020**, 127 (17), 170902. <https://doi.org/10.1063/5.0003329>.
- (128) Zhang, X.; Fu, Q.; Duan, H.; Song, J.; Yang, H. Janus Nanoparticles: From Fabrication to (Bio)Applications. *ACS Nano* **2021**, 15 (4), 6147–6191. <https://doi.org/10.1021/acsnano.1c01146>.
- (129) Tan, K. X.; Danquah, M. K.; Jeevanandam, J.; Barhoum, A. Development of Janus Particles as Potential Drug Delivery Systems for Diabetes Treatment and Antimicrobial Applications. *Pharmaceutics* **2023**, 15 (2), 423. <https://doi.org/10.3390/pharmaceutics15020423>.
- (130) Yang, Q.; Loos, K. Janus Nanoparticles inside Polymeric Materials: Interfacial Arrangement toward Functional Hybrid Materials. *Polymer Chemistry* **2017**, 8 (4), 641–654. <https://doi.org/10.1039/C6PY01795A>.
- (131) Jiang, S.; Chen, Q.; Tripathy, M.; Luijten, E.; Schweizer, K. S.; Granick, S. Janus Particle Synthesis and Assembly. *Advanced Materials* **2010**, 22 (10), 1060–1071. <https://doi.org/10.1002/adma.200904094>.
- (132) Casagrande, C.; Fabre, P.; Raphaël, E.; Veyssié, M. “Janus Beads”: Realization and Behaviour at Water/Oil Interfaces. *EPL* **1989**, 9 (3), 251–255. <https://doi.org/10.1209/0295-5075/9/3/011>.
- (133) Karadkar, S.; Tiwari, A.; Chaskar, A. C. Recent Advancements in Janus Nanoparticle-Based Biosensing Platforms. *Int Nano Lett* **2023**, 13 (2), 93–115. <https://doi.org/10.1007/s40089-022-00385-x>.
- (134) Han, Y.; Kim, H. Fabrication of Versatile Janus Microparticles through Geometry and Surface Chemistry Control. *Langmuir* **2023**, 39. <https://doi.org/10.1021/acs.langmuir.3c01917>.
- (135) Janus Particles: Design, Preparation, and Biomedical Applications. *Materials Today Bio* **2019**, 4, 100033. <https://doi.org/10.1016/j.mtbio.2019.100033>.
- (136) Lattuada, M.; Hatton, T. A. Synthesis, Properties and Applications of Janus Nanoparticles. *Nano Today* **2011**, 6 (3), 286–308. <https://doi.org/10.1016/j.nantod.2011.04.008>.



- (137) Fujimoto, K.; Nakahama, K.; Shidara, M.; Kawaguchi, H. Preparation of Unsymmetrical Microspheres at the Interfaces. *Langmuir* **1999**, *15* (13), 4630–4635. <https://doi.org/10.1021/la990023v>.
- (138) Cayre, O.; Paunov, V. N.; Velev, O. D. Fabrication of Dipolar Colloid Particles by Microcontact Printing. *Chem. Commun.* **2003**, No. 18, 2296–2297. <https://doi.org/10.1039/B307296G>.
- (139) Koo, H. Y.; Yi, D. K.; Yoo, S. J.; Kim, D.-Y. A Snowman-like Array of Colloidal Dimers for Antireflecting Surfaces. *Advanced Materials* **2004**, *16* (3), 274–277. <https://doi.org/10.1002/adma.200305617>.
- (140) Kaufmann, T.; Gokmen, M. T.; Rinnen, S.; Arlinghaus, H.; Du Prez, F.; Ravoo, B. Bifunctional Janus Beads Made by “Sandwich” Microcontact Printing Using Click Chemistry. *Journal of Materials Chemistry* **2012**, *22*, 6190. <https://doi.org/10.1039/c2jm16807c>.
- (141) The Three Different Types of PVD Coating. Bend Plating. <https://www.bendplating.com/different-types-pvd-coating/>.
- (142) Bao, Z.; Chen, L.; Weldon, M.; Chandross, E.; Cherniavskaya, O.; Dai, Y.; Tok, J. B.-H. Toward Controllable Self-Assembly of Microstructures: Selective Functionalization and Fabrication of Patterned Spheres. *Chem. Mater.* **2002**, *14* (1), 24–26. <https://doi.org/10.1021/cm010739n>.
- (143) Himmelhaus, M.; Takei, H. Cap-Shaped Gold Nanoparticles for an Optical Biosensor. *Sensors and Actuators B: Chemical* **2000**, *63* (1), 24–30. [https://doi.org/10.1016/S0925-4005\(99\)00393-7](https://doi.org/10.1016/S0925-4005(99)00393-7).
- (144) Love, J. C.; Gates, B. D.; Wolfe, D. B.; Paul, K. E.; Whitesides, G. M. Fabrication and Wetting Properties of Metallic Half-Shells with Submicron Diameters. *Nano Lett.* **2002**, *2* (8), 891–894. <https://doi.org/10.1021/nl025633l>.
- (145) Lu, Y.; Xiong, H.; Jiang, X.; Xia, Y.; Prentiss, M.; Whitesides, G. M. Asymmetric Dimers Can Be Formed by Dewetting Half-Shells of Gold Deposited on the Surfaces of Spherical Oxide Colloids. *J. Am. Chem. Soc.* **2003**, *125* (42), 12724–12725. <https://doi.org/10.1021/ja0373014>.
- (146) Hugonnot, E.; Carles, A.; Delville, M.-H.; Panizza, P.; Delville, J.-P. “Smart” Surface Dissymmetrization of Microparticles Driven by Laser Photochemical Deposition. *Langmuir* **2003**, *19* (2), 226–229. <https://doi.org/10.1021/la0261085>.
- (147) Dendukuri, D.; Pregibon, D.; Collins, J.; Hatton, T.; Doyle, P. Continuous-Flow Lithography for High-Throughput Microparticle Synthesis. *Nature materials* **2006**, *5*, 365–369. <https://doi.org/10.1038/nmat1617>.
- (148) Paunov, V. N.; Cayre, O. J. Supraparticles and “Janus” Particles Fabricated by Replication of Particle Monolayers at Liquid Surfaces Using a Gel Trapping Technique. *Advanced Materials* **2004**, *16* (9–10), 788–791. <https://doi.org/10.1002/adma.200306476>.
- (149) Paunov, V. N.; Cayre, O. J. Supraparticles and “Janus” Particles Fabricated by Replication of Particle Monolayers at Liquid Surfaces Using a Gel Trapping Technique. *Advanced Materials* **2004**, *16* (9–10), 788–791. <https://doi.org/10.1002/adma.200306476>.
- (150) Ekanem, E. E.; Zhang, Z.; Vladislavjević, G. T. Facile Production of Biodegradable Bipolymer Patchy and Patchy Janus Particles with Controlled Morphology by Microfluidic Routes. *Langmuir* **2017**, *33* (34), 8476–8482. <https://doi.org/10.1021/acs.langmuir.7b02506>.
- (151) Chevalier, Y.; Bolzinger, M.-A. Emulsions Stabilized with Solid Nanoparticles: Pickering Emulsions. *Colloids and Surfaces A: Physicochemical and Engineering Aspects* **2013**, *439*, 23–34. <https://doi.org/10.1016/j.colsurfa.2013.02.054>.
- (152) Wu, J.; Ma, G.-H. Recent Studies of Pickering Emulsions: Particles Make the Difference. *Small* **2016**, *12* (34), 4633–4648. <https://doi.org/10.1002/sml.201600877>.
- (153) Zhu, Y.; Jiang, J.; Liu, K.; Cui, Z.; Binks, B. P. Switchable Pickering Emulsions Stabilized by Silica Nanoparticles Hydrophobized in Situ with a Conventional Cationic Surfactant. *Langmuir* **2015**, *31* (11), 3301–3307. <https://doi.org/10.1021/acs.langmuir.5b00295>.
- (154) Frelichowska, J.; Bolzinger, M.-A.; Chevalier, Y. Pickering Emulsions with Bare Silica. *Colloids and Surfaces A: Physicochemical and Engineering Aspects* **2009**, *343* (1–3), 70–74. <https://doi.org/10.1016/j.colsurfa.2009.01.031>.
- (155) Zou, S.; Wang, C.; Gao, Q.; Tong, Z. Surfactant-Free Multiple Pickering Emulsions Stabilized by Combining Hydrophobic and Hydrophilic Nanoparticles. *Journal of Dispersion Science and Technology* **2013**, *34* (2), 173–181. <https://doi.org/10.1080/01932691.2012.657947>.
- (156) Perro, A.; Meunier, F.; Schmitt, V.; Ravaine, S. Production of Large Quantities of “Janus” Nanoparticles Using Wax-in-Water Emulsions. *Colloids and Surfaces A: Physicochemical and Engineering Aspects* **2009**, *332* (1), 57–62. <https://doi.org/10.1016/j.colsurfa.2008.08.027>.
- (157) Avossa, J.; Esteves, A. C. C. Influence of Experimental Parameters on the Formation and Stability of Silica-Wax Colloidosomes. *Journal of Colloid and Interface Science* **2020**, *561*, 244–256. <https://doi.org/10.1016/j.jcis.2019.11.011>.
- (158) Hong, L.; Jiang, S.; Granick, S. Simple Method to Produce Janus Colloidal Particles in Large Quantity. *Langmuir* **2006**, *22* (23), 9495–9499. <https://doi.org/10.1021/la062716z>.
- (159) Binks, B. P.; Lumsdon, S. O. Influence of Particle Wettability on the Type and Stability of Surfactant-Free Emulsions. *Langmuir* **2000**, *16* (23), 8622–8631. <https://doi.org/10.1021/la000189s>.
- (160) Qiang, W.; Wang, Y.; He, P.; Xu, H.; Gu, H.; Shi, D. Synthesis of Asymmetric Inorganic/Polymer Nanocomposite Particles via Localized Substrate Surface Modification and Miniemulsion Polymerization. *Langmuir* **2008**, *24* (3), 606–608. <https://doi.org/10.1021/la703607s>.
- (161) Khoei, S.; Nouri, A. Preparation of Janus Nanoparticles and Its Application in Drug Delivery. In *Design and Development of New Nanocarriers*; Elsevier, 2018; pp 145–180. <https://doi.org/10.1016/B978-0-12-813627-0.00004-1>.
- (162) Walther, A.; Müller, A. H. E. Janus Particles: Synthesis, Self-Assembly, Physical Properties, and Applications. *Chem. Rev.* **2013**, *113* (7), 5194–5261. <https://doi.org/10.1021/cr300089t>.

- (163) Shemi, O. *Self-Assembly and Self-Propulsion of Colloidal Particles Using Shape and Janus Anisotropy*. 2016. <https://hdl.handle.net/2027.42/135804>.
- (164) Wang, Y.; Shang, M.; Wang, Y.; Xu, Z. Droplet-Based Microfluidic Synthesis of (Au nanorod@Ag)–Polyaniline Janus Nanoparticles and Their Application as a Surface-Enhanced Raman Scattering Nanosensor for Mercury Detection. *Anal. Methods* **2019**, *11* (31), 3966–3973. <https://doi.org/10.1039/C9AY01213C>.
- (165) Petit, L.; Manaud, J.-P.; Mingotaud, C.; Ravaine, S.; Duguet, E. Sub-Micrometer Silica Spheres Dissymmetrically Decorated with Gold Nanoclusters. *Materials Letters* **2001**, *51* (6), 478–484. [https://doi.org/10.1016/S0167-577X\(01\)00338-X](https://doi.org/10.1016/S0167-577X(01)00338-X).
- (166) Ghosh, A.; Sheridon, N. K.; Fischer, P. Voltage-Controllable Magnetic Composite Based on Multifunctional Polyethylene Micro-Particles. *Small* **2008**, *4* (11), 1956–1958. <https://doi.org/10.1002/smll.200701301>.
- (167) Sheridon, N. K.; Richley, E. A.; Mikkelsen, J. C.; Tsuda, D.; Crowley, J. M.; Oaha, K. A.; Howard, M. E.; Rodkin, M. A.; Swidler, R.; Sprague, R. The Gyrotron Rotating Ball Display. *J. Soc. Inf. Display* **1999**, *7* (2), 141. <https://doi.org/10.1889/1.1985284>.
- (168) Hwang, H.; Jeong, U. Microparticle-Based Soft Electronic Devices: Toward One-Particle/One-Pixel. *Advanced Functional Materials* **2020**, *30* (2), 1901810. <https://doi.org/10.1002/adfm.201901810>.
- (169) Marina Santana Vega; Andrés Guerrero Martínez; Fabio Cucinotta. Facile Strategy for the Synthesis of Gold@Silica Hybrid Nanoparticles with Controlled Porosity and Janus Morphology. *Nanomaterials (Basel, Switzerland)* **2019**, *9* (3), 348. <https://doi.org/10.3390/nano9030348>.
- (170) Kaufmann, T.; Gokmen, M. T.; Wendeln, C.; Schneiders, M.; Rinnen, S.; Arlinghaus, H. F.; Bon, S. A. F.; Du Prez, F. E.; Ravoo, B. J. “Sandwich” Microcontact Printing as a Mild Route Towards Monodisperse Janus Particles with Tailored Bifunctionality. *Advanced Materials* **2011**, *23* (1), 79–83. <https://doi.org/10.1002/adma.201003564>.
- (171) Nakahama, K.; Kawaguchi, H.; Fujimoto, K. A Novel Preparation of Nonsymmetrical Microspheres Using the Langmuir–Blodgett Technique. *Langmuir* **2000**, *16* (21), 7882–7886. <https://doi.org/10.1021/la000684o>.
- (172) Katuri, J.; Ma, X.; Stanton, M. M.; Sánchez, S. Designing Micro- and Nanoswimmers for Specific Applications. *Acc. Chem. Res.* **2017**, *50* (1), 2–11. <https://doi.org/10.1021/acs.accounts.6b00386>.
- (173) Schattling, P. S.; Ramos-Docampo, M. A.; Salgueiriño, V.; Städler, B. Double-Fueled Janus Swimmers with Magnetotactic Behavior. *ACS Nano* **2017**, *11* (4), 3973–3983. <https://doi.org/10.1021/acsnano.7b00441>.
- (174) Šípová-Jungová, H.; Andrén, D.; Jones, S.; Käll, M. Nanoscale Inorganic Motors Driven by Light: Principles, Realizations, and Opportunities. *Chem. Rev.* **2020**, *120* (1), 269–287. <https://doi.org/10.1021/acs.chemrev.9b00401>.
- (175) Jalilvand, Z.; Haider, H.; Cui, J.; Kretzschmar, and I. Pt-SiO<sub>2</sub> Janus Particles and the Water/Oil Interface: A Competition between Motility and Thermodynamics. *Langmuir* **2020**, *36* (25), 6880–6887. <https://doi.org/10.1021/acs.langmuir.9b03454>.
- (176) Baraban, L.; Streubel, R.; Makarov, D.; Han, L.; Karnaushenko, D.; Schmidt, O. G.; Cuniberti, G. Fuel-Free Locomotion of Janus Motors: Magnetically Induced Thermophoresis. *ACS Nano* **2013**, *7* (2), 1360–1367. <https://doi.org/10.1021/nn305726m>.
- (177) Pourrahimi, A. M.; Villa, K.; Ying, Y.; Sofer, Z.; Pumera, M. ZnO/ZnO<sub>2</sub>/Pt Janus Micromotors Propulsion Mode Changes with Size and Interface Structure: Enhanced Nitroaromatic Explosives Degradation under Visible Light. *ACS Appl. Mater. Interfaces* **2018**, *10* (49), 42688–42697. <https://doi.org/10.1021/acsami.8b16217>.
- (178) Si, B. R.; Patel, P.; Mangal, R. Self-Propelled Janus Colloids in Shear Flow. *Langmuir* **2020**, *36* (40), 11888–11898. <https://doi.org/10.1021/acs.langmuir.0c01924>.
- (179) Bednarz, S.; Ryś, B.; Bogdał, D. Application of Hydrogen Peroxide Encapsulated in Silica Xerogels to Oxidation Reactions. *Molecules* **2012**, *17* (7), 8068–8078. <https://doi.org/10.3390/molecules17078068>.
- (180) Pinnaratip, R.; Forooshani, P. K.; Li, M.; Hu, Y. H.; Rajachar, R. M.; Lee, B. P. Controlling the Release of Hydrogen Peroxide from Catechol-Based Adhesives Using Silica Nanoparticles. *ACS Biomater. Sci. Eng.* **2020**, *6* (8), 4502–4511. <https://doi.org/10.1021/acsbiomaterials.0c00572>.
- (181) Zeglinski, J.; Piotrowski, G.; Piekos, R. A Study of Interaction between Hydrogen Peroxide and Silica Gel by FTIR Spectroscopy and Quantum Chemistry. *Journal of Molecular Structure* **2006**, *794*, 83–91. <https://doi.org/10.1016/j.molstruc.2006.01.043>.
- (182) Belowich, M. E.; Roberts, J. M.; Peterson, T. H.; Bellinger, E.; Syverud, K.; Sidle, T. Lewis Acids As Highly Active Silanol Polycondensation Catalysts Affording Low Levels of Cyclosiloxanes. *Macromolecules* **2020**, *53* (17), 7487–7495. <https://doi.org/10.1021/acs.macromol.0c01069>.
- (183) Védrine, J. Concluding Remarks and Challenges of Heterogeneous Catalysis on Metal Oxides \* \*Personal Views and Conclusions/Challenges Drawn for the Different Chapters in This Book; 2018; pp 551–569. <https://doi.org/10.1016/B978-0-12-811631-9.00009-0>.
- (184) Kondo, J. N.; Yoda, E.; Ishikawa, H.; Wakabayashi, F.; Domen, K. Acid Property of Silanol Groups on Zeolites Assessed by Reaction Probe IR Study. *Journal of Catalysis* **2000**, *191* (2), 275–281. <https://doi.org/10.1006/jcat.1999.2807>.
- (185) Kondo, Y.; Hino, K.; Kuwahara, Y.; Mori, K.; Kobayashi, H.; Yamashita, H. Lewis Acid-Triggered Photocatalytic Hydrogen Peroxide Production in an Aluminum-Based Metal–Organic Framework. *Chem. Commun.* **2022**, *58* (88), 12345–12348. <https://doi.org/10.1039/D2CC04454D>.
- (186) Culver, D. B.; Venkatesh, A.; Huynh, W.; Rossini, A. J.; Conley, M. P. Al(ORF)<sub>3</sub> (RF = C(CF<sub>3</sub>)<sub>3</sub>) Activated Silica: A Well-Defined Weakly Coordinating Surface Anion. *Chem. Sci.* **2020**, *11* (6), 1510–1517. <https://doi.org/10.1039/C9SC05904K>.

- (187) Yi, F.; Chen, Y.; Tao, Z.; Hu, C.; Yi, X.; Zheng, A.; Wen, X.; Yun, Y.; Yang, Y.; Li, Y. Origin of Weak Lewis Acids on Silanol Nests in Dealuminated Zeolite Beta. *Journal of Catalysis* **2019**, *380*, 204–214. <https://doi.org/10.1016/j.jcat.2019.10.008>.
- (188) Muñoz, M. I. CRISTALES FOTÓNICOS BASADOS EN ÓPALOS. 2003. [https://wp.icmm.csic.es/wp-content/uploads/sites/22/2019/11/Tesis\\_Marta.pdf](https://wp.icmm.csic.es/wp-content/uploads/sites/22/2019/11/Tesis_Marta.pdf).
- (189) Englebienne, P.; Hoonacker, A. V.; Verhas, M. Surface Plasmon Resonance: Principles, Methods and Applications in Biomedical Sciences. *Spectroscopy* **2003**, *17* (2–3), 255–273. <https://doi.org/10.1155/2003/372913>.
- (190) Tauran, Y.; Brioude, A.; Coleman, A. W.; Rhimi, M.; Kim, B. Molecular Recognition by Gold, Silver and Copper Nanoparticles. *World J Biol Chem* **2013**, *4* (3), 35–63. <https://doi.org/10.4331/wjbc.v4.i3.35>.
- (191) Xin, Y.; Yu, K.; Zhang, L.; Yang, Y.; Yuan, H.; Li, H.; Wang, L.; Zeng, J. Copper-Based Plasmonic Catalysis: Recent Advances and Future Perspectives. *Advanced Materials* **2021**, *33* (32), 2008145. <https://doi.org/10.1002/adma.202008145>.
- (192) Kimling, J.; Maier, M.; Okenve, B.; Kotaidis, V.; Ballot, H.; Plech, A. Turkevich Method for Gold Nanoparticle Synthesis Revisited. *J Phys Chem B* **2006**, *110* (32), 15700–15707. <https://doi.org/10.1021/jp061667w>.
- (193) Lupa, D.; Oćwieja, M.; Piergies, N.; Baliś, A.; Paluszkiwicz, C.; Adamczyk, Z. Gold Nanoparticles Deposited on Silica Microparticles - Electrokinetic Characteristics and Application in SERS. *Colloid and Interface Science Communications* **2019**, *33*, 100219. <https://doi.org/10.1016/j.colcom.2019.100219>.
- (194) Pham, X.-H.; Tran, V.-K.; Hahm, E.; Kim, Y.-H.; Kim, J.; Kim, W.; Jun, B.-H. Synthesis of Gold-Platinum Core-Shell Nanoparticles Assembled on a Silica Template and Their Peroxidase Nanozyme Properties. *International Journal of Molecular Sciences* **2022**, *23* (12), 6424. <https://doi.org/10.3390/ijms23126424>.
- (195) Kowalska, E.; Abe, R.; Ohtani, B. Visible Light-Induced Photocatalytic Reaction of Gold-Modified Titanium(IV) Oxide Particles: Action Spectrum Analysis. *Chem. Commun.* **2009**, No. 2, 241–243. <https://doi.org/10.1039/B815679D>.
- (196) Ye, Y.; Luan, J.; Wang, M.; Chen, Y.; Wilson, D. A.; Peng, F.; Tu, Y. Fabrication of Self-Propelled Micro- and Nanomotors Based on Janus Structures. *Chemistry – A European Journal* **2019**, *25* (37), 8663–8680. <https://doi.org/10.1002/chem.201900840>.
- (197) Busch, R. T.; Karim, F.; Weis, J.; Sun, Y.; Zhao, C.; Vasquez, E. S. Optimization and Structural Stability of Gold Nanoparticle–Antibody Bioconjugates. *ACS Omega* **2019**, *4* (12), 15269–15279. <https://doi.org/10.1021/acsomega.9b02276>.
- (198) Sangwan, S.; Seth, R. Synthesis, Characterization and Stability of Gold Nanoparticles (AuNPs) in Different Buffer Systems. *J Clust Sci* **2022**, *33* (2), 749–764. <https://doi.org/10.1007/s10876-020-01956-8>.
- (199) Ben Haddada, M.; Huebner, M.; Casale, S.; Knopp, D.; Niessner, R.; Salmann, M.; Boujday, S. Gold Nanoparticles Assembly on Silicon and Gold Surfaces: Mechanism, Stability, and Efficiency in Diclofenac Biosensing. *J. Phys. Chem. C* **2016**, *120* (51), 29302–29311. <https://doi.org/10.1021/acs.jpcc.6b10322>.
- (200) López-Miranda, J. L.; Esparza, R.; Rosas, G.; Pérez, R.; Estévez-González, M. Catalytic and Antibacterial Properties of Gold Nanoparticles Synthesized by a Green Approach for Bioremediation Applications. *3 Biotech* **2019**, *9* (4), 135. <https://doi.org/10.1007/s13205-019-1666-z>.
- (201) He, W.; Zhou, Y.-T.; Wamer, W. G.; Hu, X.; Wu, X.; Zheng, Z.; Boudreau, M. D.; Yin, J.-J. Intrinsic Catalytic Activity of Au Nanoparticles with Respect to Hydrogen Peroxide Decomposition and Superoxide Scavenging. *Biomaterials* **2013**, *34* (3), 765–773. <https://doi.org/10.1016/j.biomaterials.2012.10.010>.
- (202) Matar, G. H.; Andac, M. Highly Efficient Degradation of Basic Dyes Using Gold-Coated Nature-Based Supermagnetic Iron Oxide Nanoparticles as Eco-Friendly Nanocatalysts. *Environmental Science and Pollution Research* **2024**, *31* (17), 24894–24912. <https://doi.org/10.1007/s11356-024-32775-3>.
- (203) Garg, N.; Bera, S.; Rastogi, L.; Ballal, A.; Balaramakrishna, M. V. Synthesis and Characterization of L-Asparagine Stabilised Gold Nanoparticles: Catalyst for Degradation of Organic Dyes. *Spectrochimica Acta Part A: Molecular and Biomolecular Spectroscopy* **2020**, *232*, 118126. <https://doi.org/10.1016/j.saa.2020.118126>.
- (204) Deokar, G. K.; Ingale, A. G. Exploring Effective Catalytic Degradation of Organic Pollutant Dyes Using Environment Benign, Green Engineered Gold Nanoparticles. *Inorganic Chemistry Communications* **2023**, *151*, 110649. <https://doi.org/10.1016/j.inoche.2023.110649>.
- (205) Lin, C.-C.; Liao, C.-W.; Chao, Y.-C.; Kuo, C. Fabrication and Characterization of Asymmetric Janus and Ternary Particles. *ACS Appl. Mater. Interfaces* **2010**, *2* (11), 3185–3191. <https://doi.org/10.1021/am1006589>.
- (206) Fujii, S.; Yokoyama, Y.; Miyanari, Y.; Shiono, T.; Ito, M.; Yusa, S.; Nakamura, Y. Micrometer-Sized Gold–Silica Janus Particles as Particulate Emulsifiers. *Langmuir* **2013**, *29* (18), 5457–5465. <https://doi.org/10.1021/la400697a>.
- (207) Le, T. C.; Zhai, J.; Chiu, W.-H.; Tran, P. A.; Tran, N. Janus Particles: Recent Advances in the Biomedical Applications. *IJN* **2019**, Volume 14, 6749–6777. <https://doi.org/10.2147/IJN.S169030>.
- (208) Influence of experimental parameters on the formation and stability of silica-wax colloidosomes | Elsevier Enhanced Reader. <https://doi.org/10.1016/j.jcis.2019.11.011>.
- (209) Gu, H.; Yang, Z.; Gao, J.; Chang, C. K.; Xu, B. Heterodimers of Nanoparticles: Formation at a Liquid–Liquid Interface and Particle-Specific Surface Modification by Functional Molecules. *J. Am. Chem. Soc.* **2005**, *127* (1), 34–35. <https://doi.org/10.1021/ja045220h>.
- (210) Kierulf, A.; Azizi, M.; Eskandarloo, H.; Whaley, J.; Liu, W.; Perez-Herrera, M.; You, Z.; Abbaspourrad, A. Starch-Based Janus Particles: Proof-of-Concept Heterogeneous Design via a Spin-Coating Spray Approach. *Food Hydrocolloids* **2019**, *91*, 301–310. <https://doi.org/10.1016/j.foodhyd.2019.01.037>.

## Introduction

- (211) Lyu, X.; Liu, X.; Zhou, C.; Duan, S.; Xu, P.; Dai, J.; Chen, X.; Peng, Y.; Cui, D.; Tang, J.; Ma, X.; Wang, W. Active, Yet Little Mobility: Asymmetric Decomposition of H<sub>2</sub>O<sub>2</sub> Is Not Sufficient in Propelling Catalytic Micromotors. *J. Am. Chem. Soc.* **2021**, *143* (31), 12154–12164. <https://doi.org/10.1021/jacs.1c04501>.
- (212) Gao, C.; Feng, Y.; Wilson, D. A.; Tu, Y.; Peng, F. Micro-Nano Motors with Taxis Behavior: Principles, Designs, and Biomedical Applications. *Small* **2022**, *18* (15), 2106263. <https://doi.org/10.1002/sml.202106263>.
- (213) Kumagai, Y.; Nagaishi, R.; Kimura, A.; Taguchi, M.; Nishihara, K.; Yamagishi, I.; Ogawa, T. Measurement and Evaluation of Hydrogen Production from Mixtures of Seawater and Zeolite in Decontamination of Radioactive Water. *Transactions of the Atomic Energy Society of Japan*. <https://doi.org/10.3327/taesj.J11.021>.
- (214) Romanovskaia, V.; Rokitko, P.; Malashenko, I.; Krishtab, T.; Chernai, N. Sensitivity of Soil Bacteria isolated from the alienated zone around the Chernobyl Nuclear Power Plant to various stress factors. <https://europepmc.org/article/med/10576090>.

# CHAPTER 2

## Chapter 2. Particle Production

### 2.1 Introduction

As discussed in Chapter 1 chemotactic nano/micro particles present a promising perspective in the field of nanotechnology (to mimic nature). However, the mechanism of the chemotaxis by these particles is still under debate. To better understand the motion at work, we choose to compare different types of particle for the targeted nanorobots chosen as a model of radiotactic colloids (that would derive its motion from the catalytic reaction with the product of radiolysis coming from contamination hotspots). In Chapter 1, the choice of gold/silica Janus particles have been argued to be chosen as a model of radiotactic particles. However, as underlined in paragraph “1.6.2” of Chapter 1, the particular role of asymmetry in the particles properties is not obvious. To better identify the key parameters for chemotaxis, a family of different SiO<sub>2</sub>/Gold particles have been selected. Colloids with pristine silica particles (SP), covered with Gold (nanoparticles or homogeneous thin layer) in Janus or isotropic patterns are the centre of interest in this thesis. This chapter describes the synthesis of silica particles with isotropic and anisotropic surface modifications by gold. A large batch production of these colloidal particles is necessary to ensure repeatability of the experiments, and the use of multi-technique approaches for dimensional and dynamic characterisations. This chapter focuses on the synthesis of the different kind of nanoparticles from bottom-up chemical synthesis protocols; ideal for bulk production of particles, control in functionalization for reproducibility, and characterization. Primarily SP and gold nanoparticles (AuNPs) were first synthesized following the classical protocols described in the literature, Stöber method<sup>219</sup> and Turkevich method,<sup>220</sup> respectively. In the second step, these particles were treated for surface modifications in order to obtain the AuNPs functionalized SP (isotropic or Janus coverage).

Further highlights of chapter two are the intricate complications of Janus particle synthesis and advancing our understanding of the structure-property relationships that these particle bring along. As attention has been given in the understanding and optimizing the different factors (selection of the precursors, of the proportions between each and reaction conditions) to obtain a control over the size, coverage rate, reproducibility, yield and large quantity of Janus SP/AuNPs particles. For comparison, a set of SP covered by thin layer of gold (PVD-JP) will be synthesized through a method of physical vapour deposition (PVD) and compared. Even though the method of physical vapour deposition (for the production of Janus Particles) is limited to low quantity, this method ensures high quality yield (surface modification of all the particles is homogenous). Further, dimensional and plasmonic characterizations were conducted by Dynamic Light Scattering (DLS), and UV-Vis spectrometry (UV-Vis), respectively and combined dimensional and shape characterization have been done by Scanning Electron Microscopy (SEM). Some images and results shared in this chapter were produced by an M2 master thesis (titled “Synthesis of chemotactic Janus nanoparticles”<sup>221</sup>) intern Arthur Allaire,<sup>221</sup> who worked on the reproducibility and scale-up of Janus particles during 5 months between March and July 2023.

## 2.2 Material

### 2.2.1 Chemicals and Materials

(3-Aminopropyl) triethoxysilane (APTES) 99% (CAS N°: 919-30-2), Hexane (CAS N°: 110-54-3), Paraffin wax (CAS N°: 8002-74-2), Poly-L-lysine (PLL) solution 0.1 % (w/v) in H<sub>2</sub>O (CAS N°:25988-63-0), Poly(allylamine hydrochloride) (PAH) average M<sub>w</sub> ~ 17500 (CAS N°:71550-12-4), Tetraethyl orthosilicate (TEOS) 99.99% (CAS N°: 78-10-4), Sodium chloride (NaCl) (CAS N°:7647-14-5) and Sodium citrate tribasic dehydrate (CAS N°: 6132-04-3) were purchased at Sigma Aldrich. Cetyltrimethylammonium bromide (CTAB 98%) (CAS N°:57-09-0) from G BIOSCIENCES and Citric acid monohydrate (CAS N°: 5949-29-1) from Fluka. Ammonia 28% and Ethanol Absolute were purchased from VWR Chemicals. All the chemicals purchased were of analytical grade and thus, were used without further purification. Mili-Q water was used for all the experiments, treatment processes and storage (unless mentioned otherwise). Whatman 1 filter paper from Cytiva (Ø 90 mm, Cat. 1; CAS N°: 1001-090).

### 2.2.2 Apparatus

Ultra-Turrax® T25 from JANKE & KUNNEL, IKA®-Labortechnik, Centrifuge 3K10 from BIOBLOCK SCIENTIFIC, SIGMA®, Mini centrifuge F-45-12-11 from miniSpin, Eppendorf, Rotating agitator LD-76 from LABINCO BV, Hot Plat MR 3002 from Heidolph and Rotamag, Thermometer EKT 3001 from Heidolph, Balances: METTLER AE200 and New Classic MS from METTLER TOLEDO, Vacuum Pump by KIF LABOPORT from ateliers Cloup, Spin Coater Spin 150 by SPS international, Ultra 55 SEM Microscope by ZEISS with EDX set-up by Bruker (at LEDNA, CEA – Saclay), Thermal Evaporation deposition Set-up with Reflection Machine by PLASSYS (at LICSEN, CEA – Saclay), Plasma Machine CUTE by Femto Science. All the synthesis were conducted under the Bench-mounted fume cupboard from SCALA.

### 2.2.3 Glassware and Plastic-ware

Polypropylene Conical Tube (15mL) (Nonpyrogenic) Falcon® Blue Max™ Jr. 352097 by BECTON DICKINSON, Polypropylene Conical Tube (50mL) (Nonpyrogenic), Corning, Glass slide by Thermo Fischer.

## 2.3 Method: Synthesis, Protocol-Optimization and Characterization Techniques

### 2.3.1 Synthesis of gold nanoparticles

The gold nanoparticles were synthesized by following an adaptation of the classical Turkevich protocol<sup>220</sup> described by Sivaraman et al.<sup>222</sup> Typically, the addition of chloroauric acid salt into sodium citrate/water boiling solution produces gold nanoparticles suspension (Figure 51). As any sort of impurity can hugely impact the synthesis and quality of the synthesized gold nanoparticles, all glassware underwent thorough cleaning using aqua regia before any reactions. Protocol for the synthesis of gold nanoparticle used in this work is shared in the following points:

## Particle Production

1. In an Erlenmeyer flask, 47.75 mL of water was brought to a boil.
2. To this boiling water, 2 mL of sodium citrate solution (34 mM concentration) prepared in citric acid (0.05% w/v), was added.
3. Following the addition of the sodium citrate solution, 250  $\mu\text{L}$  of  $\text{HAuCl}_4 \cdot 3\text{H}_2\text{O}$  from the stock solution of  $\text{HAuCl}_4 \cdot 3\text{H}_2\text{O}$  (0.05 M concentration) was quickly introduced to the boiling mixture (citrate to chloroauric molar ratio MR = 5.44).
4. Boiling was maintained for two minutes. The solution was observed to turn maroonish red from in about 2 mins since the introduction of sodium citrate, followed by red color within 30 mins.
5. Then, the Erlenmeyer flask was covered with aluminum foil and the solution cooled down at room temperature for 24 hours.
6. The solution was finally transferred to a plastic bottle and stored in the refrigerator.

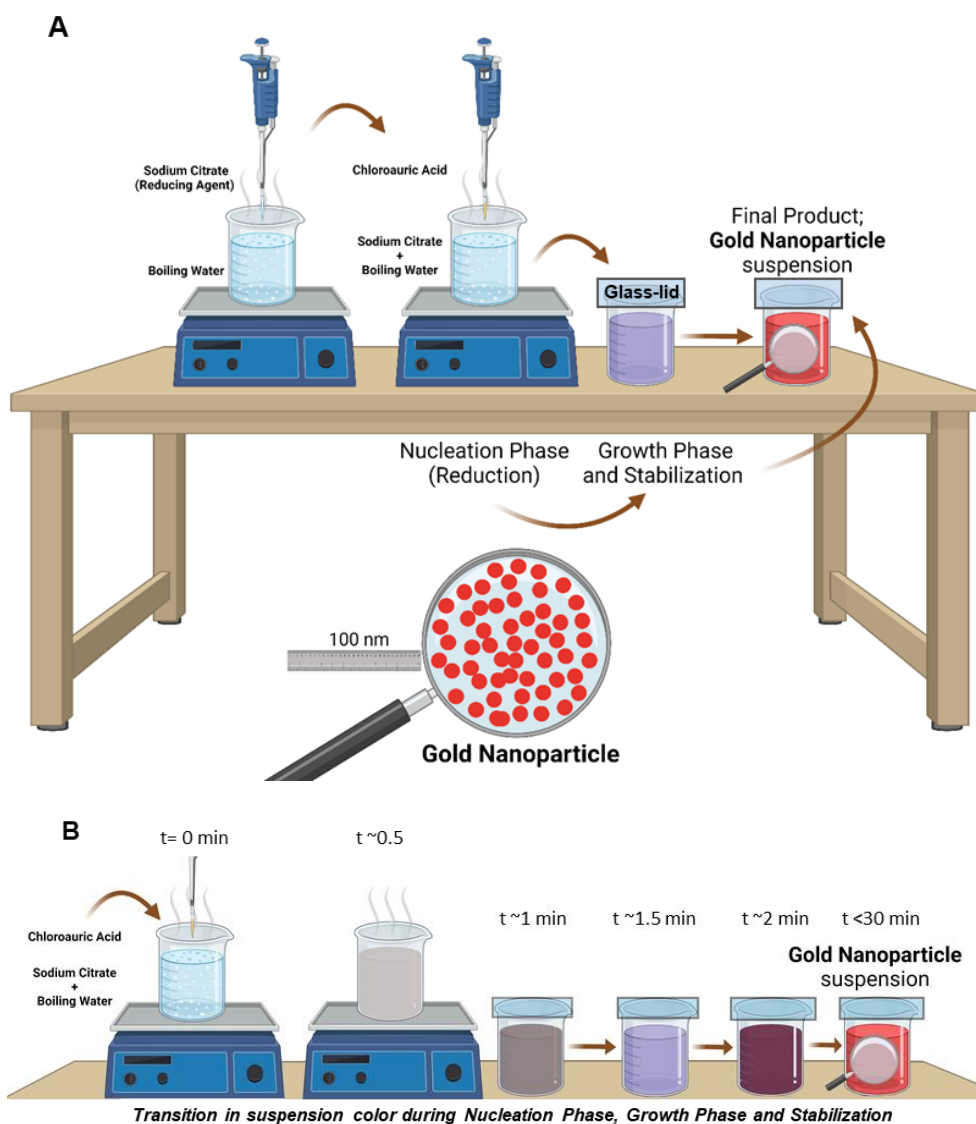


Figure 51: Scheme of reverse Turkevich protocol to synthesize gold nanoparticle (A) and Transition in colour during nucleation to growth phase and stabilization of synthesized gold nanoparticles (B). Starting with addition of sodium citrate to boiling water which acts as the reducing agent for the further added chloroauric acid to the boiling mixture. After the addition of precursors, the mixture is cooled down at room temperature giving a stable suspension of gold nanoparticles



The nanoparticles were characterized by UV-Vis and DLS to measure their size distribution, their morphology (isotropy/anisotropy) and their colloidal stability. The concentration of gold nanoparticles (shared in “2.4.1”) was calculated by considering reduction of all the  $\text{Au}^{3+}$  to gold nanoparticles.

### 2.3.2 Synthesis of silica particle

The Stöber method<sup>219</sup>, a widely recognized approach, involves the controlled hydrolysis and condensation of silicate precursors to produce monodisperse silica particles (Figure 52). The protocol from Marta Ibisate Muñoz thesis<sup>194</sup> (based on Stöber method<sup>219</sup>) was followed for the synthesis of Silica particle (SP). Preliminary experiments were done in collaboration with Miguel Comesana-Hermo at ITODYS.

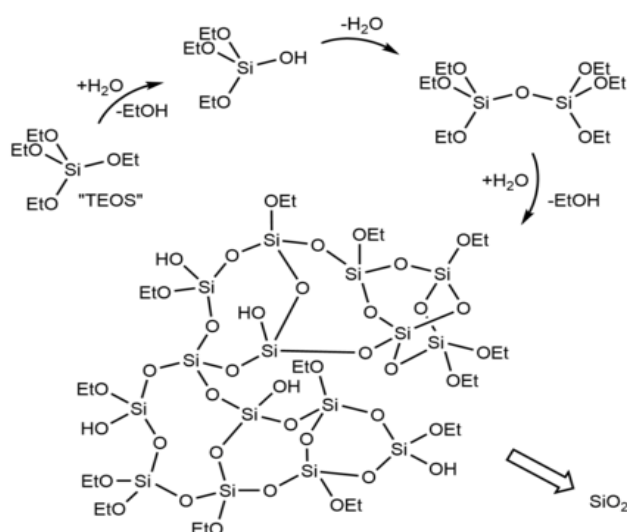


Figure 52: Stöber Method mechanism for synthesis of Silica particles ( $\text{SiO}_2$ ); from hydrolysis and condensation of TEOS. Image extracted from Echesky, et al., 2023.<sup>223</sup>

Muñoz has investigated the variations of different parameters (reaction vessel specifications, temperature control, and reaction time) to achieve reproducibility and control over the size and morphology of the synthesized silica particles, systematically. Following Muñoz work<sup>224</sup>, mixture of Ammonia, TEOS and Water (in a predefined proportion 1.5M:0.25M:24M, respectively; for avg. dia.  $\sim 484$  nm) was added into EtOH in a glass flask, followed by continuous stirring (2 h) at low RPM (40-45). Later, SP were collected by washing any residual ammonia and TEOS in the mixture via centrifugation. The details of SP synthesis are shares in the following paragraphs (and summarized in Figure 53).

1. For a 50 mL stock preparation of SP, 20.5 mL EtOH was taken in 50 mL beaker.
2. Added 21.6 mL (24 M) miliQ water to EtOH and stirred magnetically at 50 RPM for 1 min
- 5.1 mL (1.5 M)  $\text{NH}_4\text{OH}$  was mixed in the water-ethanol mixture at 50 RPM for 2 min.

## Particle Production

3. Lastly, 2.8 mL (0.25 M) TEOS was mixed magnetically in water-ethanol-ammonia mixture at 45 RPM for 2 hr. After ~1 min the solution gradually turned milky in appearance.
4. After 2 hours of magnetic-stirring, the mixture was transferred into polypropylene falcon tubes of (40 mL volume) and centrifuged at ~12600 RCF (7500 RPM) for 15 min.
5. Collected pellet was re-dispersed into 40 mL EtOH and centrifuged again in order to eliminate all the residual ammonia and TEOS. This washing step was performed three times before final collection and storage.
6. The resulting SP were re-dispersed into 30 mL EtOH and stored in refrigerator.

To obtain an approximate value of the concentration of silica particle, 100  $\mu\text{L}$  of the SP suspension was taken into a small plastic tray (dimension 3 x 3 x 0.5 cm (length, breadth, and height)), dried in oven (50  $^{\circ}\text{C}$ ) and weighed (before and after drying). For characterization of size distribution of synthesized SP, DLS (giving hydrodynamic size) and SEM (absolute size) was used. Sample (SP in EtOH) was diluted in water by a factor of 1000 (1  $\mu\text{L}$  SP + 999  $\mu\text{L}$  water) for the DLS observation. Particle size was measured from SEM observations for 50 SP.

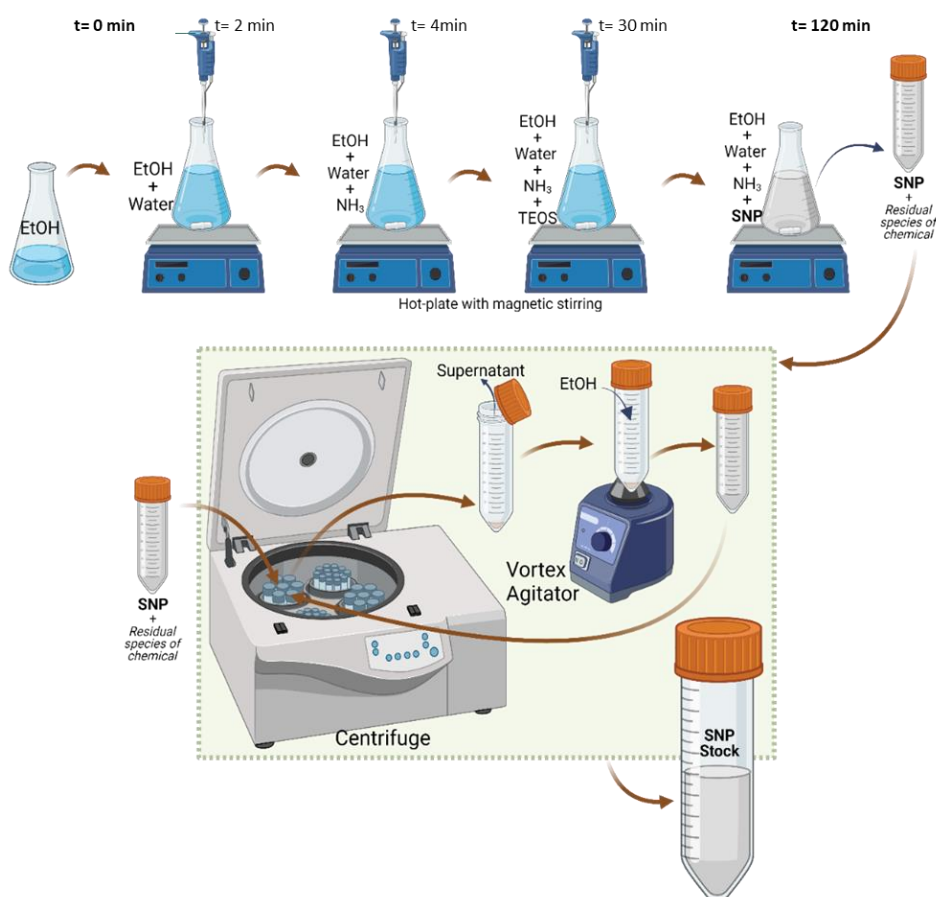


Figure 53: Scheme of Silica particle (SP) synthesis and washing steps. Starting with a pre-calculated volume of MilliQ water and ethanol (EtOH) with step-wise addition of precursor molecules. After 2-3 minutes of addition of TEOS, the mixture starts turning milky with the formation of SP and finally after 2 hours excessive chemicals are washed from centrifugation. In the washing step (highlighted with green background), for the part of re-centrifugation, it is made sure that the pellet (SP) is well re-dispersed in the solvent (EtOH) by mixing it via vortex mixer before each centrifugation cycle.

### 2.3.3 Synthesis of Janus AuNPs/Silica particles

The protocol for synthesizing Janus Particle of Gold/Silica was carried out via the method of Pickering emulsion (see 1.5.1.2.2, Chapter 1), where initially, colloidosomes were produced (by quenching the Pickering emulsion made from silica particles and wax), followed by functionalization of the SP embedded at the surface of the solidified wax droplets with gold nanoparticles (Figure 54). Some variations could be possible amongst different batches (aggregates in some batches).

The process is summarized in Figure 54. First, the sub-unit “2.3.3.1” describes the colloidosomes production and secondly, the sub-unit “2.3.3.2” describes the procedures for the functionalization.

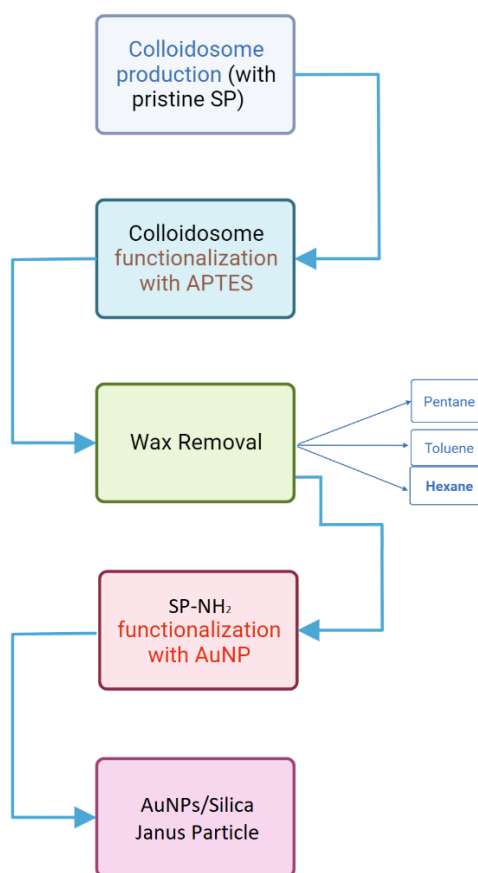


Figure 54: Summary flowcharts of strategy used for Janus Particle Synthesis via Pickering Emulsion Method.

#### 2.3.3.1 Synthesis of Colloidosomes

The synthesis of Colloidosomes was adapted and optimized from Avossa et al<sup>225</sup> procedure and previous literature on the subject.<sup>226–228</sup> The optimized protocol is described in the following paragraph:

1. In a 25 mL borosilicate glass beaker, 20 mL Milli-Q water and 2.5 mL of SP suspension (at 7.4 mg/mL concentration corresponding to 0.09 m<sup>2</sup> total surface area SP) were added. The suspension was placed in an ultrasonic bath<sup>229</sup> (continuous pulse of 37 Hz at 60 – 70 % power) for 10 min to ensure the dispersion of the SP.

2. The above suspension (Water and SP) was heated to 50 °C before addition of 2.5 mL of CTAB (0.02 mM) aqueous solution followed by magnetic stirring at ~11 RCF (1000 RPM) for 30 min.
3. The mixture (Water+SP+CTAB) was heated to 75°C and 1.6 g of pre-melted wax (0.8/10 weight of water) was added and let under 2 minutes Ultra-turrax mixing at ~606 RCF (9500 RPM) to get Pickering Emulsion (Figure 55. A).
4. The emulsion was quenched in 80 mL cold water (pre-cooled water in an ice bath) for ~2 min (Figure 55. B).
5. Quenched emulsion was filtered via a Buchner funnel set with a Whatman 1 filter paper.
6. The obtained solid residue was rinsed with ~150 mL Milli-Q water, followed by drying at room temperature, under safety fume cupboard for two days.

The dry powder of solid residues (Figure 55. C) was characterized via SEM to verify the colloidosome structure (solidified wax droplets with partially embedded SP onto it), see “2.4.4.1”.

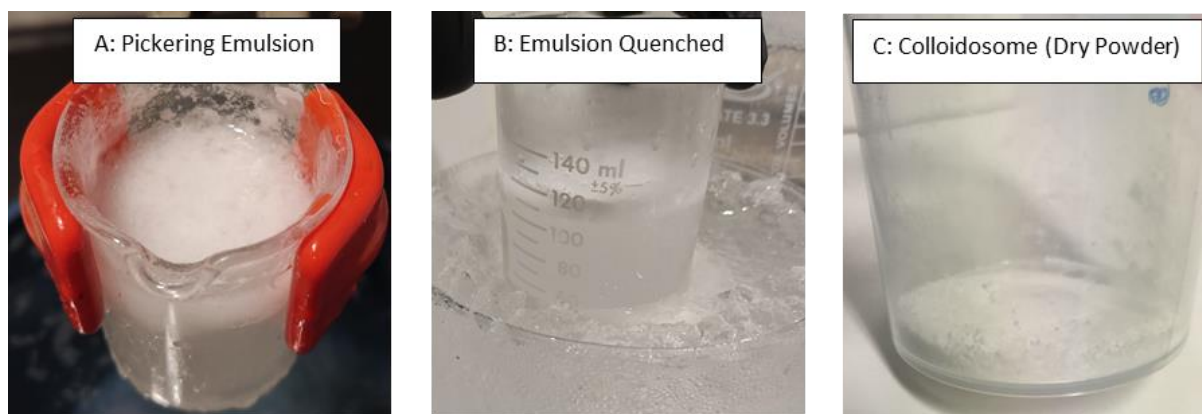


Figure 55: Pickering Emulsion right after formulation process (A), after quenching in water cooled from ice-bath (B), Dry Colloidosomes appearing like a white powder (C), after filtering Pickering Emulsion and drying at room temperature.

### 2.3.3.2 Functionalization of Colloidosome

To get Gold/Silica Janus Particle (JP) from Colloidosomes, the exposed surface of SP (not embedded in the wax) should be functionalized with a linker molecule. A total of three linker molecules were tested; APTES ((3-Aminopropyl) triethoxysilane), PLL (Poly-L-Lysine) and PAH (Poly(allylamine hydrochloride)) before finalization of the chosen linker molecule to proceed with. It was found that APTES ligand was the best to produce Janus particles (SEM characterization particles from APTES functionalization shared in “2.4.3”, confirmed this). So, only the protocol with APTES is described in this paragraph (the protocol with PLL and PAH are given in annex). As well studied,<sup>230–233</sup> SP surface functionalization via APTES is done in organic solvent (toluene being one of the common one), where APTES is grafted on SP surface through reaction with the triethoxysilane group. In our case, the SP to be functionalized are at the surface of the Colloidosomes (SP are partially embedded in the solidified wax droplets from Pickering emulsion). The use of toluene as solvent for SP functionalization with APTES is not a feasible option, as toluene is known for its good solubilization properties for wax.<sup>234–236</sup> Therefore, the SP functionalization with APTES was followed as per the description by Cuoq et al.<sup>231</sup>; using 7% ethanol mixture (EtOH/Water (7% v/v)) as solvent instead of the classically used toluene (Figure 56).<sup>232</sup>

## Particle Production

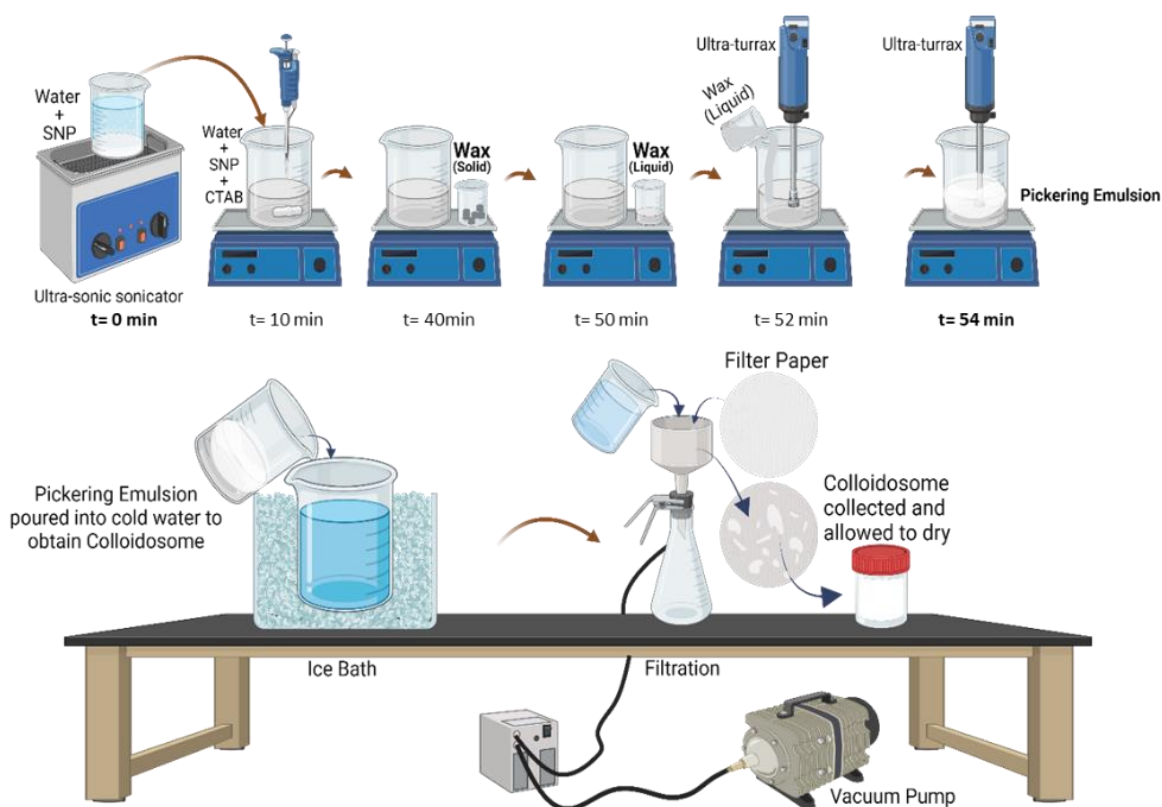


Figure 56: Schematic representation of making Pickering Emulsion (left to right). Silica particle (SP) suspension and water mixture is given 10 minute under ultra-sonication followed by heating to 50 °C before adding CTAB. In parallel, wax is melted to liquid and water is cooled under ice-bath. After 30 minutes of magnetic stirring of CTAB+SP+Water mixture, melted wax is added and mixed instantly at 9500 RPM using an Ultra-turrax, giving resultant Pickering Emulsion. Emulsion was quenched (to solidify the wax droplets in Colloidosomes) and colloidosome were separated by filtering (Buchner Filter) and water-rinsing. Solidified residues of Colloidosomes are dried and stored.

The APTES-functionalized silica particle surface offers amino groups ( $-NH_2$ ) that are available for subsequent reactions. This step allows for tailoring the surface properties of the silica particles based on the specific application requirements.<sup>230,232,237,238</sup> Here, the protocol used to functionalize SP with APTES was achieved by following the steps shared in “2.3.3.2.1” from point 1 to point 8 (Figure 57) in the succeeding paragraph, and further functionalization with gold nanoparticles, following point 10 to 13 (Figure 58).

### 2.3.3.2.1 Procedure

1. 7% (v/v) Ethanol/Water mixture was prepared from 7 mL EtOH and 93 mL miliQ water.
2. 50 mL EtOH/H<sub>2</sub>O (7% v/v) solution (from step 1) was taken in a Teflon jar, followed by addition of 0.5 g of Colloidosomes.
3. Teflon jar was put on vortex mixer to disperse the Colloidosomes with EtOH/H<sub>2</sub>O mixture, followed by the addition of an excessive quantity (0.2 mL) of APTES. Excessive quantity of APTES is chosen to obtain an assured concentration of 15 APTES nm<sup>-2</sup>.<sup>237</sup>
4. The Teflon jar was placed on a rotatory agitator at 50 rpm for a duration of 18 hours.
5. Suspension was filtered from a Buchner funnel with a Whatman filter-1 paper and subsequent washing with ethanol to eliminate excess APTES.

6. Wax was removed from Colloidosomes to obtain functionalized silica particles by adding to the filter-residue approximately 40 mL of hexane in a polypropylene centrifuge tube of 50 mL capacity and letting the tube to ultrasonic sonication<sup>229</sup> at 37 kHz with 60% power, for 30 minutes with a final vortex-mixing immediately afterward.
7. The nanoparticles were washed via two cycles of centrifugation at  $\sim 11000$  RCF (7000 RPM) for 15 minutes each. Hexane was replaced with ethanol after the second centrifugation, followed by re-dispersion of APTES functionalized SP in ethanol.
8. After another centrifugation at  $\sim 11000$  RCF (7000 RPM) for 15 minutes, removal of the supernatant with EtOH was done, followed by single washing with water.
9. Lastly, the obtained (clean) silica particles were partially functionalized with APTES ( $\text{NH}_2$ -SP) were re-dispersed into approximately 10 mL water and stored in refrigerator at  $6^\circ\text{C}$ . Characterization of these particles using Dynamic Light Scattering (DLS) and Scanning Electron Microscopy (SEM) was done within five days since synthesis.
10. For the functionalization of silica particles (with gold nanoparticles), approximately 5 mL of the SP- $\text{NH}_2$  suspension were transferred into a Falcon tube and kept under ultra-sonic bath for 1-2 minutes for well dispersion of particles.
11. SP- $\text{NH}_2$  suspension was placed under ultra-sonication bath (allowing proper interaction of gold nanoparticles with well-suspended functionalized silica particle<sup>229</sup>) with gradual addition of 1 mL AuNPs suspension (from "2.3.1") (AuNP concentration in suspension is shared in "2.4.1").
12. The AuNPs and SP- $\text{NH}_2$ s were then mixed on rotatory agitator at 50 rpm for 10 hours.
13. The AuNPs in excess were removed by centrifugation at  $\sim 1400$  RCF (2500 RPM) for 15 minutes and suspended in 5 mL of water. The washing steps were repeated twice, reducing the pink appearance of the supernatant solution (indicative of excess AuNPs).

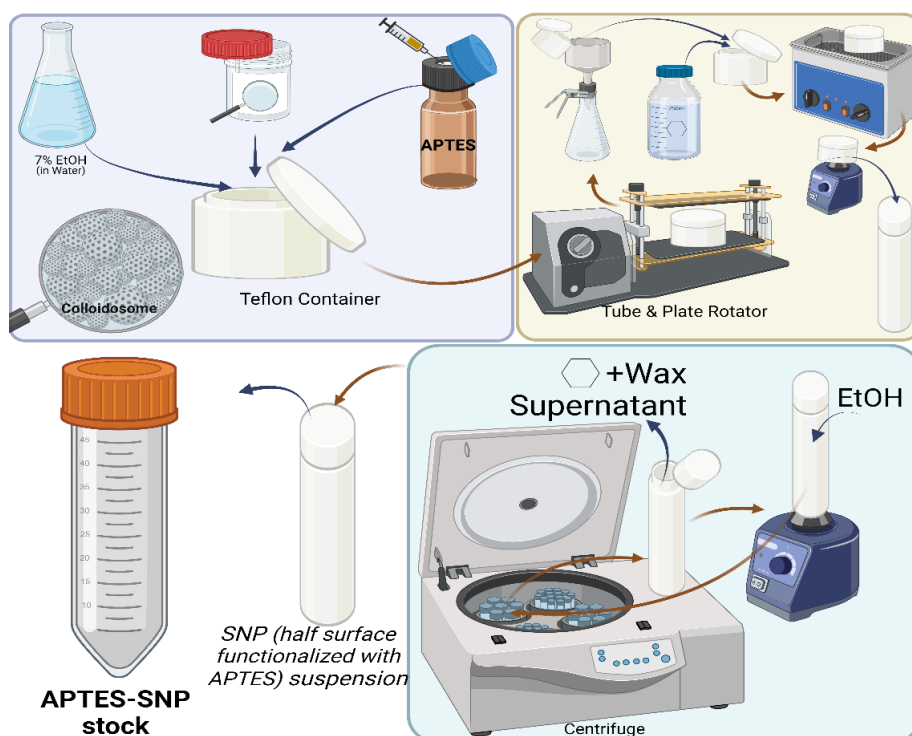


Figure 57: Scheme for Colloidosomes functionalization with APTES in water/ethanol mixture at 7% (v/v) of ethanol (in a Teflon container) and washing off wax with hexane, with further cleaning of APTES functionalized (partial) Silica particle ( $\text{NH}_2$ -SP) via centrifugation. Teflon container is placed in ultra-sonic bath and vortex-mixing for wax dissolution, before centrifugation.

## Particle Production

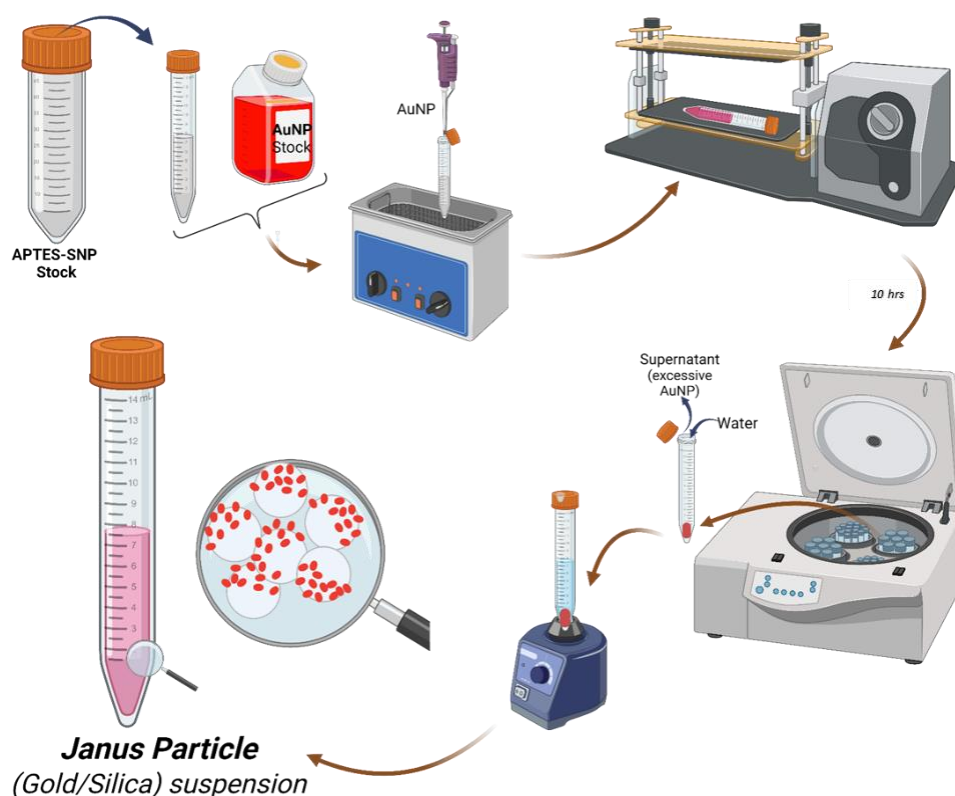


Figure 58: Scheme of functionalization of APTES functionalized (partially) silica particle ( $SP-NH_2$ ) with gold nanoparticles to obtain AuNPs/Silica Janus Particles. A pre-calculated volume of  $SP-NH_2$  is taken into a polypropylene centrifuge tube and placed in an ultra-sonication bath. Suspension of AuNPs is added gradually to the  $SP-NH_2$  suspension (while keeping the tube in ultra-sonication bath), followed by 10 hours mixing at a rotatory agitator. Lastly, excessive AuNPs is eliminated by centrifugation for 15 minutes at 2500 RPM. Depending upon the colour of supernatant (pink/pinkish colour indicates the presence of free gold nanoparticles), the step of centrifugation is done thrice with lastly re-dispersing the pellet; AuNPs/Silica Janus Particle (JP) is done in Milli-Q water.

There were some variations in synthesized Janus particles from one batch to another (with some aggregates in some of the batches). We eliminated those batches, but still there could be a possibility of the presence of some aggregates in the batch used in our study.

### 2.3.4 Synthesis of Isotropic AuNPs/Silica Particles

To synthesize isotropic gold/silica particle, surface functionalization of SP involved the same steps as for Janus case for grafting APTES on the silica particles<sup>231,237</sup>; dispersion of SP in 7% ethanol mixture (EtOH/Water (7% v/v)) followed by APTES in excessive quantity for an 18 hours interaction period. Therefore, the procedure of SP functionalization with APTES was followed as per the description by Cuoq et al.<sup>231</sup> using EtOH/Water (7% v/v) as the solvent instead of the classically used toluene.<sup>232</sup>

1. A mixture of 7% (v/v) Ethanol/Water was prepared by addition of 7 mL EtOH to 93 mL milliQ water.
2. 50 mL EtOH/H<sub>2</sub>O (7% v/v) solution (from step 1) was taken in a polypropylene tube, followed by addition of 0.5 mL SP from stock solution mixed via vortex mixer. An important point before the addition of SP to EtOH/H<sub>2</sub>O (7% v/v) solution was to re-disperse SP well, for this purpose SP stock solution was kept for a 10 min ultrasonic sonication at 37 Hz and 60% power.

3. Excessive quantity of APTES (1 mL) was added to the suspension of SP- EtOH/H<sub>2</sub>O (7% v/v) and placed on a rotatory agitator at 50 rpm for a duration of 18 hours. This excessive quantity of APTES is to obtain an assured concentration of 15 APTES nm<sup>-2</sup>.
4. After 18 hours of mixing, excessive APTES was washed and surface functionalized APTES-SP were extracted for functionalization with gold nanoparticles. The washing was achieved through centrifugation at ~11000 RCF (7000 RPM) for 15 minutes, re-dispersion of collected pellet (APTES functionalized SPs) in 50 mL EtOH and repeating the centrifugation at ~11000 RCF (7000 RPM) for 15 minutes.
5. A last centrifugation stage (third round) was done by re-dispersing the collected pellet into water and centrifuging it at ~11000 RCF (7000 rpm) for 15 minutes.
6. The obtained (clean) silica particles functionalized with APTES (SP-NH<sub>2</sub>) were re-dispersed into approximately 10 mL water. For characterization purpose, storage of sample was done in the chemistry laboratory refrigerator at 6°C.
7. For the functionalization of SP-NH<sub>2</sub> particles (with gold nanoparticle), approximately 5 mL of the SP-NH<sub>2</sub> suspension were transferred into a Falcon tube and kept under ultra-sonic bath for 1-2 minutes for well dispersion of particles.
8. While the SP-NH<sub>2</sub> suspension was under ultra-sonication bath, 1 mL gold nanoparticle suspension was gradually added to it; allowing proper interaction for gold nanoparticles with functionalized silica particle.
9. Once gold nanoparticle suspension was added to the SP-NH<sub>2</sub> suspension, the Falcon tube was put on a rotatory agitator at 50 rpm for a duration of 10 hours. After 10 hours of mixing on rotatory agitator, Gold functionalized isotropic Gold/Silica Particles were cleaned by removing free/excessive gold nanoparticle (Figure 59).
10. Removal of excessive gold nanoparticles was achieved by centrifugation of the suspension at ~1400 RCF (2500 RPM) for 15 minutes duration, eliminating suspension and adding 5 mL water, followed by redoing the centrifugation twice. A pink color solution (supernatant) suggested an excess of gold nanoparticle, thus, repetition of centrifugation step was crucial. Sample storage for characterization purpose was done in a chemistry laboratory refrigerator.

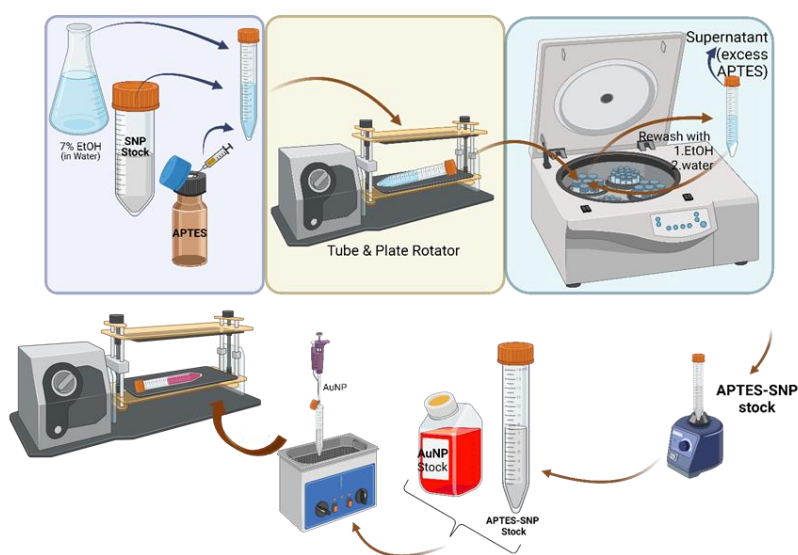


Figure 59: Scheme of synthesis of Isotropic gold/Silica Particles; starting with dispersion of silica particle (SP) in water/ethanol at 7% (v/v) Ethanol (EtOH) (in a polypropylene centrifuge tube) followed by the addition of APTES, the suspension is fixed on



*a rotatory agitator for 18 hours. Further, suspension is washed via centrifugation, to eliminate excessive APTES (in EtOH and Milli-Q water). Collected pellet (APTES functionalized SP; APTES-SP) is further re-dispersed in Milli-Q water in an ultrasonic bath followed after approximately 2 minutes, by the gradual addition of gold nanoparticle suspension and interaction on agitator for 18 hrs before final washing by centrifugation cycles.*

There were some variations in synthesized Janus particles from one batch to another (with some aggregates in some of the batches). We eliminated those batches, but still there could be the possibility of the presence of some aggregates in the batch used further in this study.

### 2.3.5 Janus Gold/Silica Particle via Physical Vapour Deposition

Physical vapour deposition (PVD) is a surface coating technique that involves vaporization of material at atomic level. PVD comprises of a high-energy source (electron beam or ions from a plasma), that evaporates the target; material to be deposited. The vapour of target material is deposited onto the substrate surface. The used PVD set-up (PLASSYS) was a thermal evaporation deposition system, based on Joule heating of Tungsten crucible comprising the metal to be evaporated. In presence of Argon gas, the substrate (glass slide) having a monolayer of silica particle (SPs) was placed in the apparatus and the metal was deposited physically. SP monolayer was obtained by spin coating SP onto a glass slide. Prior to spin coating SP, oxygen plasma treatment of the glass slide was done. In addition to removing organic, inorganic and microbial contaminants, plasma treatment makes the glass surface hydrophilic and thus improves wettability, which supports better spin coating<sup>239,240</sup>. The gold layer was attached on silica thanks to a chromium under-layer (see figure 44).<sup>241,242</sup> The details of the protocol followed for the production of Gold/Silica Janus particle via physical vapour deposition method are shared in the following paragraph and summarized in Figure 61.

1. A glass slide (substrate) was cleaned under plasma treatment with oxygen following an optimized protocol recipe (1 minute plasma under 50W power and 7.86 e-1 torr Pressure)
2. The substrate was placed in the centre of a spin coater and after proper alignment temporarily localized it via vacuum.
3. 200  $\mu$ L Silica particle (SP) suspension was poured in the centre of substrate, followed by shutting the lid of spin-coater running the program : 500 RPM for 10 sec, followed by 3400 RPM for 30 sec, resulting in a monolayer dispersion of SPs on glass substrate (see Figure 72 in Results), ready for surface modification via vapour deposition.
4. The glass substrate having monolayer of SP was placed into physical vapour deposition device at  $10^{-6}$  mbar pressure and 100 – 140 A current running through the crucible (for the purpose of sublimation or melting the metal).
5. 0.5 nm thick chromium layer was deposited at the rate of 0.5 angstrom/second, followed by 20 nm thick gold layer deposition from top at 1.6 to 1.9 angstrom/second deposition<sup>243,244</sup> (Figure 60). The deposition rate was measured using a quartz crystal microbalance placed at the same distance from the crucible as the sample.
6. The PVD Janus particles (PVD-JP) were extracted from ultrasonic procedure, the glass slide was placed into a petri dish with 10 mL MilliQ water and let under ultra-sonic bath<sup>229</sup> for 30 min at 37 Hz and 100% power.

## Particle Production

7. After ultrasonication, the water from petri dish; with PVD-JP (detached from the glass slide) were collected into a polypropylene centrifuge tube and were centrifuges at  $\sim 8064$  RCF (6000 RPM) for 15 min.
8. After discarding of the supernatant, the pellet of PVD-JP was re-dispersed in 1 mL miliQ water. For the characterization of PVD-JP, SEM was utilized.

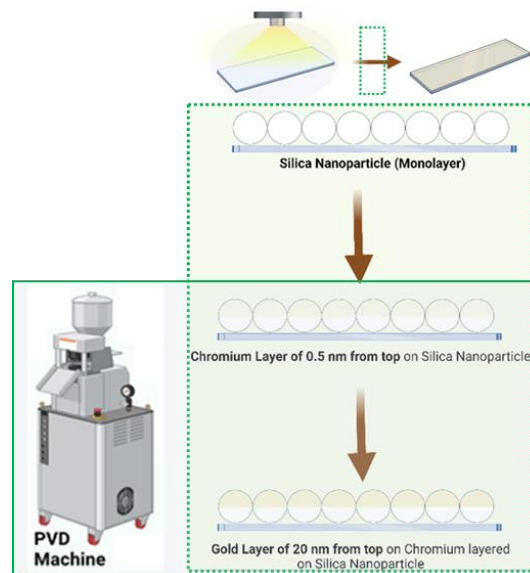


Figure 60: Scheme followed for the production of Gold/Silica Janus Particle via Physical Vapour Deposition method. Gold is deposited onto silica surface in second step, after a thin layer deposition (0.5 nm) of Chromium.

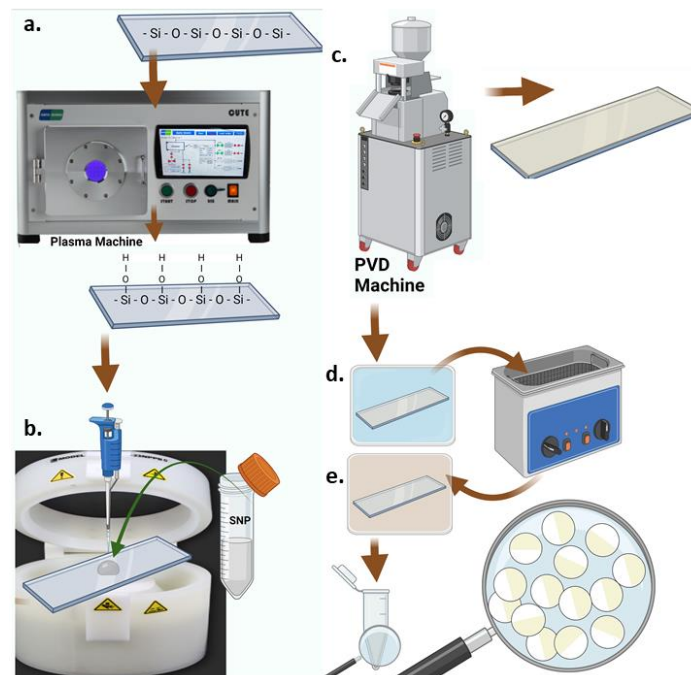


Figure 61: General scheme of steps followed for Gold/Silica Janus article production following Physical Vapour Deposition method. a. to c. shows plasma cleaning of glass substrate and spin coating Silica particle (SP) onto it, followed by coating Gold via physical vapour deposition on SP (c), and lastly extracting Gold/Silica Janus particle by ultra-sonic bath (d and e).

Table 5 briefly highlights the synthesis of particles, the methods followed and the learning outcomes as important factors for respective synthesis, covered in the section “2.3”.

Table 5: Summary of key factors in the methods followed for synthesising particles and their respective mean diameter.

Particle	Method	Important Factors
AuNP $\phi\sim 25\text{nm}$	Reverse Turkevich	Temperature, gold/citrate ratio, citrate concentration
SP $\phi\sim 475\text{nm}$	Stöber	Precursors Mixing Rate, TEOS/EtOH/H <sub>2</sub> O ratios
ISO $\phi\sim 478\text{nm}$	Surface functionalization (chemical)	<ol style="list-style-type: none"> <li>1. APTES functionalization and AuNPs concentration</li> <li>2. Interaction time (for both steps; with APTES and AuNPs)</li> <li>3. Colloidal stability</li> </ol>
JP $\phi\sim 470\text{nm}$	Pickering Emulsion And surface functionalization (chemically)	<ol style="list-style-type: none"> <li>1. SP: CTAB molar ratio (for Colloidosome preparation), SP: Water mass ratio (for SP functionalization with APTES) and SP: Wax: Water mass proportion (for Pickering emulsion production)</li> <li>2. Energy required for emulsification (Pickering Emulsion)</li> <li>3. Emulsion quenching (in ice-cooled water for 1 min)</li> <li>4. Wax solvent</li> </ol>
PVD-JP $\phi\sim 480\text{nm}$	Physical Vapor Deposition	<ol style="list-style-type: none"> <li>1. Monolayer assembly of SP</li> <li>2. Intermediate adhesion layer between SP and Gold.</li> </ol>

Particle size (for particles with gold nano particles and layer) shared in Table 5 is the mean average from SEM observation (share in result section), unlike the maximum size which is obtained by adding the diameter of gold nanoparticles in the diameter of silica particles.

### 2.3.6 Characterization techniques

#### 2.3.6.1 UV-vis Spectroscopy:

Spectrophotometer utilized in this work is a double monochromator UV-2550 from Shimadzu. 0.35 mL volume of samples were prepared (in 1 mm path length quartz cuvette) at  $\sim 4.3\%_{v/v}$  concentration in Milli-Q Water for measurements (see Figure 62 for general working principle). Throughout UV-Vis experiments, dispersant, blanks, and reference samples were Milli-Q water. For gold nanoparticles and chemically modified particles, Surface Plasmon Resonance (SPR) peak of gold nanoparticles was followed. SPR is a characteristic optical property that arises from the collective oscillation of conduction electrons on the surface upon projection of incident light (Figure 63). This collective motion

creates a strong absorption band at a specific wavelength in UV-Vis. spectrum, typically appearing as a peak  $\sim 520$ - $550$  nm for spherical gold nanoparticles in function of their size (from 10 to 100 nm).<sup>245,246</sup>

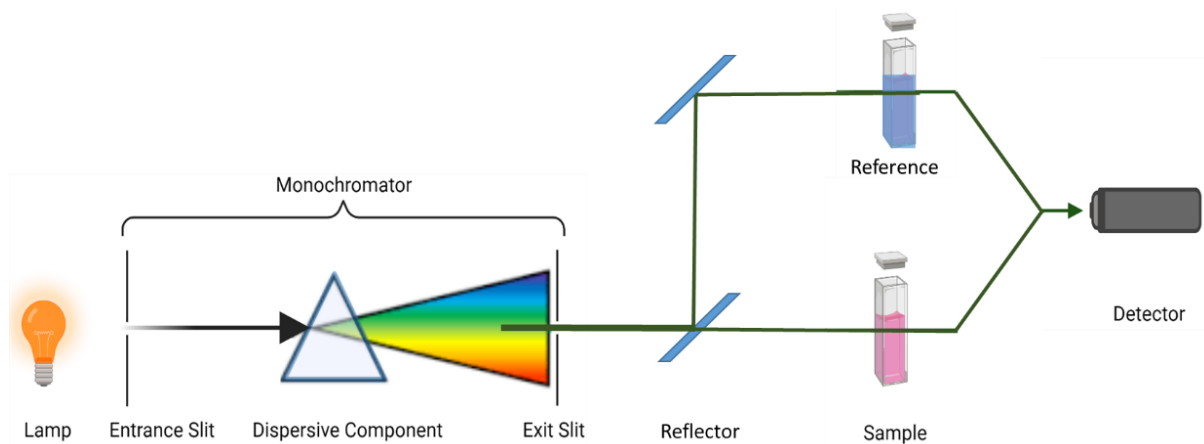


Figure 62: Schematic of a simple UV-Vis spectroscopy: Light enters the monochromator with selectively set-up wavelength of light interaction with the sample, followed by detection with the detector for output results.

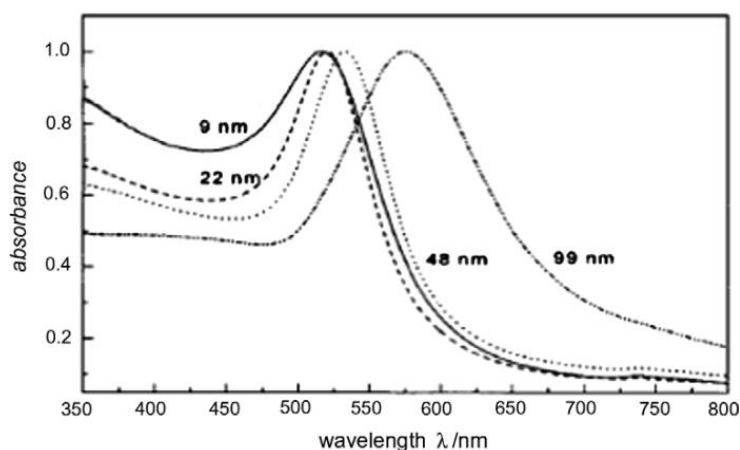


Figure 63: Surface Plasmon Resonance peak for gold nanoparticles of different size showing SPR peak at around 520 nm for particles of diameter 9, 22 and 48 nm. Image extracted from Huang et al., 2010.<sup>247</sup>

### 2.3.6.2 Dynamic light scattering (DLS) and zeta potential

A Zetasizer Nano Series Nano from Malvern Panalytical was utilized for the DLS measurements.<sup>248</sup> For measurements, once sample was prepared and loaded into DLS instrument, Standard Operating Procedure (SOP) was selected. SOP used for our DLS measurement had detector at backscatter angle of  $173^\circ$  (NIBS default), system set to  $25^\circ$  C, and equilibration time as 2 minutes. Other criteria defined in the SOP were refractive index (1.33) and viscosity (0.89 mPa.s) of water at  $25^\circ$  C. The wavelength of incident beam in this DLS instrument is 633 nm. While the particles were dispersed in water for all the sample, three experimental iterations were followed to ensure result-reproducibility (general working principle in Figure 64). Optimal range of concentration in this study was established through experimental means, involving a series of dilutions aimed at achieving measurement of particle size

independent of concentration. In this study, the mean count rates of scattered lights from the samples for optimal dilution ranged from 160 to 480 kcps. As the particles were freshly prepared before DLS measurement, aggregation from sample-aging was non-concerning, therefore filtration was avoided to limit the loss of particles and DLS samples were prepared by diluting particles directly from the stock solutions. To mitigate the risk of dust contamination for the DLS experiments, plastic container used for storing dispersing medium (mili-Q water) was rinsed with Milli-Q water thrice and changed for each set of experiment. This precautionary measure ensured the integrity of the experimental setup and minimized the impact of external contaminants on the DLS measurements.<sup>97,249–251</sup>

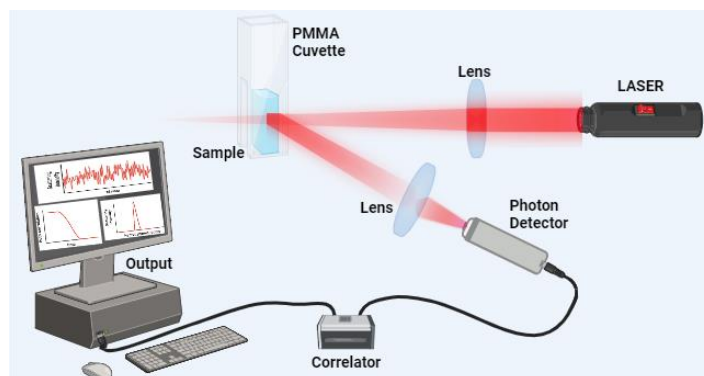


Figure 64: Scheme of Dynamic Light Scattering (DLS); speckle observation due to scattered photons observed from dynamic particles interacting with incident LASER beam. Correlator giving the autocorrelation of fluctuating scattered photons.

### 2.3.6.3 Scanning electron microscopy & Energy Dispersive X-ray spectroscopy (SEM/EDX):

The SEM microscope utilized in this thesis is ZEISS Ultra 55 (Figure 65) equipped with a field emission gun (FEG), coupled with a Bruker EDX (Energy Dispersive X-ray Spectrometry) chemical analysis. Depending upon the resolution requirement, the material accelerating voltage (EHT; Electron High Tension) was maintained between 1.5 kV and 10kV. For example, higher density sample (gold) would require higher EHT than a low density sample (wax). The observations were made either on carbon tape (for Colloidosomes) or silicon wafer (for particles) to allow charge dissipation.



Figure 65: Scanning Electron Microscope set-up (left) besides its display set-up (right) at LEDNA facility, CEA Saclay

Colloidosomes (which are too large to evacuate the charges efficiently) samples were metallized with 20 nm gold layer via physical vapor deposition. Silicon wafer was used especially for well spreading of samples aiding better surface-view of particles. SEM sample preparation involved 1  $\mu\text{L}$  particle suspension (after 15 minutes ultrasonic bath) spread on silicon wafer and dried well. Before dispersing particle suspension onto wafers, it was cleaned with isopropanol and UV/ozone (UVO-Cleaner Model 18, from Jelight) for 45 seconds. The UV-O cleaning method has been demonstrated as a highly efficient approach for swiftly eliminating diverse contaminants from surfaces.<sup>252</sup>

## 2.4 Result and Discussion

### 2.4.1 Gold Nanoparticles

Gold nanoparticles (AuNPs) have a central core of gold atoms organized in a face centered cubic structure, surrounded by a protective organic layer (Figure 66).<sup>253</sup> The ligand shell ensures the colloidal stability of the suspension. The nature of the ligand participates with the other parameters (reducing agent, reactant concentration, ratios between each reactants) to a control over the final properties of the gold nanoparticles (size, shape, surface chemistry). The well-known Turkevich method involves the reduction of gold ions ( $\text{HAuCl}_4$ ) through a reducing agent (citrate ions), which also play the role of a stabilizing agent of the AuNPs through electrostatic stabilization.

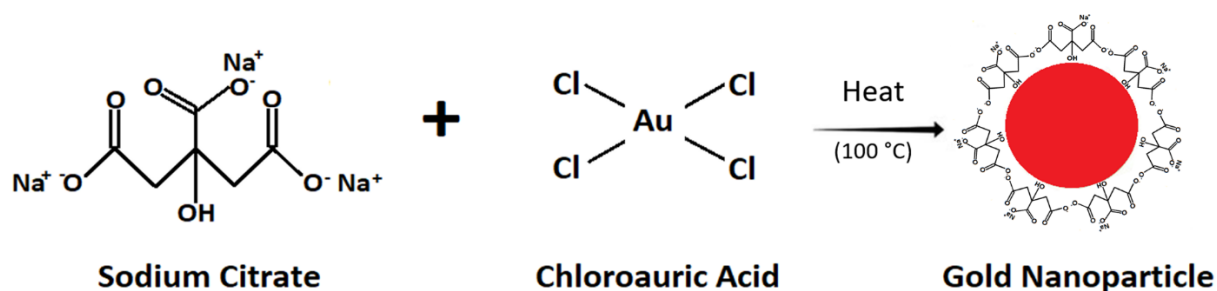


Figure 66: Sodium citrate reacting with chloroauric acid producing Gold Nanoparticle (reverse Turkevich method).

Sivaraman<sup>222</sup> showed that by reversing the sequence of precursors for a given citrate to chloric acid molar ratio ( $\text{MR} > 5$  for 5.2mM of final citrate concentration), particles with size inferior to 10 nm could be produced, which is a consequence of counter balanced pH dependent redox reactivity of citrate and chloroauric species for a given temperature. This strategy is however dependent on the citrate concentration. In our case, the synthesis have been performed with 1.36mM of citrate leading to nanoparticles size around 18 nm and 25 nm (batch 1 and 2, respectively). The suspensions were characterized by a typical localized surface plasmon resonance (LSPR) peak at  $\sim 520$  nm in the UV-Vis spectra (Figure 67) and an absorbance value of 0.029 and 0.038, respectively at 400 nm (sample diluted at  $\sim 4.3\%_{\text{v/v}}$  for the UV-Vis analysis). This value at 400 nm can be related to the total gold atoms. Polte et al<sup>254</sup> have found an extinction coefficient between 2.63 and 2.68  $\text{Lmmol}^{-1}\text{cm}^{-1}$  for 20 to 28 nm size AuNPs stabilized by citrate and issued from Turkevich synthesis.<sup>254</sup> In our case, the absorbance at 400 nm served for comparison of different synthesis (Table 6).

Values for plasmon peak and absorbance at 400 nm and corresponding Au(0) concentrations are summarized in Table 6. These values demonstrate that the reduction of gold was not complete for the different batches and the synthesis of AuNP lacked reproducibility.

DLS can be used for characterization of particle size distribution. The smooth baseline in a typical DLS correlogram (presented in in Figure 68. A) is the characteristic of mono-dispersity of particles i.e. no large aggregates are in coexistence. Two batches of AuNP were synthesized and their size distribution were extracted from the DLS correlogram (shown on one example in Figure 68. B). The hydrodynamic diameter and polydispersity index (PDI) for two batches of AuNPs summarized in Table 6 showed average diameter of ~18 nm and ~28 nm with a polydispersity ranging from 0.25 and 0.09, respectively.

The lack of reproducibility in the sizes of AuNP comes from the variation in temperature of the added gold solution; initially at room temperature and the absence of control of the mixing rate during addition. The plasmon peak position is slightly influenced by the nanoparticle size in agreement with the literature data.<sup>198,220,255</sup> For the following parts, the AuNPs for the synthesis of isotropic gold/silica particles and chemically synthesized gold/silica Janus particles are from the batch with higher monodispersity; second batch. SEM observation of particles with AuNPs-batch 2 showed mean diameter of AuNPs as ~25 nm (Figure 154).<sup>257</sup> This value was obtained via manual assessment of SEM images on ImageJ platform.

The concentration of AuNPs in number of particles/L can be estimated from the density of gold and the size of the NPs following the equation 1, taking as a first approximation the initial gold concentration.

$$N = \frac{V(Au(0)) (total)}{V(part)} = [Au(0)] * \frac{6}{\pi} \cdot \frac{M}{\rho D^3} \quad \text{Eq. 1}$$

With [Au(0)] the initial concentration in mol/L,  $\rho = 19.3 \text{ g/cm}^3$  the volumetric mass of gold,  $M = 196.96 \text{ g/mol}$  the molar mass of gold and  $D$  the diameter in cm of the gold nanoparticles. The concentration issued from UV-Vis analysis at 400 nm gave an estimation of the concentration in Au(0).

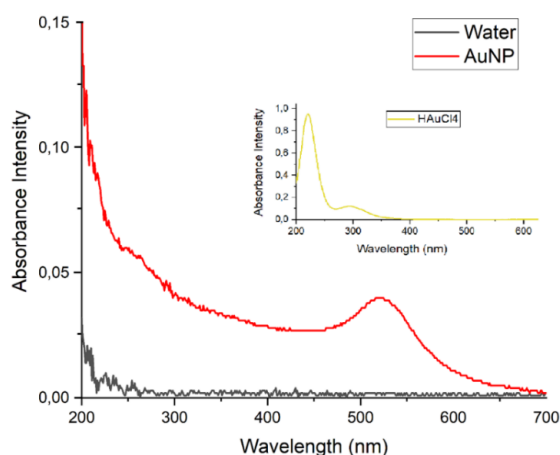


Figure 67: SPR at ~520 nm for gold Nanoparticle (Red) from UV-Vis (comparison from HAuCl<sub>4</sub> peaks in yellow spectrum) in 1mm path-length Helmma quartz cell.

It clearly showed that only a fraction of the gold salt have been reduced to Au(0). Since the extinction coefficient depends on size and environment of the AuNPs,<sup>254</sup> SAXS analysis could be performed to extract the precise density numbers,<sup>256</sup> however, the analysis was not performed in this study. The values for two batched of AuNPs are indicated in the Table 6.

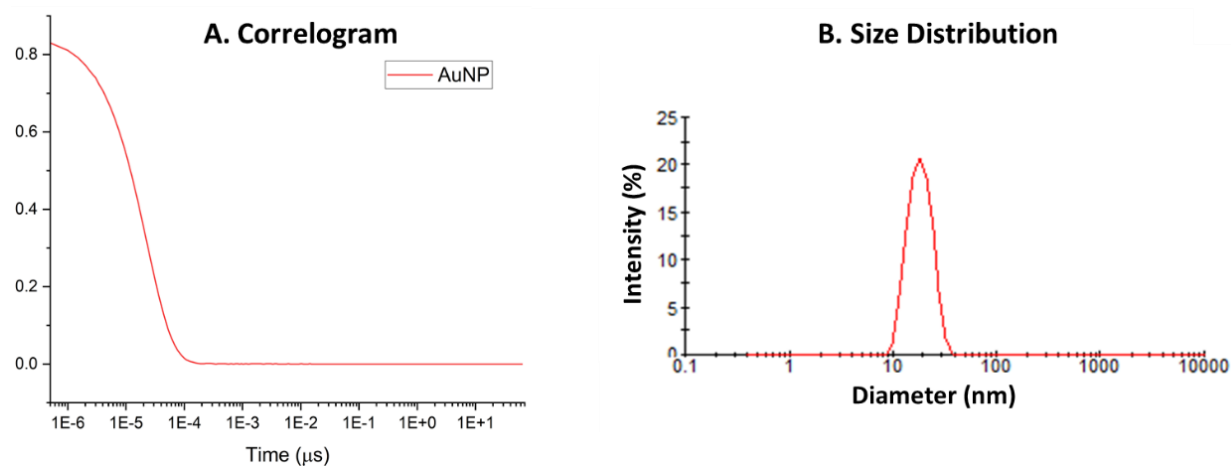


Figure 68: A. Correlogram for gold nanoparticles from Dynamic Light Scattering. B. Size distribution of gold nanoparticles (suspended in water) obtained from DLS measurement.

Table 6: Surface Plasmon Peak by gold nanoparticle, absorbance at 400 nm of a typical AuNPs batches with the respective hydrodynamic size (Mean size) issued from DLS. The [Au(0)] concentration and the AuNPs density numbers have been calculated from  $A_{\lambda=400nm}$  and from equation 1.

AuNP Batch	1	2
[Au <sup>3+</sup> ] in mM	0.25	0.25
$\lambda_{max}$ (nm)	520	521
$A_{\lambda_{max}}$	0.040	0.015
$A_{400nm}$	0.029	0.038
( $A_{400nm} / A_{\lambda_{max}}$ ) %	73	39
[Au(0)] in mM (*)	0.109	0.143
FWHM	145	56
Mean Size (nm)	18	25
PDI	0.25	0.09
[AuNPs] (~part/mL) (+)	$8.36 \times 10^{14}$	$3.12 \times 10^{14}$
[AuNPs] (~part/mL) (-)	$3.66 \times 10^{11}$	$1.88 \times 10^{11}$



(\*) an average extinction coefficient of  $2.65 \text{ L}\cdot\text{mmol}^{-1}\cdot\text{cm}^{-1}$  was taken to calculate the  $[\text{Au}(0)]$  concentration of the AuNPs suspension issued from Turkevich synthesis prepared with  $[\text{Au}^{3+}] = 0.25 \text{ mM}$ . (+) calculated from the initial gold concentration or (-) from the gold concentration calculated by the  $A_{400 \text{ nm}}$  value

We used the estimated number of particles from the initial gold concentration to evaluate the number of cycles needed for the SP functionalization by AuNPs.

#### 2.4.2 Silica particle

Silica particles exhibit a distinctive structure characterized by a three-dimensional network of silicon and oxygen atoms. The core of this structure comprise of the building block of nanoparticle comprising silicon dioxide ( $\text{SiO}_2$ ) tetrahedron; central silicon atom is bonded covalently to four surrounding oxygen atoms. The repeated linkage of these silicon dioxide tetrahedron forms a robust and intricate network, resulting in the spherical or variously shaped silica particle.<sup>219</sup> Moreover, the surface of silica particles can be modified to introduce functional groups or coatings, enhancing the versatility and tailoring properties for specific uses. Weight of silica particle obtained from oven drying SP suspension used for further modification (for making Iso and Janus particles) was  $7.4 \text{ mg SP per mL SP suspension}$ .

Smooth baseline (highlighted area) in obtained correlogram from DLS in Figure 69 shows that the SP synthesized in this study lacked aggregates or multiple size population. This is primary indicator of a desired good quality of silica particles. SEM observation (Figure 70) was helpful in determination of mean size of silica particles. Over 50 particles were observed with a mean diameter of  $475 \pm 51 \text{ nm}$ , which is around 2.66% less than the hydrodynamic diameter of  $488 \text{ nm}$  obtained from DLS. Polydispersity index of these silica particles was 0.04 (DLS result).

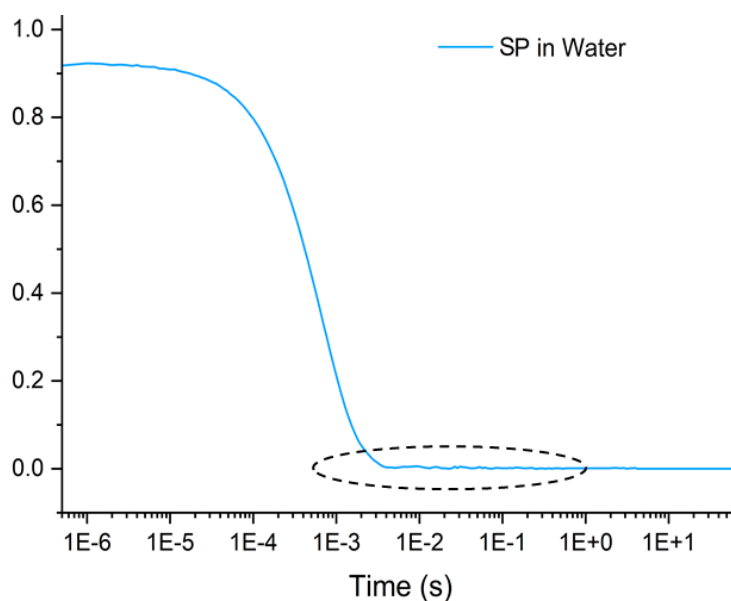


Figure 69: Correlogram of silica particles with smooth baseline indicating monodisperse particles (Broader plateau than in gold nanoparticle correlogram; Figure 67 refers to slower motion in silica particles than gold nanoparticle).

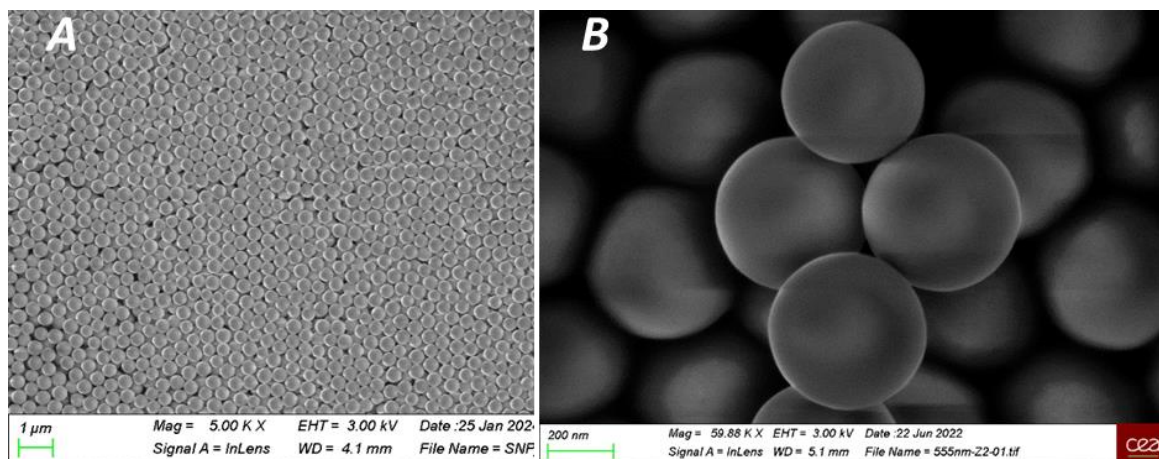


Figure 70: Smooth spherical Silica Particles confirmed from SEM at 5x and ~60x magnification (A and B respectively). Mean diameter obtained from fifty SP is  $475 \pm 51$  nm. Image b) shows quadruplet pattern artistically arranged four silica particles.

No negative effect of ultrasonic bath was observed on the shape and structure of silica particle. A mean diameter of  $472 \pm 38$  nm for 50 particles was retrieved by SEM after one hour of ultrasonic bath. Similar range of size distribution (Figure 71. C), smooth and spherical surface from before (Figure 71. A) and after (Figure 71. B) one hour of ultrasonic bath confirms that the silica particle synthesized during this thesis are of robust quality with good mono-dispersity. Figure 72 shows monolayer of SP can be achieved from spin coating, from the protocol followed for PVD-JP production.

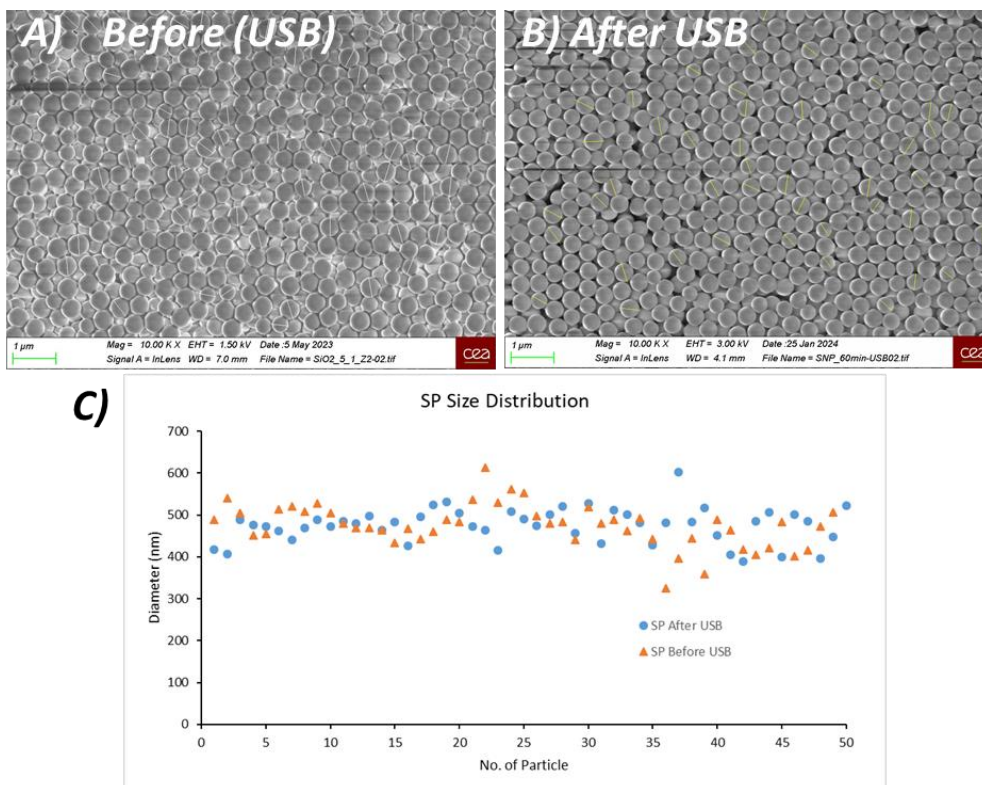


Figure 71: SEM images of SP at 10K x magnification confirming robustness and stability. A) Showing smooth surface and structure of SP before an hour long ultrasonic bath (USB). B) Showing SP after 60 min USB with no structural damage. C) Showing the size distribution of SP before (orange) and after (blue) 60 min USB.

## Particle Production

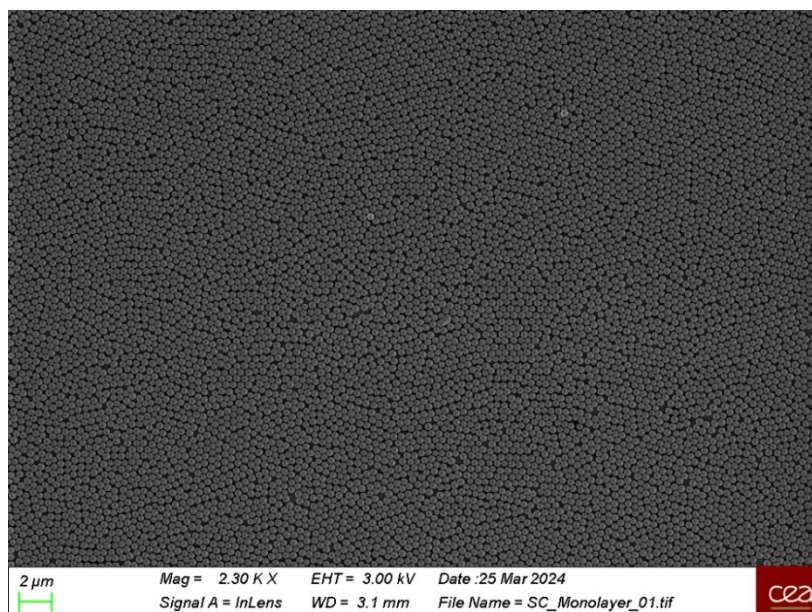


Figure 72: Monolayer of SP from spin-coating (for PVD Janus particle production)

Table 7 enlists the typical calculated values for synthesized silica particle. Values like particle concentration in SP suspension, size, and total surface area are essential for synthesis of isotropic and Janus gold/silica particle.

Table 7: Properties of silica particle synthesized and utilized to make isotropic and Janus gold/silica particles (\*)

Diameter	475 nm
$v_p$ (Vol. of 1 Particle)	$5.61 \times 10^{-20} \text{ m}^3$
$w_p$ (Weight of 1 particle) ( $v_p \times \rho$ )	$1.30 \times 10^{-13} \text{ g}$
$W_p$ (Weight of particles in 1 mL suspension)	$7.4 \pm 0.37 \text{ mg}$
$N$ = No. of particle/mL suspension ( $W_p/w_p$ )	$5.69 \times 10^{10}$
$V_p$ (Vol of particles/ mL Particle suspension) ( $N \times v_p$ )	$3.19 \times 10^{-9} \text{ m}^3$
t <sub>sa</sub> (total surface area per particle)	$7.08 \times 10^{-13} \text{ m}^2$
TSA ( $N \times t_{sa}$ )	$4.03 \times 10^{-2} \text{ m}^2/\text{mL}$
c <sub>sa</sub> (curved surface area) SP hemisphere	$3.54 \times 10^{-13} \text{ m}^2$
CSA ( $N \times c_{sa}$ )	$2.01 \times 10^{-2} \text{ m}^2/\text{mL}$

(\*) where  $v_p$  is the volume of single particle,  $V_p$  is total volume of particles per 1 mL particle suspension,  $w_p$  is weight of 1 particle,  $W_p$  is total weight of particles per 1 mL particle suspension,  $t_{sa}$  is total surface area of 1 particle,  $TSA$  is total surface area of particle per 1 mL particle suspension,  $c_{sa}$  is curved surface area of 1 SP hemisphere and  $CSA$  is curved surface area of SP hemisphere per 1 mL SP suspension

### 2.4.3 Isotropic Gold/Silica Particle

As mentioned in “2.1” of Chapter 2 and section “2.3.3.2”, functionalization of silica particles was tested with three chemical species; APTES, PLL and PAH. SEM observations confirms poor functionalization of SP with PLL (Figure 73 A). While higher AuNPs population in Figure 73 B is an indicative of better functionalization of SP from PAH than PLL. But it is still not preferable due to non-homogeneous and less-isotropic distribution of AuNPs. Additionally, rough SP surface in some of Iso synthesized from PAH were observed (arrowed in Figure 73 B), which could be due to long interaction time between PAH and SP that were not well stabilized during synthesis. Compared to PLL and PAH (Figure 73 A and B, respectively) treatment with APTES and AuNPs, Figure 74 shows highest AuNPs coverage. APTES comprises of an amino ( $NH_2$ ) and a silane group. This creates silinol group from hydrolysis forming covalent Si-O-Si bonds between APTES and SP. The  $NH_2$  function brought by APTES with a high affinity for gold ensures strong and durable linkage between AuNPs and SP.<sup>237</sup>

As per the theoretical calculation  $\sim 5.2 \times 10^{-4}$   $\mu L$  APTES is required to graft 1 APTES per  $15 \text{ nm}^2$  for total surface area of  $0.02 \text{ m}^2$  (in our case), like in Avossa paper for  $0.75 \text{ m}^2$  (see Table 7 and calculations from Eq. 1).<sup>227</sup>

$$V_{APTES} \Rightarrow \frac{\text{No.of APTES for } s=0.75 \text{ m}^2 \text{ SP area}}{N_A \times \text{No.of Mole (APTES) per mL}} = 0.02 \mu L$$

$$\Rightarrow \frac{S (0.02 \text{ m}^2 \text{ SP area})/n_{APTES}}{N_A \times [APTES] \times 10^{-3}} = 0.00052 \mu L \quad \text{Eq. 2}$$

With  $S$ , the total surface of SP to be functionalized ( $0.75 \text{ m}^2$ ),  $n_{APTES}$  the number of APTES molecule per  $15 \text{ nm}^2$  required for a full coverage of SP,  $N_A$  the avogadro number and  $[APTES]$  the concentration in mol/L of APTES reactant.

While UV-Vis in Figure 75 compares AuNP, Iso and APTES functionalized SP. Presence of AuNP in Iso is characterized by the presence of a LSPR between 520-540 nm wavelengths. From SEM images, the coverage rate of SP by AuNPs can be quantified. In our case the number of AuNP were counted manually from the visible-side of particles and multiplied by 2 to assume the total number of AuNP per SP. The Table 8 summarizes the size of SP and AuNPs, observed mean count of AuNPs calculated from 50 particle Isotropic gold/silica (Figure 155), the number of gold nanoparticle per isotropic gold/silica particle theoretically calculated from single geometrical considerations, the required volume of AuNP suspension to achieve the full coverage.

## Particle Production

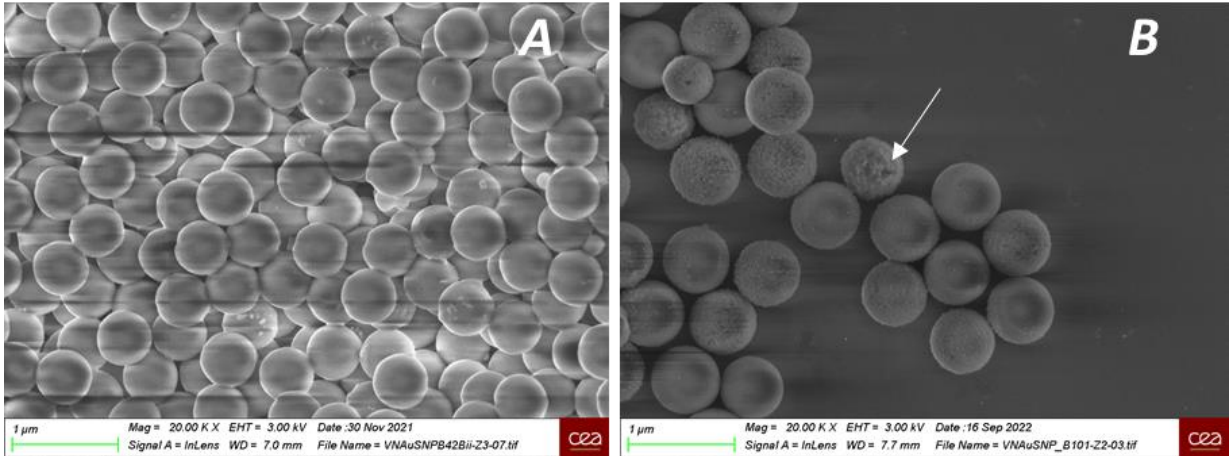


Figure 73: SEM image of Isotropic Gold/Silica particle; A) functionalization of silica particles from PLL and b) functionalization of Silica particles (SP) from PAH. A) showing poor count of gold nanoparticles (AuNP) (small dots on bigger spheres; SP), while B) having higher AuNP population than A) but non-homogeneous coverage.

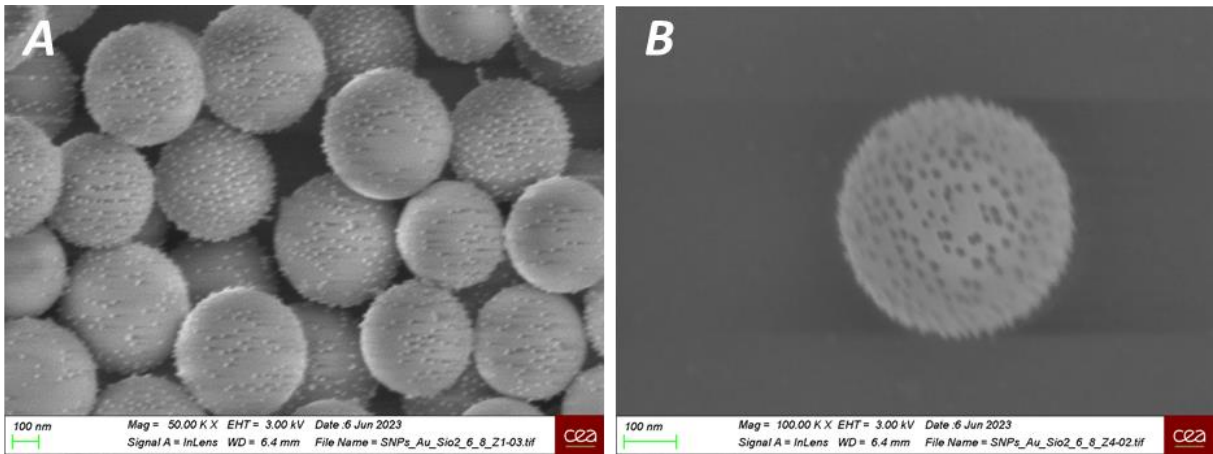


Figure 74: SEM images of isotropic gold/silica particles from APTES functionalization at 20K (image a) and 100K (image b). Gold nanoparticles (AuNP) (small dots on bigger spheres; silica particles (SP)) can be noticed covering big sphere (SP) homogeneously in B while some particles in A lacks homogeneous distribution of gold nanoparticles.

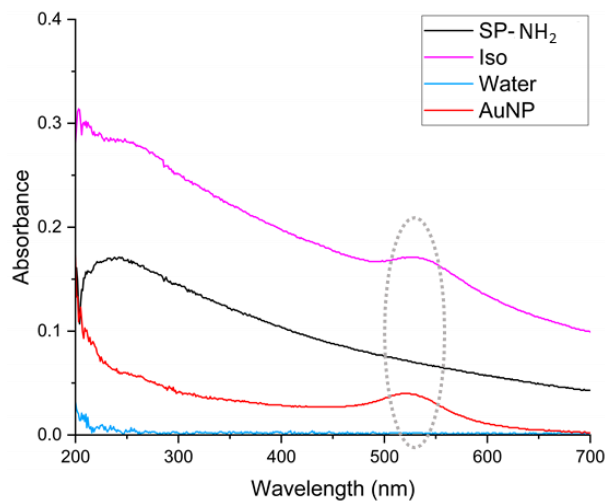


Figure 75: Comparative UV-Vis of respective particles. LSPRs in Iso and AuNP is visible between 520-540 nm wavelengths.

The theoretical coverage rate number can be obtained from the projected surface of AuNPs and the area of the voids when particles are compacted self-assembled (Figure 76). The obtained (theoretical) values are larger than the measured value (from SEM observations), as the calculation (Table 8) is based on neglecting the unoccupied area due to electrostatic and steric repulsions between AuNPs.

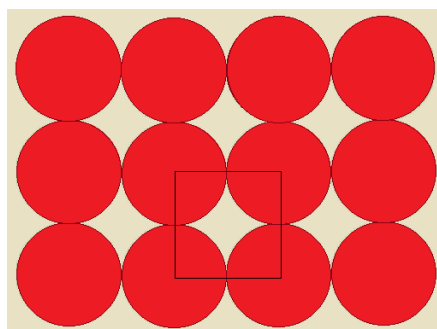


Figure 76: Scheme of representing top view of Gold Nanoparticle (red circles) in simple compact 2D monolayer assembly neglecting the electrostatic repulsion. The black highlight represents a square lattice.

SEM results show observed mean count of AuNPs in Iso is ~19% of the theoretical maximal AuNP count. While the average distance (center-center) between two AuNP was observed to be around 35 to 40 nm. This can be explained by the electrostatic and steric repulsion between AuNPs that prevents a compact assembly, and a partial coverage of the SP surface by APTES functionalisation. Additionally, tentative for multiple cycle (of AuNP introduction) did not give a higher number of attached particles either, and for each cycles not a lot of particles were attached (coloured supernatant is an indication of free AuNPs). We decided to use the particles as it was, with the experimentally obtained AuNPs coverage of 217 AuNPs per SP.

Table 8: Theoretical Values for number of gold nanoparticles per Isotropic Gold/Silica Particles calculated from AuNP radius, SP radius.

tsa SNP (nm <sup>2</sup> ) per particle of $\phi$ 475 nm	$7.08 \times 10^5$
TSA SP (m <sup>2</sup> ) per batch synthesis (ie 0.5 mL of SP suspension)	$2.01 \times 10^{-2}$
S, Projected Area of AuNP of $\phi$ 25 nm (nm <sup>2</sup> )	491
A, Area of lattice unit cell from compacted AuNPs assembly (nm <sup>2</sup> )	625
Theoretical No. of AuNP per Iso (tsa/(A))	1134
Experimental AuNP/SP (from manual counting of 50 particles from SEM images)	217
Volume of AuNPS suspension (ml) used for the functionalization	1
Estimated required volume of AuNPs suspension (*) (ml)	1.98

(\*) calculated from the estimated number of AuNPs in the suspension (see paragraph 2.4.1).

Further confirmation of isotropic presence of AuNPs in Iso samples were achieved by EDX measurements where Iso sample was dried onto a silica wafer followed by SEM-EDX observations. Figure 77. A shows the SEM image of observed Iso sample, while Figure 77. B shows the same image with cartography for gold. Cartography image typically refers to an elemental distribution map within a sample and here provides visual information about AuNPs location on the surface of Iso particles. Distinguishing elemental spectra shown in Figure 77. C reflects the quantity of elements present in the observed sample.

As the penetration depth for used EDX set-up was of 1 $\mu$ m, and sample was spread on silica wafer, strong  $K_{\alpha}$  X-ray peaks for Silicon (Si) is justified, thus, giving a biased analysis for elemental distribution, leaving EDX unfit for quantitative analysis. This could have been overcome by reducing the scattering volume (3D region within sample where electron beam interact with sample-atoms to generate X-rays) by reducing the electron beam energy to 5 kV (from 10kV). Oxygen in silica particle contributes to the  $K_{\alpha}$  X-ray peak of oxygen, while sodium identified by the Na  $K_{\alpha}$  X-ray peak in Figure 77. C. probably comes from contaminated stub.

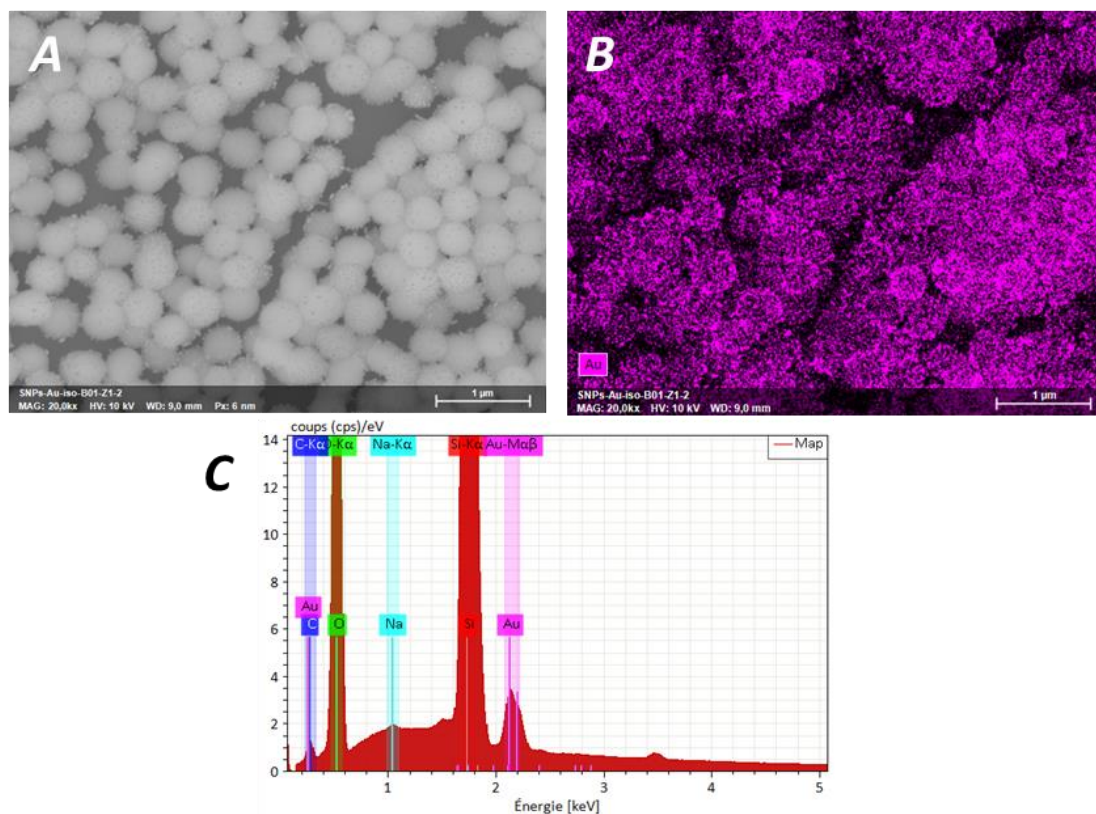


Figure 77: SEM-EDX image and Cartography result of Iso sample (A and B respectively). Cartography image and elemental spectra map confirming the presence of gold nanoparticles (Au) in Isotropic gold/silica particle. High intensity of Si is due to the silica wafer used for placing samples on.

The characteristic correlogram of final Isotropic Gold/Silica particles (Iso) is shown Figure 78. It has similar plateau as SP correlogram (Figure 69) but differs in the baseline. Proper re-dispersion of particles in suspension samples was ensured by vortex mixing (10 sec) before each DLS measurements.

## Particle Production

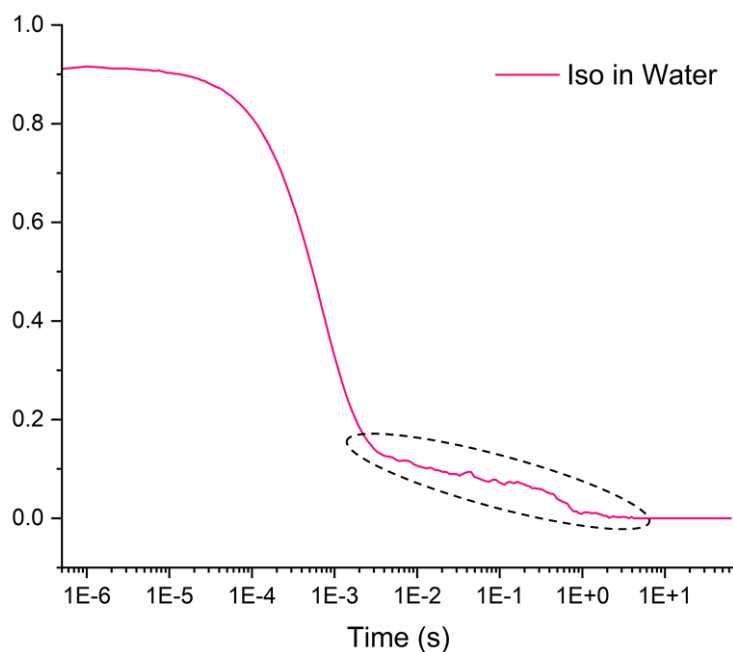


Figure 78: Correlogram of Isotropic Gold/Silica Particles suspended in water, with not-smooth baseline signature.

Thus, these fluctuating baseline can also be related to signature of particle with unsmooth surface; gold nanoparticle covering SP in this case.<sup>258–260</sup> The analysis of these correlogram will be detailed in section “3.2.2.3”, Chapter 3.

### 2.4.4 Gold/Silica Janus Particle

#### 2.4.4.1 Colloidosome Production

While influence of CTAB on silica particles is multifaceted, the primary role in this study was to influence the surface charge and zeta potential of the SP. This ultimately changed the wetting properties of SP and improved its dispersibility in water-oil interface by making SP partially hydrophobic. CTAB presence is pivotal in achieving stable Pickering Emulsion. The hydrophilic head of CTAB is adsorbed onto the surface of the silica particles. The pH for the point of zero charge (PZC), for the synthesized pristine silica particles was around 3 (zeta potential values of SP suspensions at various pH values were obtained and the pH at which the zeta potential was closest to zero represented PZC of SP).<sup>221</sup> Similar to the work by Avossa et al<sup>163</sup>, pH of suspension at which SP surface functionalization was done was 9, while the SPs were initially negatively charged. The difficulty was to find the optimum CTAB concentration to have a monolayer of CTAB on the SP, with CTAB exposing their hydrophobic tail to be included in the oil at the water oil interface. The modification of the hydrophobicity of the SP optimized the wetting of SPs on the oil droplets dispersed in water to form a so-called Pickering Emulsion.<sup>163,261,262</sup>

To find out the most suitable concentration of CTAB to produce Colloidosomes with a SP monolayer at its surface, multiple values of CTAB concentration (0.004, 0.01, 0.02, 0.04 and 0.08 mM) were tested: all below the critical micellar concentration (CMC) of CTAB in water (1 mM).<sup>163,261</sup> First, following the



Avossa<sup>163</sup> protocol, zeta potential of SP was measured with increasing the CTAB concentration. Reproducibility of zeta potential results was challenging, however, saturation of the zeta potential value after 15 to 30 min interaction period (between CTAB and SP) was found to be sufficiently stable for the measurements. Figure 79 shows the increasing zeta potential of SP as a function of CTAB concentration. At 0.004 mM CTAB, the zeta potential increased with  $\sim 10$  mV and stay in the same range at 0.02 mM CTAB (with a little increase of  $\sim 2$  mV at 0.04 mM). Zeta potential assessments in Figure 79 revealed negative charge of around -60 mV on pristine silica, which alters upon the introduction of positively charged CTAB that adheres to the SP through electrostatic interactions. After 0.04 mM of CTAB, the zeta potential increased, indicating that CTAB is adsorbing on the surface of the SP. Zeta potential measurements provided valuable insights into the modification of surface properties, facilitating a quantitative assessment of CTAB adsorption on silica. Contrary to Avossa et al<sup>163</sup>, the increase of the zeta potential is appearing in two steps in the measurements. We can conclude that a concentration between 0.04 mM and 0.08 mM of CTAB is required to change the surface charge of the SPs.

SEM analysis of Colloidosomes synthesized with different CTAB concentrations are compared in Figure 80. The figure shows irregular size of Colloidosomes at 0.004 mM and 0.08 mM CTAB (Figure 80. A and D respectively). While Colloidosomes from CTAB concentration 0.02 mM and 0.04 mM are of similar size range (0.02 mM having least amount of non-spherical Colloidosomes) in Figure 80. C and D, respectively.

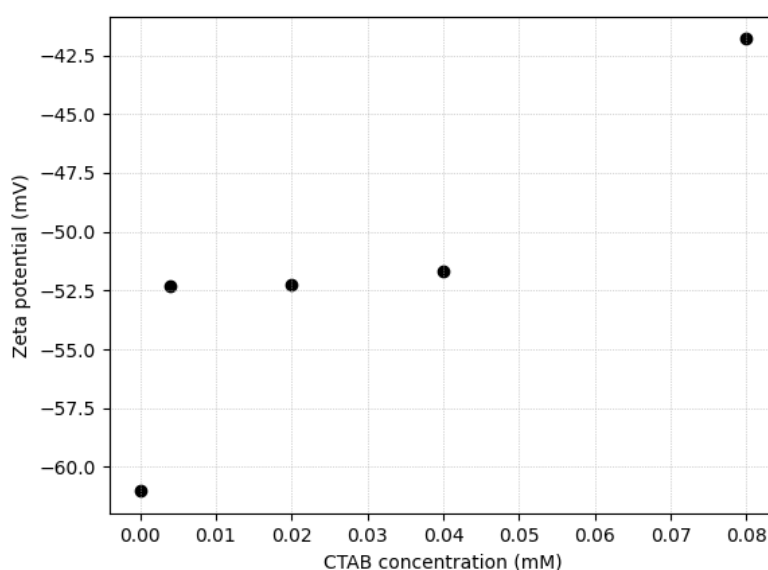


Figure 79: Zeta potential values (mV) of silica particle (size $\sim 475$  nm) suspension with CTAB, in function of the concentration of CTAB (mM). Measurements are taken 30 min after mixing SP and CTAB at a temperature of 50 °C.

This indicates that at 0.02 mM and 0.04 mM CTAB more homogeneous and stable Pickering Emulsion is obtainable. For the 0.08 mM CTAB case, in addition to high increase of zeta potential value ( $\sim 20$  mV; Figure 79), particle aggregation and clustered colloidosomes are evident on SEM images (Figure 80. D), referring to reduced stability of suspension.

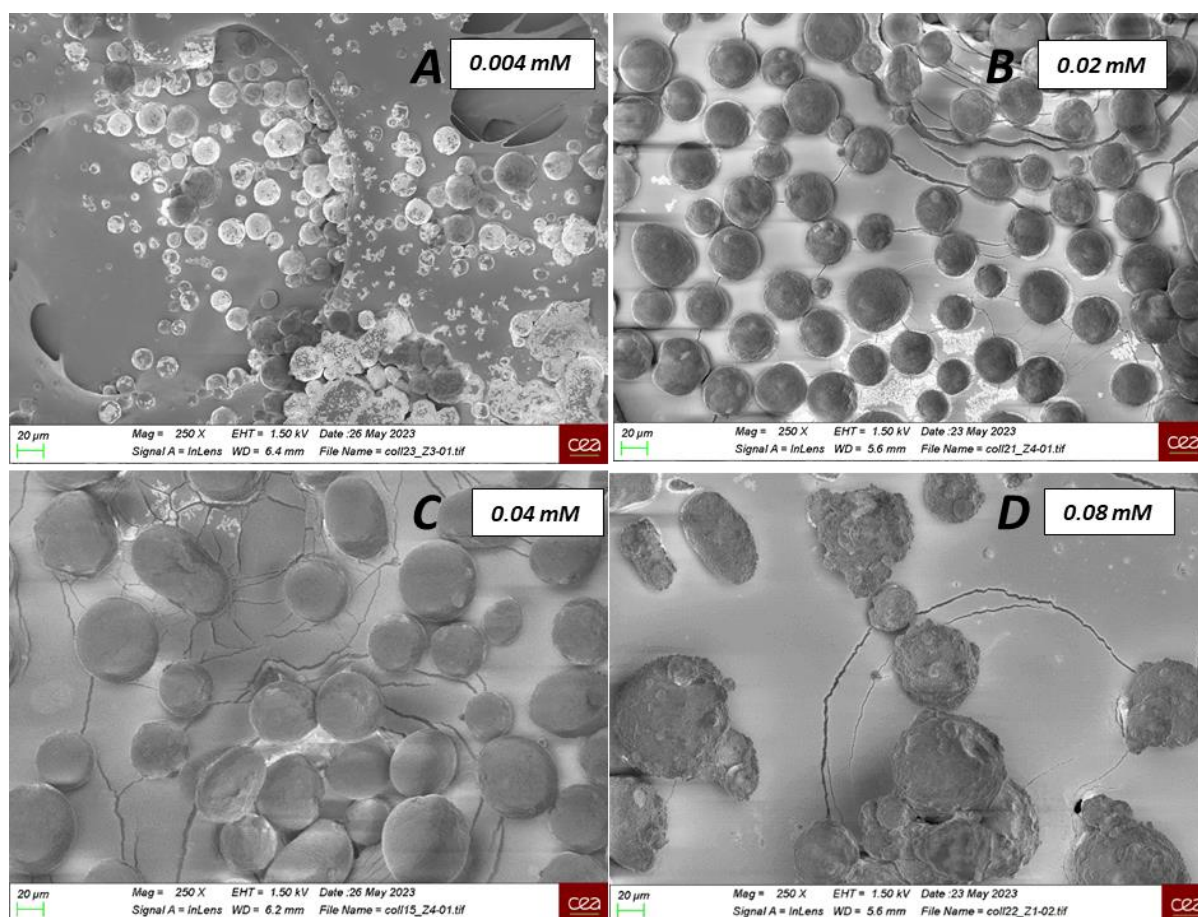


Figure 80: SEM images of Colloidosomes at 250x magnification for respective concentrations of CTAB in A-D images. A) Featuring various size of Colloidosomes (spherical structures) clustered together, while D) has bigger Colloidosomes with rough surfaces. C) and D) features the desired spherical and smooth Colloidosomes with least size variations.

While zeta potential for 0.02 and 0.04 mM CTAB were in similar range, SEM results (Figure 80 to Figure 81) narrowed down to the finalization of 0.02 mM CTAB concentration for Colloidosome production in this thesis. Colloidosomes with least SP coverage was obtained for 0.004 mM CTAB (Figure 82. A), monolayer of partially embedded SP in 0.02 and 0.04 mM CTAB (observed at higher magnification in Figure 82. B and C, respectively) confirmed desirable amount of SP wettability altered via aliphatic chains of CTAB. Whereas, less stable suspension and insufficient/excessive wettability of SP was confirmed from Colloidosome having <50% surface coverage (with SP) at 0.004 mM CTAB and aggregates at 0.08 mM CTAB in Figure 82. A and D, respectively. Following SEM observation, mean size of Colloidosomes was calculated from 60 Colloidosomes that showed increasing size of Colloidosomes with increasing CTAB concentration (Table 9 and Figure 81) and also summarized that highly poly-disperse colloidosomes were produced at 0.004 and 0.08 mM CTAB (Figure 82. A and D, respectively), unlike at 0.02 and 0.04 mM CTAB concentration.

Contrary to our result for size evaluation of Colloidosomes, Avossa and team<sup>163</sup> observed decrease in the size of Colloidosome with increasing concentration of CTAB. In addition to increased competition for space occupation by SP (our SP is ~40% bigger than Avossa's<sup>163</sup> SP), this contradiction could also be due to the difference in the nature of the used paraffin wax which could influences the wetting properties of the SP at the wax/water interface.

## Particle Production

Table 9: Colloidosome mean size at respective CTAB concentration

CTAB (mM)	Colloidosome Mean Dia. ( $\mu\text{m}$ ) $\pm$ SD
0.004	9.1 $\pm$ 6.3
0.02	38.5 $\pm$ 8.4
0.04	54.9 $\pm$ 12.8
0.08	53.0 $\pm$ 28.5

To conclude, SP suspension with zeta potential -51 to -52 mV (at 0.02 and 0.04 mM CTAB concentration, respectively) results in spherical Colloidosome with monolayer SP coverage. Higher zeta potential about -42 mV (at 0.08 mM CTAB) leads to particle aggregates and non-monolayer of SP clustering on Colloidosome surface, which continued with further increasing CTAB concentration.

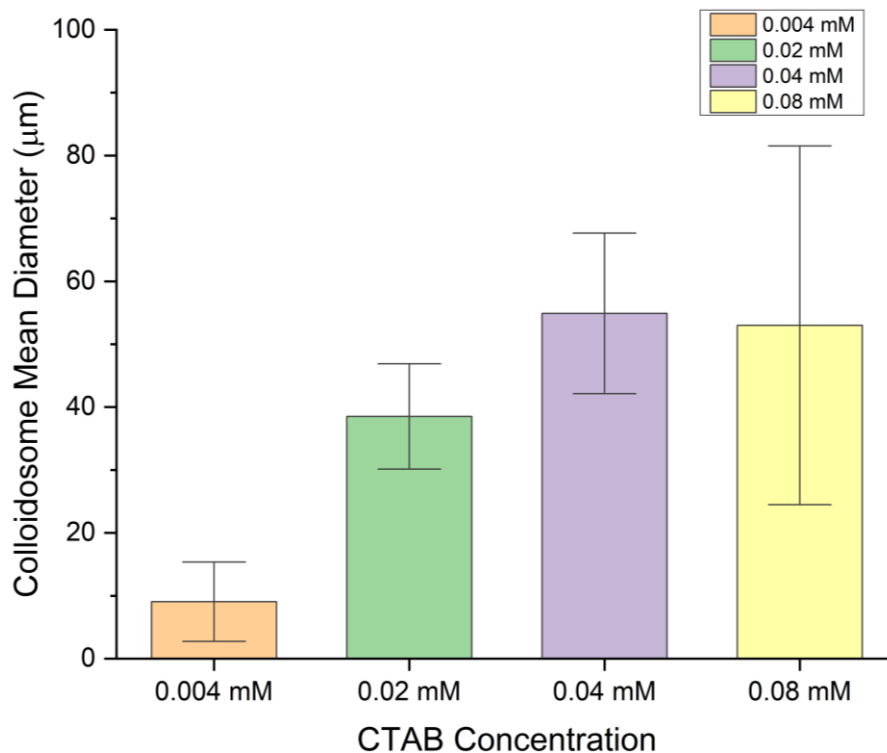


Figure 81: Mean size calculated from 60 Colloidosomes at respective concentration of CTAB

## Particle Production

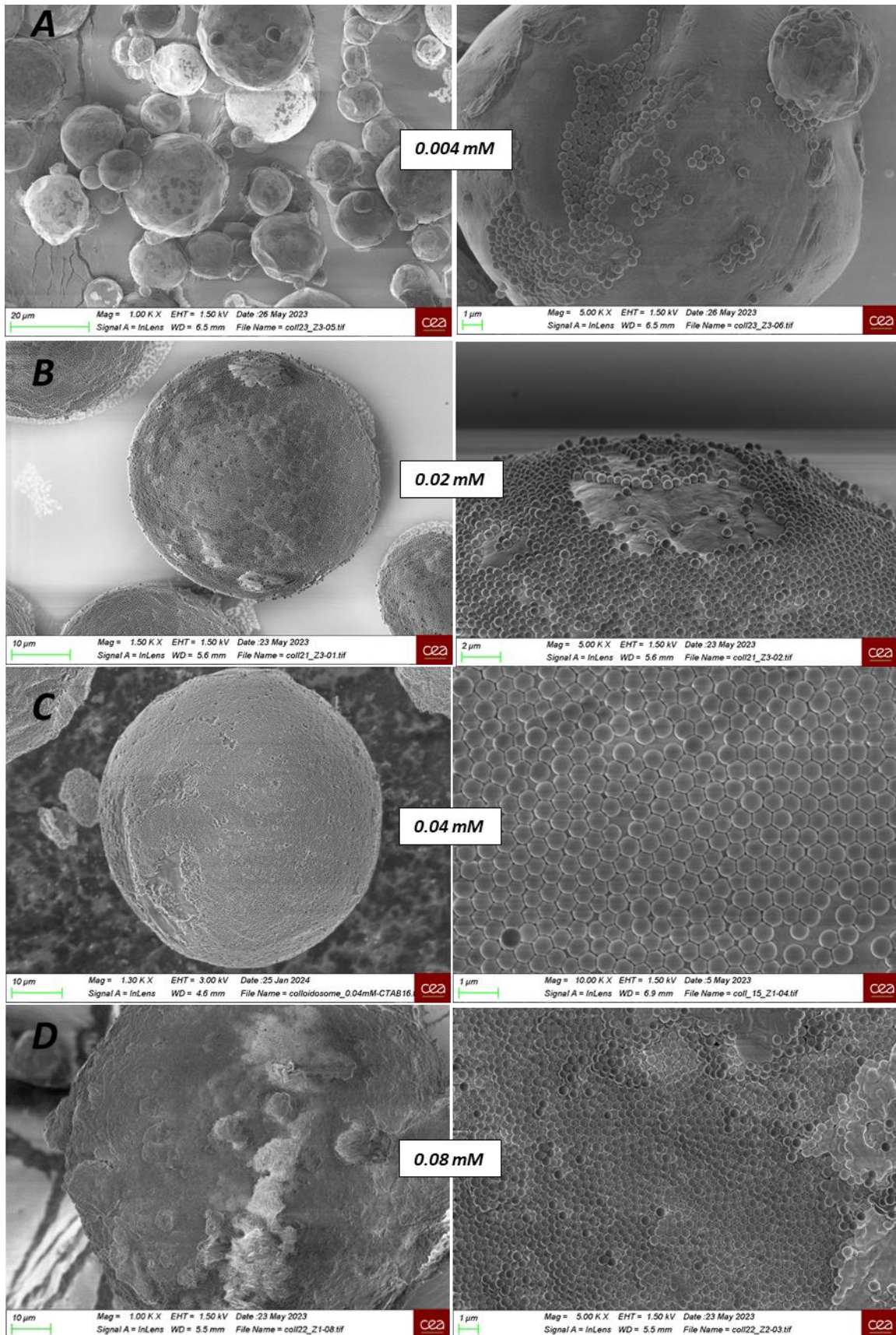


Figure 82: SEM images of Colloidosome at  $\sim 1000\times$  (Left) to and  $5000\times$  (Right) magnification for respective concentrations of CTAB in A-D images. A) Clusters of different size of Colloidosomes with majority surface lacking SP is observed. Big Colloidosomes with monolayer of partially embedded SP featured in B) and C), while D) featuring aggregated SP in D with rough surface and abruptions in spherical structures.

#### 2.4.4.2 Wax Removal of Colloidosomes

As per the protocol followed (in section “2.3.3.2”) for the synthesis of Gold/Silica Janus Particle, functionalization of SP with APTES is crucial and equally crucial parameter is the removal of wax from colloidosomes after APTES grating. The solvents tried for the wax removal for the chosen wax (melting 57-65°C) were Pentane, Toluene and Hexane. Figure 83 shows the SEM images of the particles after wax removal cycles. Both the images obtained after pentane or toluene wax extraction cycles, show silica particles with wax remains, these solvents were insufficiently capable of dissolving wax. They are not ideal for wax removal after colloidosomes-functionalization with APTES.

On the contrary, when hexane is used, the SP were not embedded in wax and no residual wax is observed on the SEM images (Figure 83 C and D). Hexane was therefore the solvent of choice for the wax removal (for the wax reference used to produce the Colloidosomes in this study). Wax removal is crucial and to avoid the use of hexane, a possible approach could be to utilize softer paraffin wax with narrow range of melting point (42-44°C) instead of the chosen one which has a higher and wider range melting point (57-65 °C). Advantage of using softer wax would be its quicker solubility and would require less harsh solvents.

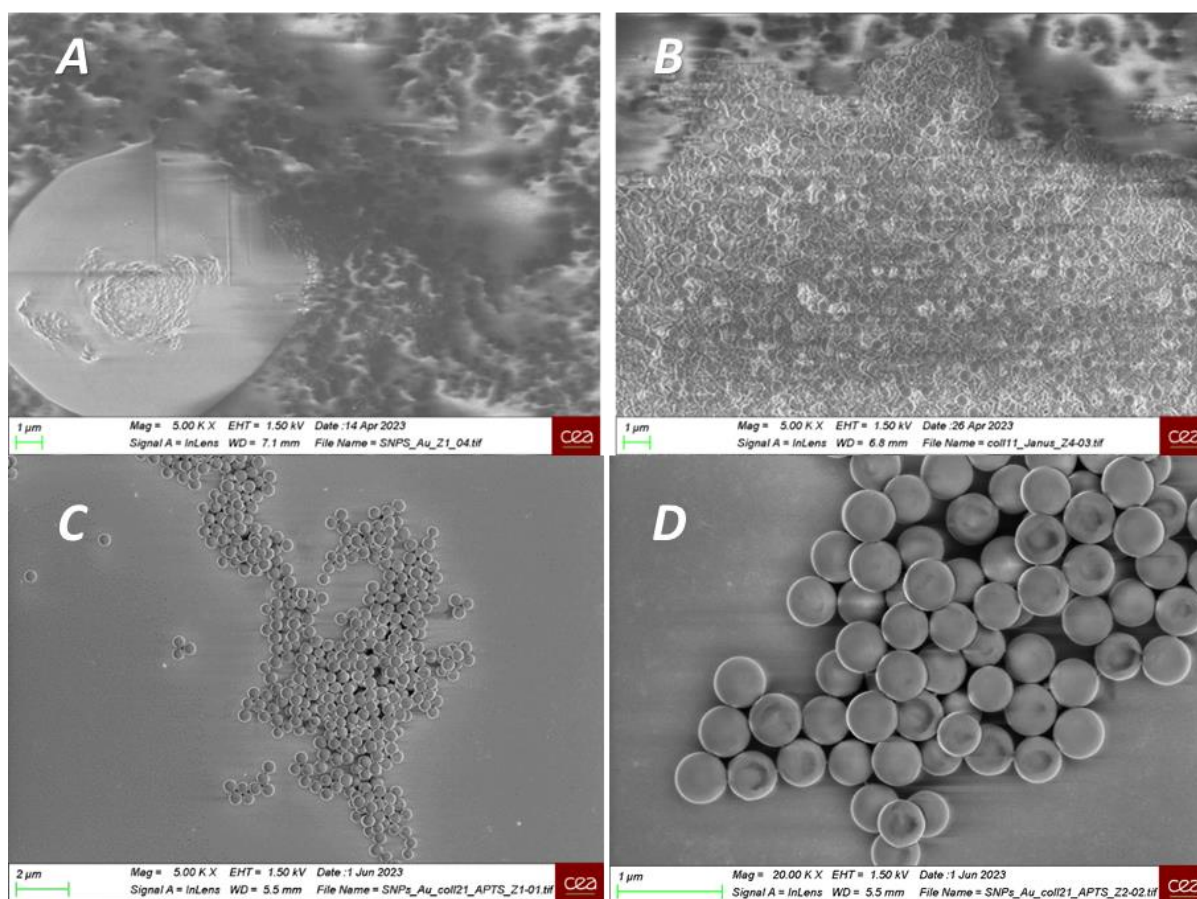


Figure 83: SEM images for wax dissolution off Colloidosomes using Toluene (A) and Pentane (B)) and Hexane at 5K x and 10K x magnification (image C) and D) respectively).

### 2.4.4.3 Janus Particle (Functionalization with Gold Nanoparticle)

Optimal functionalization of SP-NH<sub>2</sub> (obtained from washing wax off colloidosomes) is crucial for getting good surface homogeneity (of AuNP on SP). As per theoretical calculation  $\sim 5 \times 10^{-4}$   $\mu\text{L}$  APTES was required to graft 1 APTES per 15 nm<sup>2</sup> for total surface area (0.09 m<sup>2</sup>) of SP per batch (like in Avossa et al<sup>163</sup> for 0.75 m<sup>2</sup> total surface area). Multiple synthesis performed with this quantity resulted in poor APTES-SP functionalization (confirmed from SEM observation (Figure 84) with low and non-homogeneous AuNP population per SP). Therefore, to ensure an optimized functionalization of SP-NH<sub>2</sub>, an excessive quantity of APTES was used to have optimal grafting of APTES in the protocol.

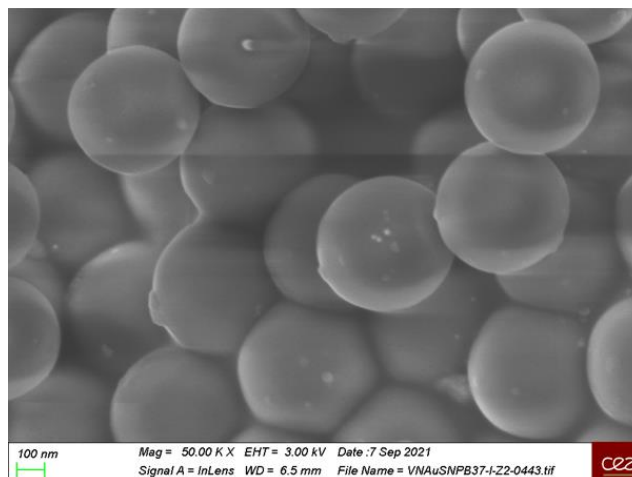


Figure 84: SP with insufficient functionalization of APTES causing poor and non-homogeneous functionalization with AuNP.

UV-Vis comparative study of JP with different particles gave the first hint of AuNP functionalization in JP samples where faint LSPR could be seen between 520 – 550 nm wavelength (Figure 86). Correlogram from final Gold/Silica Janus Particles (JP) is represented in Figure 85 having a plateau similar to that of SP (Figure 69) and Iso (Figure 78) but differs in the baseline.

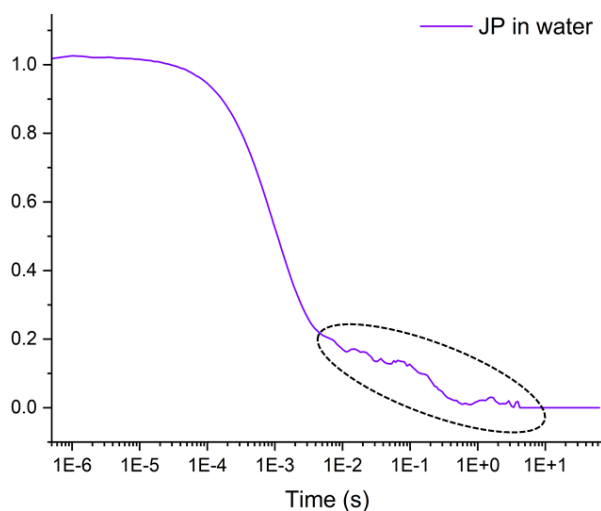


Figure 85: Correlogram of chemically synthesized Janus gold/silica Janus Particle (JP) suspended in water. Observed plateau is similar to SP and Iso, while unsmooth baseline (in highlighted elliptical area) persists in JP samples.

Proper re-dispersion of JP in DLS samples was ensured by vortex mixing of 10 seconds before each DLS measurements, thus, these fluctuating baseline can also be related to a signature of particle with unsmooth surface; gold nanoparticle covering SP anisotropically in this case.<sup>258–260</sup>

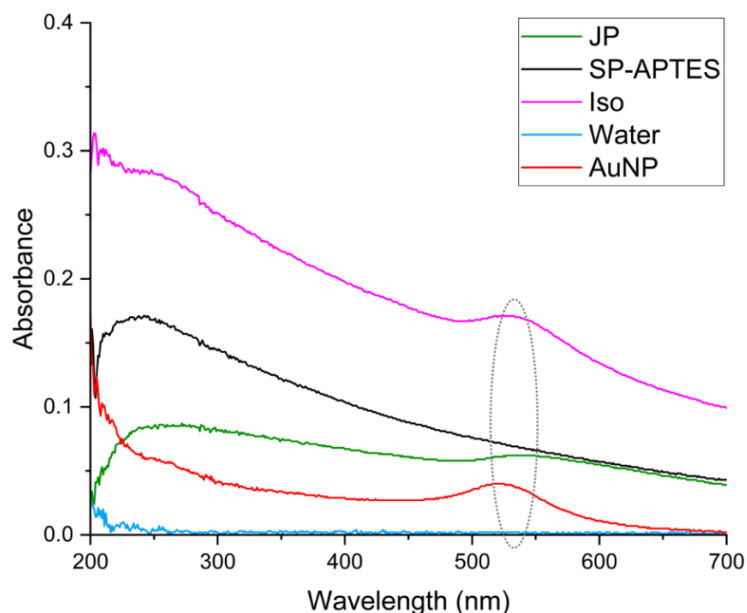


Figure 86: UV-Vis spectra for respective samples. Highlighted area shows peaks from 520 to 540 nm for respective samples

Difference in population density of gold nanoparticles for some particle is evident in Figure 87 due to its orientation; some Janus particle have its silica side of surface exposed, while others have gold nanoparticle side of surface exposed. Mean count of gold nanoparticle per chemically synthesized gold/silica Janus Particle (calculated manually from ~ 50 particles) is 109.

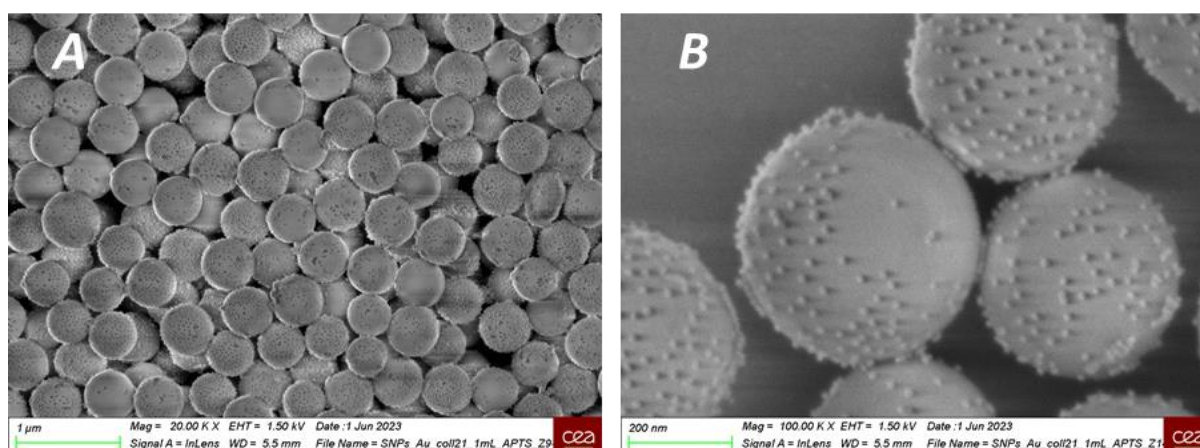


Figure 87: SEM images of Gold/Silica Janus Particle at 20K x magnification (a) and 100K x magnification (b). It can be clearly observed that half of the surface of silica particles (SP) is functionalized with AuNPs (small dots), confirming the synthesis of Gold/Silica Janus particles from chemical synthesis protocol of Pickering Emulsion.

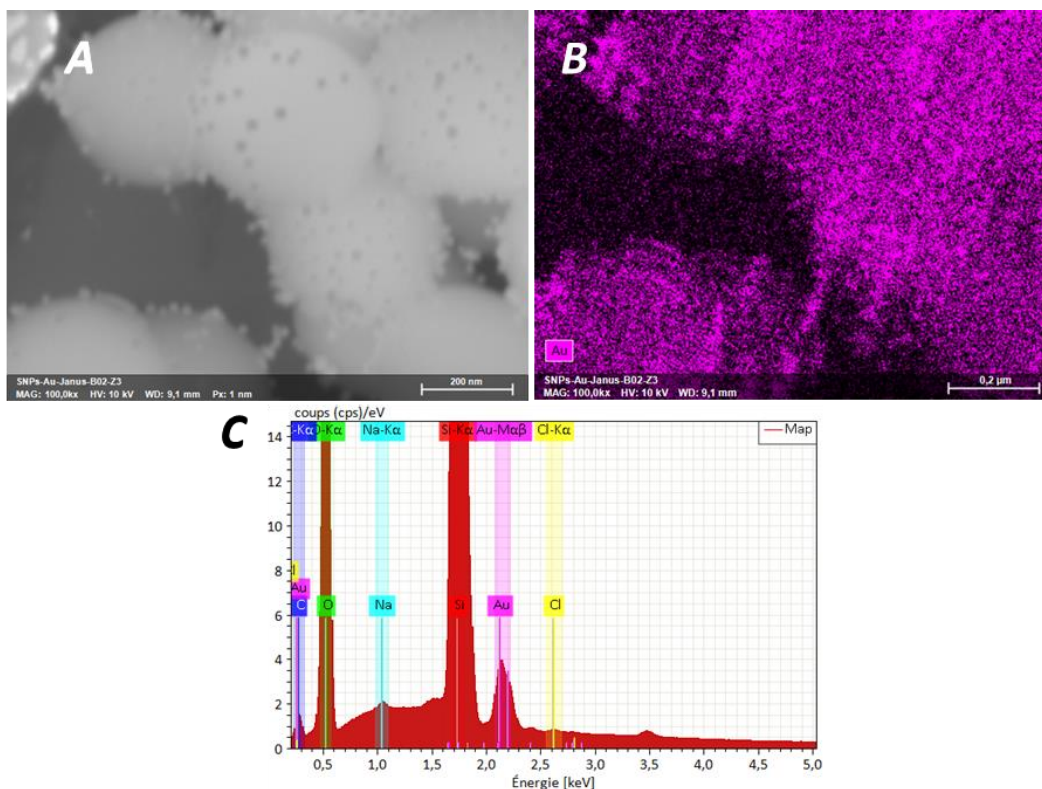


Figure 88: SEM-EDX image and Cartography result for chemically synthesized Gold/Silica Janus particle (JP) sample (A and B respectively). Cartography image and elemental spectra map (C) confirms the presence of gold nanoparticles (Au) in JP. Contaminated stub giving Na-Kα and Cl-Kα peaks.

Further confirmation of presence of AuNP in JP samples was achieved by EDX measurements where JP sample (placed on silica wafer) were observed to give cartography images and elemental distribution map shown in Figure 88. Similar to Iso samples (Figure 77), EDX results for JP samples are quantitatively non-conclusive because of biasness from silica wafer, hence making EDX qualitative analysis in our work. Additionally, transmission electron microscopy (TEM) could have been more helpful in affirmation of janus structure, however, due to limited accessibility (within the restricted time frame) it was not performed.

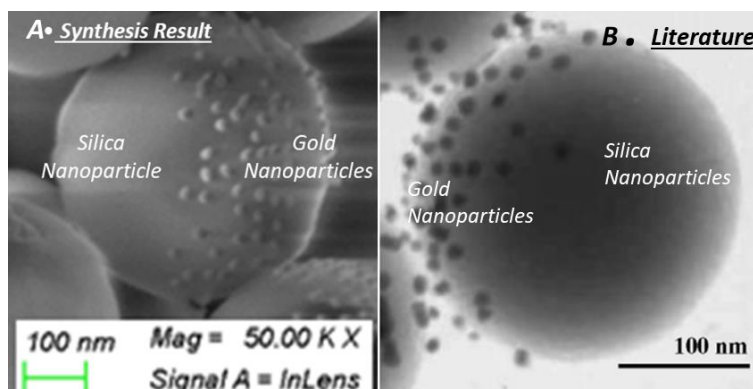


Figure 89: Comparison of chemically synthesized Gold/Silica Janus Particle (JP) from Pickering Emulsion Method in this thesis (A) versus JP synthesized by Perro<sup>227</sup> (B). JP showing one half of the total AuNP population in SEM and TEM images with SPØ 475 and 300 nm, respectively (A and B, respectively).



Comparison of mean count of gold nanoparticles (AuNP) per JP in our work (calculated from SEM observations) is 109, while Perro's work<sup>227</sup> indicated 80 AuNPs (in 300 dia. Janus particle). The calculated mean distance between AuNPs (from total surface area of silica per total count of AuNP) we found that our AuNPs are separated by ~7 nm distance, which was similar to Perro's<sup>227</sup> (~9 nm). The surface area (Janus hemisphere) covered by AuNPs from our synthesis was about 15%, which is about 1.5 times higher than surface coverage by AuNPs in Perro et al<sup>227</sup>, which was about 10%. However, work by Petit<sup>171</sup> and Yang<sup>263</sup> highlights higher concentration of gold nanoparticles in their Janus particles. Petit<sup>171</sup> showed ~48% surface coverage by gold nanoparticle in their Gold/Silica Janus nanoparticles, synthesized using gas/liquid interface strategy. Nevertheless, their synthesis strategies are restricted to Janus particle synthesis in small quantity. Whereas Yang's<sup>263</sup> Janus particles (silica particle diameter 130 and 500 nm; AuNP diameter ~15 nm) obtained ~40 to 70% AuNP coverage. Unlike our study (utilizing easily available cost-effective chemicals) Yang<sup>263</sup> worked with supercritical carbon dioxide and polystyrene for partial embedment of SP, which although gives higher AuNP surface coverage, but factors like complex protocol, scalability, cost, challenge of protocol-optimization, limits its application. Whereas, many other researchers like Lu<sup>151</sup>, Percebom<sup>264</sup>, Vega<sup>175</sup>, Trayford<sup>265</sup> prepared their Janus particles by having single (or double) gold nanoparticles per silica particle (shared in Figure 148 to Figure 153).<sup>151,175,264,265</sup>

With compatibility for bulk-production (of around 100 mg Janus Particles per batch), distinctive asymmetric assembly of gold nanoparticles with minimal aggregates from multiple SEM observations, confirms that the colloidosome protocol is successfully robust and highly reproducible. Figure 89 illustrates the high AuNP density per JP synthesized in our work compared with lower density in JP from literature.<sup>227</sup>

#### 2.4.5 Gold/Silica Janus Particle via Physical Vapour Deposition Method

For an optimized coverage of gold layer on SP for Gold/Silica Janus Particles produced from physical vapour deposition methods (from here on referred as PVD-JP), it is important to have monolayer deposition (on the chosen substrate). As per theoretical calculation (see Table 10) ~19 µL SP suspension was required to spin coat a monolayer of SP over glass slide substrate. However, loss of particles (SP) during transfer (from stock suspension to substrate) is inevitable (from sticking to micropipette tip and after multiple spin-coating attempts, an excessive quantity of 200 µL SP suspension was found optimal for obtaining SP monolayer and therefore, standardized for PVD-JP production in this thesis.

Table 10 : Minimal volume of SP suspension required for a monolayer deposited on a glass substrate.

Surface area of substrate (nm <sup>2</sup> )	No. of SP for monolayering (+)	Required volume of SP suspension (at ~114 mg/mL SP concentration) (*)
3.75 x 10 <sup>15</sup>	1.66 x 10 <sup>10</sup>	19 µL

$$(+)\text{ No. of SP for monolayering} \Rightarrow \frac{\text{Substrate surface area}}{\text{Topological area of SP} + \text{Area of void}}$$

$$(*) \text{Equivalent Vol. of SP} \Rightarrow \frac{\text{Wt. of required SP}}{\text{Wt. of SP in 1 mL SP suspension}}$$

$$\text{Surface area of substrate} = \text{Length} \times \text{Breadth of glass slide} = 3.75 \times 10^{15} \text{ nm}^2$$

Once monolayer of SP was obtained, another important aspect being making of PVD-JP was the optimal thickness of gold-layer, which was decided to be 20 nm in our work. Primary reason to finalize this thickness was the size of gold nanoparticles (used in chemical synthesis). 20 nm being close to AuNP size and avoiding further excessive weight with an add-on benefit to the ease in SEM characterization (20 nm gold metal layer was within good resolution-range of our SEM set-up) and therefore, helped in standardizing this thickness for the PVD-JP.

Lastly, hours long ultrasonication of the glass slide (submerged in Milli-Q water) ensured maximum extraction of physically produced gold/silica janus particles (PVD-JP). This step also required optimization as short period ultrasonication of ~15 to 30 mins was not helpful in extraction of the PVD-JP (confirmed from lack of particles in DLS and SEM observation). Upon successful extraction of PVD-JP, DLS observations helped in obtaining characteristic correlogram of PVD-JP (Figure 90). Plateau in correlogram of PVD-JP were similar to the correlograms of SP (Figure 69), Iso (Figure 78) and chemically synthesized gold/silica Janus particle (JP) (Figure 85). Whereas the baseline fluctuations were on similar trend with that of other surface modified particles.

Proper re-dispersion of PVD-JP in DLS samples was ensured by vortex mixing of 10 seconds before each DLS measurements. Smoother anisotropic surface of PVD-JP than JP could explain comparatively smooth fluctuating baseline in PVD-JP samples.

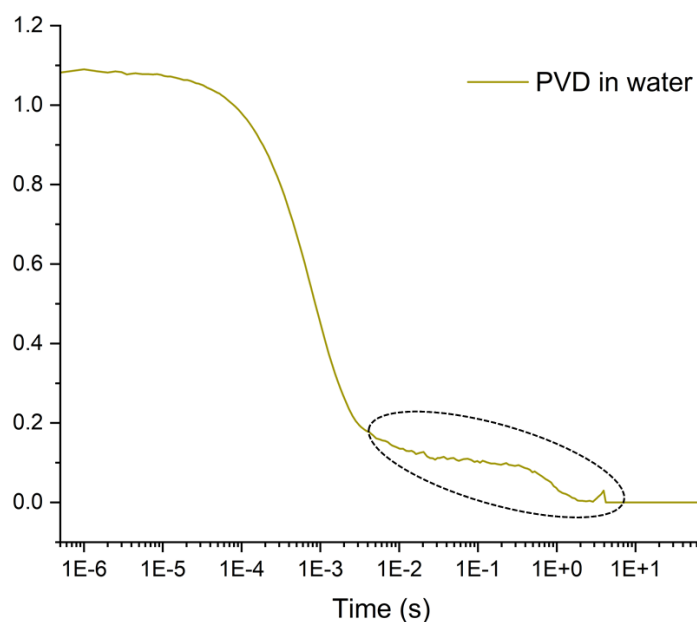


Figure 90: Correlogram for gold/silica Janus Particles produced from Physical Vapour Deposition technique. Plateau resembles with SP, Iso and JP, while fluctuating baseline signature is smoother than that in Iso and JP.

The gold layer was observed by SEM and compared to the case where gold was deposited without pre-deposition of a chromium layer. SEM observation in Figure 91 highlights the effect of adhesion layer before gold deposition on silica. Figure 91.A shows PVD-JP with stronger adhesion layer of 0.5 nm chromium layer that supports nucleation of the later deposited 20 nm Gold Layer, while Figure 91.B shows for PVD-JP having direct deposition of Gold Layer onto the surface of pristine silica particles.

Unlike PVD-JP in Figure 91.A, Gold layer in Figure 91.A possess rough boundaries, which is likely due to the mechanical stress exerted on particle during extraction via manual scrapping. As particles have weaker gold-silica adhesion, only short duration of ultrasonic-bath was used to avoid the gold detachment of the silica particles. This was insufficient to extract particles off glass substrate. While PVD-JP with Cr intermediate layer was extracted after an hour-long ultra-sonic baths; avoiding manual scrapping, therefore leading to smooth boundaries of gold layer. Rashidi<sup>266</sup> and team worked on local measurement of gold layer in gold/polystyrene Janus particle (G/PS) (5  $\mu\text{m}$  diameter) cross-section of a G/PS was obtained by using focused ion beam (FIB).

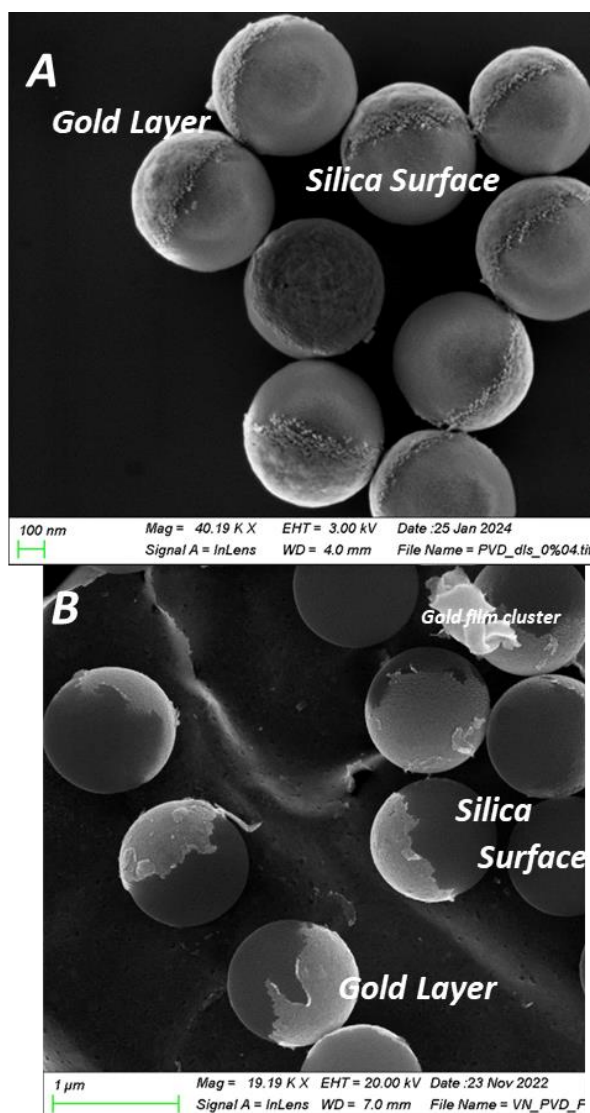


Figure 91: SEM images of PVD-JP. Image A shows PVD-JP with intermediate Chromium Layer between Gold and Silica. Image B shows PVD-JP with direct Gold Layer deposited onto the surface of Silica particles (no intermediate Chromium layer). Smooth boundaries of gold layer in A proves homogenous and better quality particle than that with rough boundaries in B.

However, as our particles are of sub-micron scale, using FIB to observe the cross-section was not a feasible option. Therefore, rough estimation of deposited gold layer was achieved by calculating the thickness gold layer from SEM observation of 17 PVD-JP. At the resolution of  $\sim 5.56$  nm/pixels, the value for gold layer in central position was  $\sim 20 \pm 2$  nm, and  $\sim 18 \pm 2$  nm around the edges, which is due to the curvature of spherical silica particles. These values were in coherence with the deposited value during physical vapour deposition.

SEM result for particle size, thickness of gold layer per PVD-JP, volume of gold cap, weight of gold cap, etc. is summarized in Table 11, where  $G_t/P$  refers to the thickness of gold layer deposited per Silica Particle via Physical Vapour Deposition to produce PVD-JP,  $V_{AuCap}$ , and  $W_{AuCap}$  is the volume and weight of gold layer, respectively,  $v_p$  and  $w_p$  is the volume and weight of single PVD-JP, respectively.

Table 11: Result for properties of PVD-JP (gold/silica Janus particle produced from Physical Vapour Deposition method) with silica density of 2.32 g/cc.

<b>Diameter (Max.)</b>	<b>495 nm</b>
<b><math>G_t/P</math></b>	20 nm
<b><math>V_{AuCap}</math></b>	$8.50 \times 10^{-21} \text{ m}^3$
<b><math>W_{AuCap}</math></b>	$1.64 \times 10^{-13} \text{ g}$
<b><math>v_p</math></b>	$6.46 \times 10^{-20} \text{ m}^3$
<b><math>w_p</math></b>	$2.94 \times 10^{-13} \text{ g}$

Values for all the finalized particles synthesized in this chapter are summarized in

Table 27 and respective different properties of these particles in Table 12, followed by the summary of characterization techniques of particles synthesized in unit “2.3 “ highlighted in Figure 92.

Table 12: Features of particles synthesized in this thesis work (\*).

Serial No.	Parameter	AuNP	SP	Iso	JP	PVD-JP
1	Concentration (in 1 mL suspension)	3.12E+11	5.68E+10	unknown	unknown	unknown
2	Diameter (m)	2.50E-08	4.75E-07	5.25E-07	5.00E-07	4.95E-07
3	G/P	-	-	217	109	-
4	AuNP/mL Suspension	3.12E+14	-	unknown	unknown	unknown
5	$v_p$ (m <sup>3</sup> )	8.18E-24	5.61E-20	5.79E-20	5.70E-20	6.46E-20
6	$V_p$ (m <sup>3</sup> )	2.55E-11	3.19E-09	unknown	unknown	unknown

## Particle Production

<b>8</b>	$w_p$ (g)	1.58E-16	1.30E-13	1.64E-13	1.47E-13	2.94E-13
<b>9</b>	$W_p$ (g)	4.93E-05	7.40E-03	unknown	unknown	unknown
<b>10</b>	$T_{sa}$ (m <sup>2</sup> )	1.96E-15	7.09E-13	1.13E-12	9.22E-13	7.70E-13
<b>11</b>	$TSA$ (m <sup>2</sup> )	6.13E-04	4.03E-02	unknown	unknown	unknown
<b>12</b>	$T_a$ (m <sup>2</sup> )	4.91E-16	1.77E-13	2.16E-13	1.96E-13	1.92E-13
<b>13</b>	$TA$ (m <sup>2</sup> )	1.53E-04	1.01E-02	unknown	unknown	unknown

\*  $G/P$  is the total number of AuNP per respective particle,  $v_p$  is volume of 1 Particle,  $V_p$  is total volume of particles per 1 mL particle suspension,  $w_p$  is weight of 1 particle,  $W_p$  is total weight of particles per 1 mL particle suspension,  $t_{sa}$  is total surface area of 1 particle,  $TSA$  is total surface area of particle per 1 mL particle suspension,  $t_a$  is topological surface of 1 particle, and  $TA$  is topological area of particles per 1 mL particle suspension.

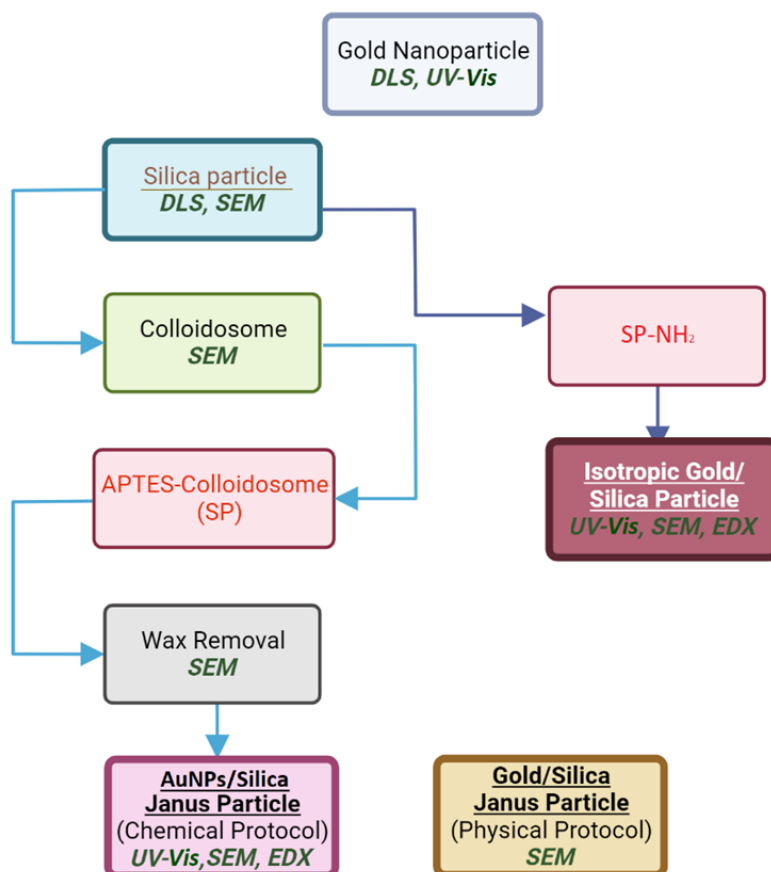


Figure 92: Summary flowchart briefing all the particle synthesis/ key steps with their respective characterization techniques (Particles inside Bold borders have been characterized and the underlined particles are further used in Chapter 3 and 4).

## 2.5 Conclusion

Customization of chemical synthesis protocol for synthesis of Gold/Silica Janus particle with asymmetrical grafting of gold nanoparticles on silica particles was successfully achieved, giving a robust protocol based on the colloidosome procedure. Outcome of the protocol adaptation was the efficiency for gram-scale production of Colloidosomes. These were produced by quenching wax/water Pickering emulsion stabilized by SP partially covered by CTAB. The optimal concentration of CTAB was found from the zeta potential variation of SP with increasing the CTAB concentration and observation of the formed colloidosomes. SEM characterization of Colloidosome confirmed that CTAB concentration leading to an increasing of the SP zeta potential to -52 to -50 mV was most suited for optimal surface coverage of SP at the surface of the colloidosomes (with respect to the wax used in our study with a melting point range of 57-65°C). This protocol has to be readapted for a different wax reference.

While "green" method inspired by Cuq<sup>237</sup> was implemented effectively for APTES grafting, choosing suitable APTES solvent (due to incompatibility of commonly used solvents with the paraffin wax) was another challenge faced during JP synthesis. Dissolution of paraffin wax off colloidosome post APTES-functionalization was achieved by using hexane coupled with ultra-sonication bath<sup>229</sup>. Considering the toxicity of hexane alternatives like softer paraffin with narrow range of low melting point for colloidosome synthesis could be an option to go towards greener solvents. While UV-Vis spectrometry and EDX characterization of JP and Iso confirmed the presence of gold nanoparticles qualitatively, SEM observations were helpful in quantitative analysis of particle, calculating the mean size, gold population. Reproducibility of JP with homogeneous distribution of gold nanoparticles in non-aggregated pattern confirmed the robustness and reliable quality of the synthesis protocol. We can conclude that the chemical-method protocol for Janus particle is controlled through an optimized hydrophobization of the SP surfaces, allowing the formation of colloidosomes for partial APTES functionalization and finally the removal of WAXS and AuNPs attachment. On the other hand, the physical-method protocol is simple, high yielding but incompatible for bulk production. PVD-JP with adverse effect of long ultra-sonication proved robustness and highlighted the importance of an intermediate adhesion layer of Chromium between gold and silica particles.

Chapter 2 not only presents successful particle production but also serves as a detailed guide for synthesizing other types of Janus particles, particularly those interacting with hydrogen peroxide, such as copper and platinum.<sup>196,197,200,201</sup> The difference in the interaction of hydrogen peroxide with particles (SP, Iso, JP and PVD-JP) studied both in bulk and individually is unraveled and discussed in the upcoming chapters.

## 2.6 Reference

- (1) Stöber, W.; Fink, A.; Bohn, E. Controlled Growth of Monodisperse Silica Spheres in the Micron Size Range. *Journal of Colloid and Interface Science* **1968**, 26 (1), 62–69. [https://doi.org/10.1016/0021-9797\(68\)90272-5](https://doi.org/10.1016/0021-9797(68)90272-5).
- (2) Turkevich, J.; Stevenson, P. C.; Hillier, J. A Study of the Nucleation and Growth Processes in the Synthesis of Colloidal Gold. *Discuss. Faraday Soc.* **1951**, 11 (0), 55–75. <https://doi.org/10.1039/DF9511100055>.
- (3) Allaire, A. *Synthesis of Chemotactic Janus Nanoparticles*. 2023.
- (4) Sivaraman, S. K.; Kumar, S.; Santhanam, V. Monodisperse Sub-10 Nm Gold Nanoparticles by Reversing the Order of Addition in Turkevich Method--the Role of Chloroauric Acid. *J Colloid Interface Sci* **2011**, 361 (2), 543–547. <https://doi.org/10.1016/j.jcis.2011.06.015>.
- (5) Muñoz, M. I. CRISTALES FOTÓNICOS BASADOS EN ÓPALOS. 2003. [https://wp.icmm.csic.es/wp-content/uploads/sites/22/2019/11/Tesis\\_Marta.pdf](https://wp.icmm.csic.es/wp-content/uploads/sites/22/2019/11/Tesis_Marta.pdf).
- (6) Echevsky, G. V.; Toktarev, A. V.; Kodenev, E. G.; Aksenov, D. G. Development of Highly Efficient Hydroisodeparaffinization Catalysts Based on Micro-Mesoporous SAPO-31: New Approaches in the Synthesis of SAPO-31 and the Preparation of Bifunctional Catalysts. *Catalysts* **2023**, 13 (5), 810. <https://doi.org/10.3390/catal13050810>.
- (7) Ibisate Muñoz, M. Cristales fotónicos basados en ópalos. <http://purl.org/dc/dcmitype/Text>, Universidad Autónoma de Madrid, 2003. <https://dialnet.unirioja.es/servlet/tesis?codigo=27392>.
- (8) Avossa, J.; Esteves, A. C. C. Influence of Experimental Parameters on the Formation and Stability of Silica-Wax Colloidosomes. *Journal of Colloid and Interface Science* **2020**, 561, 244–256. <https://doi.org/10.1016/j.jcis.2019.11.011>.
- (9) Hong, L.; Jiang, S.; Granick, S. Simple Method to Produce Janus Colloidal Particles in Large Quantity. *Langmuir* **2006**, 22 (23), 9495–9499. <https://doi.org/10.1021/la062716z>.
- (10) Perro, A.; Meunier, F.; Schmitt, V.; Ravaine, S. Production of Large Quantities of “Janus” Nanoparticles Using Wax-in-Water Emulsions. *Colloids and Surfaces A: Physicochemical and Engineering Aspects* **2009**, 332 (1), 57–62. <https://doi.org/10.1016/j.colsurfa.2008.08.027>.
- (11) Archer, R. J.; Parnell, A. J.; Campbell, A. I.; Howse, J. R.; Ebbens, S. J. A Pickering Emulsion Route to Swimming Active Janus Colloids. *Advanced Science* **2018**, 5 (2), 1700528. <https://doi.org/10.1002/adv.201700528>.
- (12) Vikash; Kumar, V. Ultrasonic-Assisted de-Agglomeration and Power Draw Characterization of Silica Nanoparticles. *Ultrasonics Sonochemistry* **2020**, 65, 105061. <https://doi.org/10.1016/j.ultsonch.2020.105061>.
- (13) Preparation of amino-functionalized silica in aqueous conditions - ScienceDirect. <https://www.sciencedirect.com/science/article/abs/pii/S0169433212020946?via%3Dihub>.
- (14) Cuoq, F.; Masion, A.; Labille, J.; Rose, J.; Ziarelli, F.; Prelot, B.; Bottero, J.-Y. Preparation of Amino-Functionalized Silica in Aqueous Conditions. *Applied Surface Science* **2013**, 266, 155–160. <https://doi.org/10.1016/j.apsusc.2012.11.120>.
- (15) Karnati, S. R.; Oldham, D.; Fini, E. H.; Zhang, L. Surface Functionalization of Silica Nanoparticles to Enhance Aging Resistance of Asphalt Binder. *Construction and Building Materials* **2019**, 211, 1065–1072. <https://doi.org/10.1016/j.conbuildmat.2019.03.257>.
- (16) Kalies, S.; Gentemann, L.; Schomaker, M.; Heinemann, D.; Ripken, T.; Meyer, H. Surface Modification of Silica Particles with Gold Nanoparticles as an Augmentation of Gold Nanoparticle Mediated Laser Perforation. *Biomed Opt Express* **2014**, 5 (8), 2686–2696. <https://doi.org/10.1364/BOE.5.002686>.
- (17) Choi, S.-S.; Im, S.-H.; Park, J.-H.; Kim, J. S. Analysis of Wax Solubility of Rubber Vulcanizates Using Wax Solution in Toluene and Molten Wax. *Polymer Testing* **2009**, 28 (7), 696–701. <https://doi.org/10.1016/j.polymertesting.2009.05.012>.
- (18) Grishin, A. P.; Kosolapova, A. P. The Solubility of Paraffin in a Mixture of Acetone and Toluene. *Chem Technol Fuels Oils* **1965**, 1 (5), 362–365. <https://doi.org/10.1007/BF00718554>.
- (19) Chiamaka, E.; Ajediti, O. B. Effect and Remediation of Wax Precipitate on Petroleum Production Tubing for A Crude Oil Sample from The Niger Delta. **2023**, 4 (6). <https://ijrpr.com/uploads/V4ISSUE6/IJRPR14351.pdf>.
- (20) Cuoq, F.; Masion, A.; Labille, J.; Rose, J.; Ziarelli, F.; Prelot, B.; Bottero, J.-Y. Preparation of Amino-Functionalized Silica in Aqueous Conditions. *Applied Surface Science* **2013**, 266, 155–160. <https://doi.org/10.1016/j.apsusc.2012.11.120>.
- (21) Ortega-Liebana, M. C.; Bonet-Aleta, J.; Hueso, J. L.; Santamaria, J. Gold-Based Nanoparticles on Amino-Functionalized Mesoporous Silica Supports as Nanozymes for Glucose Oxidation. *Catalysts* **2020**, 10 (3), 333. <https://doi.org/10.3390/catal10030333>.
- (22) Mihj, A.; Ocaña, M.; Míguez, H. Oriented Colloidal-Crystal Thin Films by Spin-Coating Microspheres Dispersed in Volatile Media. *Advanced Materials* **2006**, 18 (17), 2244–2249. <https://doi.org/10.1002/adma.200600555>.
- (23) Arutinov, G.; Brichkin, S. B.; Razumov, V. F. Self-Assembling of Polystyrene Microsphere Monolayers by Spin-Coating. *Nanotechnol Russia* **2010**, 5 (1), 67–72. <https://doi.org/10.1134/S1995078010010064>.
- (24) Moazzez, B.; O'Brien, S. M.; Merschrod S., E. F. Improved Adhesion of Gold Thin Films Evaporated on Polymer Resin: Applications for Sensing Surfaces and MEMS. *Sensors* **2013**, 13 (6), 7021–7032. <https://doi.org/10.3390/s130607021>.
- (25) Todeschini, M.; Bastos da Silva Fanta, A.; Jensen, F.; Wagner, J. B.; Han, A. Influence of Ti and Cr Adhesion Layers on Ultrathin Au Films. *ACS Appl. Mater. Interfaces* **2017**, 9 (42), 37374–37385. <https://doi.org/10.1021/acsami.7b10136>.
- (26) George, M. A.; Glaunsinger, W. S.; Thundat, T.; Lindsay, S. M. Electrical, Spectroscopic, and Morphological Investigation of Chromium Diffusion through Gold Films. *Thin Solid Films* **1990**, 189 (1), 59–72. [https://doi.org/10.1016/0040-6090\(90\)90027-B](https://doi.org/10.1016/0040-6090(90)90027-B).

- (27) Moody, N. R.; Adams, D. P.; Medlin, D.; Headley, T.; Yang, N.; Volinsky, A. Effects of Diffusion on Interfacial Fracture of Gold-Chromium Hybrid Microcircuit Films. *International Journal of Fracture* **2003**, 120 (1), 407–419. <https://doi.org/10.1023/A:1024979829573>.
- (28) Mulvaney, P. Surface Plasmon Spectroscopy of Nanosized Metal Particles. *Langmuir* **1996**, 12 (3), 788–800. <https://doi.org/10.1021/la9502711>.
- (29) Jain, P. K.; Lee, K. S.; El-Sayed, I. H.; El-Sayed, M. A. Calculated Absorption and Scattering Properties of Gold Nanoparticles of Different Size, Shape, and Composition: Applications in Biological Imaging and Biomedicine. *J. Phys. Chem. B* **2006**, 110 (14), 7238–7248. <https://doi.org/10.1021/jp057170o>.
- (30) Huang, X.; El-Sayed, M. A. Gold Nanoparticles: Optical Properties and Implementations in Cancer Diagnosis and Photothermal Therapy. *Journal of Advanced Research* **2010**, 1 (1), 13–28. <https://doi.org/10.1016/j.jare.2010.02.002>.
- (31) Koppel, D. E. Analysis of Macromolecular Polydispersity in Intensity Correlation Spectroscopy: The Method of Cumulants. *The Journal of Chemical Physics* **1972**, 57 (11), 4814–4820. <https://doi.org/10.1063/1.1678153>.
- (32) Yu, Z.; Reid, J. C.; Yang, Y.-P. Utilizing Dynamic Light Scattering as a Process Analytical Technology for Protein Folding and Aggregation Monitoring in Vaccine Manufacturing. *JPharmSci* **2013**, 102 (12), 4284–4290. <https://doi.org/10.1002/jps.23746>.
- (33) Varenne, F.; Botton, J.; Merlet, C.; Beck-Broichsitter, M.; Legrand, F.-X.; Vauthier, C. Standardization and Validation of a Protocol of Size Measurements by Dynamic Light Scattering for Monodispersed Stable Nanomaterial Characterization. *Colloids and Surfaces A: Physicochemical and Engineering Aspects* **2015**, 486, 124–138. <https://doi.org/10.1016/j.colsurfa.2015.08.043>.
- (34) Stetefeld, J.; McKenna, S. A.; Patel, T. R. Dynamic Light Scattering: A Practical Guide and Applications in Biomedical Sciences. *Biophys Rev* **2016**, 8 (4), 409–427. <https://doi.org/10.1007/s12551-016-0218-6>.
- (35) Malvern Zetasizer ZS DLS User Manual.Pdf. <https://www.chem.uci.edu/~dmitryf/manuals/Malvern%20Zetasizer%20ZS%20DLS%20User%20manual.pdf>.
- (36) Vig, J.; LeBus, J. UV/Ozone Cleaning of Surfaces. *IEEE Trans. Parts, Hybrids, Packag.* **1976**, 12 (4), 365–370. <https://doi.org/10.1109/TPHP.1976.1135156>.
- (37) Terahertz Multispectral Imaging for the Analysis of Gold Nanoparticles' Size and the Number of Unit Cells in Comparison with Other Techniques. *IJBSBE* **2018**, Volume 4 (Issue 3). <https://doi.org/10.15406/ijbsbe.2018.04.00118>.
- (38) Hendel, T.; Wuithschick, M.; Kettemann, F.; Birnbaum, A.; Rademann, K.; Polte, J. In Situ Determination of Colloidal Gold Concentrations with UV–Vis Spectroscopy: Limitations and Perspectives. *Anal. Chem.* **2014**, 86 (22), 11115–11124. <https://doi.org/10.1021/ac502053s>.
- (39) Kimling, J.; Maier, M.; Okenve, B.; Kotaidis, V.; Ballot, H.; Plech, A. Turkevich Method for Gold Nanoparticle Synthesis Revisited. *J Phys Chem B* **2006**, 110 (32), 15700–15707. <https://doi.org/10.1021/jp061667w>.
- (40) Dong, J.; Carpinone, P. L.; Pyrgiotakis, G.; Demokritou, P.; Moudgil, B. M. Synthesis of Precision Gold Nanoparticles Using Turkevich Method. *KONA* **2020**, 37 (0), 224–232. <https://doi.org/10.14356/kona.2020011>.
- (41) Geertsen, V.; Barruet, E.; Gobeaux, F.; Lacour, J.-L.; Taché, O. Contribution to Accurate Spherical Gold Nanoparticle Size Determination by Single-Particle Inductively Coupled Mass Spectrometry: A Comparison with Small-Angle X-Ray Scattering. *Anal. Chem.* **2018**, 90 (16), 9742–9750. <https://doi.org/10.1021/acs.analchem.8b01167>.
- (42) Liu, X.; Atwater, M.; Wang, J.; Huo, Q. Extinction Coefficient of Gold Nanoparticles with Different Sizes and Different Capping Ligands. *Colloids and Surfaces B: Biointerfaces* **2007**, 58 (1), 3–7. <https://doi.org/10.1016/j.colsurfb.2006.08.005>.
- (43) Leong, S. S.; Ng, W. M.; Lim, J.; Yeap, S. P. Dynamic Light Scattering: Effective Sizing Technique for Characterization of Magnetic Nanoparticles. In *Handbook of Materials Characterization*; Sharma, S. K., Ed.; Springer International Publishing: Cham, 2018; pp 77–111. [https://doi.org/10.1007/978-3-319-92955-2\\_3](https://doi.org/10.1007/978-3-319-92955-2_3).
- (44) Lorber, B.; Fischer, F.; Bailly, M.; Roy, H.; Kern, D. Protein Analysis by Dynamic Light Scattering: Methods and Techniques for Students. *Biochemistry and Molecular Biology Education* **2012**, 40 (6), 372–382. <https://doi.org/10.1002/bmb.20644>.
- (45) Misono, T. Dynamic Light Scattering (DLS). In *Measurement Techniques and Practices of Colloid and Interface Phenomena*; Abe, M., Ed.; Springer: Singapore, 2019; pp 65–69. [https://doi.org/10.1007/978-981-13-5931-6\\_10](https://doi.org/10.1007/978-981-13-5931-6_10).
- (46) Avossa, J.; Esteves, A. C. C. Influence of Experimental Parameters on the Formation and Stability of Silica-Wax Colloidosomes. *Journal of Colloid and Interface Science* **2020**, 561, 244–256. <https://doi.org/10.1016/j.jcis.2019.11.011>.
- (47) Irfan, M.; Usman, M.; Mansha, A.; Rasool, N.; Ibrahim, M.; Rana, U. A.; Siddiq, M.; Zia-Ul-Haq, M.; Jaafar, H. Z. E.; Khan, S. U.-D. Thermodynamic and Spectroscopic Investigation of Interactions between Reactive Red 223 and Reactive Orange 122 Anionic Dyes and Cetyltrimethyl Ammonium Bromide (CTAB) Cationic Surfactant in Aqueous Solution. *The Scientific World Journal* **2014**, 2014, e540975. <https://doi.org/10.1155/2014/540975>.
- (48) Liu, Y.; Tourbin, M.; Lachaize, S.; Guiraud, P. Silica Nanoparticles Separation from Water: Aggregation by Cetyltrimethylammonium Bromide (CTAB). *Chemosphere* **2013**, 92 (6), 681–687. <https://doi.org/10.1016/j.chemosphere.2013.03.048>.
- (49) Petit, L.; Manaud, J.-P.; Mingotaud, C.; Ravaine, S.; Duguet, E. Sub-Micrometer Silica Spheres Dissymmetrically Decorated with Gold Nanoclusters. *Materials Letters* **2001**, 51 (6), 478–484. [https://doi.org/10.1016/S0167-577X\(01\)00338-X](https://doi.org/10.1016/S0167-577X(01)00338-X).
- (50) Yang, Q.; De Vries, M. H.; Picchioni, F.; Loos, K. A Novel Method of Preparing Metallic Janus Silica Particles Using Supercritical Carbon Dioxide. *Nanoscale* **2013**, 5 (21), 10420. <https://doi.org/10.1039/c3nr81280d>.



- (51) Lu, Y.; Xiong, H.; Jiang, X.; Xia, Y.; Prentiss, M.; Whitesides, G. M. Asymmetric Dimers Can Be Formed by Dewetting Half-Shells of Gold Deposited on the Surfaces of Spherical Oxide Colloids. *J. Am. Chem. Soc.* **2003**, *125* (42), 12724–12725. <https://doi.org/10.1021/ja0373014>.
- (52) Percebom, A. M.; Giner-Casares, J. J.; Claes, N.; Bals, S.; Loh, W.; Liz-Marzán, L. M. Janus Gold Nanoparticles Obtained via Spontaneous Binary Polymer Shell Segregation †Electronic Supplementary Information (ESI) Available: Experimental Procedures, Results of SAXS, UV-Vis and DLS for NPs of Different Core Sizes, Polymer Coatings and in Different Solvents; Details of Emulsification Using Janus Au NPs; TEM Images after Silica Coating of Janus Au NPs; 3D Images of Different Stained Au NPs. See DOI: 10.1039/C5cc10454h Click Here for Additional Data File. *Chem Commun (Camb)* **2016**, *52* (23), 4278–4281. <https://doi.org/10.1039/c5cc10454h>.
- (53) Marina Santana Vega; Andrés Guerrero Martínez; Fabio Cucinotta. Facile Strategy for the Synthesis of Gold@Silica Hybrid Nanoparticles with Controlled Porosity and Janus Morphology. *Nanomaterials (Basel, Switzerland)* **2019**, *9* (3), 348. <https://doi.org/10.3390/nano9030348>.
- (54) Trayford, C.; Crosbie, D.; Rademakers, T.; van Blitterswijk, C.; Nuijts, R.; Ferrari, S.; Habibovic, P.; LaPointe, V.; Dickman, M.; van Rijt, S. Mesoporous Silica-Coated Gold Nanoparticles for Multimodal Imaging and Reactive Oxygen Species Sensing of Stem Cells. *ACS Appl. Nano Mater.* **2022**, *5* (3), 3237–3251. <https://doi.org/10.1021/acsnm.1c03640>.
- (55) Rashidi, A.; Issa, M. W.; Martin, I. T.; Avishai, A.; Razavi, S.; Wirth, C. L. Local Measurement of Janus Particle Cap Thickness. *ACS Appl. Mater. Interfaces* **2018**, *10* (37), 30925–30929. <https://doi.org/10.1021/acsami.8b11011>.
- (56) Tauran, Y.; Brioude, A.; Coleman, A. W.; Rhimi, M.; Kim, B. Molecular Recognition by Gold, Silver and Copper Nanoparticles. *World J Biol Chem* **2013**, *4* (3), 35–63. <https://doi.org/10.4331/wjbc.v4.i3.35>.
- (57) Xin, Y.; Yu, K.; Zhang, L.; Yang, Y.; Yuan, H.; Li, H.; Wang, L.; Zeng, J. Copper-Based Plasmonic Catalysis: Recent Advances and Future Perspectives. *Advanced Materials* **2021**, *33* (32), 2008145. <https://doi.org/10.1002/adma.202008145>.
- (58) Kowalska, E.; Abe, R.; Ohtani, B. Visible Light-Induced Photocatalytic Reaction of Gold-Modified Titanium(IV) Oxide Particles: Action Spectrum Analysis. *Chem. Commun.* **2009**, No. 2, 241–243. <https://doi.org/10.1039/B815679D>.
- (59) Pham, X.-H.; Tran, V.-K.; Hahm, E.; Kim, Y.-H.; Kim, J.; Kim, W.; Jun, B.-H. Synthesis of Gold-Platinum Core-Shell Nanoparticles Assembled on a Silica Template and Their Peroxidase Nanozyme Properties. *International Journal of Molecular Sciences* **2022**, *23* (12), 6424. <https://doi.org/10.3390/ijms23126424>.
- (60) Dynamic Light Scattering Particle Size Distribution Analysis. <https://www.horiba.com/int/scientific/technologies/dynamic-light-scattering-dls-particle-size-distribution-analysis/dynamic-light-scattering-dls-particle-size-distribution-analysis/>.
- (61) Kaszuba, M. A basic introduction to Dynamic Light Scattering (DLS) for particle size analysis - Q&A - Materials Talks. <https://www.materials-talks.com/a-basic-introduction-to-dynamic-light-scattering-dls-for-particle-size-analysis-qa/>.
- (62) Rayleigh Scattering. <https://site.physics.georgetown.edu/~vankeu/webtext2/Workspace/Rayleigh%20scattering/Rayleigh%20scattering.htm>.
- (63) Pons, T.; Uyeda, H. T.; Medintz, I. L.; Mattoussi, H. Hydrodynamic Dimensions, Electrophoretic Mobility, and Stability of Hydrophilic Quantum Dots. *J. Phys. Chem. B* **2006**, *110* (41), 20308–20316. <https://doi.org/10.1021/jp065041h>.
- (64) Carpenter, D. K. Dynamic Light Scattering with Applications to Chemistry, Biology, and Physics (Berne, Bruce J.; Pecora, Robert). *J. Chem. Educ.* **1977**, *54* (10), A430. <https://doi.org/10.1021/ed054pA430.1>.
- (65) The principles of dynamic light scattering | Anton Paar Wiki. Anton Paar. <https://wiki.anton-paar.com/en/the-principles-of-dynamic-light-scattering/>.
- (66) Jia, Z.; Li, J.; Gao, L.; Yang, D.; Kanaev, A. Dynamic Light Scattering: A Powerful Tool for In Situ Nanoparticle Sizing. *Colloids and Interfaces* **2023**, *7* (1), 15. <https://doi.org/10.3390/colloids7010015>.
- (67) Hassan, P. A.; Rana, S.; Verma, G. Making Sense of Brownian Motion: Colloid Characterization by Dynamic Light Scattering. ACS Publications. <https://doi.org/10.1021/la501789z>.
- (68) Akhtar, K.; Khan, S. A.; Khan, S. B.; Asiri, A. M. Scanning Electron Microscopy: Principle and Applications in Nanomaterials Characterization. In *Handbook of Materials Characterization*; Sharma, S. K., Ed.; Springer International Publishing: Cham, 2018; pp 113–145. [https://doi.org/10.1007/978-3-319-92955-2\\_4](https://doi.org/10.1007/978-3-319-92955-2_4).

# CHAPTER 3

## Chapter 3. Investigation of Particle Kinematics

### 3.1 Introduction

After the synthesis of particles (in Chapter 2), an essential focus of this thesis involved investigating the motion of particles and the influence of hydrogen peroxide on particles in motion in 3D and 2D. In Chapter 3, we try to understand the dynamics of various particle types; SP (Pristine Silica Particle), Iso (Isotropic Gold/Silica Particle), JP (chemically synthesized Gold/Silica Janus Particle), and PVD (physically synthesized Gold/Silica Janus Particle via Physical Vapour Deposition) and examined the impact of Hydrogen Peroxide ( $H_2O_2$ ) using two distinct techniques DLS and PTV (in realistic  $[H_2O_2]$  range; 0.1- 1.5 mM, refer Chapter 1). The first technique, dynamic light scattering (DLS), is a non-destructive technique that provided insights into three-dimensional motion. DLS measures the time-dependent fluctuations in scattered light intensity caused by the Brownian motion of the particles. DLS is a simple and time saving technique that has wide range of application in various fields like Nanoparticle Sizing (determining the hydrodynamic diameter of nanoparticles, colloids, and macromolecules in solution). It is particularly valuable for analyzing poly-disperse samples and can be useful in calculating diffusion coefficient of particles and understand the effects of hydrogen peroxide interaction. Outputs like polydispersity index, intercepts, hydrodynamic size helps in adjusting the sample concentration while values for diffusion coefficients is extractable from DLS correlogram. In the context of motion study, DLS emerges as an alternative high-throughput method for characterizing the 3D active motion in colloids, with capabilities to quantify time-dependent behavior across a various size of colloidal particles. DLS can act as a valuable tool for fast-screening characterization of active motion in Janus systems.<sup>1</sup> Despite its widespread use, DLS is not without challenges, especially in our case where some samples are prone to sedimentation. The technique may encounter limitations in the analysis of very large or highly aggregated particles, individual particle counting (unlike nanoparticle tracking analysis). Additionally, proper sample preparation and choice of measurement conditions are crucial for obtaining accurate and meaningful results.

Subsequently, the second technique Particle Tracking Velocimetry (PTV) is a detail-oriented technique, providing insights into the intricate motion of particles within a fluidic environment. The PTV studies discussed in Chapter 3 focused on 2D analysis of particles in motion in homogeneous concentration of  $H_2O_2$ . Optical observations for precise monitoring and analysis of individual particle trajectories, enabling a comprehensive understanding of fluid flow patterns and dynamics are the base of PTV. As  $H_2O_2$  is a strong oxidizing agent sensitive to light and heat, a well secure environment is essential, therefore, we performed PTV experiments in microfluidic channel to reduce the volume sample and offer a controlled environment for particle tracking experiments. Microfluidic chip used in this work was made of PDMS by soft-lithography technique (see further for more detail). PTV experiment set-up comprised of optical microscope, microfluidic chip, and pressure pump. In this work, real-time monitoring of particles-motion via PTV acts as a bridge between particle-motion and DLS-limitation by offering real-time optical monitoring of particles-motion. PTV set-up used in the experiments of this thesis was limited to monitoring particle-motion in two-dimensions. Therefore, motion in z-axis made particle out of focus causing multiple short-tracks instead of the real longer 3D paths that acted as a limitation for accurate path measurements. Coupling PTV, microfluidics and tracking software such as TrackMate (a plugin in Fiji) enhanced the precision and efficiency of particle tracking, with detailed

investigations into phenomena like Brownian motion, diffusion, and fluid velocity profiles at the microscale. TrackMate (TrackMate version 7)<sup>2</sup> is a versatile semi-automatic particle-tracking tool, excels in processing images or videos, allowing extraction of valuable information about particle trajectories and flow dynamics.<sup>2</sup> Plotting of these measurements is simple and can be done by browsing and exporting these measurements directly from the user interface (Figure 104). A master-intern Zakariya Ait Athmane developed Python code that was used in processing the results obtained from Trackmate during this thesis work.

## 3.2 Materials and Method

### 3.2.1 Material

#### 3.2.1.1 Chemicals and Material

Hydrogen Peroxide (30% (v/v)) (CAS N°: 7722-84-1) by Sigma Aldrich, Polydimethylsiloxane (PDMS) by, Sylgard 184 Ethanol Absolute by VWR Chemicals. Mili-Q water was used for all the experiments and storage (unless mentioned otherwise).

#### 3.2.1.2 Apparatus

Rotating agitator LD-76 from LABINCO BV, Ultrasonicator by, DLS instrument from Zetasizer Nano Series Nano by Malvern Panalytical, Biopsy Puncher 0.5 mm (SKU: PT-T983-05) by Fischer Scientific, Optical Microscope by Olympus CKX41, camera sCMOS PCO.edge model 3.1 by PCO .

#### 3.2.1.3 Glassware and Plastic ware

Eppendorf (1.5 mL), PMMA disposable cuvette (model ZEN0118, Cat. No. 7591 15) by BRAND® – Sigma Aldrich, Polypropylene cylindrical bottle (100 mL) (Nonpyrogenic) by Corning, UV Grade Fused Silica Wafer (Ø100mm) flat Corning 7980, Tube PEEK (external Ø510µm and internal Ø125µm) by CLUZeau Info Labo, Glass slide by Thermo Fischer.

### 3.2.2 Method (Experiment and Data Treatment)

#### 3.2.2.1 Experiment: Dynamic Light Scattering (DLS)

1. Thorough homogenization/re-dispersion of mother-batches of each particle (SP, Iso, JP and PVD) was done by a 5 min ultrasonic bath, followed mixed for 10 seconds vortex mixing.
2. Starting with SP sample at 0% (v/v) [H<sub>2</sub>O<sub>2</sub>], 999 µL Milli-Q water was added in a PMMA disposable cuvette, followed by the addition of 1 µL SP suspension (from the dedicated Eppendorf) and manual gentle mixing of suspended SP in Milli-Q water via micropipette for 10 seconds (avoiding bubble formation due to rigorous mixing). As particles were freshly synthesized, therefore did not required filtration. In case of old samples and aging, it is important to filter the samples with compatible filters, in order to counter particle aggregates.
3. Once the sample was prepared, transferred the cuvette into DLS sample holder, and ran DLS measurement (DLS parameters are same as that in the section “2.3.6.2”, Chapter 2).

4. Similarly, for SP at 0.5% (v/v) [H<sub>2</sub>O<sub>2</sub>], 982  $\mu$ L Milli-Q water was added in a PMMA disposable cuvette (model ZEN0118, Cat. No. 7591 15), followed by the addition of 1  $\mu$ L SP suspension (from the dedicated Eppendorf), 17  $\mu$ L 30% H<sub>2</sub>O<sub>2</sub> and manual gentle mixing of suspended SP in Milli-Q water and H<sub>2</sub>O<sub>2</sub> mixture, via micropipette for 10 seconds (avoiding bubble formation due to rigorous mixing).
5. For the other H<sub>2</sub>O<sub>2</sub> concentrations, similar protocol was used, adapting the volume of H<sub>2</sub>O<sub>2</sub> from mother solutions and keeping the final volume at 1000  $\mu$ L.

The particles (SP, Iso, JP and PVD) were analysed at five different concentrations of H<sub>2</sub>O<sub>2</sub> (0, 0.5, 1, 3 and 5 % (v/v)) and measurements were performed thrice; Round 1 Round 2 and Round 3 (R1, R2 and R3 respectively), with [H<sub>2</sub>O<sub>2</sub>] ranging between 0.1 – 1.5 mM. Optimal range of particle concentration in this study was established by testing a series of dilutions aimed at achieving a particle size measurement (independent of concentration). The mean value of counts (per second) was maintained in the range of 160-480 kcps (kilo counts per second). To mitigate the risk of dust contamination, the plastic container used for storing dispersing medium (Milli-Q water) underwent three rounds of rinsing with Milli-Q water and were changed for each set of experiment. This precautionary measure ensured the integrity of experiment setup and minimized the impact of external contaminants on the DLS measurements. While size and polydispersity are summarized in DLS output, sample quality can be understood from ratio of signal to background (intercept value shared in Table 32).<sup>3-6</sup>

### 3.2.2.2 Experiment: Particle Tracking Velocimetry (PTV)

#### 3.2.2.2.1 Soft Lithography (Microfabrication of PDMS microfluidic chip)

A mixture of PDMS (Polydimethylsiloxane) and crosslinking chemical (PDMS curing agent) poured onto the master mould, and heated for solidification. Upon curing, the negative replica of PDMS was peeled off the master mould, and inlets/outlets were created by the help of a biopsy punch. The PDMS block was then treated with oxygen plasma to make its surface hydrophilic, enabling bonding to a glass support to seal the microchannels. The specifications of procedures followed to make master mould (via photolithography) and PDMS chip (via soft-lithography) are shared in Chapter 4. The microfluidic chip (Figure 94) used here in Chapter 3 PTV experiments had two parallel channels connected with a small connecting channel, similar to the H-shape design (Figure 93). This device had height and width of about 45 $\mu$ m and 180  $\mu$ m respectively.

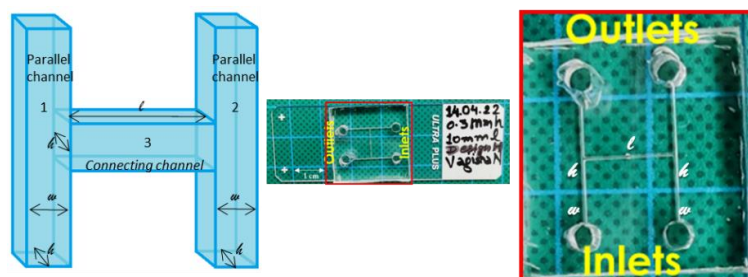
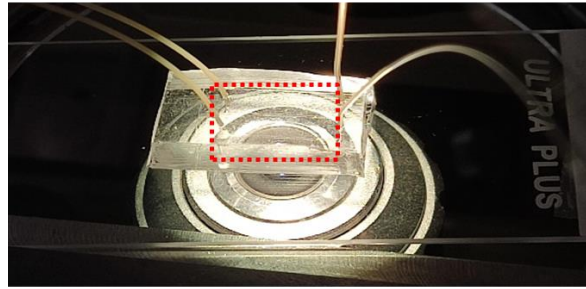


Figure 93: 3D illustration of H-design microfluidic channel (left); parallel channels (1 and 2) connected with a horizontal channel (3) of length  $l$  called bridge while the width and height throughout the chip is  $w$  and  $h$ . Microfluidic chip adhered onto a glass slide with inlets and outlets punched (centre) and zoomed image of chip (right)



Microfluidic Chip (H design) on Glass Slide

Figure 94: Microfluidic chip with H-design channels (red highlighted region, zoomed image is shared in figure 1), connected with inlet and outlet tubes

### 3.2.2.2.2 Experiment (PTV)

1. Filtered 1 mL SP from mother solution using PTFE syringe filter (pore size  $0.65\ \mu\text{m}$ ), followed by dilution in Milli-Q water (1:2) (and stored in refrigerator in new Eppendorf). Similarly, filter Iso and JP, followed by a dilution in Milli-Q water (1:1). This step eliminated any aggregates that could arise due to aging of samples.
2. Installed pressure-pump and loaded sample in it. Added 0, 17 and  $33\ \mu\text{L}$   $\text{H}_2\text{O}_2$  in 100, 83 and  $67\ \mu\text{L}$  particle suspension, respectively in sample-tube and mix manually for 10 seconds with micropipette, for experiment at 0, 5 and 10% (v/v) [ $\text{H}_2\text{O}_2$ ].
3. Connected the inlet of microfluidic chip with pressure-pump using a PEEK tube, and allowed sample flow into the microfluidic chip by maintaining system pressure at 1mBar.
4. Disconnected pressure-pump from the microfluidic chip to avoid convection driven motion in particle and make observations at ambient pressure.
5. After two-minute stabilization time (same as DLS) recorded 200 images at 40x magnification. Set camera exposure to 10 ms and frame rate at 10 FPS (frames per second).

In order to minimize light induced decomposition of hydrogen peroxide and motion due to thermal effects, microscope-lamp was maintained at medium intensity and was validated by experiments with SP samples.

### 3.2.2.3 Data Treatment (DLS)

Correlogram for SP, Iso, JP and PVD at different concentrations (0, 0.5, 1, 3 and 5% (v/v)) of  $\text{H}_2\text{O}_2$  are shown from Figure 95 to Figure 98 respectively. These correlograms are from the mean values of correlograms from all the three rounds (Round 1, Round 2 and Round 3) of independent DLS experiment. The correlogram graphs are representing the autocorrelation as function of time (decay time (s)) on a semi-log scale. SP correlogram in Figure 95 curves were very similar and unaffected by  $\text{H}_2\text{O}_2$ . They all had an initial change in slope at  $\sim 200\ \mu\text{s}$  lag time (red-squared region) and had smooth baselines (black-encircled region).

## Investigation of Particle Kinematics

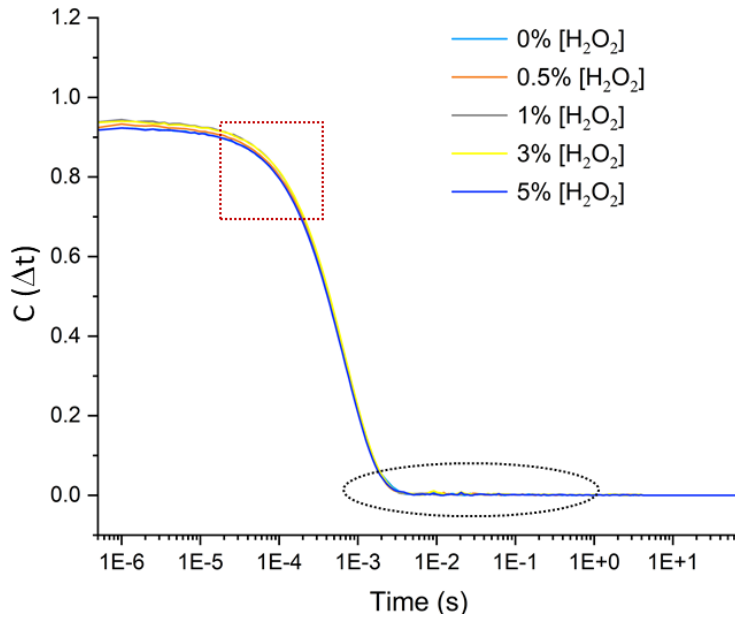


Figure 95: Mean correlograms for SP samples at respective concentrations of  $H_2O_2$ . Correlograms dropping in the same range (red-squared region) and have smooth baseline at all the concentrations of  $H_2O_2$  (black-encircled region).

For all the Iso samples (Figure 96), the baselines were not smooth as for SP samples (black-encircled region), an observation that is usually related to the presence of aggregates. We will discuss this point a little further. The red squared area (Figure 96) shows Iso at 1%  $H_2O_2$  (gray) bending first amongst the observed samples, while Iso at 0%  $H_2O_2$  (light blue) bending last.

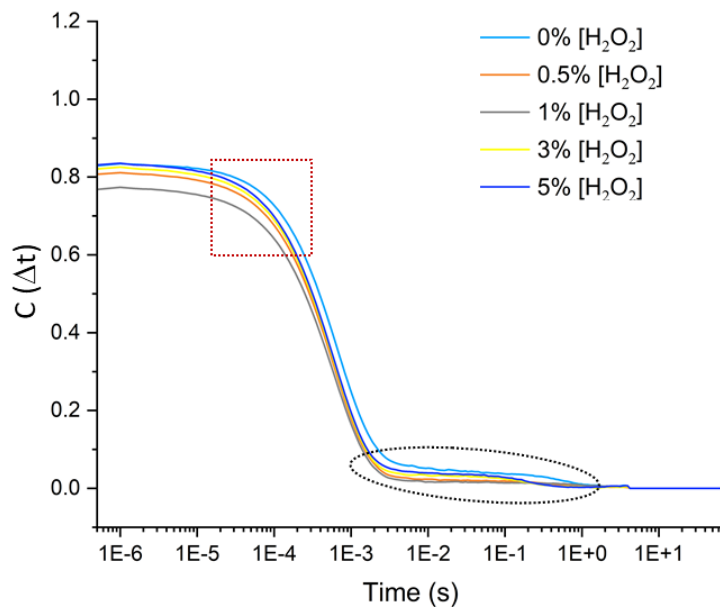


Figure 96: Mean correlograms for Iso samples at respective concentrations of  $H_2O_2$ . The red squared area highlights different behaviours regarding the  $H_2O_2$  concentration while unsmooth/fluctuating baseline (black-encircled zone) observed with all the Iso samples.

In the same manner for all the JP samples (Figure 97), the baseline were not smooth (black-encircled region). In the red squared area JP at 3% and 1% H<sub>2</sub>O<sub>2</sub> bends first while JP at 0% H<sub>2</sub>O<sub>2</sub> bending last (right most), and rest concentration samples (0.5 and 5%) in between.

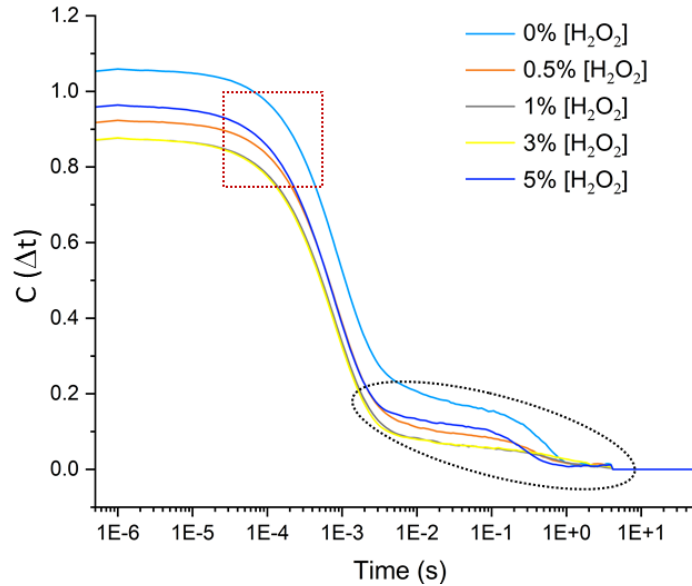


Figure 97: Mean correlograms for JP samples at respective concentrations of H<sub>2</sub>O<sub>2</sub>. The red squared area highlights different behaviours regarding the H<sub>2</sub>O<sub>2</sub> concentration. Highly unsmooth/fluctuating baseline (black-encircled zone) observed with JP at 0% H<sub>2</sub>O<sub>2</sub> (light blue) vs. comparatively lesser unsmooth baseline for rest of the samples.

For PVD samples (Figure 98), slope at 0% H<sub>2</sub>O<sub>2</sub> dropped at ~200 μs lag time whereas samples with 0.5 - 5% H<sub>2</sub>O<sub>2</sub> drop at ~100 μs lag time. Baseline for PVD at 0% H<sub>2</sub>O<sub>2</sub> had fluctuations that reduced on the introduction of H<sub>2</sub>O<sub>2</sub>.

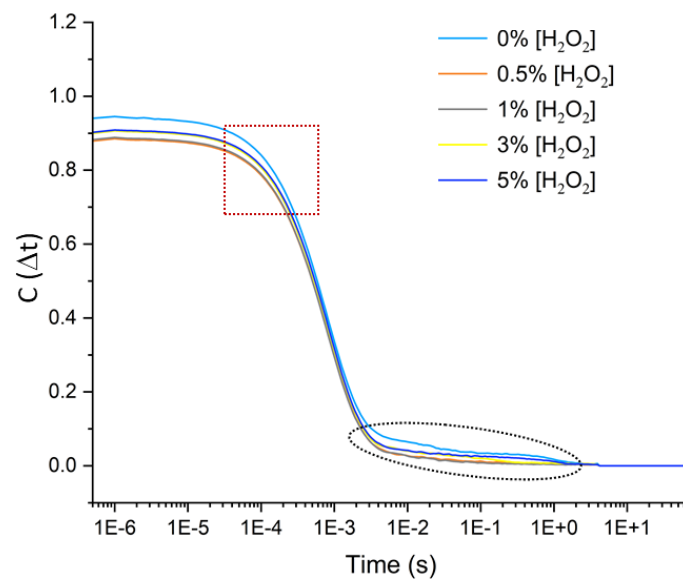


Figure 98: Mean correlograms for PVD at respective H<sub>2</sub>O<sub>2</sub> concentrations. Slope in the red squared area show at 0% H<sub>2</sub>O<sub>2</sub> (light blue) bends first (left most) and have more unsmooth/fluctuating baseline (black-encircled zone) than others.



DLS report gave us an estimate mean values for different properties for the analysed sample. Retrieval of physical values (diffusion coefficient) were done from the data obtained from correlation function (Eq. 1):

$$C(\Delta t) = \langle I_s(t) * I_s(t - \Delta t) \rangle \quad \text{Eq. 1}$$

$$= A \exp(-2Dq^2 \Delta t) + B \quad \text{Eq. 2}$$

$$q = \frac{4\pi n}{\lambda} \left( \sin \frac{\theta}{2} \right) \quad \text{Eq. 3}$$

For uniformly diffusing spherical particles, the correlation function is Eq. 2, while the relation between translational diffusion coefficient and particle size were deduced from the Stokes-Einstein equation (Eq. 4):

$$D = \frac{k_B T}{6\pi\mu R} \quad \text{Eq. 4}$$

Stokes-Einstein equation incorporates the viscosity of the dispersant and the temperature (as they exert direct influence on particle motion) at which the DLS observations were performed. In Equation 1,  $C(\Delta t)$  is the correlogram (autocorrelation function) as a function of lagging time.  $I_s(t)$  is the instantaneous scattering intensity at time  $t$ ,  $I_s(t-\Delta t)$  is the intensity at the previous time;  $t-\Delta t$ ,  $A$  is the scattering amplitude,  $B$  is an instrumental factor,  $q$  is the scattering vector and  $D$  is the diffusion coefficient of the particles. To calculate diffusion coefficient, determination of the normalization factor (scattering amplitude) and instrumental factor values is crucial and obtainable from curve fitting of correlogram.<sup>7-10</sup>

The scattering vector  $q$  (Eq. 3) is difference between the scattering wave vector and the incident wave vector which depends upon the refractive index (particle-dispersant), wavelength (incident light) and the detector solid angle. For our set-up, scattering vector ( $q$ ) is  $2.62 \times 10^7 \text{ m}^{-1}$ , where  $n$  is refractive index (1.33),  $\theta$  is the angle of detector ( $173^\circ$ ),  $\sin(\theta/2)$  is solid angle and  $\lambda$  is wavelength (633 nm).

Theoretical values of diffusion coefficient from eq. 4, where  $D$  is the diffusion coefficient ( $\text{m}^2/\text{s}$ ) for translational diffusion;  $k_B$  is the Boltzmann constant ( $1.380649 \times 10^{-23} \text{ m}^2\text{kg}/\text{K}\cdot\text{s}^2$ );  $T$  is Temperature (298 K);  $\mu$  is the dispersant-viscosity (0.00089 Kg/m.s);  $R$  is the hydrodynamic radius of the particle (m) is summarised in Table 13. The size of particles mentioned in Table 13 is the maximum diameter. As viscosity of water changes less than 1% on addition  $\text{H}_2\text{O}_2$  up to 10%<sub>v/v</sub> therefore dispersant-viscosity was taken as 0.00089 Kg/m.s in our calculations.<sup>11</sup>

Initial step in obtaining diffusion coefficient ( $D$ ) of particles from DLS correlograms involved function-determination by curve fitting of correlograms (refer to Table 14 for time  $\Delta t$  data derived from fitting autocorrelation plots) and implementing the values in Eq. 6 to obtain  $D$ .

Table 13: Theoretically values of diffusion coefficient (from Eq. 4) for respective samples.

Particle	Diffusion Coefficient (Theoretical) ( $\mu\text{m}^2/\text{s}$ )
SP $_{\phi 475 \text{ nm}}$	0.96
ISO $_{\phi 525 \text{ nm}}$	0.87
JP $_{\phi 500 \text{ nm}}$	0.91
PVD $_{\phi 495 \text{ nm}}$	0.89

The function obtained from fitting curves of correlogram (Figure 99) using Origin version 2022 for SP sample at 0%  $\text{H}_2\text{O}_2$  was a single exponential decay function (Eq. 5). Coefficient of determination for curve fitting  $R^2$  was greater than 0.99. Comparing Eq. 5 and Eq. 2 we get Eq. 6 that helped in obtaining diffusion coefficient of particles from DLS correlograms, which was the inverse of twice the square of solid angle ( $q^2 = 6.88 \times 10^{14} \text{ m}^{-2}$ ) times the time ( $t_1$ ).

$$y = A_1 * \exp\left(-\frac{x}{t_1}\right) + y_0 \quad \text{Eq. 5}$$

$$D = \frac{1}{2q^2 t_1} \quad \text{Eq. 6}$$

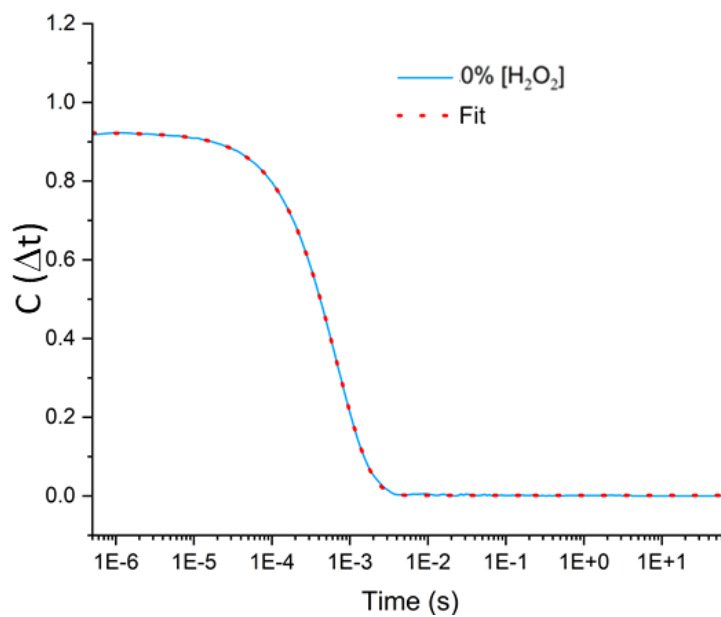


Figure 99: Curve fitting of SP sample at 0%  $H_2O_2$ . Solid lines represent the correlograms from DLS experiment, along the fit (single exponential decay function) represented with dotted (red) line.

Curve-fittings for correlogram for SP at other  $H_2O_2$  concentrations are in Figure 100 while the data derived is shared in Table 3. Similarly, curve fitting of all the correlograms was performed from each round (Round 1, 2 and 3) of experiment for each sample.

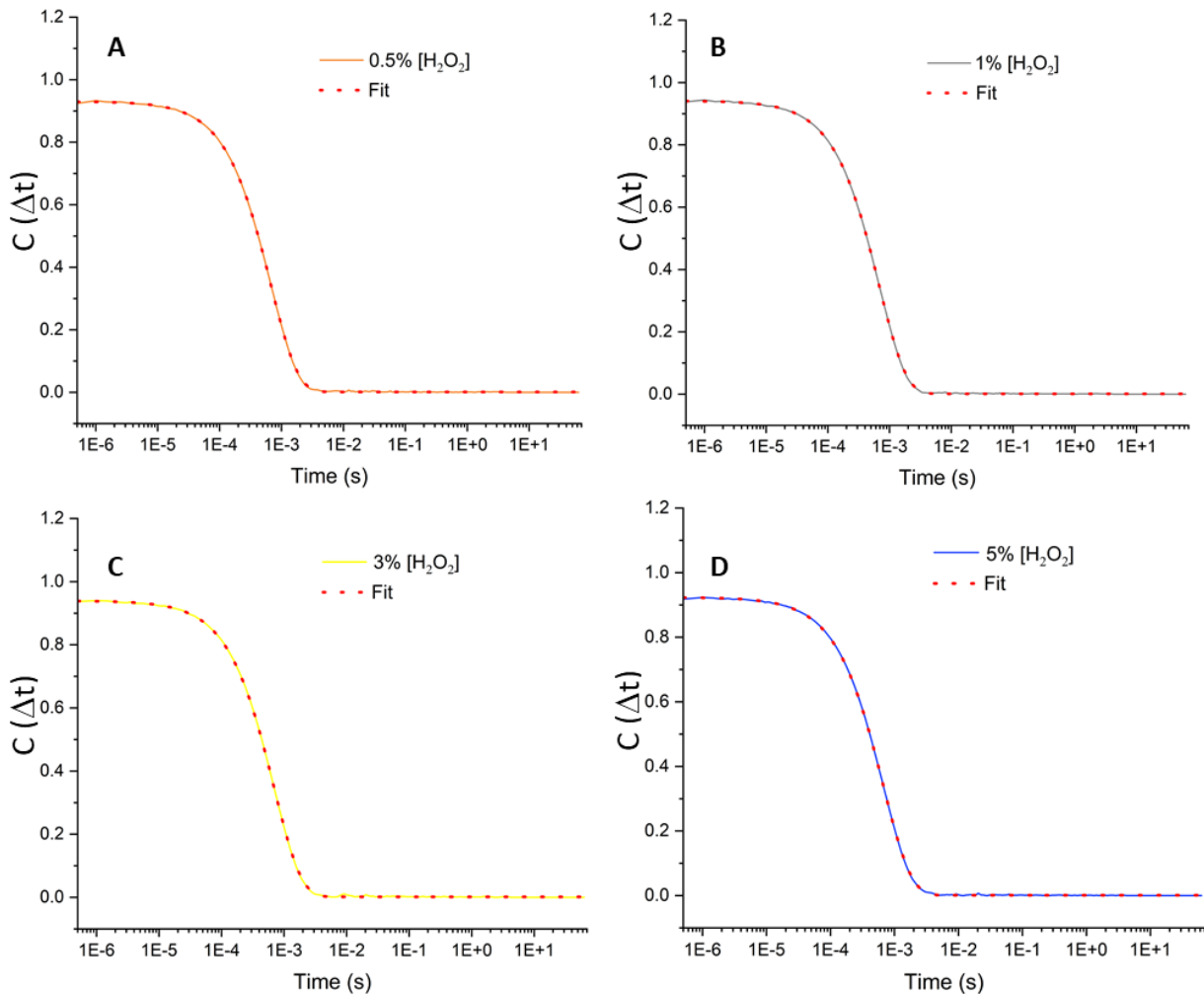


Figure 100: Curve fitting of SP sample at 0.5, 1, 3 and 5% (v/v)  $H_2O_2$  (A, B, C and D respectively). Solid line denotes autocorrelation function (Correlogram) obtained from DLS measurements. Red colour dotted lines denote the curve fitting from single exponential decay function.

### 3.2.2.3.1 Curve Fitting of Correlogram: Samples comprising gold

Single exponential decay function (1 Expo) when used for fitting correlograms from gold loaded nanoparticles gave poor fit. Therefore, in a succeeding manner, curve fitting with double exponential decay function (2 Expo) was attempted and outcome obtained was positive; see Figure 101.

Similar to Iso samples, correlograms from both the Janus Particles (JP and PVD) experienced poor fitting with single exponential decay function, and good fit with double exponential decay function (Figure 102).

## Investigation of Particle Kinematics

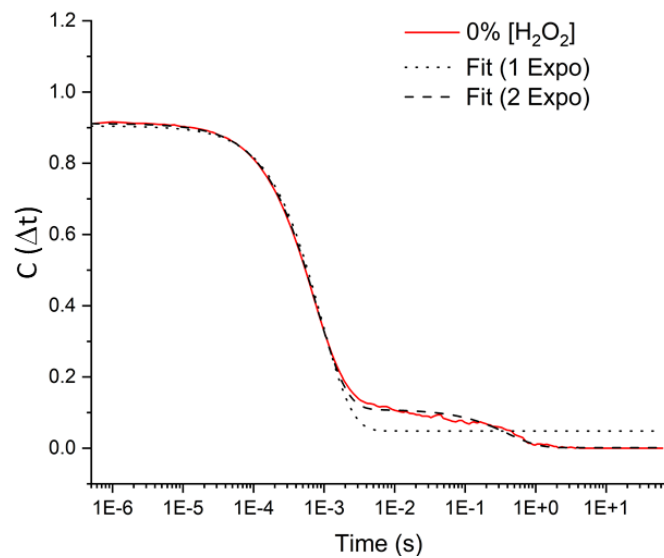


Figure 101: Curve fitting of Iso sample at 0%  $\text{H}_2\text{O}_2$  from Round 1 experiment. Solid lines represents the mean correlograms from a single DLS experiment, along the fits with single exponential decay function (represented by the dotted lines) and double exponential decay function (represented by the dashed lines).

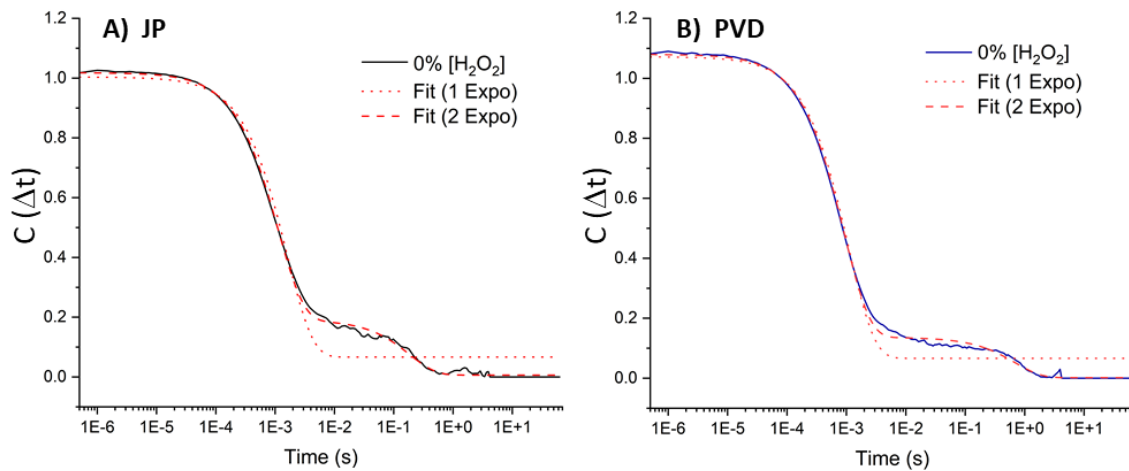


Figure 102: Curve fitting of correlograms from JP and PVD samples in 0%  $\text{H}_2\text{O}_2$ . Solid lines represents the correlograms from DLS experiment and curve fittings are represented with dotted and dashed line in red. Dot-lines denote fit from single exponential decay function, and dash-lines denote fits from double exponential decay function. In both JP and PVD double exponential decay (dash-lines) fits better.

The time ( $\Delta t$ ) data in Table 14 is the mean values for time from all the experimental rounds (R1 to R3). Time value obtained from the single exponential decay function is denoted with  $t_1$ , whereas those obtained from the double exponential decay function are represented as  $T_1$  and  $T_2$ . Notably,  $T_2$  values are considerably greater than  $T_1$  values (often exhibiting a magnitude difference on the order of  $10^{-2}$  to  $10^{-3}$  times). We chose  $T_1$  for calculating the diffusion coefficient as the diffusion process operates on a shorter time scale, making  $T_1$  significant in understanding the dynamics of particle motion in the

context of this study. Moreover, in the literature  $T_2$  is sometimes attributed to the rotational diffusion time.

Table 14: Mean values of 'diffusion time' obtained from fitting correlogram of each rounds of experiment for respective sample with single or double exponential models.  $t_1$  denotes time obtained from single exponential while  $T_1$  and  $T_2$  values of time obtained from double exponentials fits. Number in nRi refers to n the concentration of  $H_2O_2$  in % v/v and i to the number of DLS analysis, while R refers to number of round of experiment.

Exp. Round	SP	Iso	JP		PVD		
	$t_1$ (s)	$T_1$ (s)	$T_2$ (s)	$T_1$ (s)	$T_2$ (s)	$T_1$ (s)	$T_2$ (s)
<b>OR1</b>	6.76E-04	7.48E-04	3.99E-01	1.07E-03	3.57E-01	8.90E-04	8.10E-01
<b>OR2</b>	7.05E-04	7.04E-04	6.42E-01	1.08E-03	4.44E-01	8.14E-04	1.05E-02
<b>OR3</b>	6.89E-04	6.69E-04	2.05E-02	9.74E-04	4.13E-01	8.18E-04	1.45E-02
<b>0.5R1</b>	6.81E-04	6.07E-04	3.23E-01	9.09E-04	4.21E-01	8.93E-04	1.34E-01
<b>0.5R2</b>	6.72E-04	5.90E-04	6.34E-01	8.70E-04	2.16E-02	8.50E-04	2.27E-02
<b>0.5R3</b>	6.74E-04	5.53E-04	1.91E-03	9.29E-04	3.15E-01	7.86E-04	2.09E-02
<b>1R1</b>	6.80E-04	5.43E-04	2.30E+00	9.05E-04	4.69E-01	8.19E-04	1.65E-02
<b>1R2</b>	6.95E-04	5.16E-04	7.27E-04	7.45E-04	6.15E-03	8.07E-04	1.93E-02
<b>1R3</b>	6.97E-04	6.00E-04	7.22E-01	8.52E-04	7.44E-01	7.99E-04	1.45E-02
<b>3R1</b>	7.07E-04	5.96E-04	1.59E-01	7.49E-04	1.50E-02	8.49E-04	6.13E-02
<b>3R2</b>	6.87E-04	5.99E-04	2.01E-01	8.38E-04	1.04E+00	8.25E-04	4.28E-02
<b>3R3</b>	6.82E-04	5.92E-04	2.80E-01	8.65E-04	4.98E-01	8.57E-04	9.34E-02
<b>5R1</b>	6.71E-04	5.95E-04	2.27E-01	8.52E-04	2.37E-01	8.40E-04	3.01E-02
<b>5R2</b>	6.90E-04	5.87E-04	1.30E-01	7.89E-04	2.43E-01	8.22E-04	4.63E-02
<b>5R3</b>	7.02E-04	5.94E-04	1.97E-01	7.93E-04	2.79E-01	8.92E-04	5.70E-01

### 3.2.2.4 Data Treatment (PTV)

For tracking, objects were detected across multiple frames, and their trajectories were reconstructed in the form of respective tracks. These tracks helped in the visualization of various analysis results,

including velocity, total displacement, diffusion characteristics, etc. TrackMate uses bright spot-like objects against a dark background to derive information X, Y and Z coordinates over time. Main components of TrackMate for particle tracking and visualization are Detectors (detects objects in images), Trackers (links objects to build tracks), Analysers (computes numerical values on spots, edges, and tracks), Actions (performs miscellaneous actions in regard with tracking results), and Views (utilized for tracking-result viewing).<sup>12</sup> TrackMate version used during this thesis work is TrackMate 7<sup>2</sup>, while the detector utilized is the Laplacian of Gaussian (LoG) detector (calculations in LoG detectors are made in the Fourier space and the maxima is searched for in the filtered image and maxima in close proximities are suppressed). For results like tracked speed the total displacement of all tracks over the duration of the tracking was divided by the total duration, while the displacement was calculated by measuring the distance between the start and end points of the tracks between two consecutive frames.<sup>13</sup>

#### 3.2.2.4.1 An Optical Microscopy with Digital Imaging

The primary step towards particle tracking was selection of region of interest (ROI) by locating a desirable particles density in observed zones. As this PTV study was limited to 2D and sticking of particle on the surface of glass slide is inevitable, finalized ROI (away from channel boundaries) for all the PTV experiments were based areas away from wall, observation of maximum number of particles exhibiting motion and least number of stuck-particle, disappearing (moving out of focal plane) particles. Figure 103 A is a raw digital image from optical microscopy showing selected region of interest in the microfluidic device. Figure 103. A clearly shows boundaries of the microfluidic channels but for visualizing the particles, image treatments essential. Basic adjustments like image brightness and contrast aids in particle observation as seen in Figure 103 B; encircled particle (white spots) are pristine silica particles (SP) suspended in Milli-Q water (from PTV experiment of SP at 0% $[H_2O_2]$ ). Visual observations lacked directional motion in all the samples.

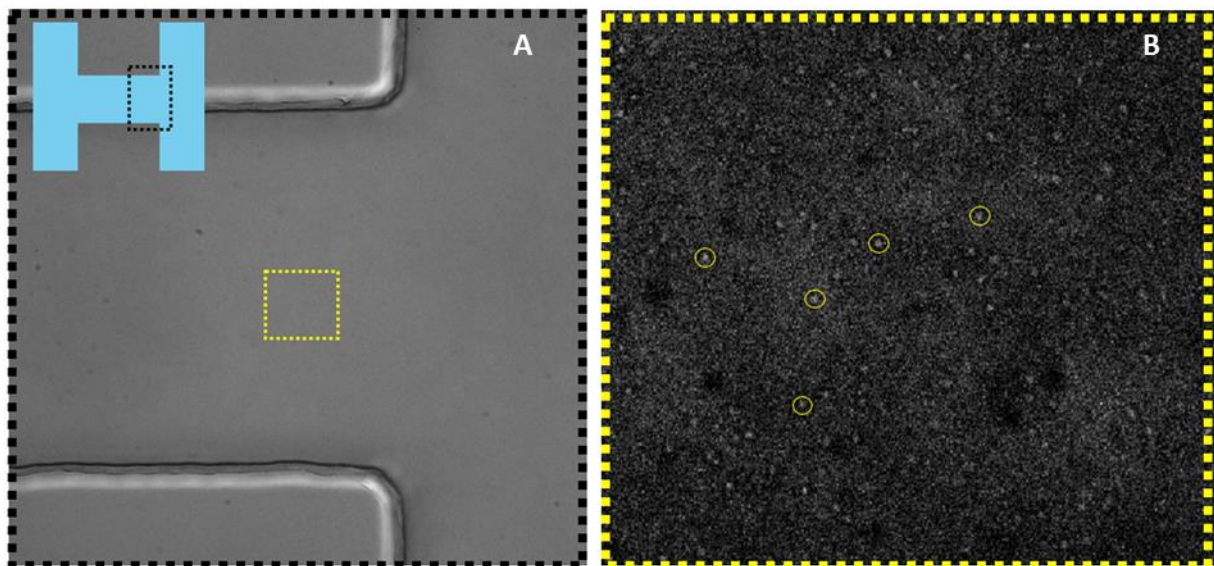


Figure 103: Raw image of SP suspended in Milli-Q water observed from Optical Microscopy (40x magnification). Image A shows the highlighted area of microfluidic chip (top left corner) with channel walls, but not the particles. Image B is after basic

## Investigation of Particle Kinematics

image treatment (brightness and contrast adjustments) of ROI (yellow square in image A) shows particles as white spots (encircled in yellow).

First impression of particles with gold (Iso, JP and PVD) at 10% (v/v) hydrogen peroxide hinted towards a brisk mobility, although it was unclear at lower concentration. Therefore, studying speed profile and directional preferences (if exhibited by particles) remained of high interest, making image processing from TrackMate the succeeding step in PTV. TrackMate performed particle tracking and trajectory-production by monitoring particle-coordinates in observed images. Starting with calibration of pixel width, height and voxel depth to unit value and crop settings adjustments of the selected region of interest (ROI), LoG detector was set for image processing with the suitable input values for object diameter and quality threshold (of the targeted entity to be tracked). Once the detector finished the initial filter, number of identified spots were then filtered via tracker type.

In this thesis, a ‘Simple LAP tracker’ was utilized for PTV image processing because of the advantage in gap-closing between spots, linking-distance (unlike other trackers); beneficial for our two dimensional set-up with particles appearing-disappearing within close proximity. Lastly, details like particle-track, speed, travelled-distance, etc for targeted particles were obtained in .csv format along with chosen output file (avi files in this study). As the obtained result (csv files) were big data, they were further processed by using Python codes for quicker and less-tedious profiling. Spot Result in Figure 104 is an examples of details like Labels for identified spots (Spot ID, Track ID), Quality (mean of the distribution Quality in a track), X, Y Z coordinates (Z coordinates are zero because the set-up was in 2D). The Quality parameter in spot result helped in understanding the accuracy of the detected spots (or detected particles).

Spot ID	Track ID	Quality (quality)	X ( )	Y ( )	Z ( )
30337	9	46.267	254.345	399.579	0
31394	9	50.072	275.991	398.087	0
30211	9	78.368	249.684	396.053	0
30691	9	65.059	262.854	399.801	0
30180	9	70.663	251.593	399.23	0
30987	9	49.599	262.423	397.465	0

### Spot Result

Mean sp. (/frame)	Max speed (/frame)	Min speed (/frame)	Med. speed (/frame)	Std speed (/frame)
4.845	12.817	0.227	3.961	3.048
2.962	6.022	0.771	2.56	1.557
3.685	6.598	1.069	3.505	1.62
3.427	12.594	0.653	3.203	2.76
3.382	8.963	0.44	3.408	2.05
4.473	12.506	0.5	3.914	3.019

### Track Result

Figure 104: Example of Results from TrackMate for tracking pristine silica particles.

Quality value of 70 and above represents high accuracy and minimal noise, while a range of 50 – 70 represents good quality of detected spots with a reasonable level of accuracy and some minor noise. A quality value of 30 to 50 refers to a moderate spot detection quality with potential to noise, whereas values below 30 are low in accuracy and not suggested for tracking purposes. Quality of our most of the tracked particles showed high to good quality of tracking (spot result in Figure 104). Track results in Figure 104 is an example of details like speed (Mean, Maximum, Minimum, etc. denoted with Mean sp., Max speed, Min speed, etc. respectively). As the frame rate (10 FPS), exposure time (10 ms) and pixels per  $\mu\text{m}$  (6.67) were known, speed obtained from TrackMate (Track Mean Speed) was converted from pixels per frame to  $\mu\text{m}/\text{s}$  by utilizing Eq. 7. Once the mean velocity of particles was known, the mean diffusion coefficient was calculated following Eq. 8 and 9.

$$\text{Total time per frame} = \frac{1}{\text{frame rate}}$$

$$\text{Time interval per frame} = \text{Total time per frame} - \text{Exposure time (s)} = 0.09\text{s}$$

$$\text{Speed} \left( \frac{\text{px}}{\text{frame}} \right) = \frac{\text{Displacement}}{\text{Time interval per frame}} \left( \frac{\mu\text{m}}{\text{s}} \right) \quad \text{Eq. 7}$$

$$\text{MSD} = 2nDT_d \quad \text{Eq. 8}$$

Where MSD is mean square displacement, n is the number of dimensions (2), D is the diffusion coefficient and  $T_d$  is the diffusion time (0.09s). As MSD can also be derived by  $\text{Velocity}^2 \times \text{Time}^2$ , therefore by comparing it with Eq. 8 we get:

$$D = \frac{v^2 T_d}{2n} \quad \text{Eq. 9}$$

#### 3.2.2.4.2 Image Processing (TrackMate)

A substantial challenge was the particle adhesion to glass slides. To eliminate these particles from the analysis, adjustments to filtering and tracking parameters in TrackMate were optimized enhancing the accuracy of particle motion observations. Figure 105 B illustrates the outcome of optimizations made in TrackMate-setting for targeting the selection of desired spots (particles) for tracking. Particles used in Figure 105 are SP suspended in Milli-Q water at 40x magnification. Figure 105 A shows all the bright spots, while brightest and biggest spots are shown encircled in Figure 105 B. Identification of spots during image processing was achieved by filtering particles based on size and greyscale values (threshold quality). This ensured that the selected particles were from same plane, thereby reducing the frequency of disappearing/appearing particles along the z-axis (although this did not address the issue of particles stuck on the glass slide).



## Investigation of Particle Kinematics

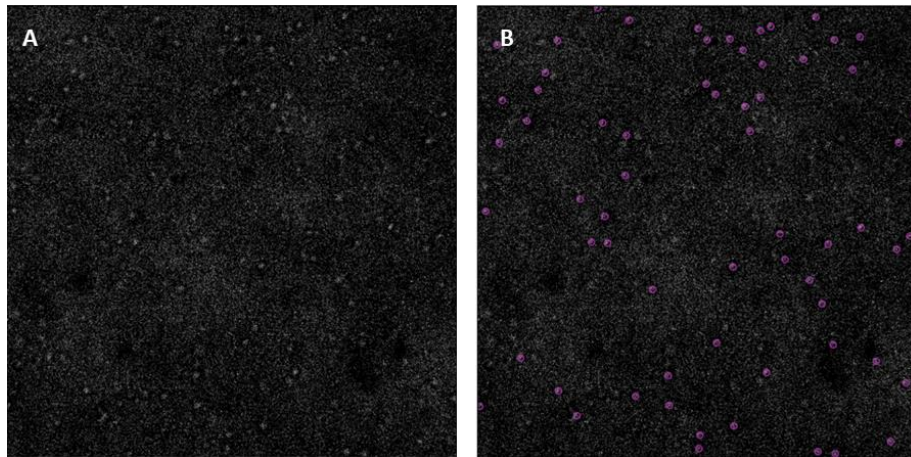


Figure 105: Identification of particles for tracking; elimination of weak signals (less bright or small spots) in image. White spots in the image from observations made for SP sample suspended in Milli-Q water. A: shows all the bright spots in various size, while B: Shows selected spots with an overall size 5.5 pixel size and signal quality threshold above 45 (TrackMate detector thresholds Greyscale).

Later, short tracks were disregarded from tracking by setting track-filters. An example of varying track filters is shown in Figure 106, where filter set at 18.12 pixels (Figure 106. A) resulted in a combination of long and short tracks (Figure 106. C), whereas filter set at 55.19 (pixels) (Figure 106. B) produced predominantly long tracks (Figure 106. D).

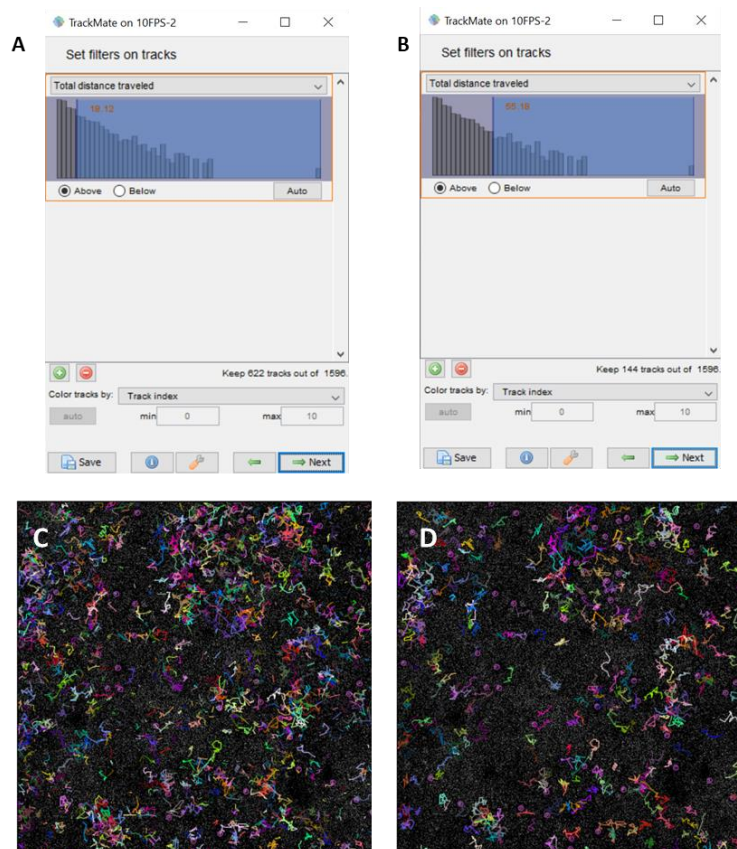


Figure 106: Example of filtration of short tracks by manually set track filters; A with low value of filter for tracks: tracks longer than 18.12 (pixel) to be accounted during tracking, while B having higher value of track-filter of 55.19 (pixels). The corresponding observations for tracked particles are C and D respectively. Due to low filter, more number of total tracks (colourful lines) seen in C and on the contrary, high filter values corresponded in lesser number of track but bigger path.

Different colours in Figure 106 represent the path of respectively tracked particles, while colourful patches correspond to short tracks of particles moving out of the focused-plan. Additionally, stuck particles leads to colourful patches or blob-like appearance due to repeated detection in same spot. Therefore, setting a reasonable track-filter was beneficial in skipping contributions of unwanted tracks in particle tracking results, followed by assessment of obtained data (Spot Result and Track Result, shown in Figure 104) by Python codes for quicker and less-tedious data-profiling.

#### 3.2.2.4.3 Data Processing (Python)

To understand the effect of hydrogen peroxide in studies samples, it was important to study net directional orientation of particle-motion. For this purpose, entire track (obtained from Spot Result in TrackMate) of each trajectory was repositioned to origin axis (zero, zero coordinates) by fetching the respective x and y coordinates of each trajectory and combining it with its displacement-paths. Figure 107 shows native trajectories for observed SP (in 0% [H<sub>2</sub>O<sub>2</sub>]) with its corresponding repositioned trajectories.

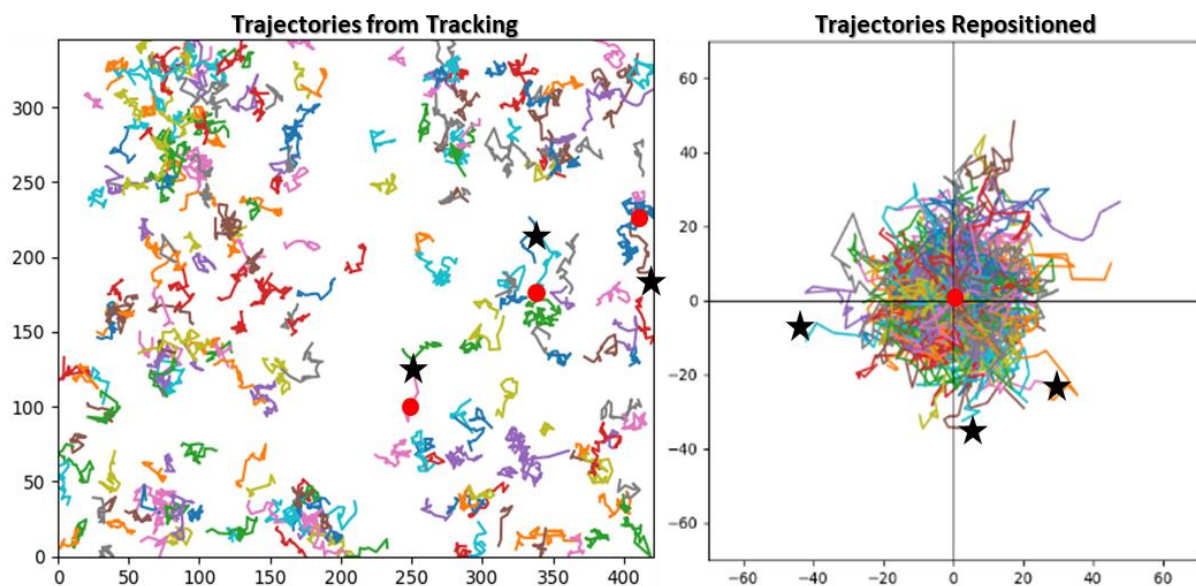


Figure 107: Trajectories obtained from SP in 0% [H<sub>2</sub>O<sub>2</sub>] sample. Trajectories from Tracking (Left) shows tracks for SP as given by TrackMate, whereas Trajectories Repositioned (Right) show all the tracks brought to a starting point of zero axis. The x and y-axis represents respective coordinates of trajectories.

The objective here is to understand the impact of H<sub>2</sub>O<sub>2</sub> on particles motion by monitoring the trajectories in a particular direction. For this purpose, SP trajectories were repositioned to same point in Figure 107 (Trajectories Repositioned) showing that particles had no directional motion. Tracks in each quadrant appearing similar to each other reflected motion of particle were isotropic in direction. Similar trend existed for all the particles in all 0, 5 and 10% (v/v) [H<sub>2</sub>O<sub>2</sub>]. Another tool for assessing particle motion was mean square displacement (MSD) plot; providing insights into diffusion and randomness. An increasing MSD with time indicates diffusive behaviour. In a 2D system, particles undergoing Brownian motion show a near-linear increase in MSD (shared in section “1.3.2”, Chapter

1). The slope of MSD plot is proportional to the diffusion coefficient, therefore a steeper slope indicates higher mobility, which can be linked with directed motion or active transport motion (and the opposite reflects sub-diffusive motion).<sup>14,15</sup> In our study, python code (Github location: Vevitek/CEA\_PFE\_Zak<sup>23</sup>) utilized the extracted coordinates of tracked particles from TrackMate for each frame, to produce MSD plots as a function of time.

### 3.3 Result and Discussion

#### 3.3.1 DLS (Result and Discussion)

##### 3.3.1.1 DLS Correlogram

Correlogram results from our DLS study showed smooth baseline for pristine silica particle (SP) in comparison to undulated-baselines for modified particles (Isotropic gold/silica (Iso), chemically synthesized Gold/Silica Janus Particle (JP) and physically produced Gold/Silica Janus Particle (PVD-JP)) was in concurrences with the study by McGlasson and Bradley.<sup>1</sup> DLS investigations by McGlasson et al.,<sup>1</sup> for Platinum/Polystyrene Janus microparticles (produced from PVD) in pure water showed fluctuating baseline signature, while smooth baseline for pristine polystyrene, similar to our findings are summarized in Figure 108. Another interesting similarity was the smoothing of baseline-fluctuations in presence of hydrogen peroxide. As shown in Figure 109 baselines of correlogram smoothed on addition of hydrogen peroxide (correlograms in red), versus fluctuating baselines (correlograms in black) in absence of hydrogen peroxide.

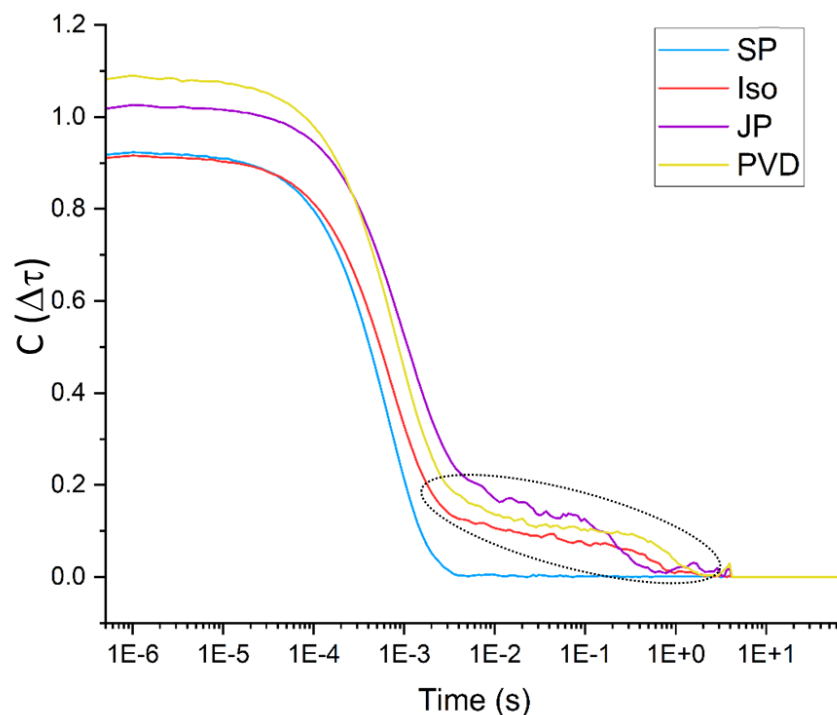


Figure 108: Comparison of Pristine Silica (Blue) correlogram (autocorrelation function (y-axis) as a function of decay time (x-axis)) with modified particles (Isotropic gold/silica (Red), Chemically synthesized Gold/Silica Janus Particle (Purple) and Physically produced Gold/Silica Janus Particle (Yellow) in pure water. Only pristine silica has smooth baseline signature. Iso, JP and PVD (Yellow and Purple correlograms) having higher delay time is indicative of being bigger particle.

McGlasson et al.<sup>1</sup> related these baseline-fluctuations with rotational diffusion. Indeed colloidal particles in a fluid undergo translational movements as well as rotations. For symmetrical particles, these are not detected, but when the particles are anisotropic (as in the case of Janus particles), it is possible to detect them, particularly in DLS. In this case, the correlograms are fitted by a double exponential decay with  $T_2$  linked to the characteristic time of rotational diffusion ( $\tau_R = 6 T_2$  and theoretical value is  $\tau_R = k_b T / 8 \pi \eta R^3$ ). In our experiments, we favoured the interpretation of traditional colloid science that these fluctuation were an indication of presence of bigger particles or particle clusters or aggregates for the following reasons:

- i. The fluctuating baseline signal was observed not only for anisotropic particles (JP and PVD) but also for Iso samples that had isotropic surface. Therefore, nullifying the contribution from scattering due to rotational diffusion.
- ii. Long-term sedimentation was observable in our samples, which indicated that an aggregation process indeed occurred.

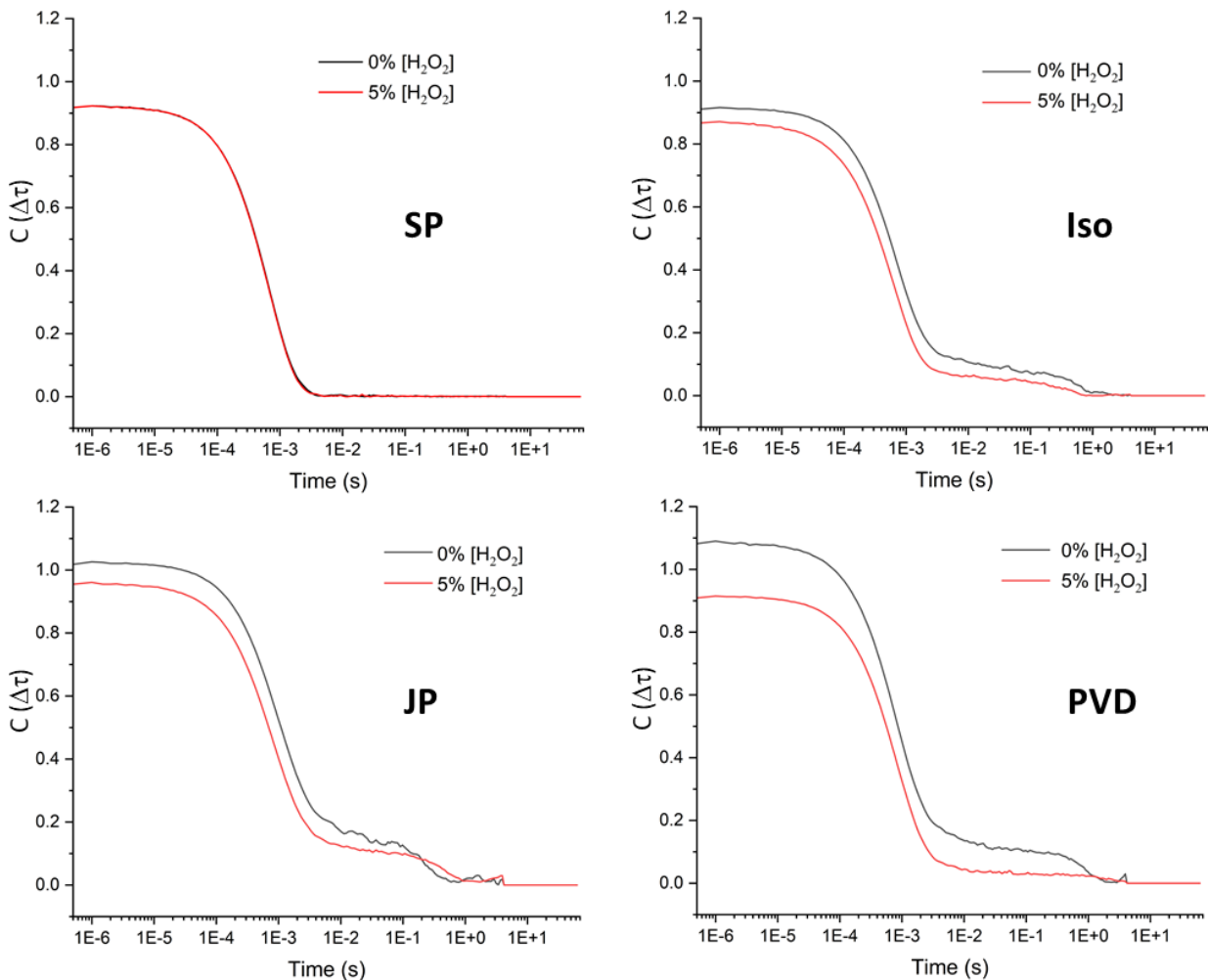


Figure 109: Comparison of correlograms in pure water (Black: OR1') and 5% (v/v) hydrogen peroxide (Red: 5R1'). Black correlograms (pure water) of Iso, JP and PVD are bumpier than smoother red correlograms (5% hydrogen peroxide). Correlograms for Gold/Silica PVD Janus particle is similar to correlograms for Platinum/Polystyrene PVD Janus particles in McGlasson's results<sup>1</sup>

### 3.3.1.2 Diffusion time ( $t_1$ and $T_1$ ) obtained from curve fitting of Correlograms

Mean diffusion time was highest in absence of  $H_2O_2$  for all the samples (Figure 110). SP samples experienced less than 5% relative difference from 0% to 5% concentration of  $H_2O_2$  without any trend. In absence of  $H_2O_2$ , JP showed maximum diffusion time, followed by PVD and Iso. SP and Iso exhibited similar range of diffusion time (relative difference of  $\sim 2.5\%$ ) (Figure 110). Iso experienced sudden decrease of  $\sim 15\%$  in diffusion time upon introduction of  $H_2O_2$  and further stayed in stable range for higher concentrations of  $H_2O_2$ . For JP progressive trends in decreasing diffusion-time ( $\sim 20\%$ ) existed with increasing  $H_2O_2$  concentration, while no variation in diffusion time were observed for PVD samples.

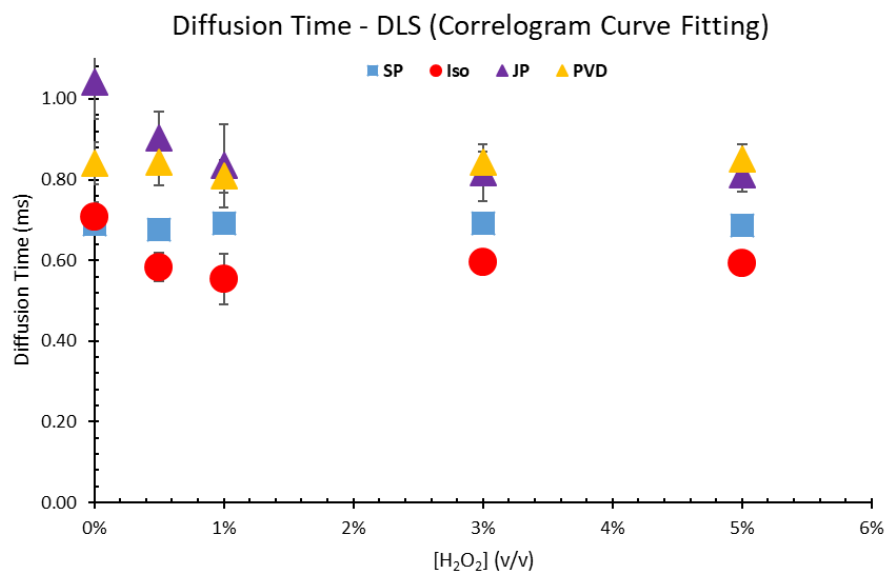


Figure 110: Mean Diffusion Time in milliseconds, obtained from curve fitting of DLS correlograms for respective samples. Diffusion time for Iso and JP decreases with introduction of hydrogen peroxide (and almost stable after 1% concentration).

### 3.3.1.3 Apparent Particle Size

DLS measurements gave hydrodynamic diameter of particles, derived from the calculated diffusion coefficient. Table 15 summarises the results obtained from each round of experiment (Round 1, 2 and 3) at its respective concentration of hydrogen peroxide. For SP particles, the diameter is constant for all  $H_2O_2$  concentration and corresponds to our expectations. A similar but noisier trend was observed for PVD particles. In contrast, the diameter decreased as a function of  $H_2O_2$  concentration for Iso and JP particles.

Amongst the investigated particles, size for Iso samples possessed highest relative difference (about 37%), followed JP (22%), PVD (5%) and SP (2.4%). The mean diameter of particles is summarized in Table 16 and the evolution of the diameter is shown as a function of the increase of hydrogen peroxide concentration (Figure 111).

## Investigation of Particle Kinematics

Table 15: Mean diameter of particles from each round of experiment for respective samples.

Exp. Round	Mean Diameter (nm)			
	SP	Iso	JP	PVD
OR1	457	506	724	602
OR2	477	476	731	551
OR3	466	452	659	553
0.5R1	461	411	615	604
0.5R2	454	399	588	575
0.5R3	456	374	628	532
1R1	460	367	612	554
1R2	470	349	504	546
1R3	471	406	576	541
3R1	478	403	507	574
3R2	465	405	567	558
3R3	462	401	585	580
5R1	454	402	576	569
5R2	467	397	534	556
5R3	475	402	537	604

Table 16: Mean diameter of SP, Iso, JP and PVD samples at respective concentration of hydrogen peroxide. JP samples showing decrement in mean diameter with increasing percentage of hydrogen peroxide, while for Iso sample diameter reduced on introduction of hydrogen peroxide (0.5%) and stays in same range further. Unlike JP and Iso, diameter of SP and PVD samples remaining unaffected with addition of hydrogen peroxide.

% (v/v) [H <sub>2</sub> O <sub>2</sub> ]	Diameter (nm) ± Std. Dev (%)			
	SP	Iso	JP	PVD
0	467 ± 2.2	478 ± 5.5	705 ± 8.9	569 ± 6.2
0.5	457 ± 1.2	394 ± 5.9	610 ± 7.3	570 ± 6.6
1	467 ± 1.4	374 ± 11.3	564 ± 12.4	547 ± 5.1
3	468 ± 2.1	403 ± 1	553 ± 8.6	571 ± 3.0
5	465 ± 2.4	400 ± 2.1	549 ± 5.1	576 ± 4.3

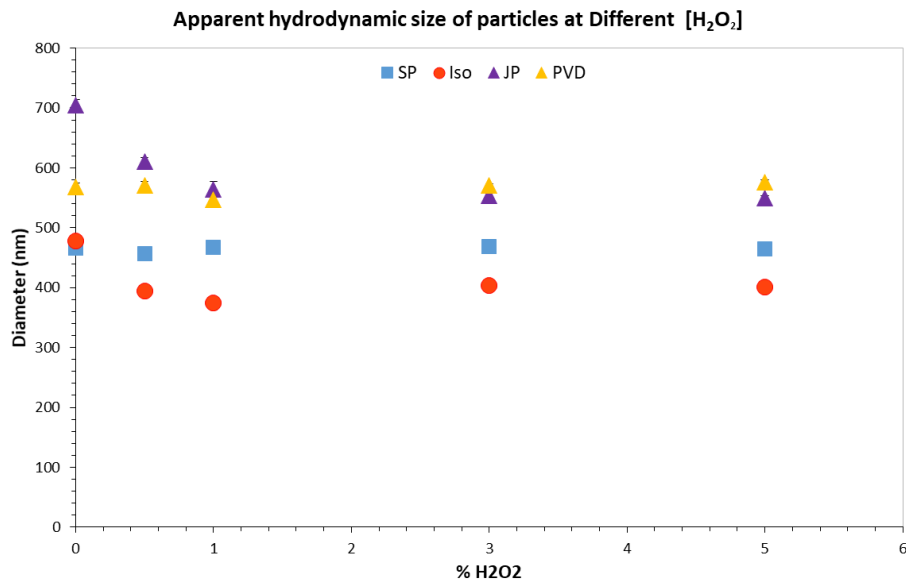


Figure 111: Apparent mean diameter (nm) for particles (SP, Iso, JP and PVD) at respective concentration of H<sub>2</sub>O<sub>2</sub>. In Iso and JP samples, particle size decreases with increase in [H<sub>2</sub>O<sub>2</sub>], but stays in constant-range for SP and PVD samples.

A few possible explanations for the results observed (decreasing size of surface modified particles with increasing H<sub>2</sub>O<sub>2</sub> concentration) are shared further. High values for JP in comparison to geometrical consideration (500 nm maximum mean diameter from SEM) are to be related with the anisotropic charge distribution of JP-surface; hydrodynamic radius of charged nanoparticles significantly increased with their charge<sup>16</sup>. DLS measurements are made for Brownian particles. In the case of pure silica particles (SP), the addition of H<sub>2</sub>O<sub>2</sub> did not disturb the measurement because the particles retained a Brownian motion. However, for catalytic particles, the addition of H<sub>2</sub>O<sub>2</sub> caused a non-Brownian movement linked to the catalytic reaction taking place in the surface of particles. The DLS measurements showed an increase in the diffusion coefficient and in a purely Brownian interpretation it corresponded to smaller particles.

In other words, non-Brownian motion in particles were compensated by reflecting decreased size (making these virtually reduced size irrelevant as result-findings). Nonetheless, this virtual decrease in particle-size; an aberrant artefact and limitation of DLS techniques proved that Janus Particles with their anisotropic surfaces carried non-Brownian motion.

#### 3.3.1.4 Diffusion Coefficient

From the values of the diffusion times obtained by the correlogram fits, equation 6 can be used to calculate the particle diffusion coefficient under the different conditions. The resultant diffusion coefficient from each round of experiment at the respective concentrations of H<sub>2</sub>O<sub>2</sub> are in Table 17. As expected, the diffusion coefficient of pure silica particles (SP) was constant even in the presence of H<sub>2</sub>O<sub>2</sub>. In contrast, for catalytic particles, the addition of H<sub>2</sub>O<sub>2</sub> led to an increase in the diffusion coefficient, mainly for Iso and JP particles, followed by stabilisation towards a plateau.

## Investigation of Particle Kinematics

Table 17: Mean values of diffusion coefficient from each round of experiment for respective samples.

<b>Mean Diffusion Coefficient (<math>\mu\text{m}^2/\text{s}</math>)</b>				
<b>Exp. Round</b>	<b>SP</b>	<b>Iso</b>	<b>JP</b>	<b>PVD</b>
<b>0R1</b>	1.07	0.97	0.68	0.82
<b>0R2</b>	1.03	1.03	0.67	0.89
<b>0R3</b>	1.05	1.09	0.74	0.89
<b>0.5R1</b>	1.07	1.20	0.80	0.81
<b>0.5R2</b>	1.08	1.23	0.83	0.85
<b>0.5R3</b>	1.08	1.31	0.78	0.92
<b>1R1</b>	1.07	1.34	0.80	0.89
<b>1R2</b>	1.04	1.40	0.97	0.90
<b>1R3</b>	1.04	1.21	0.85	0.91
<b>3R1</b>	1.03	1.22	0.97	0.85
<b>3R2</b>	1.06	1.21	0.87	0.88
<b>3R3</b>	1.06	1.23	0.84	0.85
<b>5R1</b>	1.08	1.22	0.85	0.86
<b>5R2</b>	1.05	1.24	0.92	0.88
<b>5R3</b>	1.03	1.22	0.91	0.81

With regard to the mobility of the different particles, we observed that in absence of  $\text{H}_2\text{O}_2$ , particles (SP as reference) with highest to lowest diffusion rate was  $\text{Iso} > \text{PVD} > \text{JP}$ , which is difficult to rationalize, as Iso is bigger and heavier than JP (refer to in ) but still exhibited higher diffusion rate than JP. PVD is almost twice heavier than JP, still showed high diffusion rate. This can be linked with the well-established understanding that DLS; designed to observe Brownian motion of suspended particles, any non-Brownian motion experienced by particles could be misinterpreted (due to forced fitting to a Brownian-motion model). Another hypothesis was the change in surface charge and surface charge distribution which is crucial for movement and interactions with surrounding fluids<sup>16</sup>.

Mean diffusion coefficient of particles at respective concentrations of hydrogen peroxide is in Table 18 and graphical illustration in Figure 112. In the presence of  $\text{H}_2\text{O}_2$ , SP showed a narrow span of diffusion coefficient ( $\sim 1.05$  to  $1.08 \mu\text{m}^2/\text{s}$ ) which demonstrated that variation of diffusion coefficient upto 5% are insignificant in SP (unlike particles with gold). Relative difference in diffusion-rate for Iso



upon introduction of H<sub>2</sub>O<sub>2</sub> was around 28%. Janus particles (both chemically synthesized JP and physically produced PVD) even with the presence of gold entity on its surface interacting with H<sub>2</sub>O<sub>2</sub> exhibited slowest diffusion rates amongst the observed particles. Diffusion coefficient for JP samples ranged from 0.7 to 0.9 μm<sup>2</sup>/s; increment of almost 30%, whereas PVD exhibited insignificant diffusion-enhancement with H<sub>2</sub>O<sub>2</sub>. Our result of higher relative difference in diffusion coefficient for JP than PVD contradicts with the results of Lyu on platinum<sup>17</sup>.

Our result, where PVD produced Janus particles were least reactive to H<sub>2</sub>O<sub>2</sub> is opposite to Lyu's work<sup>17</sup>, showing PVD produced Janus particle exhibiting higher catalytic activity with hydrogen peroxide. This contradiction could be due to the well-established knowledge of higher catalytic activity of platinum nanoparticles than gold<sup>18</sup> and also the difference in the synthesis of Janus particles.<sup>17</sup> PVD Janus Particles (platinum/silica microsphere) studied by Lyu and team<sup>17</sup> were produced from sputtering platinum over silica microsphere, while Janus particle with Platinum Nanoparticle were obtained from annealing sputtered platinum layer at 600 °C making them less comparable to our chemically synthesized gold/silica Janus Particle.

Table 18: Mean diffusion coefficient at 0, 0.5, 1, 3 and 5% (v/v) hydrogen peroxide for SP, Iso, JP and PVD samples showing increased value of diffusion coefficient with addition of hydrogen peroxide in Iso and JP sample, while values for SP and PVD samples remaining unaffected.

% (v/v) [H <sub>2</sub> O <sub>2</sub> ]	Diffusion Coefficient (μm <sup>2</sup> /s) ± Std. Dev (%)			
	SP	Iso	JP	PVD
0	1.05 ± 2.2	1.03 ± 5.4	0.70 ± 8.5	0.86 ± 6.2
0.5	1.07 ± 1.3	1.25 ± 6.5	0.80 ± 7.4	0.86 ± 6.8
1	1.05 ± 1.4	1.32 ± 12.5	0.88 ± 15.2	0.90 ± 5.1
3	1.05 ± 2.0	1.22 ± 1.0	0.89 ± 9.4	0.86 ± 3.0
5	1.06 ± 2.4	1.23 ± 2.1	0.90 ± 5.0	0.85 ± 4.2

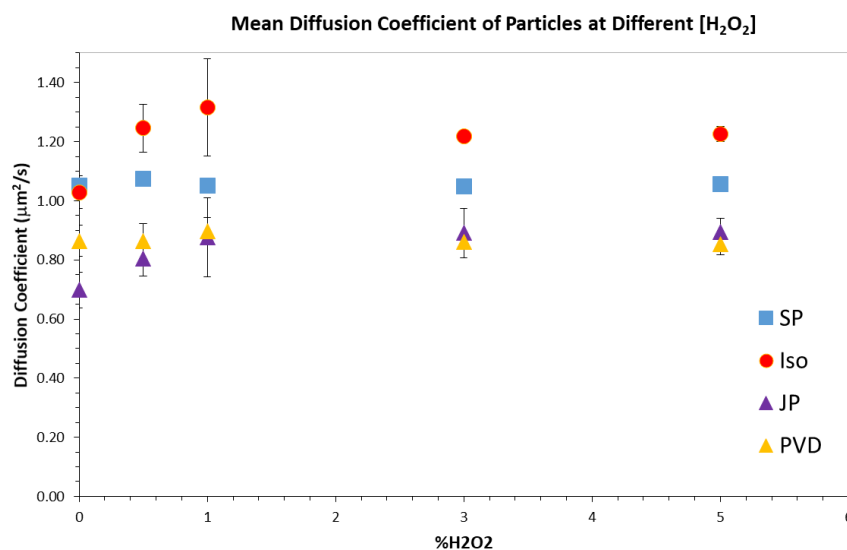


Figure 112: Mean diffusion coefficient of particles at respective concentration of hydrogen peroxide. Diffusion Coefficient is unaffected with increasing hydrogen peroxide for SP (blue square) and PVD (yellow triangle) samples, unlike the Iso (red

*rhombus*) and JP (purple triangle) samples, which increases with addition of hydrogen peroxide. High-rise in value and error found in Iso-1% [ $H_2O_2$ ] in comparison to other sample with low error.

### 3.3.2 PTV (Result and Discussion)

#### 3.3.2.1 Motion orientation and displacement

As the ROI was away from channel boundaries, wall effects had no impact on the motion and orientation of particles. Figure 107 summarizes the trajectories aligned to origin coordinates for all the particles cases for 0% and 10% of homogenous  $H_2O_2$ . Tracks in each quadrant for most of the graphs in Figure 114 appearing similarly distributed confirmed that the motion exhibited by particles in all the samples (SP, Iso, JP and PVD) was isotropic in direction.

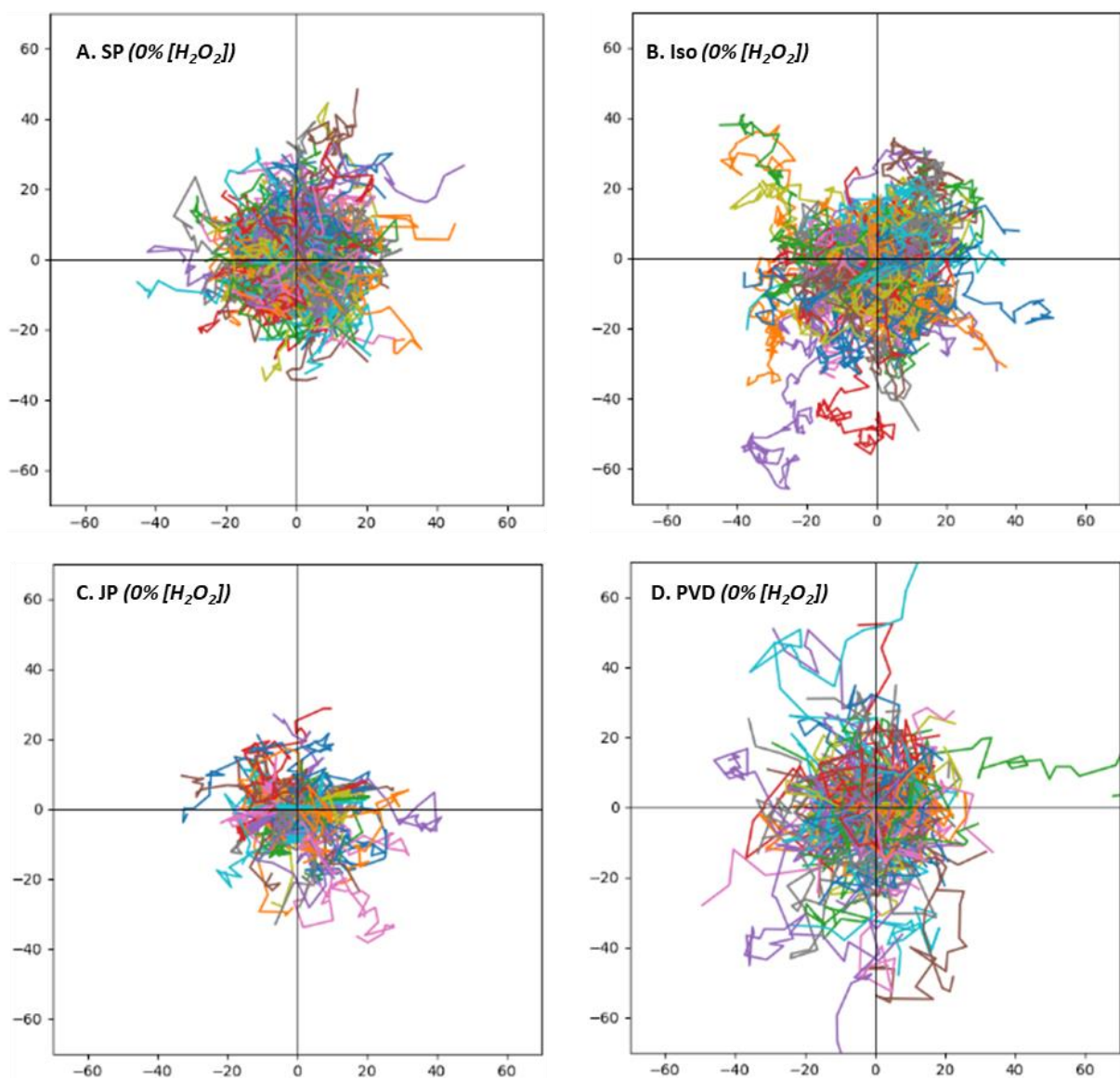


Figure 113: Trajectories from origin coordinates (0,0) showing overall non-directional motion in particles for respective samples at 0% [ $H_2O_2$ ]. The x and y-axis are representative of track coordinates in pixels for particles observed in ROI.

## Investigation of Particle Kinematics

The results were of comparable quality to that shown by Xiao et al<sup>19</sup> and affirmed minimal mechanical and hydrodynamic perturbations in our experiment setup. Some graphs in Figure 113 gave first impression of ‘a little biased motion’, which arose due to minimal number of tracks (number of particles) and therefore required careful interpretation. Example: in Figure 114 Iso in 10% [H<sub>2</sub>O<sub>2</sub>]; showing a little more tracks in first and second quadrants, was from the contribution of two tracks (green and blue). Similarly for SP in 10% [H<sub>2</sub>O<sub>2</sub>]; showing a little more tracks in third and fourth quadrants, came from two tracks (purple and green), but on overall none of the particles showed directional orientation in their motion (in both presence/absence of H<sub>2</sub>O<sub>2</sub>).

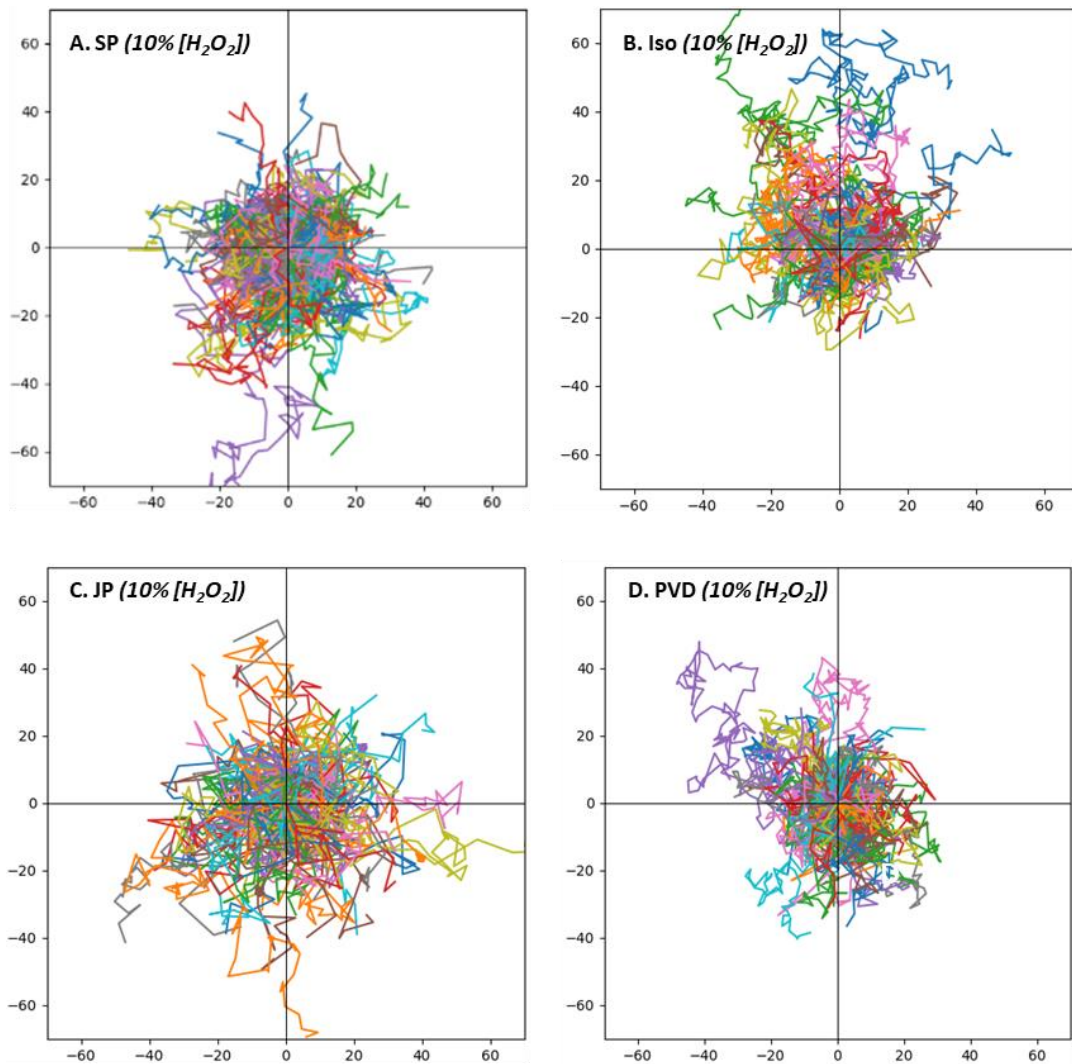


Figure 114: Representation of the trajectories in pixels from origin coordinates (0,0) showing overall non-directional motion in particles for respective samples at 10% [H<sub>2</sub>O<sub>2</sub>]. JP in 10% [H<sub>2</sub>O<sub>2</sub>] has longer tracks than in 0% [H<sub>2</sub>O<sub>2</sub>] (Figure 19.C).

Images obtained from selected part of chip over 20s recording showed no directional orientation in particles motion in presence and absence of hydrogen peroxide. Figure 113 and Figure 114 show particle tracks in all the directions. Although 2D tracking limited our knowledge of complete distance travelled, the range of observed tracks for all the particles were similar (Figure 113) with an exception of smaller range for JP in 0% [H<sub>2</sub>O<sub>2</sub>] (Figure 113) that increased on the introduction of hydrogen

peroxide (Figure 114). This would be in agreement with the higher hydrodynamic radius of the particles.

Another method used for studying the randomness of particles was ‘displacement plot’, and the ‘mean square displacement (MSD) of particles as a function of time’. As shared in Chapter 1, the Central limit theorem<sup>20</sup> describes that distribution of particle-displacement in a purely diffusive motion gives a Gaussian fit.<sup>20,21</sup> Our particle-displacement results in Figure 115 and Figure 116 were obtained by calculating particle displacement between two consecutive images, using Euclidean formula (Eq.10). For this purpose, particle coordinates (for consecutive images) were extracted from the spot-analyzers<sup>12</sup> in TrackMate.

$$\text{Displacement} = \sqrt{dx^2 + dy^2} \quad \text{Eq. 10}$$

where, x and y are the respective coordinates of particles.

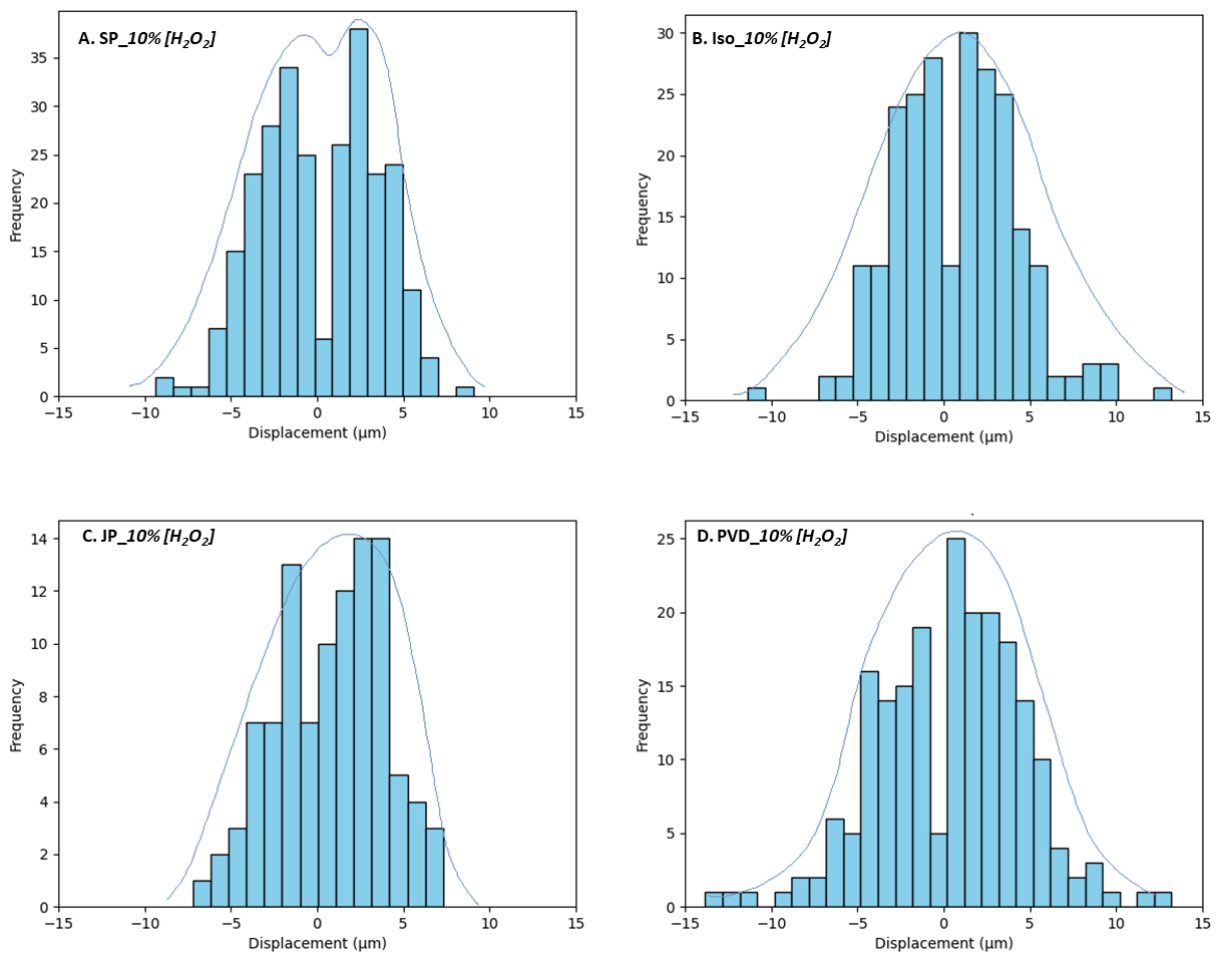


Figure 115: Displacement graphs for particles trajectories at 0%<sub>v/v</sub> H<sub>2</sub>O<sub>2</sub> calculated from total distance covered by particles throughout the observation window. Particle-displacement overall fitting Normal distribution indicates non-directional displacement of particles.

Despite poor statistics, particle-displacement results (Figure 115 and Figure 116) showed that particle-displaced in both positive and negative directions (from the centre); fitting Normal distribution<sup>20,21</sup> in all the concentrations of H<sub>2</sub>O<sub>2</sub>. This confirmed that particle interaction (in all the samples) with H<sub>2</sub>O<sub>2</sub> in surrounding did not cause any substantial scale of directional migration. Nevertheless, in some cases the fit appeared weak, which was due to poor statistics (from less count of particles).

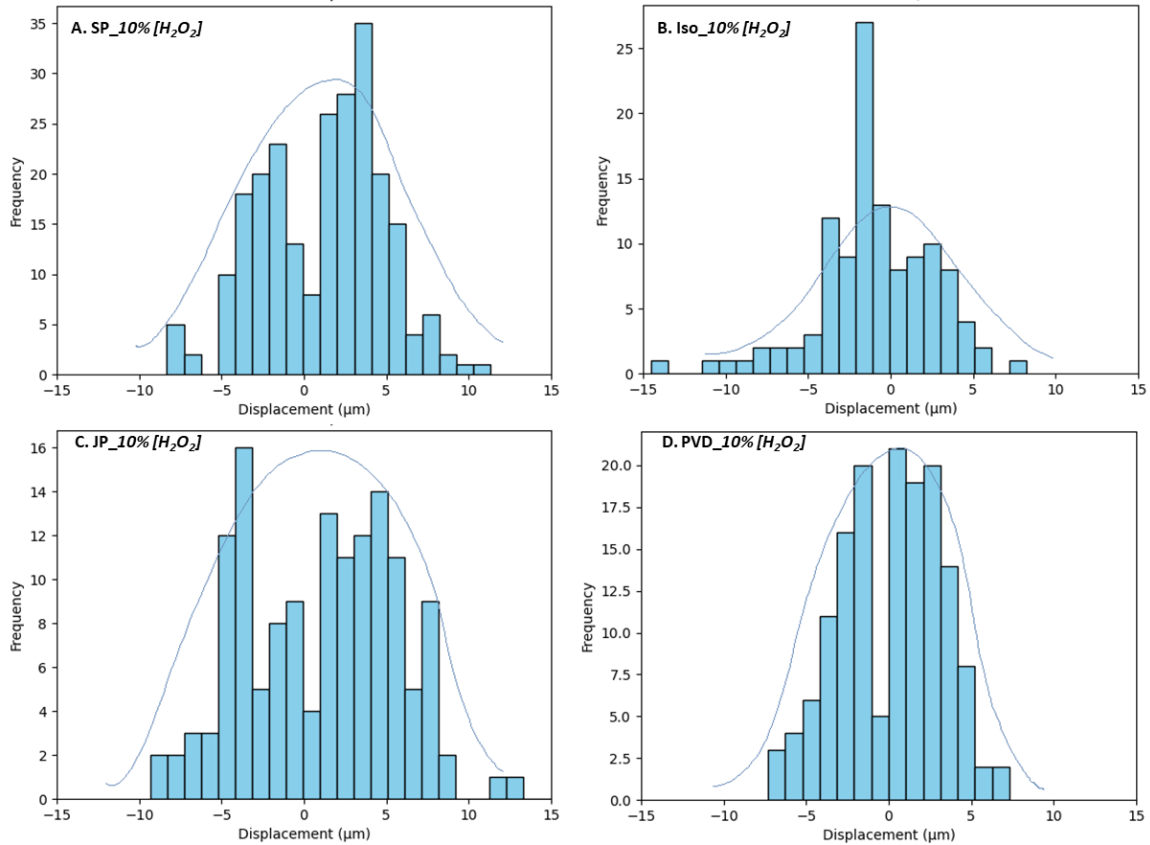


Figure 116: Displacement graphs for particles trajectories at 10%<sub>v/v</sub> H<sub>2</sub>O<sub>2</sub>. Particle-displacement overall fitting Normal distribution indicates non-directional displacement of particles.

A typical diffusion motion follows linear relationship between MSD and time (see section “1.3.2.1”, Chapter 1),<sup>22</sup> while a hyper-diffusive relation in MSD plot (as a function of time) can confirm active motion. Position of particles obtained from TrackMate helped in obtaining MSD plots (Figure 117) as a function of time using equation 10.

$$\text{MSD}(\tau) = (1 / N) * \Sigma [(x(t + \tau) - x(t))^2 + (y(t + \tau) - y(t))^2] \quad \text{Eq. 10}$$

Here,  $\tau$  is the lag time,  $N$  is the total number of particles in the system whose trajectories are being analysed,  $\Sigma$  is the summation,  $x$ ,  $y$  are the coordinate, and  $t$  is the initial time. However, the determination of particle motion as diffusive, hyper-diffusive or sub-diffusive was not observable from these plots (Figure 117).

## Investigation of Particle Kinematics

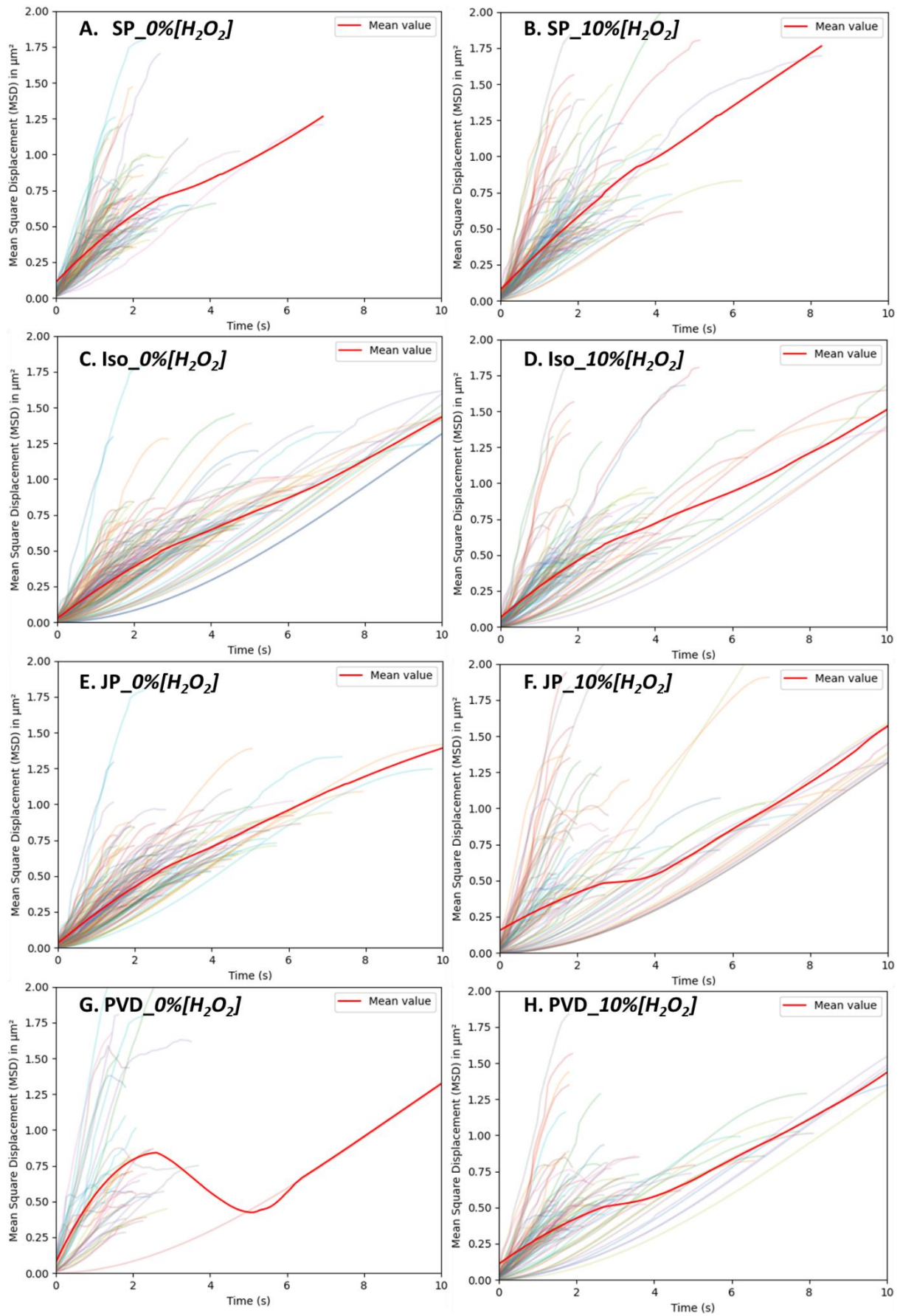


Figure 117: Mean square displacement (MSD) ( $\mu\text{m}^2$ ) as a function of time (s) for particles at respective concentration of  $\text{H}_2\text{O}_2$ . No significant differences in the trend of particle-motion is evident. Dip in PVD@0% (G) due to poor statistics.

3.3.2.2 Mean Speed

Figure 118 i) and Table 19 summarize the mean speed of particles at respective [H<sub>2</sub>O<sub>2</sub>]. In the absence of H<sub>2</sub>O<sub>2</sub> PTV found PVD as fastest of all which was also interesting as it is the heaviest of all samples (Figure 118 ii)).

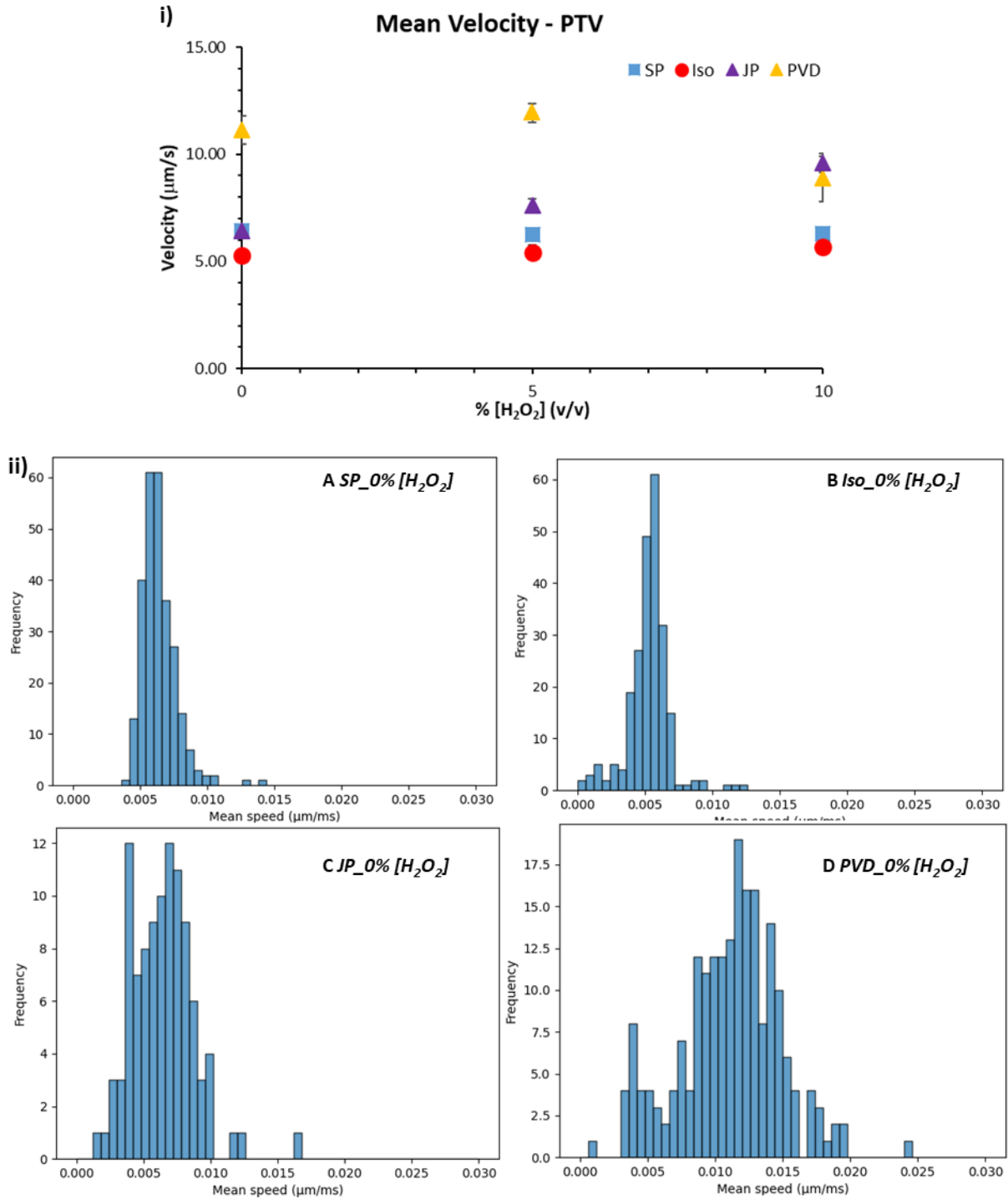


Figure 118: i) Mean Velocity of particles at respective concentration of H<sub>2</sub>O<sub>2</sub> showing highest velocity in Janus Particles. ii) Graphical representation of speed-distribution in respective particles in absence of hydrogen peroxide (0% H<sub>2</sub>O<sub>2</sub>) obtained from particle tracking via TrackMate and treating TrackMate result via Python.

## Investigation of Particle Kinematics

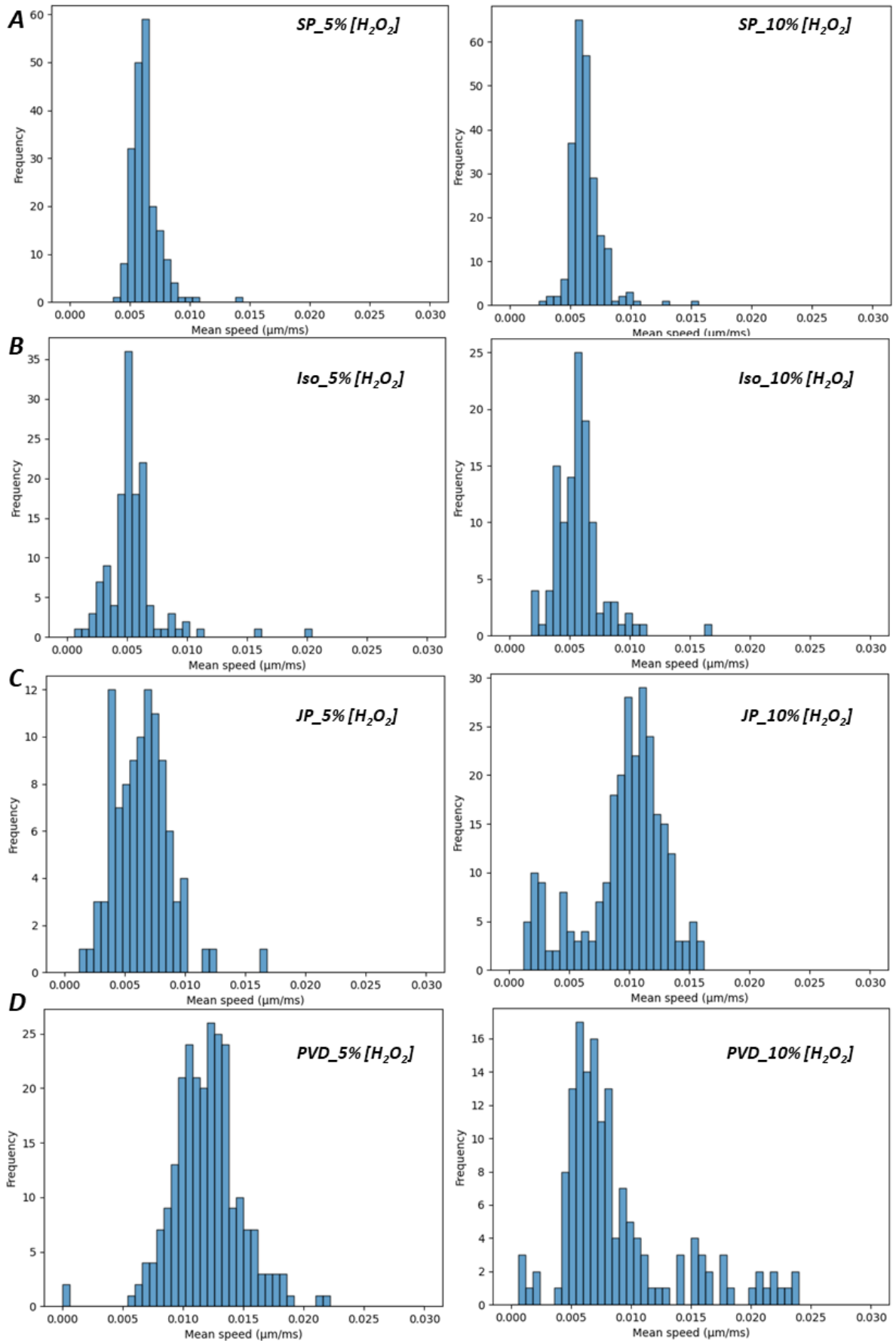


Figure 119: Graphical representation of speed-distribution in respective particles in 5% and 10%  $H_2O_2$  obtained from particle tracking via TrackMate and treating TrackMate result via Python.



In the presence of  $H_2O_2$ , particles with isotropic surface showed narrow range of distribution of speed (Figure 119: .B). Wider distribution in Janus Particles (Figure 119: .C) could be linked with high degree of variability due to surface anisotropy. Our result for Janus Xiao et al<sup>19</sup> and affirmed minimal mechanical and hydrodynamic perturbations in our experiment setup. Mean speed of particles in Table 19 showed the increasing mean speed in Janus particles with increasing hydrogen peroxide with an exception of PVD at 10% with high standard deviation.

Overall PVD was fastest amongst all, which could seem strange, as PVD is the heaviest particle, while the Copper-Silica Janus micromotors ( $\phi$  5  $\mu$ m) studied by Xiao<sup>19</sup> have 6 to 12  $\mu$ m/s range of speed. An explanation behind the high speed of our PVD could be collective hydrodynamics processes, or effect of the illumination (microscope-lamp).

Table 19: Mean speed of particles in respective concentration of hydrogen peroxide. JP, SP and Iso follow PVD having highest speed in 0 and 5% (v/v) hydrogen peroxide, while JP and SP having equal mean speed in absence of hydrogen peroxide.

% (v/v) [H <sub>2</sub> O <sub>2</sub> ]	Mean Speed $\pm$ Std. Dev ( $\mu$ m/s)			
	SP	Iso	JP	PVD
0	6.4 $\pm$ 1.3	5.3 $\pm$ 1.6	6.4 $\pm$ 2.3	11.1 $\pm$ 3.7
5	6.2 $\pm$ 1.1	5.4 $\pm$ 2.2	7.6 $\pm$ 2.1	11.9 $\pm$ 1.3
10	6.3 $\pm$ 1.3	5.7 $\pm$ 1.9	9.6 $\pm$ 3.4	8.9 $\pm$ 5.0

### 3.3.2.3 Derived Diffusion Coefficient

For most particles derived diffusion rate from PTV (calculated from Eq. 9, section "0") is comparable with the one measured from DLS (calculated from Eq. 6, section "3.2.2.3") (Table 21 and Figure 121), except for the PVD where the values were over three times higher. Another difference between DLS and PTV lied in the variation of behavior in the presence of  $H_2O_2$ . The variation of speed were more pronounced for JP and PVD in 2D PTV, which could be explained with non-diffusive motion in PVD and JP that were difficult to evidence by DLS. Table 20 summarizes the mean value of diffusion coefficient derived from the mean speed of PTV tracked particles while Figure 120 illustrates impact of hydrogen peroxide on respective particles graphically.

## Investigation of Particle Kinematics

Table 20: Mean Diffusion Coefficient values for particles at respective concentration of hydrogen peroxide. SP showing no impact of hydrogen peroxide, while Janus particles (JP and PVD) shows highest relative difference amongst all the samples.

% (v/v) [H <sub>2</sub> O <sub>2</sub> ]	Diffusion Coefficient (μm <sup>2</sup> /s) ± Std. Dev			
	SP	Iso	JP	PVD
0	0.96 ± 0.45	0.68 ± 0.41	1.04 ± 0.79	3.10 ± 1.87
5	0.91 ± 0.40	0.77 ± 0.94	1.40 ± 0.87	3.38 ± 1.25
10	0.93 ± 0.48	0.81 ± 0.69	2.33 ± 1.27	2.32 ± 2.94

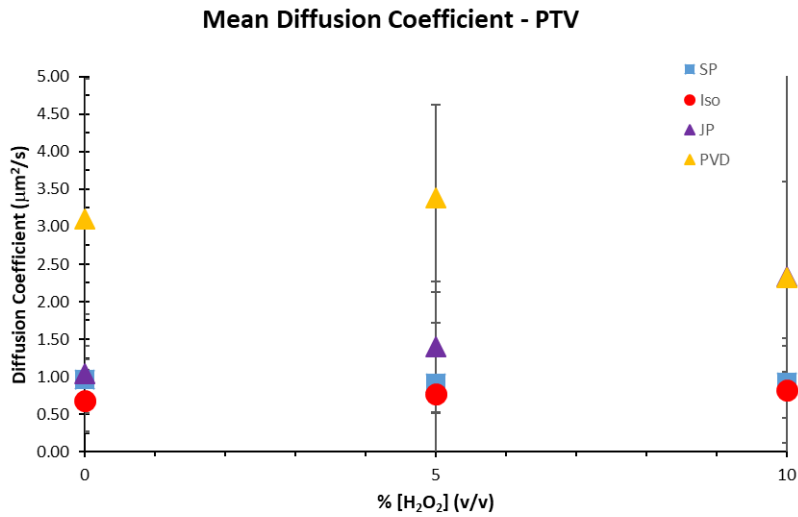


Figure 120: Mean values of derived diffusion coefficient of particle at respective concentration of hydrogen peroxide from Particle Tracking Velocimetry (PTV) technique shows Janus particle with highest diffusion rate.

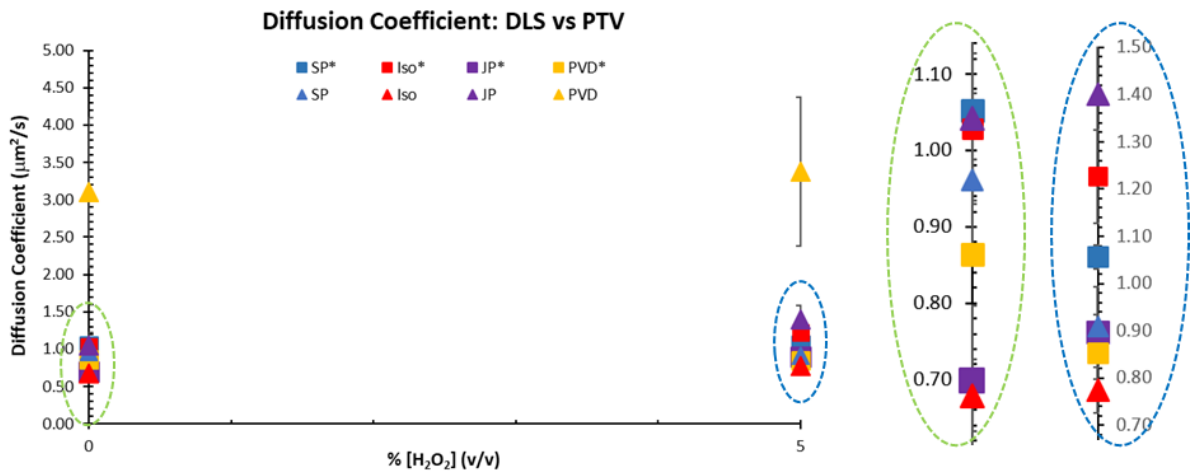


Figure 121: Comparison of diffusion coefficient from PTV (solid lines) and DLS (dash-lines) at 0% and 5% (v/v) hydrogen peroxide. Particles other than PVD-PTV have similar range of diffusion coefficient.

## Investigation of Particle Kinematics

*Table 21: Diffusion coefficient comparison table between DLS and PTV. Iso shows fastest diffusion in 3D experiments (DLS), Janus particles faster diffusion in 2D experiment (PTV).*

<b>[H2O2]</b>	<b>Technique</b>	<b>SP</b>	<b>Iso</b>	<b>JP</b>	<b>PVD</b>
<b>0%</b>	DLS	1.05	1.03	0.70	0.86
	PTV	0.96	0.68	1.04	3.10
<b>5%</b>	DLS	1.06	1.23	0.90	0.85
	PTV	0.91	0.77	1.40	3.38

Relative change in particle diffusion rate calculated from maximum and minimum values from DLS and PTV experiments in Table 22 showed that the higher relative difference were observed for JP (123%) and PVD (46%), confirming the original behaviour of Janus Particle, while SP remained as the least varying particle specie in both 3D and 2D motion study techniques.

*Table 22: Relative change (%) in mean diffusion coefficient calculated from DLS and PTV experiments for respective samples.*

<b>Particle</b>	<b>DLS (Relative Change Diffusion Coefficient) (%)</b>	<b>PTV (Relative Change Diffusion Coefficient) (%)</b>
<b>SP</b>	3	6
<b>Iso</b>	18	20
<b>JP</b>	22	123
<b>PVD</b>	4	46

### 3.4 Conclusion

Our study highlights the importance, limitations and considerations associated with DLS measurements, particularly in the context of particle dynamics. SP exhibits uniform dispersion while surface-modified particles (Iso, JP, and PVD) implied particle clustering (or aggregation). Reduction of baseline-undulates upon introduction of hydrogen peroxide suggested non-steady state active motion from catalytic interaction between gold and hydrogen peroxide. Limitations of DLS, particularly its reliance on Brownian motion demands careful interpretation of results as inevitable artefact for compensating non-Brownian motion can be misleading by not reflecting the true dynamics of active particles. While, Particle Tracking Velocimetry (PTV) study, despite its tedious nature, proves to be a valuable method for in monitoring individual particle and understanding particle-motion better by subsiding collective motion. Overall, the observation of particle-movement (due to enhanced

diffusivity) at  $[H_2O_2]$  as low as 0.3 mM indicates that the  $[H_2O_2]$  is favourable to conduct this type of motion study. However, diffusive/non-diffusive trends in particle motion from the PTV study in chapter three remained inconclusive. The utilization of TrackMate provided crucial insight regarding the orientation of particle motion, which is isotropic in direction across all the samples. Relative differences in diffusion coefficient of particles confirmed higher catalytic activity in chemically synthesized gold/silica Janus particles. Overall, our results in this chapter suggest that for the synthesis of Janus particles, nanoparticle grafting is a good strategy to compare to PVD. Although in some condition, this grafting may be detrimental as it leads to a very large increase of the hydrodynamic radius.

We also conclude that upon catalytic activation, janus nature is not necessarily required to obtain an increase in diffusion, although wider time-window for PTV observations may be more interesting for more/better profound trends (if any) from impact of hydrogen peroxide on particle-motion. PTV study aligned with the findings of non-steady state active motion from DLS study and supported for steady state investigation of particle motion in presence of hydrogen peroxide gradient.

## 3.5 Reference

- (1) McGlasson, A.; Bradley, L. C. Investigating Time-Dependent Active Motion of Janus Micromotors Using Dynamic Light Scattering. *Small* **2021**, *17* (52), 2104926. <https://doi.org/10.1002/sml.202104926>.
- (2) Ershov, D.; Phan, M.-S.; Pylvänäinen, J. W.; Rigaud, S. U.; Le Blanc, L.; Charles-Orszag, A.; Conway, J. R. W.; Laine, R. F.; Roy, N. H.; Bonazzi, D.; Duménil, G.; Jacquemet, G.; Tinevez, J.-Y. TrackMate 7: Integrating State-of-the-Art Segmentation Algorithms into Tracking Pipelines. *Nat Methods* **2022**, *19* (7), 829–832. <https://doi.org/10.1038/s41592-022-01507-1>.
- (3) Yu, Z.; Reid, J. C.; Yang, Y.-P. Utilizing Dynamic Light Scattering as a Process Analytical Technology for Protein Folding and Aggregation Monitoring in Vaccine Manufacturing. *JPharmSci* **2013**, *102* (12), 4284–4290. <https://doi.org/10.1002/jps.23746>.
- (4) Varenne, F.; Botton, J.; Merlet, C.; Beck-Broichsitter, M.; Legrand, F.-X.; Vauthier, C. Standardization and Validation of a Protocol of Size Measurements by Dynamic Light Scattering for Monodispersed Stable Nanomaterial Characterization. *Colloids and Surfaces A: Physicochemical and Engineering Aspects* **2015**, *486*, 124–138. <https://doi.org/10.1016/j.colsurfa.2015.08.043>.
- (5) Stetefeld, J.; McKenna, S. A.; Patel, T. R. Dynamic Light Scattering: A Practical Guide and Applications in Biomedical Sciences. *Biophys Rev* **2016**, *8* (4), 409–427. <https://doi.org/10.1007/s12551-016-0218-6>.
- (6) Malvern Zetasizer ZS DLS User Manual.Pdf. <https://www.chem.uci.edu/~dmityrf/manuals/Malvern%20Zetasizer%20ZS%20DLS%20User%20manual.pdf>.
- (7) The principles of dynamic light scattering | Anton Paar Wiki. Anton Paar. <https://wiki.anton-paar.com/en/the-principles-of-dynamic-light-scattering/>.
- (8) Babick, F. Chapter 3.2.1 - Dynamic Light Scattering (DLS). In *Characterization of Nanoparticles*; Hodoroaba, V.-D., Unger, W. E. S., Shard, A. G., Eds.; Micro and Nano Technologies; Elsevier, 2020; pp 137–172. <https://doi.org/10.1016/B978-0-12-814182-3.00010-9>.
- (9) Misono, T. Dynamic Light Scattering (DLS). In *Measurement Techniques and Practices of Colloid and Interface Phenomena*; Abe, M., Ed.; Springer: Singapore, 2019; pp 65–69. [https://doi.org/10.1007/978-981-13-5931-6\\_10](https://doi.org/10.1007/978-981-13-5931-6_10).
- (10) Leong, S. S.; Ng, W. M.; Lim, J.; Yeap, S. P. Dynamic Light Scattering: Effective Sizing Technique for Characterization of Magnetic Nanoparticles. In *Handbook of Materials Characterization*; Sharma, S. K., Ed.; Springer International Publishing: Cham, 2018; pp 77–111. [https://doi.org/10.1007/978-3-319-92955-2\\_3](https://doi.org/10.1007/978-3-319-92955-2_3).
- (11) Huang, X.; Sheng, L.; Lu, Y.; Li, S. Atomization Characteristics of Hydrogen Peroxide Solutions in Electrostatic Field. *Micromachines* **2022**, *13* (5), 771. <https://doi.org/10.3390/mi13050771>.
- (12) TrackMate Analyzers. ImageJ Wiki. <https://imagej.github.io/plugins/trackmate/analyzers/index>.
- (13) TrackMate. <https://imagej.net/plugins/trackmate/>.
- (14) Introduction. [https://web.mit.edu/savin/Public/Tutorial\\_v1.2/Introduction.html](https://web.mit.edu/savin/Public/Tutorial_v1.2/Introduction.html).
- (15) Nandi, A.; Heinrich, D.; Lindner, B. Distributions of Diffusion Measures from a Local Mean-Square Displacement Analysis. *Phys. Rev. E* **2012**, *86* (2), 021926. <https://doi.org/10.1103/PhysRevE.86.021926>.
- (16) Weiss, L. B.; Dahirel, V.; Marry, V.; Jardat, M. Computation of the Hydrodynamic Radius of Charged Nanoparticles from Nonequilibrium Molecular Dynamics. *J. Phys. Chem. B* **2018**, *122* (22), 5940–5950. <https://doi.org/10.1021/acs.jpcc.8b01153>.
- (17) Lyu, X.; Liu, X.; Zhou, C.; Duan, S.; Xu, P.; Dai, J.; Chen, X.; Peng, Y.; Cui, D.; Tang, J.; Ma, X.; Wang, W. Active, Yet Little Mobility: Asymmetric Decomposition of H<sub>2</sub>O<sub>2</sub> Is Not Sufficient in Propelling Catalytic Micromotors. *J. Am. Chem. Soc.* **2021**, *143* (31), 12154–12164. <https://doi.org/10.1021/jacs.1c04501>.
- (18) Pham, X.-H.; Tran, V.-K.; Hahm, E.; Kim, Y.-H.; Kim, J.; Kim, W.; Jun, B.-H. Synthesis of Gold-Platinum Core-Shell Nanoparticles Assembled on a Silica Template and Their Peroxidase Nanozyme Properties. *International Journal of Molecular Sciences* **2022**, *23* (12), 6424. <https://doi.org/10.3390/ijms23126424>.
- (19) Xiao, Z.; Nsamela, A.; Garlan, B.; Simmchen, J. A Platform for Stop-Flow Gradient Generation to Investigate Chemotaxis. *Angewandte Chemie International Edition* **2022**, *61* (21), e202117768. <https://doi.org/10.1002/anie.202117768>.
- (20) Nandi, A.; Heinrich, D.; Lindner, B. Distributions of Diffusion Measures from a Local Mean-Square Displacement Analysis. *Phys. Rev. E* **2012**, *86* (2), 021926. <https://doi.org/10.1103/PhysRevE.86.021926>.
- (21) Campbell, C. E. Diffusivity and Mobility Data. In *Fundamentals of Modeling for Metals Processing*; Furrer, D. U., Semiatin, S. L., Eds.; ASM International, 2009; pp 171–181. <https://doi.org/10.31399/asm.hb.v22a.a0005430>.
- (22) Islam, M. A. Einstein–Smoluchowski Diffusion Equation: A Discussion. *Phys. Scr.* **2004**, *70* (2–3), 120–125. <https://doi.org/10.1088/0031-8949/70/2-3/008>.
- (23) [https://github.com/Vevitek/CEA\\_PFE\\_Zak/blob/main/MSDtraj.py](https://github.com/Vevitek/CEA_PFE_Zak/blob/main/MSDtraj.py)

# CHAPTER 4

## Chapter 4. Particle Motion in Gradient

### 4.1 Introduction

As Chapter 3 discussed the inherent complexities of Dynamic Light Scattering (DLS) measurements and particle tracking observations in homogeneous concentrations of hydrogen peroxide, Chapter 4 aims for motion study of particles in concentration gradient of hydrogen peroxide. For this purpose dedicated microfluidics chip was utilized making of which is described in the methodology. As highlighted in Chapter 1 the fluid dynamics inside of the microfluidic chip is an essential aspect of steady state motion study, the related numerical simulation work were performed on COMSOL Multiphysics platform (named COMSOL hereafter), which also helped in better configuration of chips.

COMSOL is a powerful and versatile platform for modelling complex physical phenomena. It offers time-dependent studies that helps us understanding the transient behaviour and dynamic processes in a system. Additionally, COMSOL offers robust capabilities for steady-state studies, which is essential for understanding the long-term behaviour and equilibrium conditions of systems. In our study Navier-Stokes equation has been assimilated by physics-solvers in COMSOL, enabling the comprehensive analysis of systems with both transient and equilibrium behaviour.<sup>1</sup>

The contents of chapter 4 are the methods followed to design gradient generator microfluidic device (using drawing software Klayout), optimization by simulation of chip-functioning (using COMSOL), manufacturing of the microfluidic chip (via photolithography and soft-lithography) and lastly the studying the motion of particle in presence of concentration gradient of hydrogen peroxide (by optical microscopy and PTV via ImageJ-Trackmate).

### 4.2 Material and Method

#### 4.2.1 Material

##### 4.2.1.1 Chemicals and Materials

Hydrogen Peroxide (30% (v/v)) (CAS N°: 7722-84-1) by Sigma Aldrich, Polydimethylsiloxane (PDMS), Sylgard 184 from Neyco, Isopropanol absolute from VWR Chemicals, SU8 2007, SU8 2050, SU8 3005, Rhodamine 6G from Merck. Milli-Q water used for all the experiments and storage (unless mentioned otherwise).

##### 4.2.1.2 Apparatus and Softwares

Rotating agitator LD-76 from LABINCO BV, Ultrasonicator from, Biopsy Puncher 0.5 mm (SKU: PT-T983-05) from Fischer Scientific, Optical Microscope from Olympus CKX41, camera sCMOS PCO.edge model 3.1 from PCO, Syringe Pump from Nemesys, 0.25, 0.5 and 1 mL Glass Syringe from SGE, Pressure box controller from Fluigent, KLayout (v 0.28.13), COMSOL Multiphysics (v 5.1), Micromanager (v 2.0), ImageJ, PyCharm (v 2023.2.5).

#### 4.2.1.3 Glassware and Plastic ware

Eppendorf (1.5 mL), UV Grade Fused Silicon Wafer ( $\varnothing$ 100mm) flat Corning 7980 from, Tube PEEK (external  $\varnothing$ 510 $\mu$ m and internal  $\varnothing$ 125 $\mu$ m) from CLUZeau Info Labo, Glass slide from Thermo Fischer.

#### 4.2.2 Method

In order for microfabrication the concentration gradient generating microfluidic device, the primary step is to configure the geometry and simulate the functioning of chip for our desired result. To obtain the gradient generator, selected geometry was optimized (via numerical simulation using COMSOL), followed by microfabrication and PTV experiments. The design chosen for our microfluidic channel was an H-design (Figure 122. A). This H-shaped microfluidic channel design was a practical choice due to its ability to promote controlled diffusion between merging streams while maintaining a well-defined flow path (Figure 122). The idea here was to have a continuous flow of particle (suspended in water) in one of the two parallel channels and a fixed concentration of hydrogen peroxide from another. At zero pressure difference between the parallel channels there would not be any flow between the connecting bridge, thus, decoupling the channels completely. Therefore, generating continuous gradient of hydrogen peroxide in the bridge.

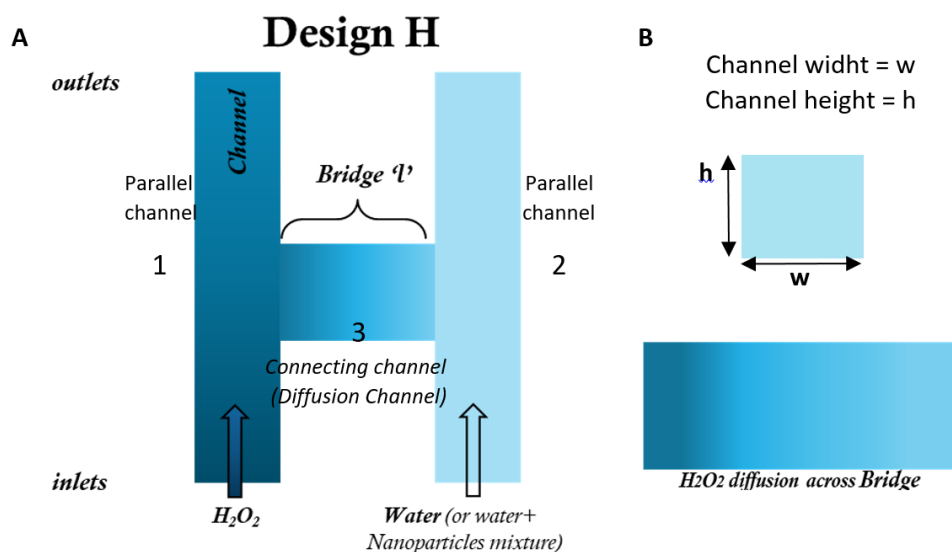


Figure 122: (A) Labeled diagram of microfluidics channel Design-H with expected  $[H_2O_2]$  gradient across Bridge of length 'l', (B) showing the  $[H_2O_2]$  gradient across Bridge and Channel dimension width and height. Inlets and outlets are in the main channels parallel to each other (Parallel Channel 1 and 2), which are connected by the horizontal bridge (Connecting Channel 3).

Understanding the fluid dynamics played key role here. In presence of pressure differences within a microfluidic channel, fluid flows from regions of high pressure to regions of low pressure. This leads to mixing of fluid layers due to convection and hinders the process of pure diffusion, causing unpredictable flow patterns, disruption and maintenance of the desired well-defined and stable concentration gradient. Convection is the bulk movement of a fluid due to external forces like pressure gradients, density differences, or shear forces.<sup>2</sup> To have diffusion as the dominant mass transfer



mechanism and generation of a predictable, stable and controlled concentration gradient across the channel absence of pressure-driven convection is an essential requirement. When diffusion dominates in the transverse direction (across the width of the bridge channel), longitudinal mixing along the length of the channel is minimized due to the absence of convective flows ensures a well-defined; steady-state gradient in the bridge over time, ultimately maintaining the integrity of the concentration gradient established by pure diffusion.

H-design's flexibility and compatibility with simulation tools further enhance its suitability for microfluidic chip applications. Photolithography is a technique in microfabrication, enabling the creation of patterned structures on a substrate. It utilizes light-sensitive materials (photoresists) to transfer a geometric design from a mask onto the underlying material. Photolithography offers high resolution, good feature definition, and the ability to create complex patterns. It's a versatile technique widely used in microfabrication of various devices, including microfluidic chips.<sup>3,4</sup>

#### 4.2.2.1 Design and Simulation (COMSOL)

To design a closed-wall H-geometry microfluidics channel for simulating fluid flow in COMSOL Multiphysics 5.1, to obtain a stable concentration gradient of hydrogen peroxide was simulated by following some major steps like designing the geometry, physics setting, solver setting, post processing and result extraction. Physics applied here to understand the sum of forces (right hand side in Eq. 1) acting upon the molecules in flowing fluid is calculated by the Navier-Stokes Equation (Eq. 1). Here  $\rho$  is fluid density,  $v$  is fluid velocity,  $t$  is time,  $P$  is the pressure,  $\mu$  is the dynamic viscosity of fluid,  $\nabla$  is the del operator and  $\nabla^2$  is the Laplacian operator.<sup>5</sup>

$$\rho \left( \frac{\partial v}{\partial t} + (v \cdot \nabla)v \right) = -\nabla P + \mu \nabla^2 v \quad \text{Eq. 1}$$

Here,  $\rho (\partial v / \partial t)$  is the rate of change of velocity,  $\rho (v \cdot \nabla) v$  refers to the convective acceleration,  $-\nabla P$  is the pressure force,  $\mu \nabla^2 v$  is the contribution from friction force; fluid viscosity.<sup>5</sup> As our study is in steady state, rate of change of velocity and convective acceleration stands as nil ( $\rho ((\partial v / \partial t) + (v \cdot \nabla) v) = 0$ ), therefore making Eq. 2 as accounting factor in our numerical simulation study on COMSOL.

$$\nabla P = \mu \nabla^2 v \quad \text{Eq. 2}$$

Steps followed during COMSOL simulation are:

1. Designed the geometry in 2D using the CAD tools available in COMSOL and extruded it along the z-axis to obtain microfluidics channel in 3D. For H- design geometry two parallel main channels were made by two parallel rectangles, connected by smaller perpendicular channels (bridge).
2. Closed the geometry; all the channels were internally connected with singular boundary system, and then the inlet and outlet walls were assigned.

3. Defined all the parameters with respected to the fluid and flow (example concentration, flow rate, etc.) under a global parameter.
4. For simulating adequate dynamics, selected a medium size mesh ensuring accurate simulation results for the designed H-design.
5. Set up the fluid flow physics by selecting the laminar flow module in COMSOL.
6. Defined the material properties of the fluid such as density and viscosity.
7. Assigned the inlet and outlet boundary conditions for the fluid flow.
8. For steady state simulations, chose the stationary solver configuration, while for obtaining time steps chose time dependant study as transport of diluted specie from solver configuration. This was helpful in time-estimation for obtaining a stable concentration gradient of hydrogen peroxide in Bridge (horizontal bar in H-design).
9. Ran the simulation to solve for the fluid flow within the designed microfluidics channel.
10. To understand the fluid-flow behaviour, visualized and analysed the simulation results like Data Sets, Velocity Profile, Concentration Profile (Figure 125), etc. under Results section.
11. Extracted Velocity and Concentration Profile data and generate plots for result.

COMSOL outputs for H-design microfluidic channel showed that to obtain stable gradient across bridge, the flow rates in parallel channels ( $Q_1$  and  $Q_2$ , respectively) must be equal (Figure 123 A) and the length of the bridge should be above  $1000 \mu\text{m}$  to prevent “entrance” effect (Figure 123 B).

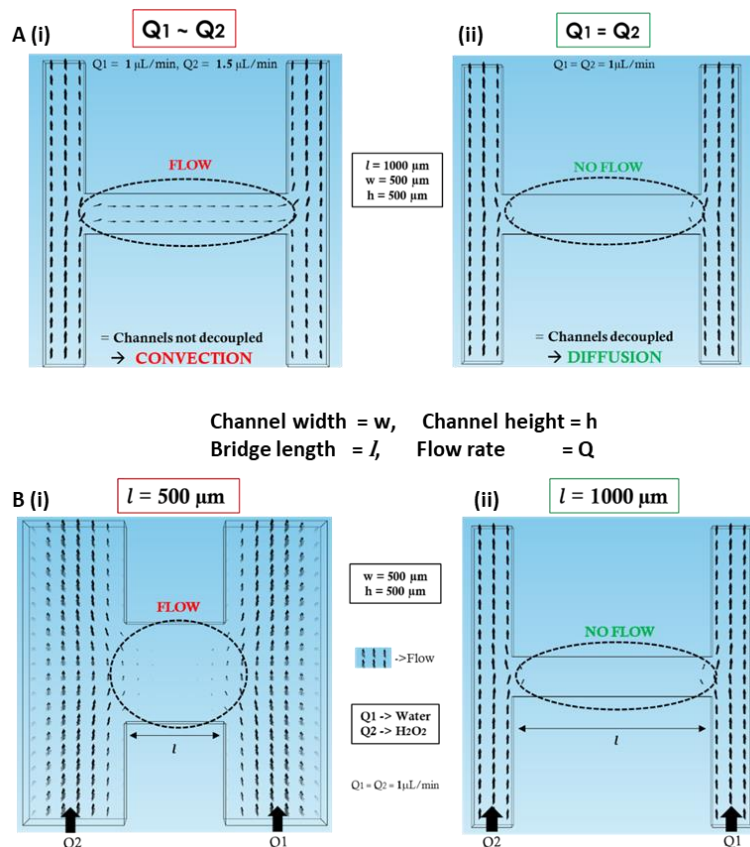


Figure 123: Shows crucial factors like flow rate (A) and length (B) for achieving diffusion in bridge of H-design microfluidic channel. A (i) shows convection across bridge due to unequal flow rate, A (ii) is compatible for diffusion across bridge due to complete decoupling of parallel channel from equal flow rate. B (i) shows partial decoupling of parallel channels unlike B (ii).

Upon achievement of a stable gradient, it was important to determine the time required to achieve it. According to the Fick's 2<sup>nd</sup> law of diffusion<sup>6</sup> the approximate diffusion time ( $t_d$ ) of a substance is the square of the diffusion distance ( $l$ ) by its diffusion coefficient ( $D$ ) (Eq. 3).

$$t_d = \frac{l^2}{2D} \quad (\text{Eq. 3})$$

For diffusion coefficient of hydrogen peroxide  $D = 1.5 \times 10^{-9} \text{ m}^2/\text{s}$ ,<sup>7</sup> and 2 mm distance of bridge, the approximate time to obtain a stable gradient would be 1333 second, while time dependant study from COMSOL simulation showed stable gradient achievement after ~1300 seconds (Figure 124), proving the theoretical credibility of H-design.

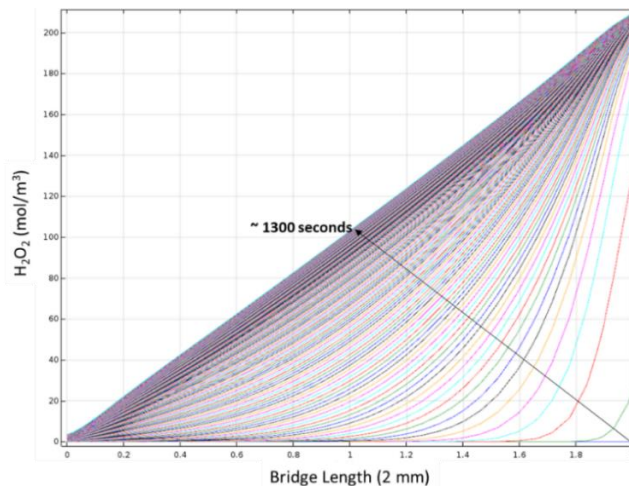


Figure 124: COMSOL result to achieve stable gradient for 2 mm long bridge.

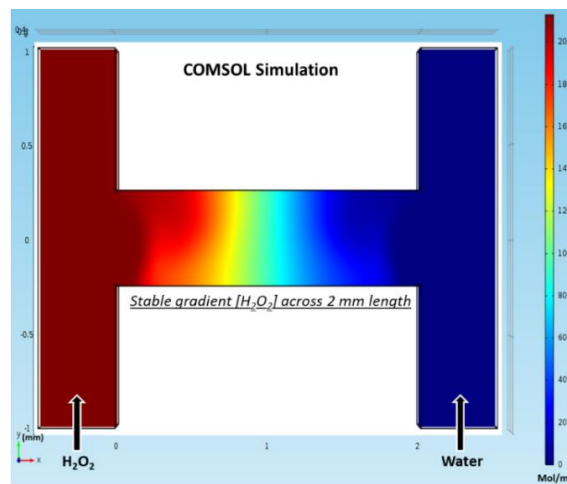


Figure 125: Stable gradient of H<sub>2</sub>O<sub>2</sub> across Bridge of 'l' = 2 mm from COMSOL simulation in H-design microfluidic channel.

#### 4.2.2.2 Microfabrication

Succeeding COMSOL simulation and optimization, the pre-requirement for microfabrication (photolithography) is photomask for the making of master mould. To design photomask KLayout was used, while the photomask was ordered to commercial manufacturer. Fabrication of the master mould was achieved by pouring SU8 photosensitive resin onto a silicon wafer, followed by controlled rotations to achieve the desired height. The key steps of photolithography are substrate preparation, Photoresist Deposition, Soft Baking, Photomask Alignment, UV (Ultraviolet) Exposure, Development, Post Bake and Pattern Transfer. Substrate Preparation (e.g., silicon wafer) is done by contaminants removal (using Plasma) that might affect photoresist adhesion or subsequent processing steps, followed by deposition of a uniform layer of photoresist onto the substrate (by spin-coating method). The coated substrate is then soft baked at a controlled temperature and time (this step removes residual solvents from the photoresist, optimizing its film properties for the subsequent steps). Further, the selected photomask is aligned precisely with the photoresist-coated substrate and exposed to UV light source, causing polymerization. The specific wavelength and exposure time depend on the chosen photoresist. In a positive photoresist, exposed areas become more soluble, while unexposed areas remain less soluble. Conversely, in a negative photoresist, exposed regions become less soluble (our followed procedure is summarized in Figure 126). After exposure, the photoresist is immersed in a developer solution. The developer selectively removes either the exposed or the unexposed regions based on the photoresist type, creating a patterned resist layer that reflects the photomask design. Lastly, a final bake step helps solidify the developed photoresist pattern and enhance its resistance to subsequent processing steps.<sup>3,4</sup>

After development, the mould was characterized using optical interferometry, and the resulting negative replica of PDMS was obtained by pouring PDMS mixed with a crosslinking chemical (PDMS curing agent) into the mould and heating it to solidification. Upon curing, the negative replica of PDMS was peeled off the master mould, and inlets/outlets were created by the help of a biopsy puncher. The PDMS block was then treated with oxygen plasma to create silanol groups onto the surface, enabling bonding to a glass support (formation of siloxane bond) to seal the microchannels (summarized pictorially in Figure 128). The specifications of these procedures followed during the thesis is shared in section “4.2.2.2.1” and “4.2.2.2.2”.

##### 4.2.2.2.1 Photolithography

1. Substrate Preparation: Cleaned the glass slide with Isopropyl Alcohol, dried with nitrogen and followed by surface cleaning with plasma.
2. Spin Coating of photoresist: Applied a layer of photoresist (SU8 3050) at 4000 rpm for 10 seconds with an acceleration of 300 rpm/second, followed by coating for 30 seconds with an acceleration of 300 rpm/second.
3. Soft Baking: Baked the above at 95°C for 13 minutes and allowed to cool down to room temperature.
4. Design introduction via mask alignment: Carefully placed the photolithography polymer mask (containing the desired design) directly on top of the photoresist-coated substrate. To make contact, placed a 4” quartz block on top of the mask.
5. Exposure: Exposed to UV light for 3 seconds at 200 mJ/cm<sup>2</sup> and proceeded for post-bake.

6. Post-bake: Baked the above at 65°C and 95°C for 1 minute and 4 minutes, respectively, followed by cooling down at room temperature for 2 hours.
7. Development: Developed the photoresist for 5-8 min and measured the height using interferometer (Figure 127).

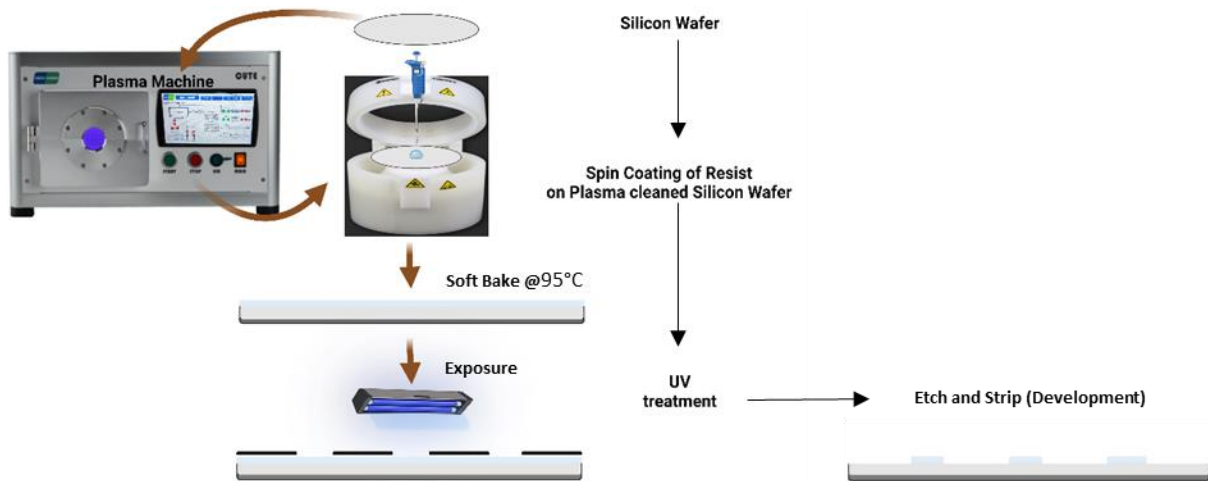


Figure 126: Schematic of Photolithography to obtain master mould on silica wafer with desired design

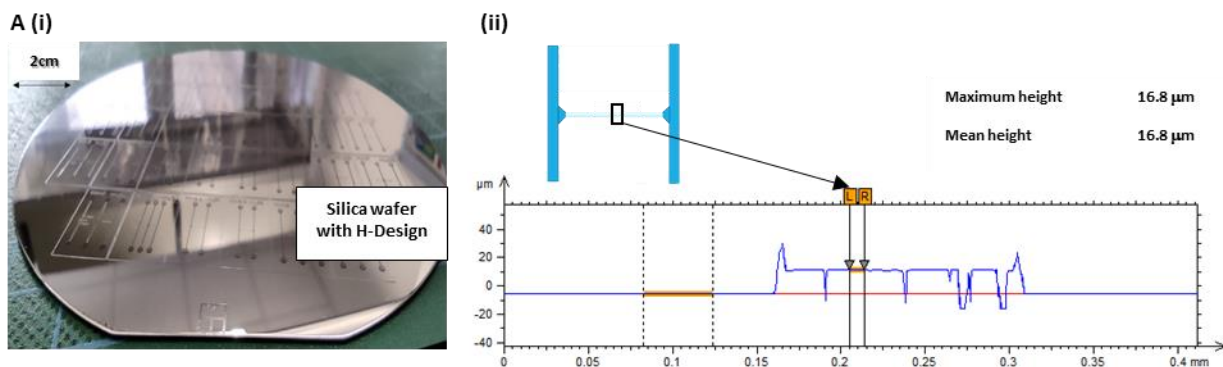


Figure 127: H-design for microfluidic channel photolithographed on silica wafers in A (i) and bridge height assessed via interferometer in A (ii).

#### 4.2.2.2.2 Soft Lithography

1. Mixed 4 g curing agent in 40 g PDMS (1:10 (w/w)) using a disposable plastic stirrer.
2. Placed PDMS mixture in vacuum degassing chamber for 15-20 min.
3. In a petri dish, placed master mould (made from photolithography on silica wafer) and poured the bubble-free PDMS mixture.
4. For PDMS-solidification, placed the petri dish (PDMS-poured master mould) in incubator 70°C for 24 hrs (Figure 128. B).
5. Demoulded by slowly peeling the solidified PDMS, followed by punching holes ( $\varnothing$  0.5 mm) for inlet(s) and outlet(s).

- Finally, activated the surface of PDMS chip and glass-slide from plasma treatment and the activated sides together (Figure 128. F and G).

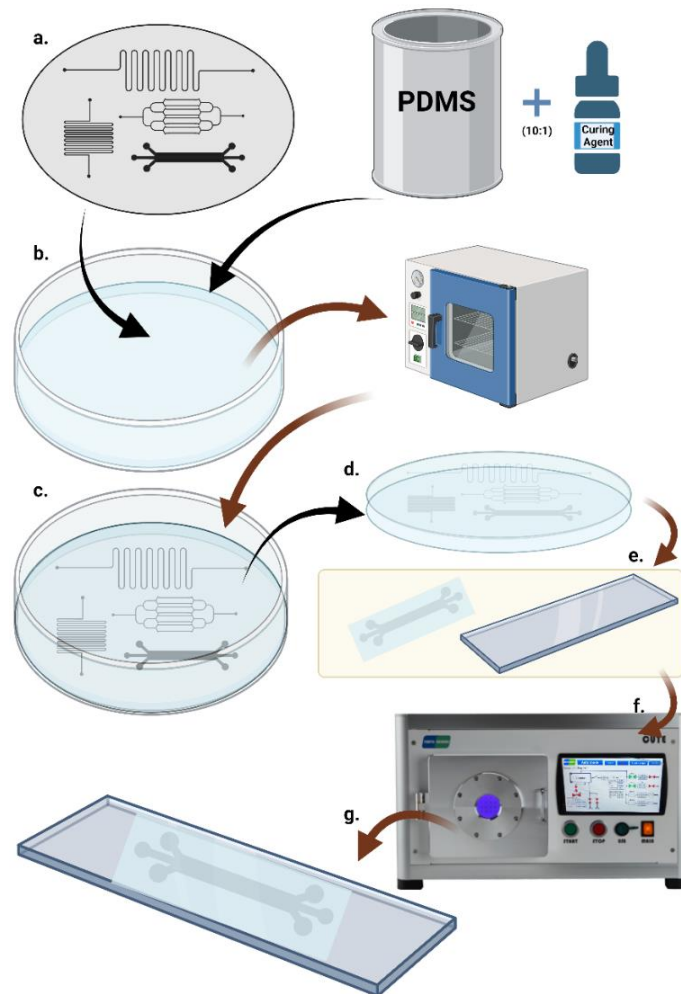


Figure 128: Illustration of the step-by-step microfabrication of PDMS chip microfabrication: a. Selection of master mould (photolithographed on a silica wafer) PDMS+curing agent (Sylgard) mixture preparation (10:1 w/w). b. PDMS mixture onto the master mould followed by incubation at 70°C for PDMS solidification; c. Solidified negative replica of PDMS peeled off the master mould; d. Inlet and outlet holes punched; e-f Surface activation in PDMS chip and glass slide, by plasma treatment for facilitating the bonding; g. PDMS chip bonded on glass ready to use.

#### 4.2.2.3 Chip Functioning Test and Alternate design

A solution to overcome convection driven mixing (verified from COMSOL simulation outcomes for pure diffusion) is the minimization of pressure difference and maintenance of laminar flow across the microfluidic channel. In an H-shaped microfluidic chip, this was achievable by decoupling of parallel channels and suppressing the unwanted convection-influenced mixing between solutions from the parallel channels; ultimately ensuring the integrity of the gradient in the bridge channel. Decoupling of parallel channels would lead to zero flow (or close to zero flow) in the bridge channel while maintaining continuous flow in the parallel channels.

One of the approach, confirmed by numerical simulation, was to balance the flow at the bridge region by adjusting the flow rate in each parallel channel. Precise manipulation of flow rates and volumes for

a steady laminar flow of the fluids in parallel channels was achievable by using syringe pumps or pressure-driven flow systems. Experimental verification of the functioning of our microfluidic chip was performed prior to the commencement of motion study of SP, Iso, JP and PVD in hydrogen peroxide gradient. This step helps us in understanding and overcoming the gap between numerical simulations and real-time experiments.

During these experiments (chip-functioning verification) diffusion of fluorescent silica micro-particles ( $\varnothing \sim 1\mu\text{m}$ ) was observed across the bridge as a consequence of decoupling of parallel channels using. To visualize the diffusion of particles across the bridge, we maintained equal flow equilibrium in the parallel channels in order to attain zero pressure difference at both sides. Set-up utilized for this purpose was shared in Figure 129, where the chip inlets were connected with syringe pump that pumped suspension of fluorescent silica particles from one channel and hydrogen peroxide from the other. In order to avoid the influence of any possible chemical contamination, new syringe (or the old syringes washed 10 times) were used throughout the experiments.

While working with H-design, reproducing channel decoupling and pure free diffusion of silica micro-particles was a major challenge. In fact, it was impossible to stabilise the flow rates for zero (or near zero) flow in the bridge (diffusion channel). Therefore, we decided to significantly increase the hydraulic resistance of the bridge channel in order to be less sensitive to fluctuations of the flow (pump sensitivity, design heterogeneity).

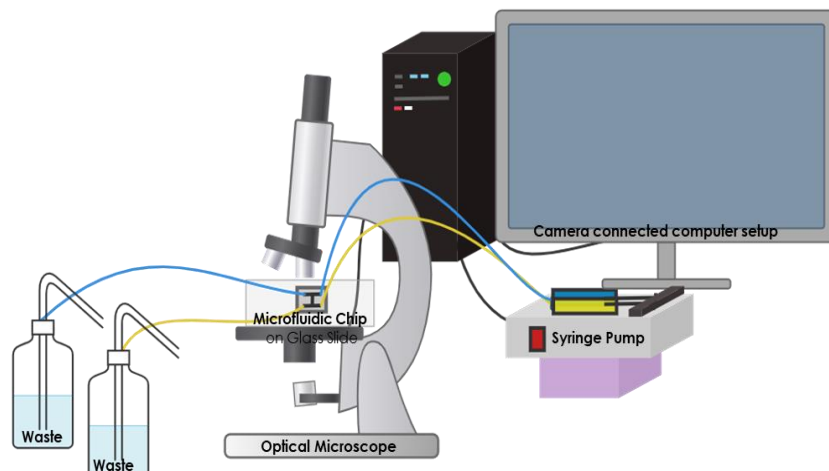


Figure 129: Schematic of Chip Functioning Test for stable gradient generation.

For this purpose, a modified design had been conceived and realised where the hydraulic resistance has been increased for better flow regulation. As per the Hagen-Poiseuille equation for a rectangular channel (Eq. 4) alteration in height largely effects the flow rate<sup>8</sup>. Thus, reducing the height and width of bridge than the parallel channels (see Figure 130) was attempted.

$$Q \approx \left( \frac{1-0.63\left(\frac{h}{w}\right)}{12\mu L} \right) h^3 w \Delta P \quad \text{Eq. 4}$$

Here,  $Q$  is the flow rate,  $h$  is the channel height,  $w$  is the channel width,  $\mu$  is the dynamic viscosity of the fluid,  $L$  is the channel length and  $\Delta P$  is the pressure drop across the channel. The modifications in the newer H-design comprises of  $\sim 60\%$  decreased height and width of the diffusion channel (bridge), than the parallel channels.

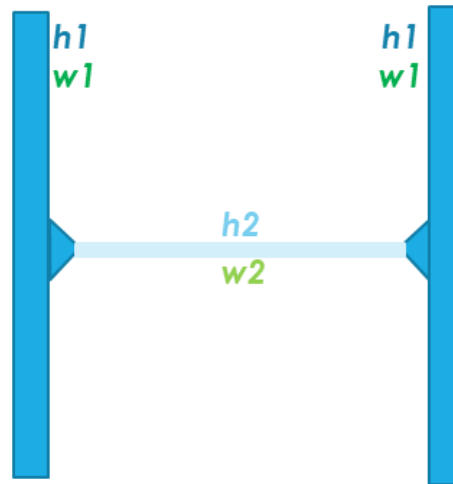


Figure 130: H-design chip with channels and bridge of different heights and width;  $h_1 \gg h_2$  and  $w_1 \gg w_2$ .

The dimensional modifications of microfluidic channels with increased hydraulic resistance gave better flow regulation, but still difficulty in reaching a stable flow equilibrium by complete decoupling of parallel channels sustained. Figure 131.B illustrates experimental-observation where maintaining equal flow rates ( $Q_1$  and  $Q_2$ ) in parallel channels did not truly decoupled the channels (unlike the case in COMSOL simulation in Figure 123. A) and caused the flow of particles through bridge.

Dark red lines in Figure 131. B) and C) are the particle-tracks from TrackMate observations. The area highlighted (white oval) in Figure 131. B) shows particles with track-colour ranging from yellow to light blue; representative of particles with observable velocity. This means that the fluctuations in flow rates or small differences in microfabrication at the level of the different channels were still perceptible. While a little adjustment in the flow rate (experimentally) was a tedious task, it helped in better decoupling of parallel channel (Figure 131. C) and achieving convection-free-diffusion of particle through the bridge of H-design microfluidic chip.

The area highlighted (white oval) in Figure 131. C) shows particles with track-colour ranging between shades of blue; representative of observed particles had reduced velocity. Therefore, in order for well utilization of time (in achieving flow equilibrium between parallel channels and subsequently decoupling them to obtain pure-diffusion in diffusion channel (bridge)) an alternative robust design for stable gradient generator microfluidic device was prepared.



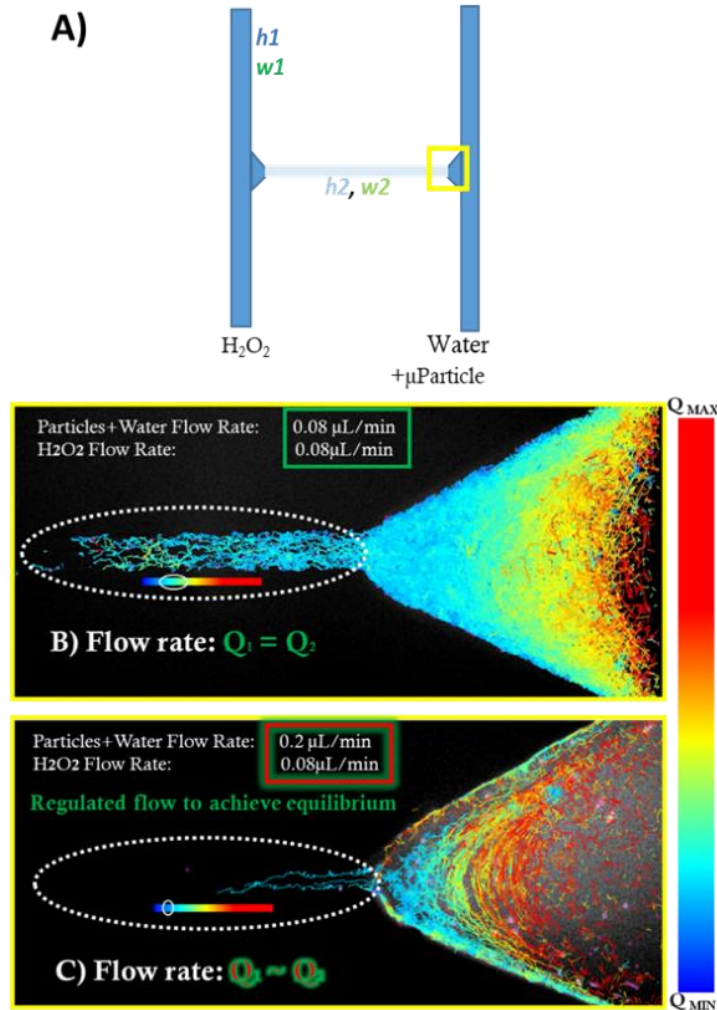


Figure 131: Modifications in H-design microfluidic channel for higher hydraulic resistance in image A) has decreased height ( $h_2$ ) and width ( $w_2$ ) in diffusion channel. Different colour lines (image B) and C)) represent mean speed and respective path of particles; dark red being the fastest and dark blue being the slowest. At equal flow rate in parallel channels, particles entering diffusion channel has light blue, green and yellow lines (white highlighted oval) in image B) confirming convection-driven movement. A little adjustment in flow-rate (red square in image C) gives convection-free diffusion of particles through the diffusion channel (confirmed by the darker blue lines in highlighted in white).

#### 4.2.2.4 Alternative Chip design and Literature

Irimia et al<sup>9</sup> presented a novel microfluidic platform for investigating the effects of localized stimuli on migrating cells. The key advantages of Irimia’s design<sup>9</sup> is the precise control of chemical gradients. The Y-shaped microfluidic design (Figure 132) shared by the team comprises of arrays of connecting channel (similar to the bridge channel of our H-design), supporting flow balancing mechanism.

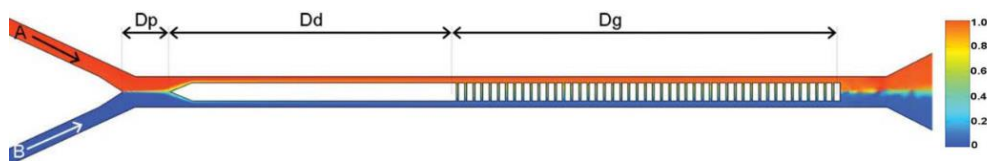


Figure 132: Two solutions A and B of different concentration flowing through channels, creating concentration gradient across the array of connecting channels.<sup>9</sup> The colour reflects the concentration; dark blue is minimum and dark red is the maximum. Figure regenerated from Irimia et al.<sup>9</sup>

Figure 132 highlights the geometry of Irimia's design<sup>9</sup> with  $D_p$  (contact zone),  $D_d$  (compensation zone) and  $D_g$  (gradient zone). Two fluid streams make primary contact in  $D_p$  before splitting towards parallel channels and the specific shape of the  $D_p$  promotes even distribution of the inflowing solutions while the gradual widening facilitates smooth merging.  $D_p$  prevents bulk flow of solutions and balances the pressure of the inflowing streams to the parallel channels. Further flow through  $D_d$  region allows the solutions in parallel channels to spread out evenly and reduce the linear flow velocity. This causes reduction in the convection influenced mixing within the bridge channel. Additionally,  $D_d$  region homogenizes the solution concentration evenly throughout the stream in parallel channels by the help of small circular motions within the fluid caused by any possible asymmetries in flow rates from the parallel channels.<sup>9</sup>

Followed by the minimization of unwanted convection currents and homogeneous concentration of inflowing solutions within the parallel channels linear gradient is generated in the transversal array of capillaries in  $D_g$  region. This allows for the creation of stable and well-defined chemical gradients across the length of the channel-array. Irimia's results<sup>9</sup> showed that their design is robust and well-functioning for generation of a continuous stable-gradient, which suits our requirement.

Thus, considering the robustness and proven experimental reproducibility from the literature, we adopted Irimia's design<sup>9</sup> for our gradient generating device. We reduced the height of bridge-array (Figure 134. B (ii)) to ~12% of the height of parallel channels (Figure 134. C (ii)). This comparative height reduction (between parallel channels and bridge-array) enhanced the hydraulic resistance in the zone of bridge-array than that in the parallel channels (refer to Eq. 4), and thus, enhancing our control over the fluid-flow across the bridges.

For the making of master mould, same method were followed as that for H-design in section "4.2.2.2" after designing the channel dimensions on KLayout for the photomask. The steps followed for obtaining differently heighted channels (smaller height of bridge arrays than the larger heighted parallel channels that would have flowing fluid) are as following:

1. Surface Preparation: Cleaned the glass slide with isopropyl alcohol followed by surface cleaning with plasma.
2. Spin Coating of photoresist: Applied a layer of photoresist (SU8 2007) at 2000 rpm for 30 seconds with an acceleration of 300 rpm/second.
3. Soft Baking: Baked the above at 95°C for 3 minutes and allowed to cool down to room temperature for 3 minutes.
4. Design introduction via mask alignment: Carefully placed the first photolithography polymer mask (containing the desired design) for first layer, directly on top of the photoresist-coated substrate. To make contact, placed 4 glass slides and a 4" quartz block on top of the mask.
5. Exposure: Exposed first layer ( $h_2$ ; region of bridge-array) to UV light (UVKUB at 100% energy) for 4 seconds with a dose of 120 mJ/cm<sup>2</sup>.
6. Post-Baking: Baked the above at 95°C for 4 minutes and allowed to cool down to room temperature for 5 minutes (Figure 133. A).
7. Development: Developed the photoresist for 5 min and measured the heights ( $h_2$ ) of first layer using interferometer.
8. Applied a second layer of photoresist (SU8 2050) at a 3500 rpm for 30 seconds with an acceleration of 300 rpm/second. For easier alignment, a scotch tape was put on the alignment

crosses of the silicon wafer, before spin coating. By removing the tape from the crosses, they are detached.

9. Performed edge removal at 3000 rpm (acceleration 1000 rpm/second) for 2 seconds.
10. Soft Baking: Baked the above at 65°C for 3 minutes, followed by baking at 95°C for 3 minutes and allowed to cool down to room temperature for 3 minutes.
11. Design introduction via mask alignment: Carefully placed the second layer of polymer mask, directly on top of the photoresist-coated substrate and placed 4 glass slides and a 4" quartz block on top.
12. Exposure: Exposed second layer ( $h_1$ ) to UV light (UVKUB at 100% energy) for 5 seconds with a dose of 160 mJ/cm<sup>2</sup>.
13. Post-Baking: Baked the above at 65°C and 95°C for 1 and 4 minutes respectively, and allowed to cool down to room temperature for 5 minutes (Figure 133. B).
14. Development: Developed the photoresist for an unspecified time and measured the heights ( $h_1$  and  $h_2$ ) of both layers after each step.

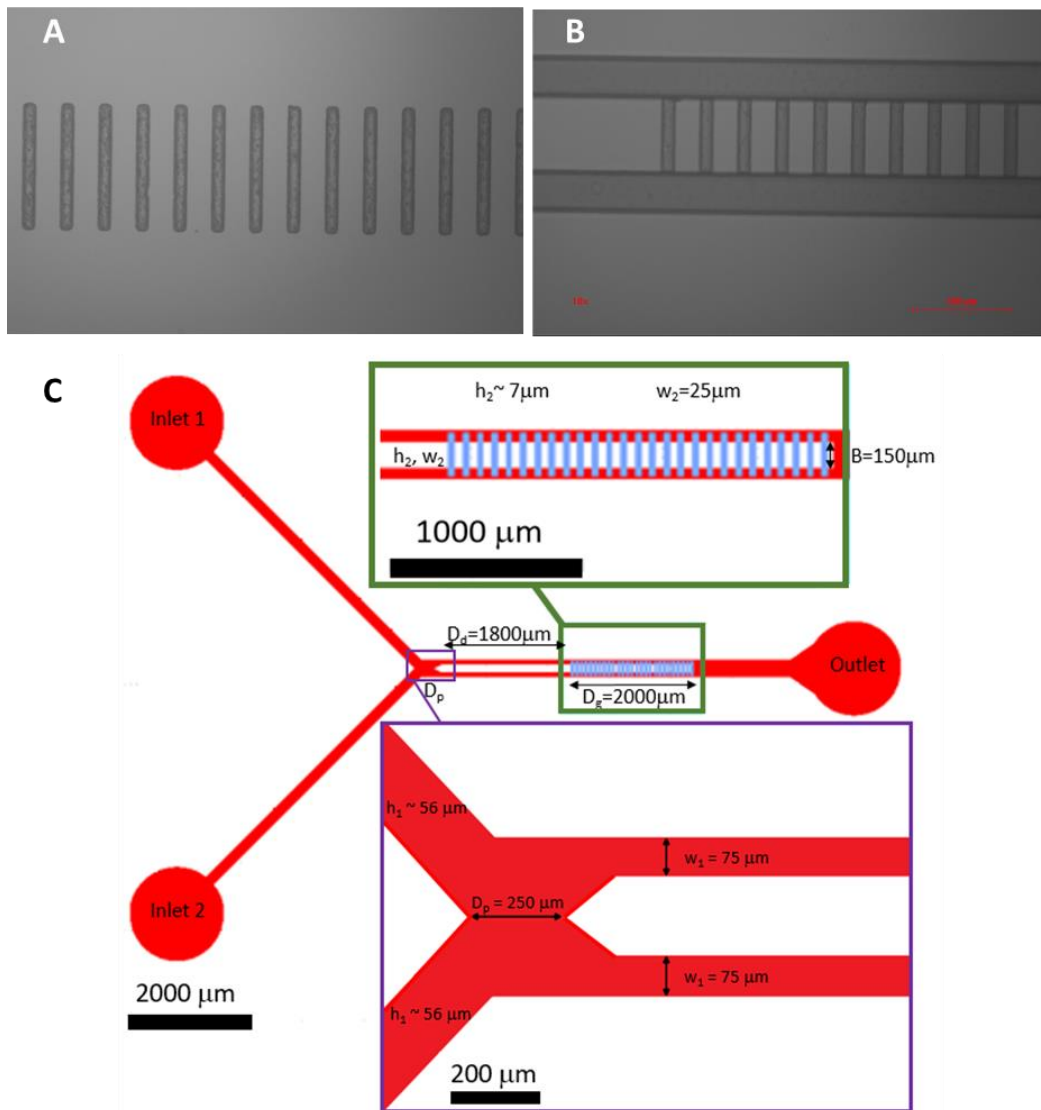


Figure 133: First and second layer after photolithography (in A and B respectively) at 10 x magnification. (C) Dimensional details of the concentration gradient generating microfluidic chip used for PTV experiments.

After the development of master mould with our desired microfluidic channel (Figure 133. C), heights within the channel of master mould, they were characterized by using interferometer that confirmed  $h_1$  to be  $\sim 56 \mu\text{m}$  for the parallel channels (Figure 134. C) and  $h_2 \sim 7 \mu\text{m}$  for the diffusion channel; bridge channels (Figure 134. B). Width of bridge ( $W_2$ ) and main channel ( $W_1$ ) designed via KLayout were  $\sim 25$  and  $\sim 75 \mu\text{m}$  respectively (Figure 133. C).

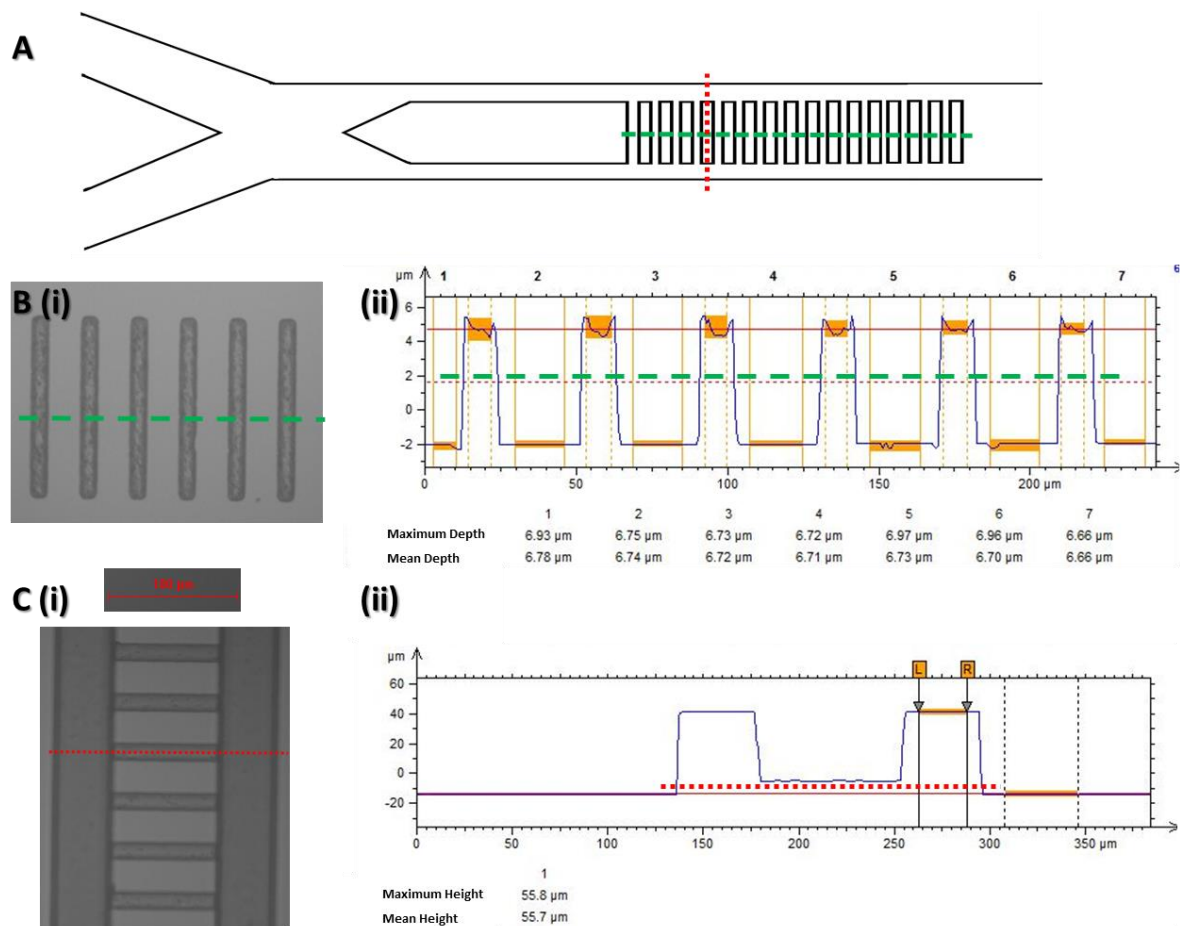


Figure 134: Y-design microfluidic channel (A). Image (ii) of B and C are the profilometric analysis (credit: Dr. Florent Malloggi), of the developed microfluidic channels.  $h_2 \sim 7 \mu\text{m}$  measured from interferometer in B (ii), is after the photolithography of first layer (array of bridges) of the microfluidic channel (B (i)). C shows image after second layer of is photolithographed and measured height from interferometer in (ii) shows  $h_1 \sim 56 \mu\text{m}$ . Magnification of the images B and C (i) is 10 x.

Further, chip functioning test confirmed the ease and reproducibility of flow-equilibrium and stable concentration gradient achievement in Y-design microfluidic chips. For this test, we used R6G (visualization substitute of  $\text{H}_2\text{O}_2$ ) to flow from one of the inlets while the other inlet carried Milli-Q water. Studying the gray-scale of R6G-fluorescence (Figure 135 (iii)) gave us the visual observations of gradient generation across the diffusion channel. Decreasing gray scale intensity from the direction of R6G towards the direction of water (Figure 135 (iii)) across bridge proved the development and maintenance of a continuous stable-gradient of R6G over time, across the diffusion channel, affirming the functioning of Y-design chip for our study. This was crucial for a clear conclusion from our study regarding the directional/non-directional motion of surface functionalized particles (especially Janus

particles). Therefore, results discussed in this chapter for motion study of samples (SP, Iso, JP and PVD) in  $H_2O_2$  gradient are from experiments in Y-design microfluidic chips.

Additionally, as we know that  $D_p$  is the zone of first contact between fluids from both the inlets, and our result from Chapter 3 confirming the influence of  $H_2O_2$  on the motion of our particles, flow of water (substitute for particle suspension in functioning test experiment) was set to dominate over the flowing  $H_2O_2$  (Figure 135 (ii) a). As shown in Figure 135 (ii) a, the highlighted area (blue) of dark trail in  $D_p$  is the water flowing dominantly (analogous to zero  $H_2O_2$ ) over the flowing R6G (analogous to  $H_2O_2$ ). This adjustment was essential for eliminating any possible pre-existing influence of  $H_2O_2$  on particle motion; allowing pure diffusion of both  $H_2O_2$  and particles from respective sides across the diffusion channels (bridge-array).

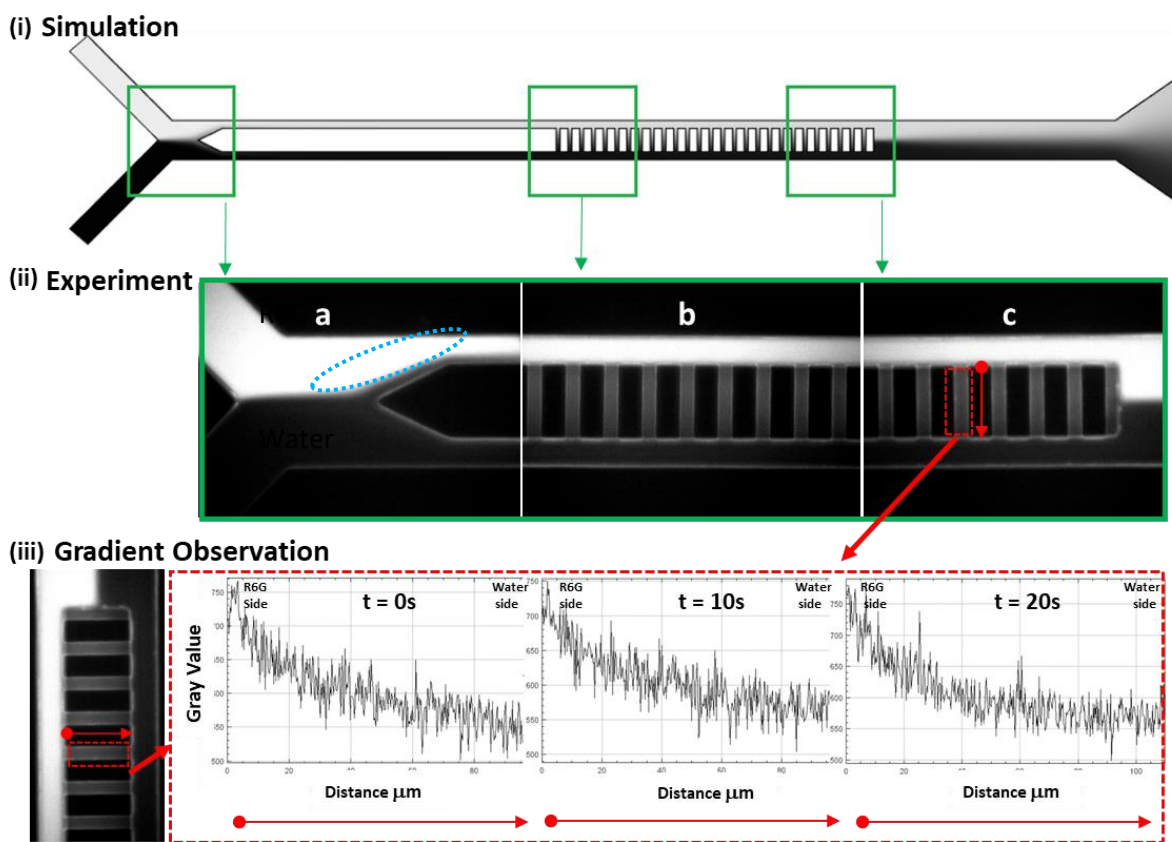


Figure 135: Chip functioning test for Y-shaped chip for continuous gradient generation. Highlighted areas (green) from simulation result in image (i) (credit: Zakariya Ait Athmane), are compared with experimental observation in image (ii). Image (ii) is obtained after 5 minutes stabilization time with water flow dominating over R6G flow (highlighted in blue). The reducing gray scale intensity in the highlighted (red) diffusion channel in image (iii) shows stable gradient achievement at time (t) 0 to 20 seconds. Red arrow (●→) represent the direction of diffusion of R6G (higher to lower concentration).

#### 4.2.2.5 Experiment (PTV)

1. Filtered 1 mL SP from mother solution using PTFE syringe filter (pore size  $0.65 \mu m$ ), followed by dilution in miliQ water (1:2). Similarly, filtered Iso and JP, followed by 1:1 dilution.
2. Installed pressure-pump (Figure 136. B) and loaded  $500 \mu L$  sample (particle suspended in water) and freshly prepared hydrogen peroxide solution (freshly prepared refers to the 5% and

## Particle Motion in Gradient

10% v/v concentration solution) in sample container. Added 170  $\mu\text{L}$  and 330  $\mu\text{L}$   $\text{H}_2\text{O}_2$  (30% (v/v)) in 830  $\mu\text{L}$  and 670  $\mu\text{L}$  water for net 5% and 10% (v/v) [ $\text{H}_2\text{O}_2$ ], respectively.

3. Connected the inlet and outlet PEEK tubes to the microfluidic chip (Figure 136).
4. Regulated the flow of sample and hydrogen peroxide in the gradient generator microfluidic chip via pressure-pump.
5. After two-minute stabilization time set camera exposure to 10 milli-seconds, frame rate at 10 FPS (frames per second) and recorded 200 images at 40 x magnification.

For minimal light induced decomposition of  $\text{H}_2\text{O}_2$  and thermal effects on gold and hydrogen peroxide, lamp of microscope was maintained at medium intensity throughout the experiments. Two sets of experiments conducted at each concentration of hydrogen peroxide.

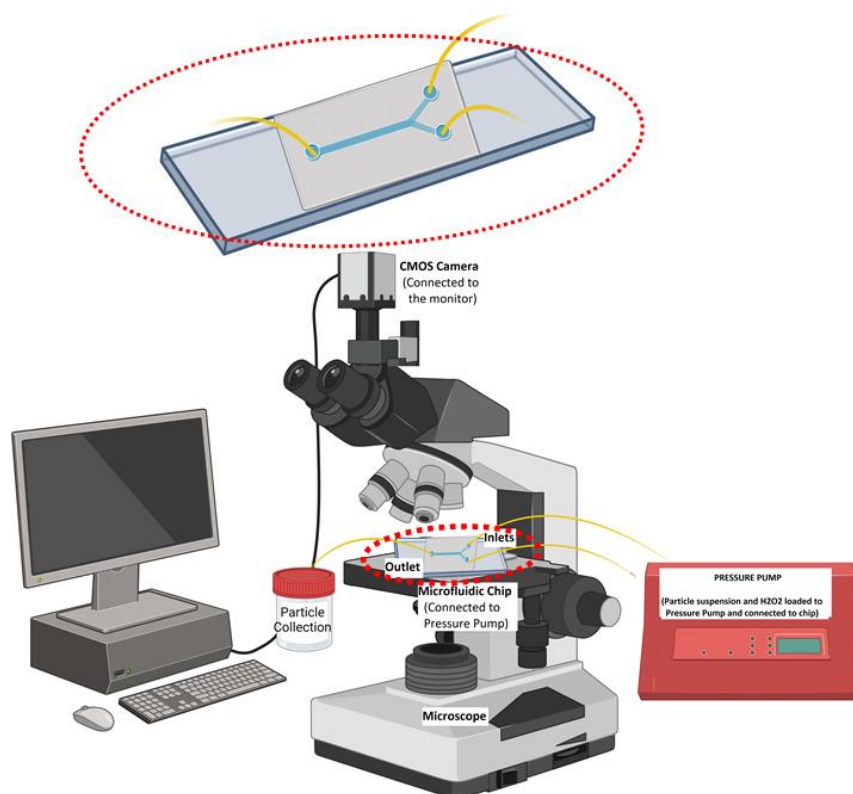


Figure 136: Scheme of PTV experiment set-up with microfluidic chip connected to a pressure pump.

To obtain results from particle tracking, similar procedures to that in Chapter 3 were followed, where microscopy images were treated with ImageJ, followed by particle tracking and data extraction from TrackMate and lastly processing the data through Python codes. During the image processing ROI homogeneity was maintained by processing particles in the central 60% area of the bridges ( $\pm 45 \mu\text{m}$  from centre) (Figure 137).

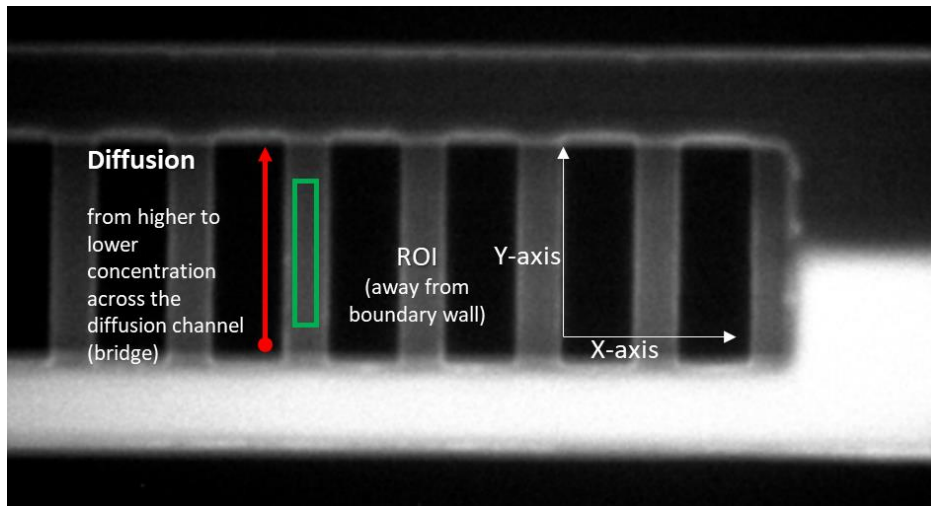


Figure 137: ROI in central region of diffusion channel, away from boundary walls of the channel

### 4.3 Result and Discussion

Similar to Chapter 3, the trajectories of particles (Figure 138) obtained from TrackMate is processed via Python to observe the direction of motion of particles. For this purpose, we re-assign the initial coordinates of trajectories to origin axis (0,0) (Figure 139). While studied ROI is away from boundaries of the microfluidic channel (Figure 137), therefore, it is important to note that no boundary-effects are accountable in our motion of particles. Additionally, both of our PTV studies (in chapter 3 and chapter 4) lacked signs of particles aggregates/clusters while reproducible results confirmed that our experiment set-up and conditions are of good standards.

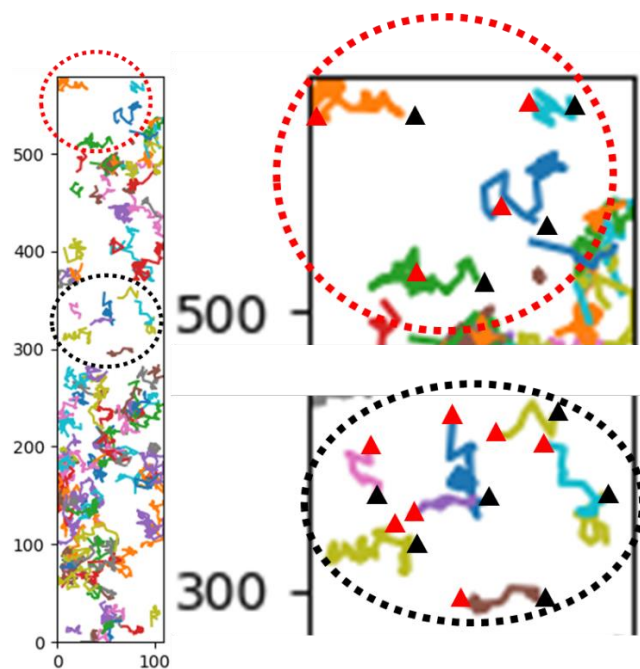


Figure 138: Complete trajectories of observed SP in one of the diffusion channel (from bridge-array) at 0% H<sub>2</sub>O on left. Selected highlighted regions are zoomed and show initial and end-points of trajectories (black and red triangles, respectively). Each colour denotes different trajectories for its respective particles.

### 4.3.1 Motion Orientation

To understand the motion orientation on particles, the dominating side of particle trajectory was of key importance. Positive and negative values in quadrants (example Figure 139 and Figure 140) were respective to particle's initial position. As the gradient of hydrogen peroxide was in y-axis (Figure 137), positive value on y-axis represents that motion was towards the hydrogen peroxide while the negative y-axis refers to the motion away from hydrogen peroxide. Motion in x-axis does not necessarily represent a directional motion. Homogeneous distribution of tracks for SP samples in each quadrant for 0, 5 and 10% (v/v) [H<sub>2</sub>O<sub>2</sub>] (Figure 139) proved that SP is unaffected in presence of hydrogen peroxide gradient, therefore exhibited movement isotropic in direction. This resonated with the behaviour we expect from pure Brownian motion. The plots in Figure 139 show tracks of particle from a single bridge of the Y-design microfluidic channel, with its starting coordinates repositioned to the origin axis. X and y-axis in example Figure 139 represents distance travelled in pixels.

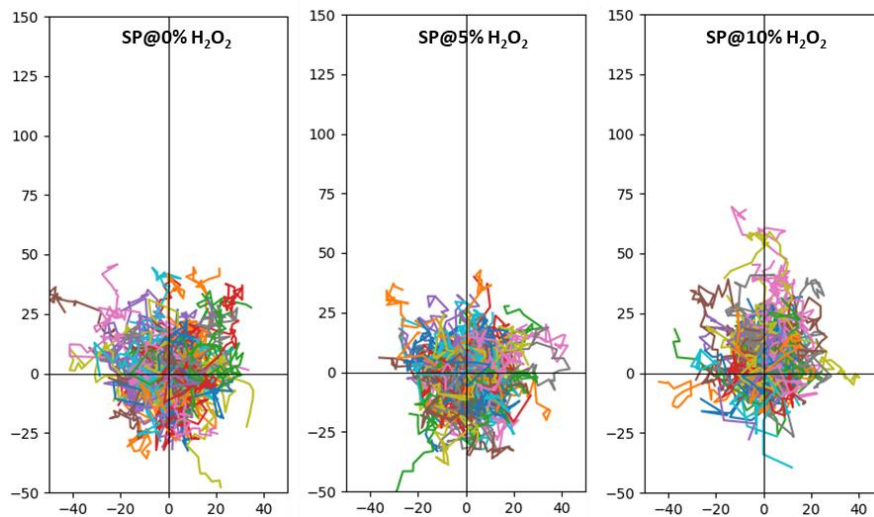


Figure 139: SP trajectory at respective concentration gradient of hydrogen peroxide showing non-directional motion.

Similarly for surface modified particles (Iso, JP and PVD) we expected diffusive (Brownian) motion in absence of hydrogen peroxide, which was confirmed from results shared in Figure 140 for particles 0% H<sub>2</sub>O<sub>2</sub>. This proved that our experimental set-up was well functioning for the desired study of particle-motion in concentration gradient environment. However, careful interpretation of results were required as some graphs in Figure 140 can give first impression of a little biased motion, for example: in Figure 140. C, PVD in 0% [H<sub>2</sub>O<sub>2</sub>] shows a little more track in first and third quadrants, which is from the contribution of two tracks (red and brown). This is due to poor statistics and less number of track.

Unlike SP, Figure 140 shows that at 5% and 10% (v/v) H<sub>2</sub>O<sub>2</sub> Iso, JP and PVD dominates in first and second quadrant (Figure 140 A, B and C, respectively). This indicated directional motion in positive y-axis; confirming particles moved towards higher concentration in H<sub>2</sub>O<sub>2</sub> gradient. Our study confirmed that particles with gold (both symmetric and asymmetric; Iso and Janus particle) showed directional in presence of H<sub>2</sub>O<sub>2</sub> gradient (motion being from low to high concentration of H<sub>2</sub>O<sub>2</sub>). Comparable results and quality with results of Xiao et al<sup>10</sup> affirmed the minimal mechanical and hydrodynamic perturbations in our experiment setup.



## Particle Motion in Gradient

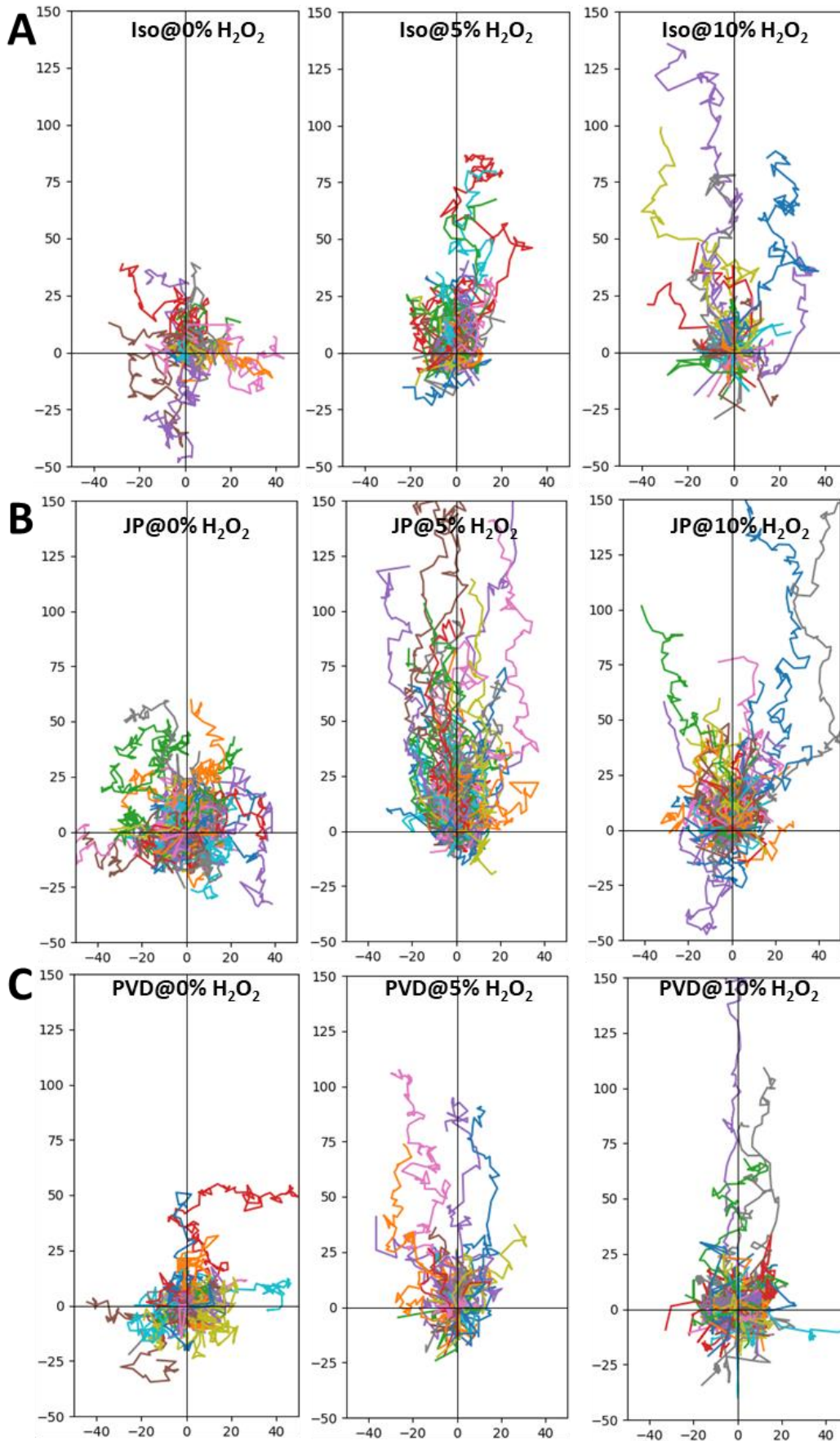


Figure 140: Trajectories for Iso, JP and PVD (A,B and C, respectively) at respective concentration gradient of  $H_2O_2$  showing directional motion in 5% and 10% (v/v)  $H_2O_2$  gradient by all the particles.

### 4.3.2 Mean Speed and Displacement

To calculate the mean speed of particles, TrackMate first detected particles in each frame, followed by linking these detected particles to form tracks of each particles (in each frame) over time. For each track, displacement (typically in pixels) between consecutive positions particle in successive frames was calculated along with the time interval between frames, and then displacement was converted into instantaneous speed of particles between each pair of frames. Lastly, the mean speed was then determined by averaging the instantaneous speeds calculated for all displacements along the track. Figure 141 and Table 23 summarizes the mean speed of particles at respective concentration of H<sub>2</sub>O<sub>2</sub>. In absence of H<sub>2</sub>O<sub>2</sub> we found that all the particles had velocity in a narrow range (varying less than 10%) of the fastest (Iso) to the slowest (JP).

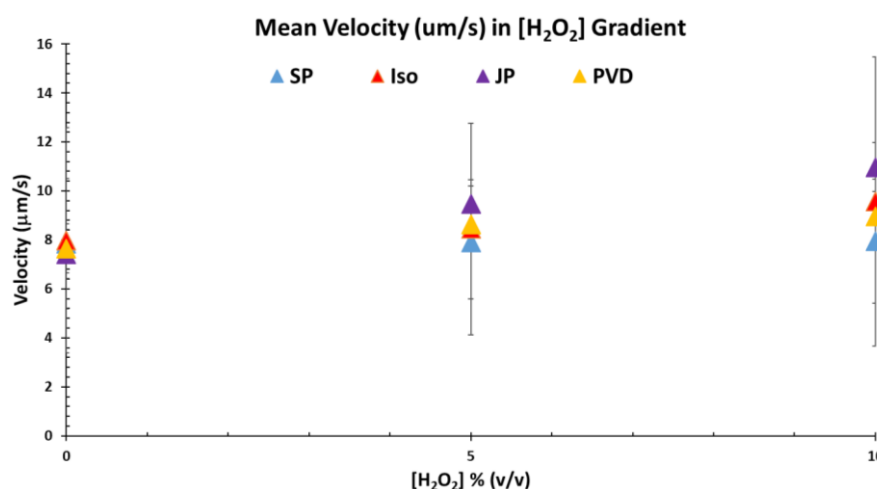


Figure 141: Mean Velocity of particles at respective concentration gradient of hydrogen peroxide

SP stayed unaffected from introduction of H<sub>2</sub>O<sub>2</sub>, it was the slowest particle in presence of all the concentration gradient of H<sub>2</sub>O<sub>2</sub> while JP stays the fastest. Amongst the surface modified particles at 5% H<sub>2</sub>O<sub>2</sub>, we found Iso as the slowest particle, followed by PVD and JP being the fastest. The order of slowest to fastest particle at 5% H<sub>2</sub>O<sub>2</sub> gradient was SP<Iso<PVD<JP.

Table 23: Mean Velocity of particles at respective concentration gradient of hydrogen peroxide

[H <sub>2</sub> O <sub>2</sub> ] % (v/v)	Mean Speed (μm/s)			
	SP	Iso	JP	PVD
0	7.84 ± 2.66	7.98 ± 4.60	7.43 ± 3.68	7.65 ± 4.02
5	7.90 ± 2.30	8.45 ± 4.31	9.46 ± 6.14	8.62 ± 5.89
10	7.94 ± 2.53	9.57 ± 5.90	10.97 ± 7.73	8.97 ± 6.13

However, this order of mean speed changes at 10% H<sub>2</sub>O<sub>2</sub> gradient; Iso attained faster mean speed than PVD (SP<PVD<Iso<JP). Overall, particles followed similar trends of mean speed in both gradient (Chapter 4) and no-gradient (Chapter 3) PTV studies were in comparable ranges. This confirmed the functioning of our experiment set-up. In gradient study isotropic surface (Iso) and physically produced janus particles (PVD) showed similar range of speed-distribution (~20% and 17~ respectively), while chemically synthesized Janus Particles (JP) exhibited widest range of speed-distribution with ~47% relative difference. This higher dispersion may reflect a lower stability of the JP in solution, or the presence of residual paraffin on some particles.

From studied literatures, Xiao's<sup>10</sup> Copper-Silica Janus micromotors attained speed range of 6 to 12 μm/s in 2.5% H<sub>2</sub>O<sub>2</sub> gradient, while our gold/silica Janus particles required 4 times higher H<sub>2</sub>O<sub>2</sub> concentration to attain comparable speed (~7.5 – 11 and 7.6 - 9 μm/s for JP and PVD, respectively). This could be because of higher catalytic activity of copper than gold.<sup>11,12</sup>

Another method for visualizing diffusive/non-diffusive particles-motion is by its displacement. The displacement graphs (Figure 142) and mean square displacement as a function of time (Figure 143) provided insights into diffusion and randomness for particles. As shared in Chapter 1, the Central limit theorem describes: distribution of particle-displacement in purely diffusive motion is a Gaussian fit.<sup>13,14</sup>

Our particle-displacement result in Figure 142 (calculated from displacement of particles between two consecutive images, see paragraph "3.3.2.1" of Chapter 3) at respective H<sub>2</sub>O<sub>2</sub> gradient showed that all the particles at 0% H<sub>2</sub>O<sub>2</sub> follow Gaussian distribution by spreading in both positive and negative directions from the centre. This proved that in absence of hydrogen peroxide all the particles experienced pure-diffusion, thus, the experimental set-up was functional for our desired study. Nevertheless, in some cases the fit appeared weak, which is due less number of observed particles leading to poor statistics.

While Gaussian distribution confirmed diffusive motion in particles, any biased shift from centre represents non-diffusive motion. In our case, displacement of particles with gold, at 5% and 10% (v/v) H<sub>2</sub>O<sub>2</sub> was towards negative x-axis (Figure 142), which represented particle trajectories towards the direction of higher concentration of H<sub>2</sub>O<sub>2</sub>. This is a signature of non-diffusive motion in particles with gold towards H<sub>2</sub>O<sub>2</sub>.

Another well-established understanding for a typical diffusion motion was that it follows linear relationship between MSD and time,<sup>15</sup> while a hyper-diffusive relation in MSD plot (as a function of time) can confirm active motion. Position of particles obtained from TrackMate helped in determination of diffusive, hyper-diffusive or sub-diffusive motion of particles as we can plot MSD as a function of time using the following formula:

$$\text{MSD}(\tau) = (1 / N) * \Sigma [ (x(t + \tau) - x(t))^2 + (y(t + \tau) - y(t))^2 ]$$

Here, τ is the lag time, N is the total number of particles in the system whose trajectories are being analysed, Σ is the summation, x, y are the coordinate, and t is the initial time.

## Particle Motion in Gradient

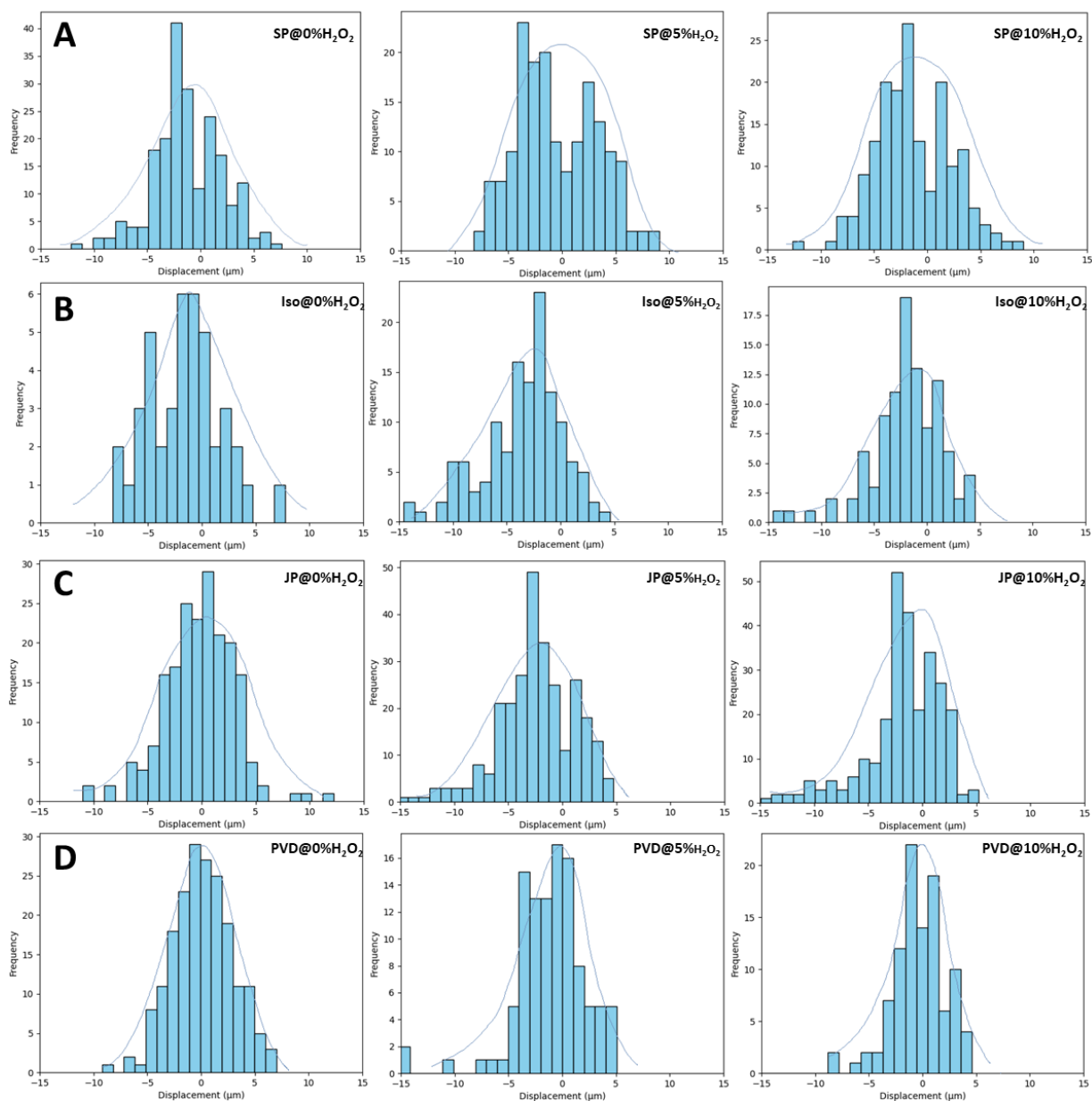


Figure 142: Displacement graphs (calculated from particle-displacement between two consecutive images) for particles at respective  $\text{H}_2\text{O}_2$  gradient. Negative shift in displacement from centre at 5% and 10%  $\text{H}_2\text{O}_2$  plots in B – D indicates directional motion towards the  $\text{H}_2\text{O}_2$

In Figure 143. A, MSD for SP for each concentration of  $\text{H}_2\text{O}_2$  followed similar to linear trend. This confirmed that there was no influence of  $\text{H}_2\text{O}_2$  on the motion of SP and thus, followed diffusive-motion behaviour. Unlike SP, surface modified particles having gold on its surface exhibits non-linear progression in MSD plot (Figure 143. B – D). Steep-rising MSD slopes for Iso and Janus particles in 5% (orange) and 10% (green)  $\text{H}_2\text{O}_2$  (Figure 143.C and D) confirmed active transport motion that was similar in trend with propulsion motion observed by Howse et al<sup>16</sup> in Platinum-PS Janus Particles ( $\phi 1.6 \mu\text{m}$ ). However, it was interesting to see that for initial 2.5 seconds, all the surface modified particles (Iso, JP and PVD) show steeper rise at 5%  $\text{H}_2\text{O}_2$  than that at 10%  $\text{H}_2\text{O}_2$ . This could be from destruction and deactivation of particle's catalytic sites, which could be caused from the higher oxidative stress and structural damage induced by the high  $\text{H}_2\text{O}_2$  concentration.

## Particle Motion in Gradient

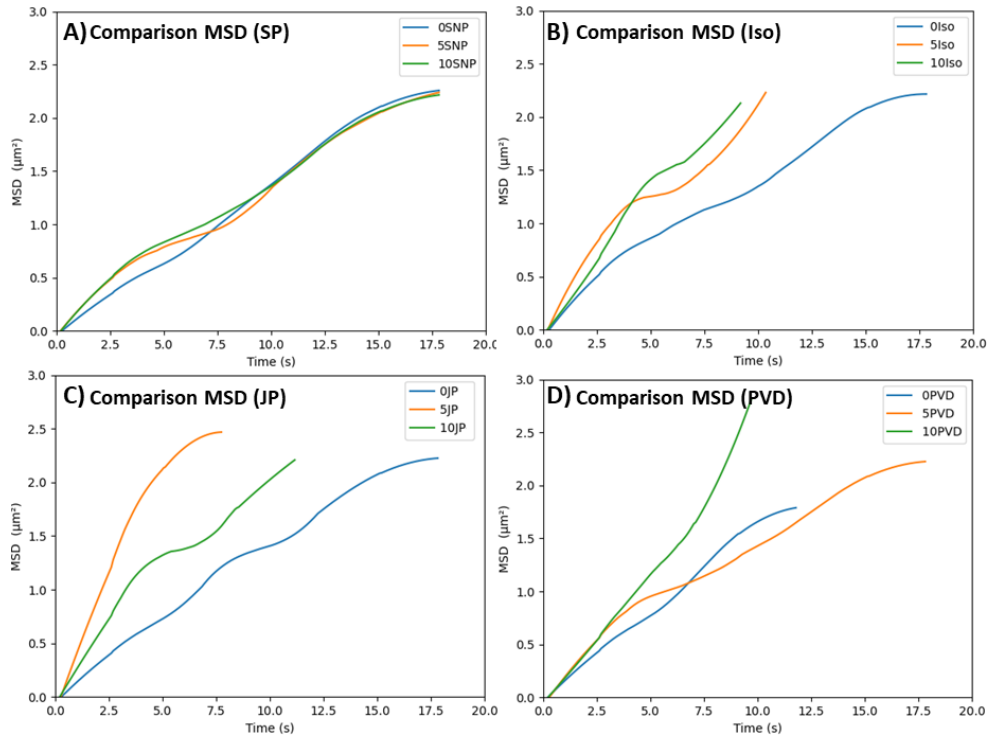


Figure 143: Comparison of MSD at different concentration of  $H_2O_2$ . With 0%  $H_2O_2$  (blue) as reference, positive shift in MSD at 5% (orange) and 10% (blue)  $H_2O_2$  confirms hyper-diffusive motion for Iso, JP and PVD in gradient of hydrogen peroxide.

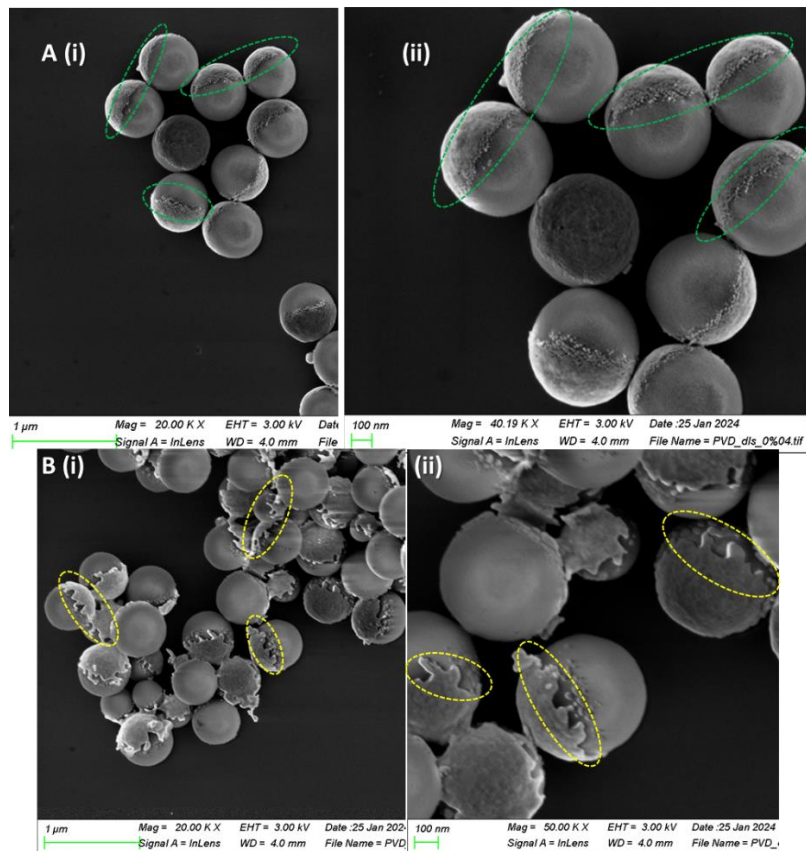


Figure 144: SEM images of PVD samples in 0% hydrogen peroxide (at 20 and 40x in A(i) and (ii), respectively), showing smooth gold layers (green highlights) on SP, while B(i) and (ii) showing PVD samples in 5% hydrogen peroxide, with melted gold layers (yellow highlights) on SP.

To understand this, we need to consider the effects of H<sub>2</sub>O<sub>2</sub> concentration on the catalytic activity and the structural integrity of the particles involved. SEM images in Figure 144 illustrates the effects on PVD in 0% and 5%<sub>v/v</sub> (A and B, respectively) H<sub>2</sub>O<sub>2</sub>, observed after six months of sample preparation (in order to have complete decomposition of H<sub>2</sub>O<sub>2</sub>). Degraded gold layer (melted boundary appearance) in Figure 144 B (i) and (ii) confirmed structural damage of gold layer at 5%<sub>v/v</sub> H<sub>2</sub>O<sub>2</sub>, which should arise from the highly oxidative nature of H<sub>2</sub>O<sub>2</sub>. Therefore, considering that higher H<sub>2</sub>O<sub>2</sub> concentrations would cause more surface damage, the catalytic reactions should be more efficient in 5%<sub>v/v</sub> (as the particles-surfaces would remain relatively intact and active) therefore, allowing larger displacement than the particles in 10%<sub>v/v</sub> H<sub>2</sub>O<sub>2</sub>. This directly supported the notion that surface integrity is crucial for catalytic performance and prolonged exposure to high concentrations of H<sub>2</sub>O<sub>2</sub> can damage surface and cause the deactivation of catalysts. Thus, reducing particle's ability to facilitate motion-causing reactions.

### 4.3.3 Mean Diffusion Coefficient

As shared in Chapter 1 and Chapter 3, relationship between diffusivity of particle and MSD can also be done from Einstein-Smoluchowski equation;  $MSD^2 = 2nD\tau$ , where MSD is the mean square displacement<sup>14</sup> of particles, D is the diffusivity or diffusion coefficient, n is the dimension-number of the observed system and t is the time.<sup>15</sup> As our particle tracking is in 2D, the dimension-number is 2, and time is 20 s, the mean diffusion coefficient calculated by following Eq. 5. higher relative difference in the diffusion rate for JP and PVD (over 100% and ~40% respectively) in Table 24 confirmed the original behaviour of Janus Particle, while SP remained least varying particle specie with 2% relative difference confirmed no influence of H<sub>2</sub>O<sub>2</sub> gradient on motion of SP. We found that at 5% H<sub>2</sub>O<sub>2</sub> Iso and PVD exhibited less than 5% difference in diffusion rate, which increased to ~14% at 10% H<sub>2</sub>O<sub>2</sub> for Iso. Additionally, our results showed that Iso attained higher mobility in gradient as the relative difference in diffusion coefficient was twice in H<sub>2</sub>O<sub>2</sub> gradient (44%) than without gradient (~20%). This was an interesting finding for application in higher concentration of H<sub>2</sub>O<sub>2</sub> as synthesis of Iso is more simple and economical than PVD. Values of mean diffusion coefficient derived from PTV for particles at respective concentration of hydrogen peroxide are enlisted in Table 25 and shown graphically in Figure 145.

$$D = (V^2 \times \tau) / 2n \quad \text{Eq. 5}$$

Where D is the diffusion coefficient, V is the mean velocity of particles tracked via TrackMate,  $\tau$  is 90 mili-seconds and n is 2. (Eq. 1 is derived from  $V^2 \times \tau^2 = 2nD\tau$ , where MSD; square displacement = Velocity<sup>2</sup> x Time<sup>2</sup>).

Table 24: Comparison of relative change (%) in diffusion coefficient from gradient/no-gradient experiments

Experiment	SP	Iso	JP	PVD
No Gradient	6	20	123	46
Gradient	2	44	118	37

Table 25: Mean Diffusion Coefficient of particles at respective gradient concentration of hydrogen peroxide

[H <sub>2</sub> O <sub>2</sub> ] % (v/v)	Mean Diffusion Coefficient (μm <sup>2</sup> /s)			
	SP	Iso	JP	PVD
0	1.38 ± 0.16	1.43 ± 0.5	1.24 ± 0.32	1.32 ± 0.38
5	1.41 ± 0.12	1.60 ± 0.45	2.01 ± 0.85	1.67 ± 0.81
10	1.42 ± 0.15	2.06 ± 0.81	2.71 ± 1.35	1.81 ± 0.91

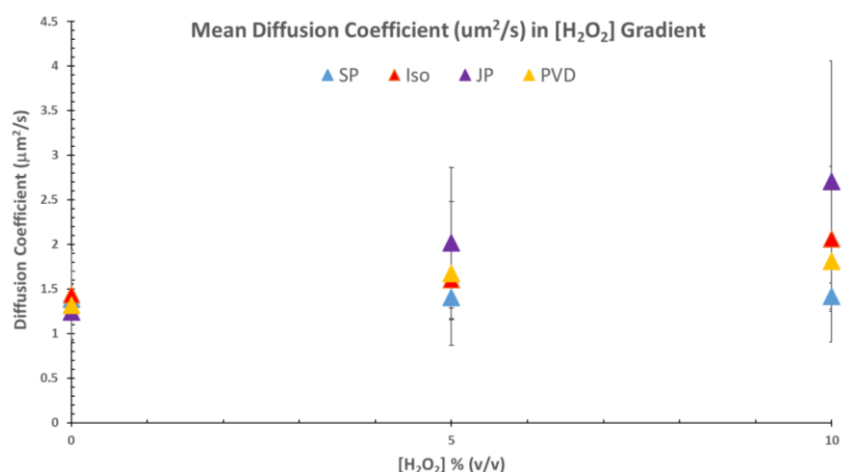


Figure 145: Diffusion Coefficient mean values for particles at respective concentration of hydrogen peroxide. With increasing hydrogen peroxide gradient concentration diffusion coefficient of Iso, PVD and PVD increases, while SP is unaffected.

#### 4.4 Conclusion

Our study concur that PTV reveals the complexities and increased dispersion in particle individually and despite its tedious nature PTV proves to be a valuable method for understanding particle-motion better. The comparison between PTV results from Chapter 3 and Chapter 4 illustrated a comprehensive understanding of particle motion and dispersion in the presence of H<sub>2</sub>O<sub>2</sub>. While chapter 3 confirmed isotropic motion across all particle types, motion study of particles by utilizing TrackMate provided crucial insight regarding the direction orientation of particle motion in Chapter 4.

Directional motion by the particles with gold proved that our synthesized particles had sufficient sensitivity to follow directional motion towards hydrogen peroxide. Highest enhancement in the movement in H<sub>2</sub>O<sub>2</sub> for JP confirmed higher catalytic activity in chemically synthesized gold/silica Janus particles and particles with Isotropic coverage of gold nanoparticle than PVD produced Janus particle. Whereas the increased dispersion chemically synthesized janus particles was considered be due to the trace wax component.

By this, we also confirmed that upon catalytic activation, Janus nature was not necessarily required to obtain an increase in diffusion or directional motion towards hydrogen peroxide. Nonetheless, in order to have deeper understanding for possible application purposes, understanding the impact of hydrogen peroxide on particle-motion for wider time-window may be more interesting.

## 4.5 Reference

- (1) COMSOL Version 5.1 Release Highlights. <https://www.comsol.com/release/5.1/chemical-reaction-engineering-module>.
- (2) Vailati, A.; Xu, S.; Aime, S.; Croccolo, F. Diffusion and Convection in Nature. *Eur. Phys. J. E* **2021**, *44* (12), 145. <https://doi.org/10.1140/epje/s10189-021-00148-0>.
- (3) *Microfluidics and Nanofluidics Handbook: Fabrication, Implementation, and Applications*; Chakraborty, S. K. M., Suman, Ed.; CRC Press: Boca Raton, 2012. <https://www.routledge.com/Microfluidics-and-Nanofluidics-Handbook-Fabrication-Implementation-and-Applications/Mitra-Chakraborty/p/book/9781138072381>.
- (4) Farah, J. Nanohybrides Intégrés à Des Pucés Microfluidiques Pour La Production d'hydrogène et La Catalyse. 2022. [https://theses.hal.science/tel-03948468/file/115783\\_FARAH\\_2022\\_archivage.pdf](https://theses.hal.science/tel-03948468/file/115783_FARAH_2022_archivage.pdf).
- (5) Bahouri, H.; Chemin, J.-Y.; Gallagher, I. On the Stability of Global Solutions to the Three-Dimensional Navier-Stokes Equations. *Journal de l'École polytechnique — Mathématiques* **2018**, *5*, 843–911. <https://doi.org/10.5802/jep.84>.
- (6) Crank, J. *The Mathematics of Diffusion*; Clarendon Press, 1979.
- (7) Tjell, A. Ø.; Almdal, K. Diffusion Rate of Hydrogen Peroxide through Water-Swelled Polyurethane Membranes. *Sensing and Bio-Sensing Research* **2018**, *21*, 35–39. <https://doi.org/10.1016/j.sbsr.2018.10.001>.
- (8) Hudson, S. D. Poiseuille Flow and Drop Circulation in Microchannels. *Rheol Acta* **2010**, *49* (3), 237–243. <https://doi.org/10.1007/s00397-009-0394-4>.
- (9) Irimia, D.; Charras, G.; Agrawal, N.; Mitchison, T.; Toner, M. Polar Stimulation and Constrained Cell Migration in Microfluidic Channels. *Lab Chip* **2007**, *7* (12), 1783–1790. <https://doi.org/10.1039/B710524J>.
- (10) Xiao, Z.; Nsamela, A.; Garlan, B.; Simmchen, J. A Platform for Stop-Flow Gradient Generation to Investigate Chemotaxis. *Angewandte Chemie International Edition* **2022**, *61* (21), e202117768. <https://doi.org/10.1002/anie.202117768>.
- (11) Mao, X.; Jiang, J.; Luo, Y.; Shen, G.; Yu, R. Copper-Enhanced Gold Nanoparticle Tags for Electrochemical Stripping Detection of Human IgG. *Talanta* **2007**, *73* (3), 420–424. <https://doi.org/10.1016/j.talanta.2007.04.004>.
- (12) Tauran, Y.; Brioude, A.; Coleman, A. W.; Rhimi, M.; Kim, B. Molecular Recognition by Gold, Silver and Copper Nanoparticles. *World J Biol Chem* **2013**, *4* (3), 35–63. <https://doi.org/10.4331/wjbc.v4.i3.35>.
- (13) Campbell, C. E. Diffusivity and Mobility Data. In *Fundamentals of Modeling for Metals Processing*; Furrer, D. U., Semiatin, S. L., Eds.; ASM International, 2009; pp 171–181. <https://doi.org/10.31399/asm.hb.v22a.a0005430>.
- (14) Nandi, A.; Heinrich, D.; Lindner, B. Distributions of Diffusion Measures from a Local Mean-Square Displacement Analysis. *Phys. Rev. E* **2012**, *86* (2), 021926. <https://doi.org/10.1103/PhysRevE.86.021926>.
- (15) Islam, M. A. Einstein–Smoluchowski Diffusion Equation: A Discussion. *Phys. Scr.* **2004**, *70* (2–3), 120–125. <https://doi.org/10.1088/0031-8949/70/2-3/008>.
- (16) Howse, J. R.; Jones, R. A. L.; Ryan, A. J.; Gough, T.; Vafabakhsh, R.; Golestanian, R. Self-Motile Colloidal Particles: From Directed Propulsion to Random Walk. *Phys. Rev. Lett.* **2007**, *99* (4), 048102. <https://doi.org/10.1103/PhysRevLett.99.048102>.



## Conclusion and Perspective

Amongst multiple investigation conducted in this thesis work, potential of asymmetric and symmetric (Janus and Non-Janus respectively) particles vs symmetric particles for motion from self-propulsion was explored. Gold/Silica Janus particles (asymmetric-surface particles) along with isotropic gold-on silica particles (symmetric-surface particles) were synthesized and characterized via techniques like SEM, EDX, UV-Vis, and DLS. As these particles were investigated for the development of a supramolecular-scale nanorobots (Radiotactic Colloids), the dynamic behaviour of the synthesized particles in presence of hydrogen peroxide was compared further. Amongst the two strategies opted for Janus Particle synthesis initial literature study (on various method for Janus particle synthesis) assured chemical synthesis via Pickering Emulsion method for bulk production of Janus particle (essential for large quantity of decontamination nanorobots). Nevertheless, adopted procedure required optimization. But, chemical synthesis methods can be prone to non-homogenous surface functionalization, Janus particles made from physical method (via Physical Vapour Deposition) were also compared. Chemically synthesized Janus particles (JP) comprised of gold nanoparticles onto half of its surface while physically produced particles (PVD) had gold film. In contrast to Janus Particles, 'pristine silica particles' (SP) and 'silica particles with isotropic coverage of gold nanoparticles' (Iso) were investigated and compared in motion study in presence of hydrogen peroxide, where SNP, due to its minimal reactivity with hydrogen peroxide acted as the 'reference particle' or 'control particle'.

Optimization of JP synthesis for bulk quantity with homogeneous coverage of gold nanoparticles gave significantly higher count of gold nanoparticles (than that in the referred literature). In this process, APTES was identified as the most effective linker molecule, helping us obtain well-defined gold hemisphere in Janus Particle. Additionally, optimized CTAB concentration (modified surface charge of silica particles enabling partial hydrophobization and thus the stable emulsion) and wax removal played key role in enhancing the yield of Pickering Emulsion method. Our conclusion for physically produced Janus particles aligns with existing literature; physical vapour deposition provides higher surface-homogeneity than the particles synthesized via chemical method (Pickering Emulsion method in this case). It also offers better control over gold layer deposition and an intermediate adhesion layer (chromium in our study) prior to gold deposition results in smoother gold layers with much stronger adhesion, ultimately enhancing the overall stability of the particles.

Our studies highlighted the importance of using techniques like DLS and PTV to gain a more complete understanding of particle behaviour in presence of hydrogen peroxide surroundings, particularly for complex systems like Janus particles. While DLS provided understanding of particle motion in bulk, PTV in controlled well-controlled environment (microfluidic system) countered bulk-motion of particle by tracking individual particles. Motion study of particles (SNP, the 'control particle' and three types of surface modified nanoparticles: Iso, JP, and PVD) and their behaviour in presence of hydrogen peroxide from DLS and PTV were found overall coherent with each other; confirming the mobility enhancement in Janus Particles; linked with its asymmetric surface. Both DLS and PTV results concluded that particles with metallic nanoparticles showed higher relative change in diffusion rate, than the particles with metallic layer. Our study revealed the differences in particle dispersion; uniform dispersion of SNP unlike the modified particles suggesting particle clustering or aggregation, but found to get suppressed upon the introduction of hydrogen peroxide. DLS deriving the apparent size of particles and the

diffusion coefficients has limitations for analyzing anisotropic particles and can be misleading when it comes to particle-size. These misleading limitations are due to its reliance of DLS on the assumption of Brownian motion: designed to fit for purely diffusive behaviour. This drawback is helpful in understanding the active motion in Janus particles in presence of hydrogen peroxide, indirectly. While PTV offers a more comprehensive understanding of particle motion by providing insights into individual particle's orientation and displacement.

PTV showed motion in isotropic direction for all particles in both the absence and presence of hydrogen peroxide but presence of hydrogen peroxide influenced motion of Janus particles (JP and PVD) more significantly than Iso particles. This confirmed that the interaction between gold and hydrogen peroxide in asymmetric pattern causes larger impact on particle-motion than interactions in symmetric pattern. However, considering the light-sensitivity of gold, effects of illumination (from light sources in utilized instruments) on particle-motion cannot be neglected completely and should be interesting to analyse in future studies. Both DLS and PTV results indicate that grafting nanoparticles onto silica particles (JP) is a more effective strategy for studying particle dynamics in comparison to gold layer deposition. However, from the observations made for Iso, we also conclude that catalytic activation might not necessarily require a Janus structure for increased diffusion, and observations of particle motion in presence of hydrogen peroxide over longer timeframes should identify more pronounced trends.

We also conclude that the most essential aspect of steady-state motion study was the development of the steady-state gradient generating microfluidic device. This was crucial for having a predictable, well-defined and well-controlled system, and therefore better understanding of motion. The initial approach towards a simple design (for a steady-state gradient generator) helped in realizing significant difference between simulation vs experiment, hydrodynamic pressure and impact of slightest deformities in design and flow-regulations. Following Irimia's<sup>1</sup> we successfully micro-fabricated the Y-shaped microfluidic device,<sup>1</sup> generated a stable and well-defined hydrogen peroxide concentration gradient. Our steady-state motion study over the timeframe of 20 seconds demonstrated directional motion of surface-modified particles (both Janus and Non-Janus) towards higher hydrogen peroxide concentrations. This study also revealed that isotropic gold-coated particles exhibit better mobility in hydrogen peroxide gradient, compared to physically produced Janus particles. This reassured our conclusion that surface modified particles with metallic nanoparticles (JP) exhibit better interaction with chemical surrounding than particles with metallic layers (PVD).

In summary key findings is that this thesis work successfully succeeded in optimizing chemical synthesis protocol for bulk production of active Janus particles. We observed directional motion towards higher concentration of hydrogen peroxide in concentration gradient supporting the initial theory of a prospective radiotactic nanorobot. Additionally, the size-range of our particles can offer high agility in small path and holds potential of exploring complex geometries, while bulk-quantity synthesis would make it cost-effective. Although directional motion does not necessarily require Janus particles and we can potentially benefit from a significantly easier and more cost-effective fabrication process compared to creating complex Janus structure. However, we also acknowledge the limitations of our study; the observation time-window, which should be increased to have deeper understanding of the self-propulsion mechanism and other possible underlying mechanisms or interactions with the surrounding environment playing a role that may come over time. Nonetheless, our findings provide

valuable insights into the design of microfluidic devices for studying and manipulating particle motion in chemical gradients.

As our research has primarily focused on the propellant and directionality parts of particles; essential aspects of nanorobots with autonomous motion, it is insufficient to qualify as nuclear decontamination nanorobot (NDN) for comprehensive decontamination. Therefore, integration of specific chelating agents would enhance their ability to bind and neutralize contaminants, making them more effective for the decontamination aspects. This makes 'introduction of chelating agent' (complexant) the next and most important perspective of this thesis; enabling these active particles to not only move effectively but also decontaminate the radioactive contaminants from the targeted sites.

To achieve effective decontamination, the Janus particles can be modified to carry chemical species such as EDTA (ethylenediaminetetraacetic acid) or DTPA (diethylenetriaminepentaacetic acid), known for their affinity for metal ions (including radioactive ones)<sup>2,3</sup>, forming stable complexes that can further be removed or neutralized. This allows wide scope of study in Chemistry of particles to strategize and investigate surface functionalization and optimization of Janus Particles with chelating agents followed by testing and validating their functioning. The surface of the Janus particles can be functionalized using surface modification techniques, ensuring that the particles have active sites that can bind to radioactive metals. While the choice of complexant can be optimized based on specific radioactive contaminant, further, studying 'collection/recovery of NDN during application' is another essential perspective this thesis leads to, followed by the evaluation of efficacy-test of complexant-functionalized Janus particles in controlled environments with known concentrations of radioactive contaminants. For this purpose, an optimized microfluidic set-up can be beneficial for initial tests followed by a decontamination of a 3D printed maze having radioactive contaminants at certain parts, and further testing on ground level-scale.

Some of the key perspectives of this thesis are as following:

1. Particle-size reduction: Smaller particles exhibit improved stability due to lower gravitational forces acting on them.<sup>4,5</sup> This stability enhancement is crucial for applications requiring uniform dispersal of particles in a medium, such as ours, therefore reducing the size of targeted particles (from current size scale 500 nm to a lower range) can reduce particle-sedimentation in the colloidal suspension.
2. Use of porous silica and chelatants-grafting: The porosity increases the surface area available for functionalization, allowing for higher loading capacities of active molecules and chelating agents.<sup>6-9</sup> Therefore, studying porous silica particles for surface functionalization can be an interesting perspective.
3. Cost-effective catalysts: Catalysts like manganese dioxide ( $\text{MnO}_2$ ) present a cost-effective alternative to gold nanoparticles (for the synthesis of Janus particles) making it a suitable choice for large-scale production. While  $\text{MnO}_2$  is environment-friendly, its catalytic properties are optimizable for various reactions, enhancing the economic feasibility of practical applications.<sup>10,11</sup>
4. Temperature and pH dependence: Parameters like pH and temperature can significantly affect particle-stability, interaction with surroundings, and overall efficacy.<sup>12,13</sup> Therefore, understanding these dependencies allows us to enhance their functionality by designing particles with better stability under different physiological condition. Thus, making

investigation of particle behaviour in pH and temperature, vital for application in dynamic environments.

5. Transition from microfluidics to milifluidics: While microfluidics offers precise control and manipulation at a small scale, mili/macrofluidics allows us for processing larger volumes. This makes it suitable for more industrial and commercial use. Therefore, expanding the application of our particles from microfluidics to macrofluidics represents a significant perspective.
6. Recovery methods: Effective recovery not only reduces waste, but also allows for the reuse of particles. This significantly lowers the operational costs and environmental impact. Therefore, developing efficient recovery methods is crucial for sustainable and cost-effective applications of the developed particles.

Lastly, although the potential applications of these NDN in decontamination can be wide-ranged, some envisioned uses (only applicable after full-fledged development of NDN) could be maintenance of facilities with radioactive materials, spillage containment, and environmental clean-up. In facilities with radioactive material, these NDN with fluorescence markers (or other chemical probes) can be used for providing data on contamination levels, locations, and the type of radioactive materials present. Considering its functioning in water, it can also be interesting to explore the possibilities of deployment of these NDN in cooling water systems, spent fuel pools, or other areas where contamination is likely to occur. Use of NDN at sites of nuclear incident/accident can aid in containing the radioactive spillage and therefore, limit contamination widespread. While customization for application as soil-decontaminator can be another aspect for exploration (for this purpose, conjugation with bacteria can be another prospective study as well). However, these prospective-applications are for far future. Before any application a thorough investigation for target specificity, stability and durability of these NDN is utmost important. Chelating-functioning test can help in target specificity test. This would ensure that the NDN are specific only for target contaminants and least interactive to the non-radioactive substances. While quantification of particle degradation/deterioration from chemical and radiation exposure can help in testing the stability and durability of NDN. Additionally, research dedicated for enhancement of structural integrity and functionality under varying environmental conditions over long-term is another crucial aspect for application of NDN, and a strong perspective from this thesis work. Last but not the least particles produced in this thesis can also have potential applications in various fields apart from nuclear decontamination industry. Tailoring the surface properties of Janus for exploring their application holds strong benefiting potential in different domains including targeted drug delivery & diagnostics (example: as contrasting agent), biomedicine (example: biocompatible drug delivery systems), catalysis and micro-sensors.

- (1) Irimia, D.; Charras, G.; Agrawal, N.; Mitchison, T.; Toner, M. Polar Stimulation and Constrained Cell Migration in Microfluidic Channels. *Lab Chip* **2007**, *7* (12), 1783–1790. <https://doi.org/10.1039/B710524J>.
- (2) Griffiths, N. M.; Van der Meer, A.; Grémy, O. Comparison of Local and Systemic DTPA Treatment Efficacy According to Actinide Physicochemical Properties Following Lung or Wound Contamination in the Rat. *Front. Pharmacol.* **2021**, *12*. <https://doi.org/10.3389/fphar.2021.635792>.
- (3) Belanger, R. Plutonium. In *Encyclopedia of Toxicology (Second Edition)*; Wexler, P., Ed.; Elsevier: New York, 2005; pp 450–453. <https://doi.org/10.1016/B0-12-369400-0/00773-0>.
- (4) Braun, A.; Couteau, O.; Franks, K.; Kestens, V.; Roebben, G.; Lamberty, A.; Linsinger, T. Validation of Dynamic Light Scattering and Centrifugal Liquid Sedimentation Methods for Nanoparticle Characterisation. *Advanced Powder Technology - ADVANCED POWDER TECHNOL* **2011**, *22*, 766–770. <https://doi.org/10.1016/j.apt.2010.11.001>.

## Conclusion and Perspective

- (5) Yokojima, S.; Takashima, R.; Asada, H.; Miyahara, T. Impacts of Particle Shape on Sedimentation of Particles. *European Journal of Mechanics - B/Fluids* **2021**, *89*, 323–331. <https://doi.org/10.1016/j.euromechflu.2021.06.007>.
- (6) Ortega-Liebana, M. C.; Bonet-Aleta, J.; Hueso, J. L.; Santamaria, J. Gold-Based Nanoparticles on Amino-Functionalized Mesoporous Silica Supports as Nanozymes for Glucose Oxidation. *Catalysts* **2020**, *10* (3), 333. <https://doi.org/10.3390/catal10030333>.
- (7) Echevsky, G. V.; Toktarev, A. V.; Kodenev, E. G.; Aksenov, D. G. Development of Highly Efficient Hydroisodeparaffinization Catalysts Based on Micro-Mesoporous SAPO-31: New Approaches in the Synthesis of SAPO-31 and the Preparation of Bifunctional Catalysts. *Catalysts* **2023**, *13* (5), 810. <https://doi.org/10.3390/catal13050810>.
- (8) Varache, M.; Bezverkhy, I.; Weber, G.; Saviot, L.; Chassagnon, R.; Baras, F.; Bouyer, F. Loading of Cisplatin into Mesoporous Silica Nanoparticles: Effect of Surface Functionalization. *Langmuir* **2019**. <https://doi.org/10.1021/acs.langmuir.9b00954>.
- (9) Trayford, C.; Crosbie, D.; Rademakers, T.; van Blitterswijk, C.; Nuijts, R.; Ferrari, S.; Habibovic, P.; LaPointe, V.; Dickman, M.; van Rijt, S. Mesoporous Silica-Coated Gold Nanoparticles for Multimodal Imaging and Reactive Oxygen Species Sensing of Stem Cells. *ACS Appl. Nano Mater.* **2022**, *5* (3), 3237–3251. <https://doi.org/10.1021/acsnm.1c03640>.
- (10) Abuzeid, H. M.; Elsharif, S. A.; Abdel Ghany, N. A.; Hashem, A. M. Facile, Cost-Effective and Eco-Friendly Green Synthesis Method of MnO<sub>2</sub> as Storage Electrode Materials for Supercapacitors. *Journal of Energy Storage* **2019**, *21*, 156–162. <https://doi.org/10.1016/j.est.2018.11.021>.
- (11) Affrald R, J.; M, N.; Narayan, S. A Comprehensive Review of Manganese Dioxide Nanoparticles and Strategy to Overcome Toxicity. *Nanomed J* **2022**, No. Online First. <https://doi.org/10.22038/nmj.2022.66131.1694>.
- (12) Avital, E. J.; Miloh, T. Self-Thermophoresis of Laser-Heated Spherical Janus Particles. *Eur. Phys. J. E* **2021**, *44* (11), 139. <https://doi.org/10.1140/epje/s10189-021-00128-4>.
- (13) Bertoni, A. I.; Passarelli, N.; Bustos-Marún, R. A. Theoretical Analysis of Metallic-Nanodimer Thermoplasmonics for Phototactic Nanoswimmers. *ACS Appl. Nano Mater.* **2020**, *3* (2), 1821–1829. <https://doi.org/10.1021/acsnm.9b02505>.
- (14) Dynamic Light Scattering Particle Size Distribution Analysis. <https://www.horiba.com/int/scientific/technologies/dynamic-light-scattering-dls-particle-size-distribution-analysis/dynamic-light-scattering-dls-particle-size-distribution-analysis/>.
- (15) Malvern Zetasizer ZS DLS User Manual.Pdf. <https://www.chem.uci.edu/~dmityrf/manuals/Malvern%20Zetasizer%20ZS%20DLS%20User%20manual.pdf>.
- (16) Kaszuba, M. A basic introduction to Dynamic Light Scattering (DLS) for particle size analysis - Q&A - Materials Talks. <https://www.materials-talks.com/a-basic-introduction-to-dynamic-light-scattering-dls-for-particle-size-analysis-qa/>.
- (17) Rayleigh Scattering. <https://site.physics.georgetown.edu/~vankeu/webtext2/Workspace/Rayleigh%20scattering/Rayleigh%20scattering.htm>.
- (18) Pons, T.; Uyeda, H. T.; Medintz, I. L.; Mattoussi, H. Hydrodynamic Dimensions, Electrophoretic Mobility, and Stability of Hydrophilic Quantum Dots. *J. Phys. Chem. B* **2006**, *110* (41), 20308–20316. <https://doi.org/10.1021/jp065041h>.
- (19) Carpenter, D. K. Dynamic Light Scattering with Applications to Chemistry, Biology, and Physics (Berne, Bruce J.; Pecora, Robert). *J. Chem. Educ.* **1977**, *54* (10), A430. <https://doi.org/10.1021/ed054pA430.1>.
- (20) The principles of dynamic light scattering | Anton Paar Wiki. Anton Paar. <https://wiki.anton-paar.com/en/the-principles-of-dynamic-light-scattering/>.
- (21) Jia, Z.; Li, J.; Gao, L.; Yang, D.; Kanaev, A. Dynamic Light Scattering: A Powerful Tool for In Situ Nanoparticle Sizing. *Colloids and Interfaces* **2023**, *7* (1), 15. <https://doi.org/10.3390/colloids7010015>.
- (22) Hassan, P. A.; Rana, S.; Verma, G. Making Sense of Brownian Motion: Colloid Characterization by Dynamic Light Scattering. ACS Publications. <https://doi.org/10.1021/la501789z>.
- (23) Lorber, B.; Fischer, F.; Bailly, M.; Roy, H.; Kern, D. Protein Analysis by Dynamic Light Scattering: Methods and Techniques for Students. *Biochemistry and Molecular Biology Education* **2012**, *40* (6), 372–382. <https://doi.org/10.1002/bmb.20644>.
- (24) Yu, Z.; Reid, J. C.; Yang, Y.-P. Utilizing Dynamic Light Scattering as a Process Analytical Technology for Protein Folding and Aggregation Monitoring in Vaccine Manufacturing. *JPharmSci* **2013**, *102* (12), 4284–4290. <https://doi.org/10.1002/jps.23746>.
- (25) Akhtar, K.; Khan, S. A.; Khan, S. B.; Asiri, A. M. Scanning Electron Microscopy: Principle and Applications in Nanomaterials Characterization. In *Handbook of Materials Characterization*; Sharma, S. K., Ed.; Springer International Publishing: Cham, 2018; pp 113–145. [https://doi.org/10.1007/978-3-319-92955-2\\_4](https://doi.org/10.1007/978-3-319-92955-2_4).
- (26) Perro, A.; Meunier, F.; Schmitt, V.; Ravaine, S. Production of Large Quantities of “Janus” Nanoparticles Using Wax-in-Water Emulsions. *Colloids and Surfaces A: Physicochemical and Engineering Aspects* **2009**, *332* (1), 57–62. <https://doi.org/10.1016/j.colsurfa.2008.08.027>.
- (27) Petit, L.; Manaud, J.-P.; Mingotaud, C.; Ravaine, S.; Duguet, E. Sub-Micrometer Silica Spheres Dissymmetrically Decorated with Gold Nanoclusters. *Materials Letters* **2001**, *51* (6), 478–484. [https://doi.org/10.1016/S0167-577X\(01\)00338-X](https://doi.org/10.1016/S0167-577X(01)00338-X).
- (28) Yang, Q.; De Vries, M. H.; Picchioni, F.; Loos, K. A Novel Method of Preparing Metallic Janus Silica Particles Using Supercritical Carbon Dioxide. *Nanoscale* **2013**, *5* (21), 10420. <https://doi.org/10.1039/c3nr81280d>.

## Conclusion and Perspective

- (29) Lu, Y.; Xiong, H.; Jiang, X.; Xia, Y.; Prentiss, M.; Whitesides, G. M. *Asymmetric Dimers Can Be Formed by Dewetting Half-Shells of Gold Deposited on the Surfaces of Spherical Oxide Colloids*. *J. Am. Chem. Soc.* **2003**, *125* (42), 12724–12725. <https://doi.org/10.1021/ja0373014>.
- (30) Percebom, A. M.; Giner-Casares, J. J.; Claes, N.; Bals, S.; Loh, W.; Liz-Marzán, L. M. *Janus Gold Nanoparticles Obtained via Spontaneous Binary Polymer Shell Segregation* †Electronic Supplementary Information (ESI) Available: *Experimental Procedures, Results of SAXS, UV-Vis and DLS for NPs of Different Core Sizes, Polymer Coatings and in Different Solvents; Details of Emulsification Using Janus Au NPs; TEM Images after Silica Coating of Janus Au NPs; 3D Images of Different Stained Au NPs*. See DOI: 10.1039/C5cc10454h [Click Here for Additional Data File](https://doi.org/10.1039/C5cc10454h). *Chem Commun (Camb)* **2016**, *52* (23), 4278–4281. <https://doi.org/10.1039/C5cc10454h>.
- (31) Marina Santana Vega; Andrés Guerrero Martínez; Fabio Cucinotta. *Facile Strategy for the Synthesis of Gold@Silica Hybrid Nanoparticles with Controlled Porosity and Janus Morphology*. *Nanomaterials (Basel, Switzerland)* **2019**, *9* (3), 348. <https://doi.org/10.3390/nano9030348>.

## Annex-1

### UV-Vis

Ultraviolet-Visible (UV-Vis) spectroscopy stands as a foundational analytical technique in the field of molecular spectroscopy, offering valuable insights into the electronic structure and concentration of molecules through the measurement of their absorption of ultraviolet and visible light. The fundamental principle of UV-Vis spectroscopy lies in the absorption of light by molecules, leading to electronic transitions. This absorption is characteristic of the molecular structure and is reflected in the generated absorption spectrum. The energy required for these electronic transitions corresponds to specific wavelengths in the UV and visible regions, producing a spectrum that serves as a unique signature for each molecular species. UV-Vis not just helps in qualitative analysis but also quantitative; through the Beer-Lambert Law, establishing a linear relationship between absorbance and concentration enabling the determination of concentrations for known absorbing species. Despite its versatility, UV-Vis spectroscopy is not without challenges. Factors such as solvent effects, impurities, and the presence of interfering substances can influence measurement accuracy. UV-Vis spectrophotometers typically consist of a light source emitting UV and visible light, a monochromator for wavelength selection, a sample compartment (and a reference compartment, depending upon the instrument-model), and a detector for quantifying the absorbed light (Figure 62).

### DLS

Dynamic light scattering (DLS) also known as Photon Correlation Spectroscopy (PCS) or Quasi Elastic Light Scattering (QELS)<sup>14</sup> is a powerful and versatile technique employed in the characterization of particles and macromolecules (nano to micro scale) suspended in a liquid.<sup>15,16</sup> This non-destructive technique provides valuable information about particle size, size distribution, and molecular interactions through the analysis of fluctuations in scattered light intensity over time. The underlying principles of DLS observation roots from the Brownian motion of particles suspended in a fluid medium (fine particles/molecules experience diffusion at a speed related to their size; smaller particles diffuses faster than larger particles). As the rate of Brownian motion is also effected by the temperature, therefore temperature is controlled accurately throughout the measurement period. DLS instrument is equipped with a laser light source, a detector, and a correlator (Figure 64). Once the incident laser light hits these particles (undergoing random thermal motion; Brownian motion), intensity of scattered light fluctuates and so does the distance between particles. When light hits particles or molecules undergoing Brownian motion, it scatters in all directions (Rayleigh scattering<sup>17</sup>). DLS analyzes the autocorrelation function of these intensity fluctuations, from which information about particle size (hydrodynamic radius<sup>18</sup>) and diffusion coefficients can be extracted.<sup>19</sup> Autocorrelation is a mathematical tool for finding pattern repetition, or similarity between observations as a function of the time lag between them. Initially, the correlation function exhibits a linear and relatively constant pattern, indicating the sustained position of particles from the previous moment. Subsequently, as the particle moves constantly thus distances itself, the function undergoes exponential reduction until it reaches the baseline (having no resemblance to the initial position, and the correlation function reverting to a linear behaviour), signifying that the molecule is now situated at a considerable distance from its initial position. The decay in correlation function reflects information about size-dependent

particle movement. Thus, this decay serves as an indirect measure of the time required for particles to alter their relative positions. Smaller particles exhibit rapid movement, resulting in a swift decay, while larger particles move more slowly, causing a delayed decay in the correlogram. The larger particles contribute to higher amplitudes of the scattering intensities. To have a good set of correlogram data from DLS study, sample preparation requires dilution; ensuring optimal range of concentration. Sample dilution is a crucial step in order to avoid the effects of collective-scattering. Sedimentation should be avoided or at least the rate of sedimentation should be much slower than the rate of diffusion for a successful measurement.

In order to perform DLS measurements sample is loaded into the instrument and the parameters to perform the analysis are defined. These parameter definitions are called Standard Operating Procedure (SOP). SOP serves as a comprehensive set of specific instructions, essential for the execution of a particular DLS measurement in a standardized and consistent manner. Primary purpose of SOP is to contribute to the precision and reproducibility of results. This provides a set of guidelines to ensure uniformity and reliability in the execution of experiments. Upon the completion of a DLS study, size and polydispersity can be observed directly from the outputs, while the sample quality can be understood from intercept value. Intercept value represents the ratio of signal to background and is contingent on the optical configuration of both the sample and the instrument. Optimal intercept values fall within the range of 10% to 100%, denoted as 0.1 to 1.0. A lower-than-anticipated intercept value may imbalance signal in sample concentration, indicating levels that are either excessively high or low. Higher sample concentrations have the potential to induce multiple scattering effects, consequently reducing the intercept value.<sup>15,20,16</sup> Another important influencing factor in a DLS measurement is sedimentation, which can be followed by checking for a stable mean count rate of scattered light, over multiple measurements on same sample. Decreasing count rate indicates loss of particles due to sedimentation and thus requires re-preparation of sample.<sup>21-24</sup>

## SEM/EDX

Scanning Electron Microscopy is widely used for visualizing surface morphology as high magnification and resolution reveals features such as grain boundaries, surface roughness, and the presence of microstructures. It operates on the principle of scanning a focused electron beam across the surface of a specimen. Electron interaction with sample generates signals, including secondary electrons, backscattered electrons, and characteristic X-rays. Detection and analysis of these signals allow for the creation of detailed high-resolution images and provide valuable information about the composition, topography, and elemental distribution of the sample at the micro- and nanoscale. Key components of a SEM instrument (Figure 146) include an electron gun, electromagnetic lenses (for focusing and scanning electron beam), scanning coil, stigmator coil, sample chamber, detectors (for capturing emitted signals), and a display system (for image visualization).<sup>25</sup> Advanced SEM instruments often incorporate features such as energy-dispersive X-ray spectroscopy (EDX) detectors, allowing for elemental analysis and mapping. While SEM is a powerful imaging technique, certain challenges like sample preparation are critical (sample must be conductive or coated with a thin layer of conductive material). Additionally, electron beam damage may occur, especially for sensitive samples, necessitating careful control of beam parameters.



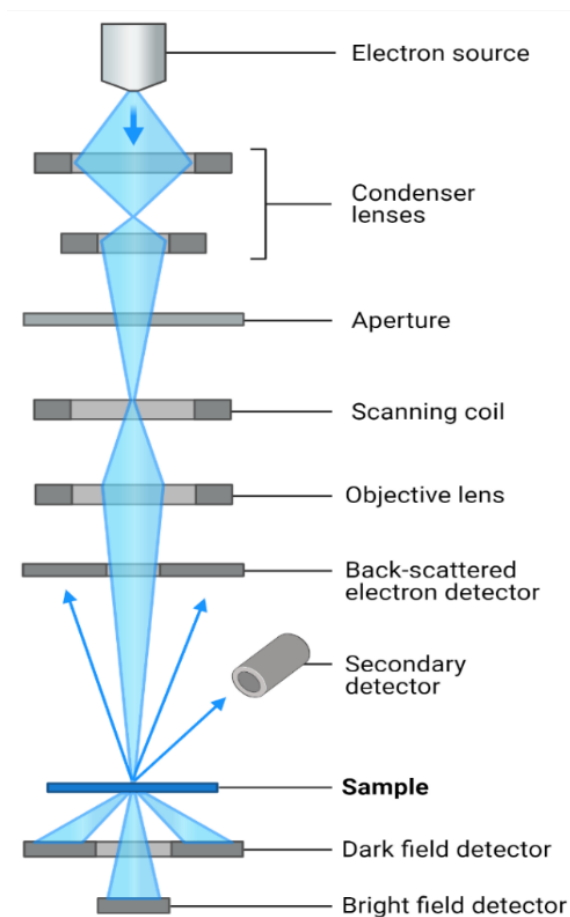


Figure 146: Labelled diagram of working principle of a Scanning Electron Microscope (FEG-SEM) with Field Emission Gun. FEG SEM allows a better resolution

Table 26: Featuring values of properties utilized for the calculation of concentration of gold nanoparticle from the synthesis.

Property	Value	Unit
FCC Density of Gold	19.3	$\text{g.cm}^{-3}$
Mean diameter of AuNP	2.50E-06	cm
Atomic weight of Au	196.96	$\text{g.mol}^{-1}$
Molar conc. of Au used in synthesis	0.25	mM
Final volume of AuNP suspension	0.05	L
Total no. of gold atom in AuNP suspension	$1.51 \times 10^{21}$	
No. of Au atom per AuNP	$4.83 \times 10^5$	
No. of AuNP (of 25 nm diameter) in AuNP suspension	$3.12 \times 10^{14}$	$\text{mL}^{-1}$

## Annex-1

Table 27: Parameter for Iso and JP synthesized in this thesis, compared (JP) with JP from A Perro's work<sup>26</sup> (both JP followed chemical synthesis protocol of Pickering Emulsion)

Parameter	Thesis (JP)	Perro <sup>26</sup>	Unit
Mean no. of AuNP/JP	109	80	
Radius of AuNP (nm)	12.5	7.5	nm
Radius of SP (nm)	238	150	nm
TSA SP hemisphere (nm <sup>2</sup> )	354411	141372	nm <sup>2</sup>
Area of AuNP (nm <sup>2</sup> )	491	177	nm <sup>2</sup>
Area of Void from AuNP (nm <sup>2</sup> )	134	48	nm <sup>2</sup>
Theoretical No. of AuNP/Iso	567	628	
Area occupied by 1 AuNP (nm <sup>2</sup> )	3260.02	1767	nm <sup>2</sup>
Diameter of occupied area per AuNP (nm)	32	24	nm
TA total AuNP	53365	14137	nm <sup>2</sup>
Area occupied by AuNP/JP hemisphere	15	10	%

Table 28: Summary of number of chemical species present in respective particles

Particle	No. of Chemical Species present
SP	1 (SP)
Iso	3 (SP, APTES, AuNP)
JP	4 (SP, CTAB, APTES, AuNP) +1 if any traces from wax (and/or wax solvent)
PVD-JP	2 (SP, Au)

## Annex-1

Table 29: Calculation table showing different properties for respective particles

Parameter	Value	Unit	Comment
<b>Silica Density</b>	2.32E+06	g/m <sup>3</sup>	<a href="https://www.aqua-calc.com/page/density-table/substance/silica">https://www.aqua-calc.com/page/density-table/substance/silica</a>
<b>Gold Density</b>	1.93E+07	g/m <sup>3</sup>	<a href="https://www.aqua-calc.com/page/density-table/substance/gold">https://www.aqua-calc.com/page/density-table/substance/gold</a>
<b>Mean Dia SP</b>	4.75E-07	m	
<b>Mean Dia AuNP</b>	2.50E-08	m	
<b>r<sub>1</sub> PVD-JP</b>	2.70E-07	m	(maximum radius of outer layer; SP+Gold Layer)
<b>r<sub>2</sub> PVD-JP</b>	2.50E-07	m	(maximum radius of inner layer; SP)
<b>AuNP/Iso</b>	217		(avg. no. of AuNP counted from 50 Iso particles)
<b>Vol SP</b>	5.61E-20	m <sup>3</sup>	$(4/3) * \pi * (r^3)$
<b>Vol AuNP</b>	8.18E-24	m <sup>3</sup>	$(4/3) * \pi * (r^3)$
<b>Vol<sub>1</sub> PVD-JP</b>	4.12E-20	m <sup>3</sup>	$(2/3) * \pi * (r_1^3)$
<b>Vol<sub>2</sub> PVD-JP</b>	3.27E-20	m <sup>3</sup>	$(2/3) * \pi * (r_2^3)$
<b>Vol AuCap</b>	8.50E-21	m <sup>3</sup>	Vol <sub>1</sub> PVD-JP - Vol <sub>2</sub> PVD-JP
<b>Wt. SP</b>	1.30E-13	g	Silica Density * Vol SP
<b>Wt. AuNP</b>	1.58E-16	g	Gold Density * Vol AuNP
<b>Wt. AuCap</b>	1.64E-13	g	Gold Density * Vol AuCap
<b>No. of SP</b>	5.68E+10		mL <sup>-1</sup> SP suspension
<b>No. of AuNP</b>	3.12E+14		mL <sup>-1</sup> AuNP suspension
<b>TSA of 1 SP</b>	7.08E-13	m <sup>2</sup>	Total surface area $(4 * \pi * (r^2))$
<b>CSA of 1 SP Hemisphere</b>	3.54E-13	m <sup>2</sup>	Curved surface area $2 * \pi * (r^2)$
<b>AuNP Topological Area</b>	4.91E-16	m <sup>2</sup>	$\pi * (r^2)$
<b>Area AuNP (Topological)</b>	1.53E-01	m <sup>2</sup> /mL	m <sup>2</sup> /mL AuNP suspension
<b>TSA SP</b>	4.03E-02	m <sup>2</sup> /mL	m <sup>2</sup> /mL SP suspension
<b>TSA SP Hemisphere</b>	2.01E-02	m <sup>2</sup> /mL	m <sup>2</sup> /mL SP suspension
<b>Vol. of AuNP per mL</b>	2.55E-09	m <sup>3</sup>	No. of AuNP per mL AuNP suspension x Vol. of 1 AuNP; $(4/3) * \pi * (r^3)$
<b>Vol. of SP per mL</b>	3.19E-09	m <sup>3</sup>	No. of SP per mL SP suspension x Vol. of 1 SP; $(4/3) * \pi * (r^3)$

Table 30: Values for APTES for covering 0.75 m<sup>2</sup> area of silica particles for making Isotropic Gold/Silica particles.

Avogadro's No.	6.022 x 10 <sup>23</sup>	molecules/mol
APTES density	0.946	g/mL
APTES molar mass	221.37	g/mol
No. of moles in 1 mL APTES	0.0043	mol
Area to cover (on Silica Particle surface to make JP)	0.75	m <sup>2</sup>
No. of APTES per 15 nm <sup>2</sup> Silica Particle	1	-
No. of APTES molecule req. for JP synthesis	5.00 x 10 <sup>16</sup>	for 0.75m <sup>2</sup> area
No. of moles required (for 0.75 m <sup>2</sup> area)	8.30 x 10 <sup>-8</sup>	mol
Equivalent volume of APTES	0.019	mL

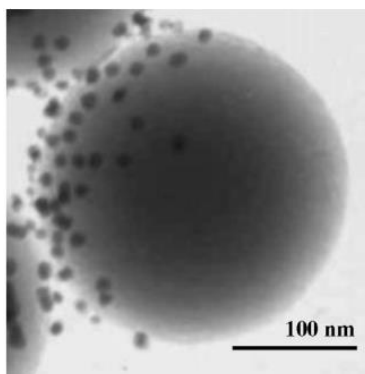
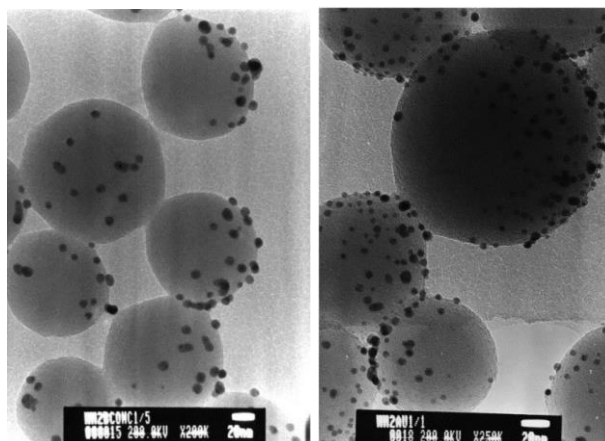


Figure 147: A Perro's<sup>26</sup> gold/silica janus particle (mean diameter ~300 nm and 15 nm for SP and AuNP respectively)<sup>26</sup>. Size of gold nanoparticles was calculated by ImageJ from the image extracted from the paper. Image extracted from Perro, 2009.<sup>26</sup>



## Annex-1

Figure 148: Petit's<sup>27</sup> gold/silica Janus nanoparticle (Silica nanoparticle mean diameter 90-120 nm and AuNP mean diameter 8 – 10 nm)<sup>27</sup>. Left image is from synthesis in gas-liquid phase of synthesis while right image is from particles synthesis from liquid-solid interface. Image extracted Petit, 2001<sup>27</sup>

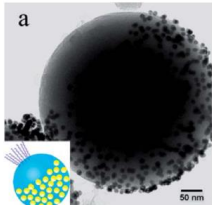
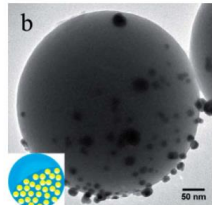
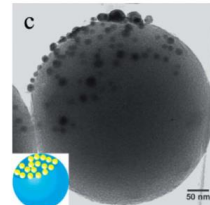
	$JB^a = 3 : 7$	$JB = 1 : 1$	$JB = 3 : 2$
Coverage of Au NPs	$\approx 70\%$	$\approx 50\%$	$\approx 40\%$
Supercritical CO <sub>2</sub> conditions	55 °C, 126 bar for 4 h 60 °C, 60 bar for 4 h	60 °C, 80 bar for 4 h 60 °C, 126 bar for 4 h	60 °C, 170 bar for 4 h
TEM images of Janus particles			

Figure 149: Gold/Silica Janus particles synthesized by Yang.  $JB^a$ ; Janus Balance is the surface area ratio of the gold nanoparticle and silica particles. Image extracted from Yang, 2013<sup>28</sup>

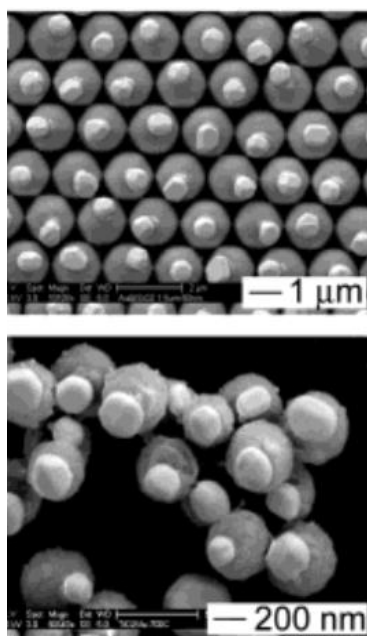


Figure 150: SEM images of gold/silica Janus particles.  $\sim 650$  nm dia. gold patch on  $1.5 \mu\text{m}$  dia. silica particle (top) and  $\sim 100$  nm dia. gold patch on  $200$  nm dia. silica particle (bottom). Image extracted from Lu et al., 2003.<sup>29</sup>

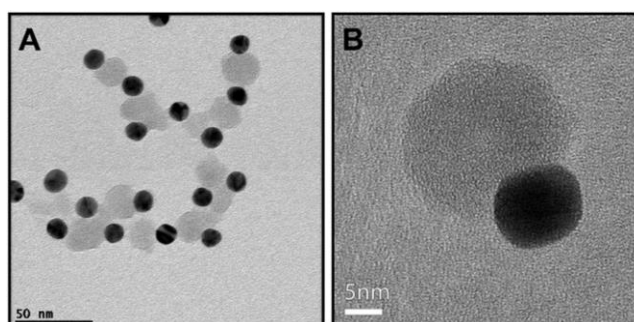


Figure 151: TEM images of gold/silica Janus particles. A)  $\sim 13$  nm dia. gold nanoparticle on  $\sim 21$  nm dia. silica particle. B) Magnified images of Gold/Silica Janus particle. Image extracted from Percebom et al., 2015.<sup>30</sup>

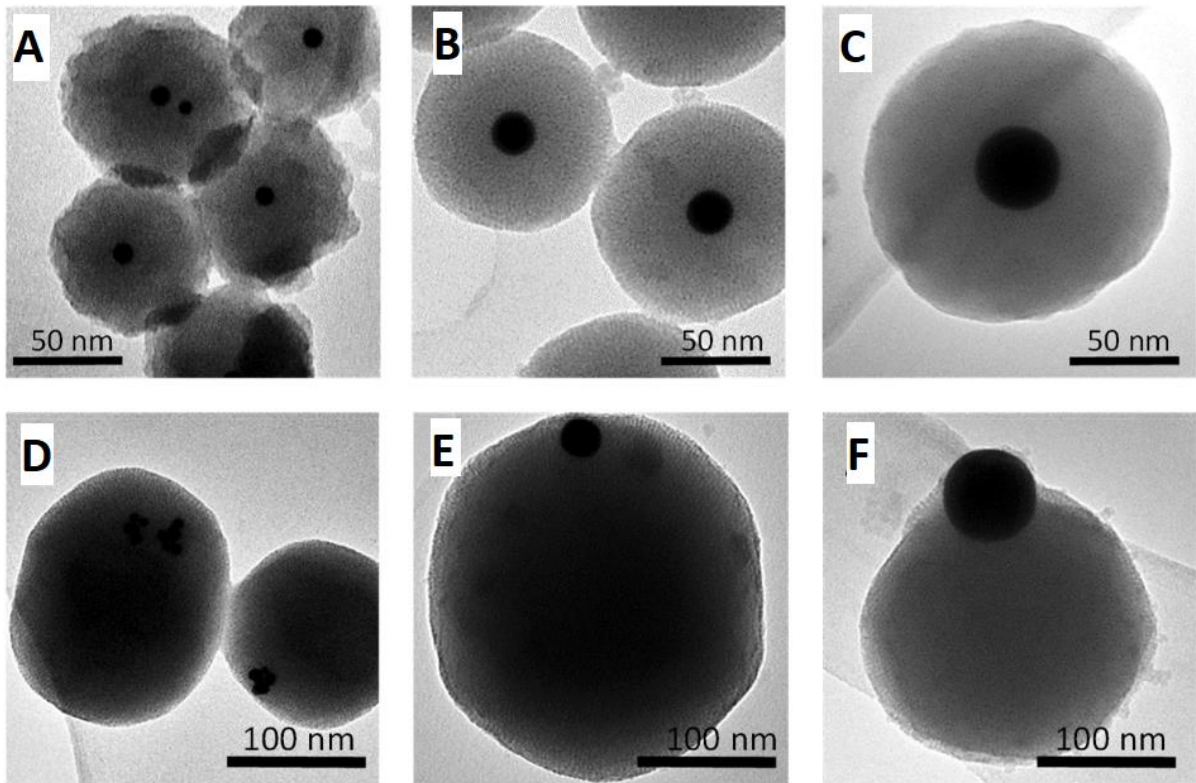


Figure 152: TEM images of gold/silica janus particles. A and D having 10 nm dia. gold nanoparticle in  $\sim 80$  nm and  $\sim 165$  nm dia. silica particles, respectively. B and E (top) having 30 nm dia. gold nanoparticle in  $\sim 100$  nm and  $\sim 270$  nm dia. silica particles, respectively. While C and F having  $\sim 70$  nm dia. gold nanoparticle in  $\sim 140$  nm and  $\sim 230$  nm dia. silica particle, respectively. Image extracted from Vega et al., 2019.<sup>31</sup>

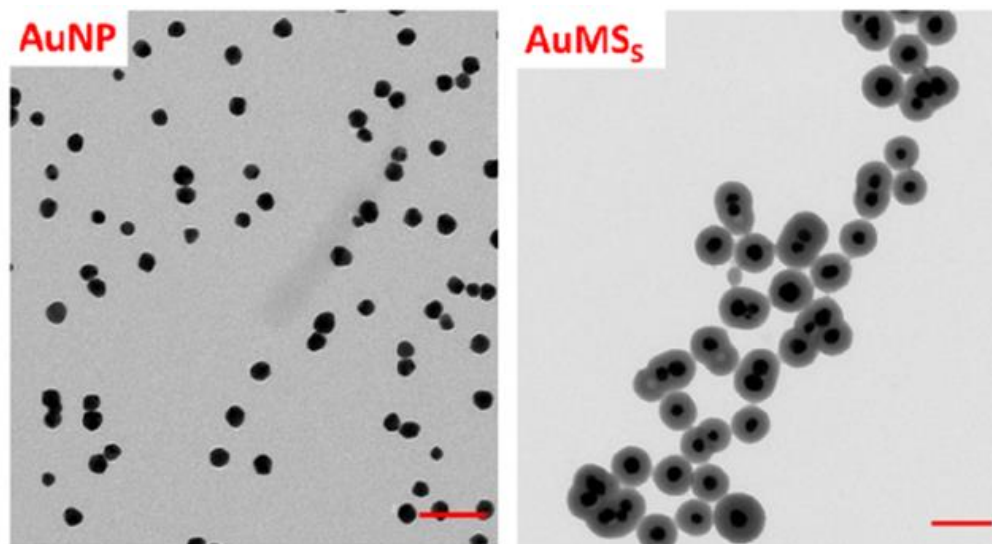


Figure 153: TEM images of gold nanoparticles (AuNP) and gold/mesoporous silica janus particles (AuMS). Mean diameter of gold nanoparticle is  $62.5 \pm 6.4$  nm, while mean diameter of AuMS is  $155 \pm 11.4$  nm. Image extracted from Trayford et al., 2022.<sup>9</sup>

### SNP functionalization with PAH

1. Took 50 mg PAH and added 1.46 g NaCl, followed by 50 mL MilliQ water and mixed well for 1-2 min using ultra sonication.
2. Took 0.22 mL SP suspension and 4.777 mL MiliQ water in centrifuge tube and mixed well.
3. Added 5 mL PAH solution (prepared above in step 1.) This addition of PAH to SNP solution was done by keeping SP solution under ultra-sonication, along with addition of PAH solution at medium pace.
4. Put the above on rotating agitator for 30 min.
5. Centrifuged the above in water @6000 RPM (~9420 RCF) for 20, thrice for purification and removal of excess PAH.
6. Re-dispersed the collected pellet (PAH functionalized SP) in 5 mL Mili-Q water (30 secs vortex mixing and 10 min ultra-sonication was done for good re-dispersion).
7. Added 1 mL AuNP added to purified PAH functionalized SNP and mixed it on rotating agitator for 3 hr.
8. Centrifuged the above in 5 mL Milli-Q water @6000 RPM for 20, thrice for purification and removal of excess AuNP.
9. Re-dispersed the collected pellet (AuNP-SP) in 1 mL Mili-Q water (30 secs vortex mixing and 10 min ultra-sonication was done for good re-dispersion).

### SNP functionalization with PLL

1. Added 0.1 g silica particles to 10 mL 6.7% (w/w) EtOH and mixed it using magnetic stirrer @500 RPM for 30 mins to obtain a homogeneous suspension.
2. Added 10 mL PLL to the above and mixed it using magnetic stirrer @500 RPM for 30 mins to obtain a homogeneous suspension.
3. Centrifuged the above in water @6000 RPM (~9420 RCF) for 20, thrice for purification and removal of excessive PLL.
4. Re-dispersed the collected pellet (PLL functionalized SP) in 5 mL Mili-Q water (30 secs vortex mixing and 10 min ultra-sonication was done for good re-dispersion).
5. Added 1 mL AuNP suspension to above for 15 mins by shaking the flask and allowed AuNP to functionalize PLL-SNP overnight.
6. Centrifuged the above @6000 (~9420 RCF) RPM for 20 mins thrice in 5 mL Milli-Q water and removed excessive AuNP.
7. Re-dispersed the collected pellet (AuNP-SP) in 1 mL Mili-Q water (30 secs vortex mixing and 10 min ultra-sonication was done for good re-dispersion).

Annex-1

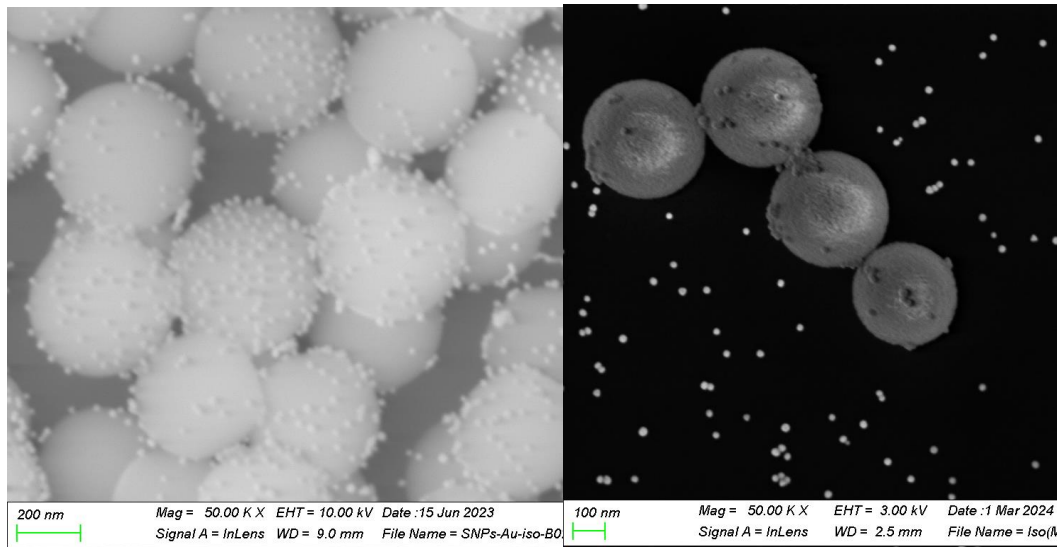


Figure 154: SEM images used for estimating the approximate mean diameter of AuNP (~25 nm)

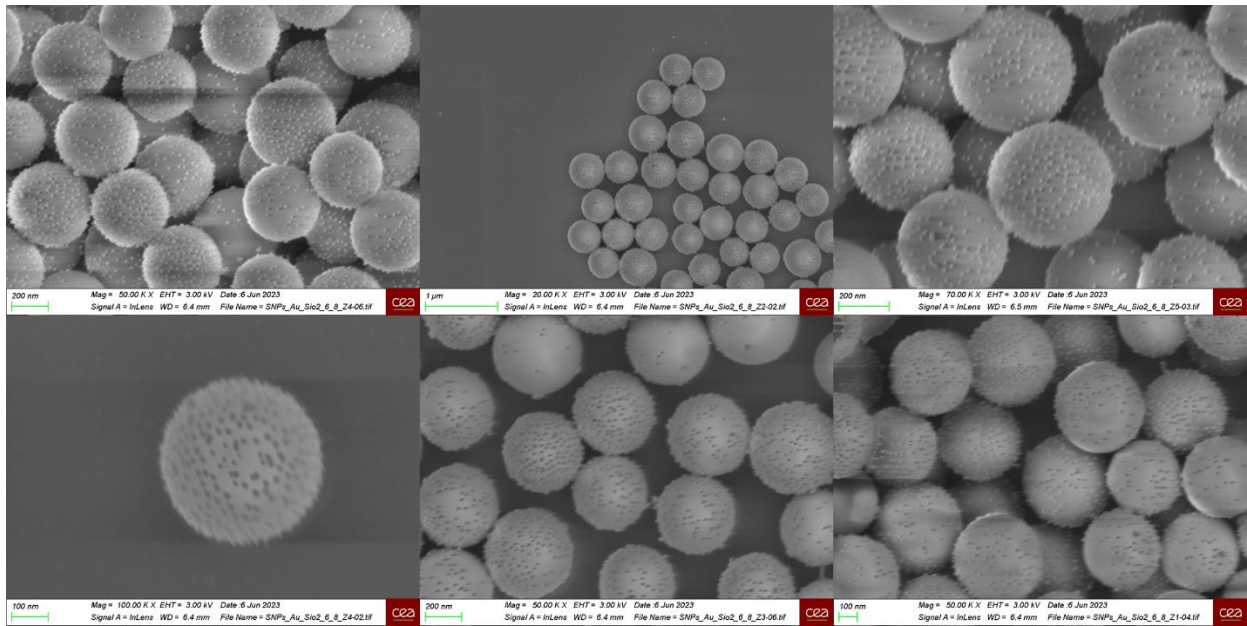


Figure 155: SEM images of Iso sample used for calculating average mean count of AuNP per Iso



## Annex-2

Table 31: Sample composition for respective DLS experiments. Volume of water and H<sub>2</sub>O<sub>2</sub> is in  $\mu\text{L}$ .

Sample	0% H <sub>2</sub> O <sub>2</sub>	0.5% H <sub>2</sub> O <sub>2</sub>	1% H <sub>2</sub> O <sub>2</sub>	3% H <sub>2</sub> O <sub>2</sub>	5% H <sub>2</sub> O <sub>2</sub>
<b>SP</b> <b>(1 <math>\mu\text{L}</math>)</b>	Water: 999 H <sub>2</sub> O <sub>2</sub> : 0	Water: 982 H <sub>2</sub> O <sub>2</sub> : 17	Water: 967 H <sub>2</sub> O <sub>2</sub> : 33	Water: 932 H <sub>2</sub> O <sub>2</sub> : 67	Water: 833 H <sub>2</sub> O <sub>2</sub> : 166
<b>Iso</b> <b>(30 <math>\mu\text{L}</math>)</b>	Water: 970 H <sub>2</sub> O <sub>2</sub> : 0	Water: 954 H <sub>2</sub> O <sub>2</sub> : 16	Water: 938 H <sub>2</sub> O <sub>2</sub> : 32	Water: 873 H <sub>2</sub> O <sub>2</sub> : 97	Water: 808 H <sub>2</sub> O <sub>2</sub> : 162
<b>JP</b> <b>(30 <math>\mu\text{L}</math>)</b>	Water: 970 H <sub>2</sub> O <sub>2</sub> : 0	Water: 954 H <sub>2</sub> O <sub>2</sub> : 16	Water: 938 H <sub>2</sub> O <sub>2</sub> : 32	Water: 873 H <sub>2</sub> O <sub>2</sub> : 97	Water: 808 H <sub>2</sub> O <sub>2</sub> : 162
<b>PVD</b> <b>(10 <math>\mu\text{L}</math>)</b>	Water: 990 H <sub>2</sub> O <sub>2</sub> : 0	Water: 974 H <sub>2</sub> O <sub>2</sub> : 16	Water: 957 H <sub>2</sub> O <sub>2</sub> : 33	Water: 891 H <sub>2</sub> O <sub>2</sub> : 99	Water: 825 H <sub>2</sub> O <sub>2</sub> : 165

Table 32: DLS Observations for polydispersity (PDI), Particle size (Mean  $\phi_{nm}$ ) and sample quality (Intercept). Obtained PDI range and intercept values confirms that the samples preparation is in optimal range to conduct DLS studies.

Particle ->	SP	Iso	JP	PVD
<b>PDI range -&gt;</b>	0.03 – 0.05	0.23 – 0.30	0.33 – 0.45	0.18 – 0.28
<b>Mean <math>\phi \pm \text{SD}</math> (nm) -&gt;</b>	467 $\pm$ 7.6	406 $\pm$ 35.2	595 $\pm$ 70.5	568 $\pm$ 23.5
<b>Mean Intercept -&gt;</b>	0.96	0.89	0.93	0.94

Table 33: Mean values for physical properties (size and weigh) of particles studied in this thesis summarized in the table. Calculated values are obtained from properties (like density, size, and gold layer-thickness for PVD) shared in section 2.4 of Chapter 2.

Particle	Maximum Mean Size (nm)	Weight (g)	Summary
<b>SP</b>	500	1.52E-13	Smallest, lightest
<b>Iso</b>	550	1.78E-13	Largest, second heavy
<b>JP</b>	525	1.65E-13	Second large, second lightest
<b>PVD</b>	520	3.16E-13	Second small, heaviest

Table 34: Number of tracked spots obtained from Particle Tracking via TrackMate (Spot Result)

% (v/v) [H <sub>2</sub> O <sub>2</sub> ]	No. of Tracked Spots obtained from Particle Tracking via TrackMate			
	SP	Iso	JP	PVD
<b>0</b>	270	234	103	208
<b>5</b>	230	135	104	252
<b>10</b>	238	117	265	152

## Annex-3

Table 35: Velocity of particles from each round of experiments.

[H <sub>2</sub> O <sub>2</sub> ] % (v/v)	R1				R2		
	SP	Iso	JP	PVD	Iso	JP	PVD
0	7.84	7.93	7.56	7.61	8.03	7.29	7.69
5	7.90	8.41	9.55	8.78	8.49	9.38	8.46
10	7.94	9.86	11.15	8.53	9.28	10.79	9.41

Table 36: Diffusion Coefficient for particles from each round of experiment

[H <sub>2</sub> O <sub>2</sub> ] % (v/v)	R1				R2		
	SP	Iso	JP	PVD	Iso	JP	PVD
0	1.38	1.41	1.29	1.30	1.45	1.20	1.33
5	1.41	1.59	2.05	1.74	1.62	1.98	1.61
10	1.42	2.19	2.80	1.64	1.94	2.62	1.99

Table 37: Comparison of diffusion coefficient from experiments with hydrogen peroxide gradient and no-gradient

[H <sub>2</sub> O <sub>2</sub> ]	Experiment	SP	Iso	JP	PVD
0%	No Gradient	0.96	0.68	1.04	3.10
	Gradient	1.38	1.43	1.24	1.32
5%	No Gradient	0.91	0.77	1.40	3.38
	Gradient	1.41	1.60	2.01	1.67
10%	No Gradient	0.93	0.81	2.33	2.32
	Gradient	1.42	2.06	2.71	5.81

## Summary

**Titre:- Colloïdes radiotactiques: vers des nanorobots de décontamination**

**Mots-clés: Colloïdes actifs, particules Janus, microfluidique, géométrie complexe, suivi des particules**

L'énergie nucléaire est une source d'électricité essentielle, notamment en France, où elle produit environ 70 % de l'électricité totale. Cependant, la décontamination, processus essentiel du déclassement nucléaire, est confrontée à des défis, en particulier dans des confinements et des géométries complexes. Cette recherche s'est concentrée sur l'exploration des perspectives de robots de décontamination au niveau supramoléculaire, en particulier des particules Janus actives. L'objectif principal était le développement et la caractérisation de particules Janus d'or/silice pour un mouvement autonome vers le peroxyde d'hydrogène ( $H_2O_2$ ) (imitant la chimiotaxie observée chez les micro-organismes). Cette recherche comprenait la synthèse, la caractérisation et l'étude du mouvement de ces particules, en mettant l'accent sur leur potentiel en tant que colloïdes radiotactiques ; particules qui se déplacent en réponse à des sources de contamination radioactive. Les deux principales techniques de synthèse utilisées ici étaient la « synthèse chimique via la méthode d'émulsion Pickering » et le « dépôt physique en phase vapeur » (PVD). La microscopie électronique à balayage (MEB), la spectroscopie à rayons X à dispersion d'énergie (EDX), la spectroscopie UV-Vis et la diffusion dynamique de la lumière (DLS) ont été utilisées pour la caractérisation des particules. Le mouvement des particules a été analysé dans des environnements de peroxyde d'hydrogène ( $H_2O_2$ ) à l'aide du DLS et de la vélocimétrie de suivi des particules (PTV). Un dispositif microfluidique a été développé pour générer des gradients  $H_2O_2$  stables, ce qui était crucial pour étudier le mouvement directionnel (dans un environnement  $H_2O_2$ ) des particules. Les particules Janus ont montré une mobilité améliorée (la plus élevée) et un mouvement directionnel vers des concentrations plus élevées de  $H_2O_2$  par rapport aux autres particules. Cependant, cette étude a également révélé que la structure Janus n'était pas une exigence absolue pour l'induction d'un mouvement directionnel dans les particules modifiées en surface. Ce comportement soutient leur utilisation potentielle pour la localisation autonome de points chauds de rayonnement (où la présence de  $H_2O_2$  est inévitable) avec une précision à l'échelle microscopique, et donc utile pour faciliter la mobilité au sein de géométries complexes. En plus de l'intégration d'agents chélateurs (spécifiques aux contaminants radioactifs) à la surface des particules (pour des capacités de décontamination), les prochaines étapes de cette thèse pourraient se concentrer sur l'optimisation de la taille des particules, l'exploration de l'utilisation de silice poreuse et le développement de particules avec des catalyseurs rentables pour production à grande échelle.

**Title:- Radiotactic colloids: towards the Decontamination Nanobots**

**Keywords: Active Colloids, Janus Particles, Microfluidics, Complex Geometry, Particle Tracking**

Nuclear power is a critical source of electricity, especially in France, where it generates ~70% of the total electricity. However, decontamination, an essential process in nuclear decommissioning, faces challenges, especially in intricate confinements and complex geometries. This research focused on exploring the prospect of supramolecular level decontamination robots, particularly active Janus particles. The primary focus was the development and characterization of gold/silica Janus particles for autonomous motion towards hydrogen peroxide ( $H_2O_2$ ) (mimicking chemotaxis observed in microorganisms). This research comprised of the synthesis, characterization, and motion study of these particles, with an emphasis on their potential as radiotactic colloids; particles that move in response to radioactive contamination sources. Two main synthesis techniques employed here were 'chemical synthesis via the Pickering emulsion method' and 'physical vapour deposition' (PVD). Scanning electron microscopy (SEM), energy-dispersive X-ray spectroscopy (EDX), UV-Vis spectroscopy, and dynamic light scattering (DLS) were utilized for particle characterization. Particle-movement was analyzed in hydrogen peroxide ( $H_2O_2$ ) environments using DLS and particle tracking velocimetry (PTV). A microfluidic device was developed to generate stable  $H_2O_2$  gradients, which was crucial for studying the directional movement (in  $H_2O_2$  environment) by particles. Janus particles showed enhanced (highest) mobility and directional movement towards higher concentrations of  $H_2O_2$  compared to other particles. However, this study also found that the Janus structure was not an absolute requirement for the induction of directional motion in surface modified particles. This behaviour supports their potential use for autonomous localization of radiation hotspot (where presence of  $H_2O_2$  is inevitable) with micro-scale precision, and thus, helpful in easier mobility within complex geometries. In addition to integration of chelating agents (specific for radioactive contaminants) onto particle-surface (for decontamination abilities), next steps from this thesis could focus on optimizing particle size, exploring the use of porous silica, and developing particles with cost-effective catalysts for large-scale production.